

Synthetic control in low dimensional 'Pb' and 'Pb-free' perovskites for rationalizing the origin of their luminescence properties

by

Anupam Biswas
10CC18A26001

A thesis submitted to the
Academy of Scientific & Innovative Research
for the award of the degree of
DOCTOR OF PHILOSOPHY
in
SCIENCE

Under the supervision of
Dr. Durba Sengupta
Supervisor
Dr. Janardan Kundu
Co-supervisor



CSIR- National Chemical Laboratory, Pune



Academy of Scientific and Innovative Research
AcSIR Headquarters, CSIR-HRDC campus
Sector 19, Kamla Nehru Nagar,
Ghaziabad, U.P. – 201 002, India

August, 2021

Certificate


This is to certify that the work incorporated in this Ph.D. thesis entitled, “Synthetic control in low dimensional 'Pb' and 'Pb-free' perovskites for rationalizing the origin of their luminescence properties”, submitted by Anupam Biswas to the Academy of Scientific and Innovative Research (AcSIR), in partial fulfillment of the requirements for the award of the Degree of Doctor of Philosophy in Science, embodies original research work carried-out by the student. We, further certify that this work has not been submitted to any other University or Institution in part or full for the award of any degree or diploma. Research material(s) obtained from other source(s) and used in this research work has/have been duly acknowledged in the thesis. Image(s), illustration(s), figure(s), table(s) etc., used in the thesis from other source(s), have also been duly cited and acknowledged.



Anupam Biswas

Research student

16th August, 2021



Dr. Janardan Kundu

Co-supervisor

16th August, 2021



Dr. Durba Sengupta

Supervisor

16th August, 2021

STATEMENTS OF ACADEMIC INTEGRITY

I *Anupam Biswas*, a Ph.D. student of the Academy of Scientific and Innovative Research (AcSIR) with Registration No. *10CC18A26001* hereby undertake that, the thesis entitled *Synthetic control in low dimensional 'Pb' and 'Pb-free' perovskites for rationalizing the origin of their luminescence properties* has been prepared by me and that the document reports original work carried out by me and is free of any plagiarism in compliance with the UGC Regulations on *"Promotion of Academic Integrity and Prevention of Plagiarism in Higher Educational Institutions (2018)"* and the CSIR Guidelines for *"Ethics in Research and in Governance (2020)"*.

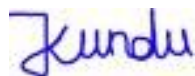


Signature of the Student

Date: 16th August, 2021

Place: Pune

It is hereby certified that the work done by the student, under my/our supervision, is plagiarism- free in accordance with the UGC Regulations on *"Promotion of Academic Integrity and Prevention of Plagiarism in Higher Educational Institutions (2018)"* and the CSIR Guidelines for *"Ethics in Research and in Governance (2020)"*.



Signature of the Co-supervisor

Name: Dr. Janardan Kundu

Date: 16th August, 2021

Place: Tirupati



Signature of the Supervisor

Name: Dr. Durba Sengupta

Date: 16th August, 2021

Place: Pune

Acknowledgements

In this pleasant moment, I would like to acknowledge the individuals who supported me throughout the journey and made it possible.

It gives me immense pleasure to thank my research supervisors, Dr. Janardan Kundu and Dr. Durba Sengupta for their immense constant support. Their exceptional guidance, constant encouragement, and constructive criticism during my doctoral studies are precious and a great source of learning. I consider myself incredibly fortunate to get the opportunity to learn from my supervisors who have taught me discipline and have shown unique ways to achieve goals. I sincerely acknowledge the freedom provided to work in the laboratory, allowing independent thinking to flourish, planning, and execution of research. I believe, the better way of thanking him would be through my future contributions to the scientific community.

I am obliged to my Doctoral Advisory Committee Members, Dr. Shatabdi Porel Mukherjee, Dr. Arup Kumar Rath, and Dr. Samir H. Chikkali, for their continued guidance and suggestions.

I am grateful to Prof. Dr. Ashwini K. Nangia (Former Director, NCL), Prof. Dr. Ashish Kishore Lele (Director, NCL), Dr. P. A. Joy (Former Head, Physical & Materials Chemistry) and Dr. B. L. V. Prasad (Head, Physical & Materials Chemistry) for providing all the necessary infrastructure and facilities.

My sincere thanks to Dr. Santosh Babu Sukumaran, Dr. Sakya S. Sen, Dr. Nandini Devi, and Dr. J. Nithyanandhan for their scientific inputs and encouragements. Furthermore, I want to express my thanks to Dr. K. Selvaraj, Mr. R. S. Gholap for their help in HR-TEM, FE-SEM measurements, Dr. Suresh Gokhale and Mrs. W. Rupali for her help in Raman measurements, and Mr. Srinivas Deo for helping in XPS measurements. I would like to extend my sincere thanks to Dr. Rajesh Gonnade, Dr. Samir Sheikh, Dr. Vir Bahadur, and Mr. Bhupendra Mali for single-crystal XRD measurement and providing me all the necessary scientific understanding.

I would like to express my gratitude to Dr. Anshuman Nag, Dr. Partha Hazra, Dr. Pinaki Talukdar from IISER, Pune, Dr. D. D. Sarma, Dr. P Tilagar from IISc, Bangalore, Dr. Dinesh Kabra from IIT, Bombay, Dr. Santosh Kumar Raavi, Mr. Chinmoy Biswas from IIT, Hyderabad, Dr. Shailaja Mahamuni from SPPU, Pune for their immense help during various characterizations.

It is my pleasure to thank Dr. Rangarajan for his immense support and productive scientific discussion. I would like to thank present and past lab members, Prasenjit, Debu, Ashish, Dr. Srikanth, Saptam, Abijith, Chandan, Neha, Asif, Haris and Salman for their scientific suggestion and making my stay at NCL memorable and enjoyable.

I would like to take the opportunity to thank my Master's supervisor Dr. Tapas Kumar Mandal, IIT Roorkee for introducing me to the field of research and being a constant source of inspiration.

I am thankful to Dr. Raja Das and Dr. Pankaj Poddar & group, for their scientific suggestion during my initial days at NCL.

I would like to appreciate DST and CSIR- New Delhi (SRF award) for providing the necessary funding to carry out the research work.

My family has always been a source of inspiration for me in not only perceiving my education but in all other aspects of my life too. I am forever indebted to Maa and Baba for their unconditional support and enthusiasm. I like to thank my brother Bapi, Boudi and nephew, Aritra for always being there for me. I appreciate my in-laws, Mummy and Papa for encouragement and showing confidence in me. I am grateful to Bhaiya, Bhabi, nephews, Shivansh and Dedvansh for adding joy to my stay here.

Cheers to the warm love from my feline family Pussu, Babli, Kukku, Whisky, Gufri and many others who made my tiring days relaxing and brought liveliness to my stay at NCL!

I would like to express my affection to my wife, *Gayatri* for being there throughout my thick and thin. She has always been my ultimate source of support during the journey. This journey would not have possible without her by my side.

My deepest love to my adorable daughter *Antra* for adding meaning to my efforts and bringing the sense of purpose to my life.

Last but not the least I want to thank *Almighty God* for the blessings and strength to deal with all the odds.

Table of contents

Abbreviations	viii
List of Symbols	viii
List of Figures	ix-xiii
List of Tables	xiv
Chapter 1	1-18
1.1 Introduction to halide perovskite	1
1.2 Dimensionality reduction in halide perovskite	2
1.3 Distortion in low dimensional perovskites	4
1.4 Luminescence in low dimensional perovskite	5
1.5 Nature of luminescence	7
1.6 Optical control/tunability with doping	8
1.7 Scope of the thesis	10
1.8 Thesis objective	11
1.9 Thesis outline	11
1.10 References	12
Chapter 2: Structure, connectivity and photophysical properties of lead-based 1D perovskite	19-40
2.1 Introduction	19
2.2 Materials	21
2.3 Synthesis	21
2.3.A) Synthesis of powdered PzPbBr 1D Perovskites	21
2.3.B) Synthesis of Single Crystals of PzPbBr 1D Perovskites	21
2.3.C) Synthesis of Single Crystals of PzPbCl 1D Perovskites	22
2.3.D) Synthesis of Single Crystals of PzPbBr _{1-x} Cl _x 1D Perovskites	22
2.4 Characterization techniques	22
2.5 Results and discussions	23
2.5.A) Optical property	25
2.5.B) Nature of emission	26
2.5.C) Thermal stability	27
2.5.D) Room temperature lifetime study	28
2.5.E) Low-temperature luminescence and lifetime study	28
2.5.F) Origin of broad band	30
2.5.G) Crystal structure analysis	32
2.5.H) Mixed halide	35
2.5.I) Structure-property correlation	36
2.6 Conclusions	37
2.7 References	38

Chapter 3: Dopant induced broadband emission in 2D lead-based perovskite	41-63
3.1 Introduction	41
3.2 Materials	43
3.3 Synthesis	43
3.3.A) Synthesis of C ₄ H ₉ NH ₃ Br (Butyl ammonium lead bromide)	43
3.3.B) Synthesis of single crystals of (C ₄ H ₉ NH ₃) ₂ PbBr ₄ 2D layered perovskite	43
3.3.C) Synthesis of Mn ²⁺ doped (C ₄ H ₉ NH ₃) ₂ PbBr ₄ 2D layered perovskite	44
3.4 Characterization methods	44
3.5 Results and discussion	45
3.5.A) Optical property	45
3.5.B) Effect of dopant concentration	48
3.5.C) Effect of thermal annealing on PL properties	49
3.5.D) Lifetime study	50
3.5.E) Morphology and elemental composition	52
3.5.F) Thermal stability	53
3.5.G) Nature of doping	54
3.6 Conclusions	58
3.7 References	58
Chapter 4: Importance of structure-distortion parameter in governing photophysical properties of 'Pb-free' perovskite	64-105
4A: Luminescent 0D organic-inorganic Antimony (III) hybrid	65
4.1 Introduction	65
4.2 Materials	67
4.3 Synthesis	67
4.3.A) Synthesis of powdered 1 tris Sb Green	67
4.3.B) Synthesis of Single Crystals of 1 tris Sb Green	67
4.3.C) Synthesis of Single Crystals of 2 tris Sb Red	68
4.3.D) Synthesis of powdered 3 tris Sb Yellow	68
4.3.E) Synthesis of Single Crystals of 3 tris Sb Yellow	68
4.4 Characterization methods	68
4.5 Results and discussion	69
4.5.A) Optical property	69
4.5.B) Lifetime study	70
4.5.C) Nature of emission	73
4.5.D) Low-temperature photoluminescence	76
4.5.E) X-ray diffraction study	77
4.5.F) Structure-property correlation in 1 tris Sb Green & 2 tris Sb Red	82
4.5.G) Effect of ligand concentration	86
4.5.H) Crystal structure of 3 tris Sb Yellow	90
4.5.I) Generality of structure-property relation	92
4.5.J) Thermal Stability	96
4.5.K) Phase purity	97
4.6 Conclusions	99
4.7 References	100

4B: Luminescent 0D organic-inorganic Tellurium (IV) hybrid	106-131
4.8 Introduction	106
4.9 Materials	108
4.10 Synthesis	109
4.11 Characterization methods	109
4.12 Results and discussion	110
4.12.A) Optical property	111
4.12.B) Nature of emission	112
4.12.C) X-ray diffraction analysis	115
4.12.D) Low-temperature photoluminescence, LED measurement	117
4.12.E) Stability & purity	122
4.12.F) Structure-property relation	125
4.13 Conclusions	126
4.14 References	127
Chapter 5: Summary and Future prospects	131-133

Abbreviations

CB	Conduction Band
VB	Valence Band
LD	Low dimension
PV	Photo voltaic
OIHP	Organic inorganic hybrid perovskite
E	Energy
FWHM	Full Width at Half Maximum
HOMO	Highest Occupied Molecular Orbital
LUMO	Lowest Unoccupied Molecular Orbital
Hz	Hertz
LED	Light Emitting Diode
mg	Milligram
min	Minute
mL	Millilitre
mm	Millimetre
mmol	Millimole
NIR	Near Infrared
PL	Photoluminescence
QDs	Quantum Dots
SEM	Scanning Electron Microscope
TEM	Transmission Electron Microscopy
XPS	X -ray Photoelectron Spectrometry
XRD	X-ray Diffraction

List of symbols

h	Plank Constant
°C	Degree Centigrade
%	Percentage

List of figures

Chapter 1

Figure no.	Figure title	Page
Figure 1	Structure of oxide and halide perovskite	1
Figure 2	Dimensionality related to the material physical dimension	2
Figure 3	Dimensionality related to connectivity of metal halide unit	3
Figure 4	Applications of low dimension perovskites	4
Figure 5	White light emission from halide perovskite	6
Figure 6	Energy states with nuclear coordinate	7

Chapter 2

Figure 1	Represents the reaction scheme of the pure halide and mixed halide perovskite. For the sake of simplicity $(\text{H}_2\text{O})(\text{C}_6\text{H}_8\text{N}_3)_2\text{Pb}_2\text{Br}_{10}$ is abbreviated as PzPbBr in the rest of the discussion	24
Figure 2	SEM and EDS analysis of PzPbBr	24
Figure 3	Photograph of single crystals of PzPbBr under (a) ambient; (b) UV light (c) optical properties (absorbance, PL, photoluminescence excitation at 580 nm); (d) CIE chromaticity coordinates for 1 (PzPbBr) and 2 ($\text{PzPbBr}_x\text{Cl}_{1-x}$)	25
Figure 4	(a) excitation dependent emission profile; (b) photoluminescence excitation collected across broad emission band	26
Figure 5	Effect of thermal annealing on luminescence properties	26
Figure 6	Intensity of broad emission increases as the excitation laser power is increased over three orders of magnitude.	27
Figure 7	Thermogravimetric weight loss analysis of PzPbBr	27
Figure 8	Room temperature time-resolved PL decay curves for PzPbBr single crystals measured across the broad emission band. Inset Table shows major and minor components of the decay time constants	28
Figure 9	(a) Steady-state low-temperature PL of PzPbBr; (b) temperature dependence of PL intensity and bandwidth	29
Figure 10	(a) Low-temperature lifetime; (b) average lifetime at different temperature	30
Figure 11	Fitting of FWHM as a function of Temperature with its associated parameters and fitting equation	31
Figure 12	Raman spectra of PzPbBr perovskite crystal excited with 633 nm laser	31
Figure 13	(a) asymmetric unit of PzPbBr; (b) sliced view highlighted the 1D contorted corner-shared structure with two octahedral unit wide chain; (c) view along c-axis; (d) clear view of the contorted 1D chain	32
Figure 14	comparison between powder XRD pattern of PzPbBr and XRD pattern simulated from single crystal data of PzPbBr	34
Figure 15	Comparison of XRD pattern with different halide compositions	35

Figure 16	Comparison of (a) Absorbance; (b) PL emission; (c) PLE; (d) Lifetime analysis for PzPbBr and Br-Cl mixed halide perovskites showing blue shifted absorbance and emission with lifetime lengthening	36
-----------	--	----

Chapter 3

Figure 1	Absorbance, PL, and PLE spectra for the undoped (top) and doped 2D perovskite	45
Figure 2	Left-image of host and Mn ²⁺ doped system. Right-optical properties of Mn ²⁺ doped (bottom) and undoped (top) host material showing the PL and PLE for the band edge and Mn ²⁺ emission	46
Figure 3	Excitation dependent PL spectra of the doped 2D perovskite	47
Figure 4	Dopant concentration-dependent PL spectra	48
Figure 5	Dopant concentration-dependent quantum yield of Mn ²⁺ emission (QY _{Mn})	48
Figure 6	Band edge PL decreases and dopant emission increases as annealing temperature is increased. Increased doping of host due to increased thermal diffusion	50
Figure 7	PL decay dynamics of (a) undoped host sample; (b) doped sample for the band edge emission; (c) doped sample for the Mn ²⁺ emission with inset showing the same at different dopant concentrations	51
Figure 8	TEM and Elemental mapping a) for (But) ₂ PbBr ₄ and b) Mn ²⁺ :(But) ₂ PbBr ₄ samples	52
Figure 9	TGA for the a) undoped and b) doped 2D perovskite	53
Figure 10	XRD pattern of (a) undoped and doped material both annealed at 125 °C with a magnified view as insets; (b) doped material annealed at 28 °C and 125 °C with a magnified view as insets	54
Figure 11	XRD pattern of (a) doped material at different dopant concentrations with their magnified views (b-e)	55
Figure 12	The mechanism of substitutional doping	

Chapter 4A

Figure 1	Absorbance (Abs), Photoluminescence (PL) and Photoluminescence excitation (PLE) spectra of a) 1 tris Sb Green , and b) 2 tris Sb Red single crystal samples	70
Figure 2	TCSPC Lifetime analysis for products 1 tris Sb Green (a,c) and 2 tris Sb Red (b,d) at room temperature across the broad band emission with estimated lifetimes in nanoseconds	71
Figure 3	Lifetime decay profiles for products 1 tris Sb Green (a) and 2 tris Sb Red (b) at room temperature collected across emission band using microsecond flash lamp excitation (360 nm)	71
Figure 4	Dependence of photoluminescence (PL) on excitation wavelength and photoluminescence excitation (PLE) spectrum collected across the broad PL peak for a) 1 tris Sb Green , and b) 2 tris Sb Red powder samples	74
Figure 5	PL/PLE of 1 tris Sb Green and 2 tris Sb Red samples upon a-b) room temperature grinding (10 mins, mortar-pestle) and c-d) annealing of the	75

	ground powders at different temperatures. The drastic drop of PL/PLE intensity for 1 and 2 at around 100 °C is related to the loss of solvent (water) molecules integral to the stability of the structure of the products through a network of hydrogen bonding	
Figure 6	Low-temperature photoluminescence spectra of a) 1 tris Sb Green and b) 2 tris Sb Red powder samples excited at 370 nm and 350 nm respectively using a μ s flash lamp	76
Figure 7	Integrated PL peak area and FWHM of the broad PL peak for a) <i>1 tris Sb Green</i> , and b) <i>2 tris Sb Red</i> powder samples as a function of temperature (300 – 80 K)	77
Figure 8	a): A view of the molecular packing down the b-axis in crystals of 1 (<i>tris Sb Green</i>) showed the associations of the metal halide, organic ligands, and water molecules	78
Figure 9	Single crystal structures of zero-dimensional chloro antimonite (III) – organic hybrids for (a-c) 1 tris Sb Green , and (d-f) 2 tris Sb Red respectively. Shown also are the metal halide units (octahedra, dimer octahedra for 1 tris Sb Green ; distorted octahedra and distorted pyramid for 2 tris Sb Red) for both the products	79
Figure 10	A view of the molecular packing down the a-axis in crystals of 2 (<i>tris Sb Red</i>) showing the associations of the metal halide, organic ligands, and water	80
Figure 11	Comparison of the PXRD pattern with the simulated pattern from the single crystal structure data for a) 1 tris Sb Green, b) 2 tris Sb Red	82
Figure 12	Qualitative molecular orbital diagram of (a) octahedral and (b) square pyramidal metal-halide framework and the associated change in the energy gap between the HOMO and LUMO that manifests as PL emission energy difference between the two structures	84
Figure 13	Optical and structural characterization of 3 tris Sb yellow -(a) Absorbance (Abs), Photoluminescence (PL), and Photoluminescence excitation (PLE) spectra	87
Figure 14	Dependence of photoluminescence (PL) on excitation wavelength and photoluminescence excitation (PLE) spectrum collected across the broad PL peak for 3 tris Sb Yellow powder samples	87
Figure 15	Dependence of PL and PLE on a) grinding and b) annealing for 3 tris Sb Yellow powder samples	88
Figure 16	Lifetime decay profiles collected across the yellow emission band using microsecond flash lamp excitation (360 nm)	88
Figure 17	An overview of single crystal structure of 0D 3 tris Sb Yellow product and metal halide units (distorted quadrangular pyramid, octahedra, and distorted octahedra) comprising the 0D structure	90
Figure 18	A view of the molecular packing down the b-axis in crystals of 3 (<i>tris Sb Yellow</i>) showing the associations of the metal halide, organic ligands, and water molecules	91
Figure 19	Comparison of the PXRD pattern with the simulated pattern from the single crystal structure data for 3 tris Sb Yellow sample	92
Figure 20	Structural unit of a) 1 tris SB green b) 2 tris Sb red c) 3 tris Sb yellow	93

Figure 21	Photographic image of the synthesized crystals under 365nm light excitation and their PLQY values written below	95
Figure 22	Thermogravimetric weight loss analysis for a) 1 tris Sb Green, b) 2 tris Sb Red, c) 3 tris Sb Yellow, d) table listing the % weight losses incurred from the plausible structural components	96
Figure 23	(a). ¹ H NMR of Tris Cl salt (400 MHz, DMSO-d ₆ , 298 K): δ 8.20 (br, 9H, NH ₃), 3.01 (br, 6H, CH ₂), 2.65 (br, 6H, CH ₂) 3.36(br, 8H, H ₂ O) ppm.	97
	(b). ¹ H NMR of 1 Tris Sb Green (400 MHz, DMSO-d ₆ , 298 K): δ 8.17 (br, 9H, NH ₃), 3.02 (br, 6H, CH ₂), 2.70 (br, 6H, CH ₂), 4.97 (br, 9H, H ₂ O & 1H, NH) ppm.	98
	(c). ¹ H NMR of 1 Tris Sb Red (400 MHz, DMSO-d ₆ , 298 K): δ 8.18 (br, 9H, NH ₃), 3.03 (br, 6H, CH ₂), 2.72 (br, 6H, CH ₂), 5.46 (br, 6H, H ₂ O & 1H, NH) ppm	98
	(d). ¹ H NMR of 1 Tris Sb Yellow (400 MHz, DMSO-d ₆ , 298 K): δ 8.19 (br, 9H, NH ₃), 3.02 (br, 6H, CH ₂), 2.69 (br, 6H, CH ₂), 5.04 (br, 8H, H ₂ O & 1H, NH) ppm	99

Chapter 4B

Figure 1	a) Reaction scheme (anti-solvent diffusion) utilized for the synthesis of single crystals of (BzTEA) ₂ TeCl ₆ ; photograph of the synthesized crystals at room temperature under b) visible and c) UV illumination (365nm)	110
Figure 2	Optical characterization of (BzTEA) ₂ TeCl ₆ showing a) Absorbance (Abs), Photoluminescence (PL), and Photoluminescence excitation (PLE) spectra; (b) Lifetime decay profiles collected across PL band (λ _{exc} = 440 nm)	111
Figure 3	a) Excitation dependent a) PL and b) PLE collected across the broad emission band for (BzTEA) ₂ TeCl ₆ crystals	113
Figure 4	Comparison of the PL and PLE profile for (BzTEA) ₂ TeCl ₆ before and after grinding of the crystals	113
Figure 5	Comparison of the PL and PLE profile for (BzTEA) ₂ TeCl ₆ before and after grinding of the crystals along with their images under visible and UV light at room temperature	114
Figure 6	Decay profiles and the estimated lifetimes components along with their relative weights of (BzTEA) ₂ TeCl ₆ crystals excited at 440 nm	114
Figure 7	Effect of thermal annealing (from room temperature to 150 °C) of (BzTEA) ₂ TeCl ₆ crystals on the PL and PLE profiles. The excitation wavelength for PL is 445 nm, and PLE is collected at 610 nm	115
Figure 8	XRD characterization of (BzTEA) ₂ TeCl ₆ hybrid. Overview of the single-crystal structure (a); asymmetric unit (b); site symmetry of Metal-Halide octahedron (c); comparison of the simulated and experimental PXRD pattern using Cu source (d). H atoms are omitted in (b) for clarity	116

Figure 9	Site symmetry of the TeCl_6 octahedron showing various bond angles. Mathematical representation of quadratic elongation (λ_{oct}) and bond angle variance (σ^2) is also shown	117
Figure 10	a) Low Temperature PL ($\lambda_{\text{exc}}=440$ nm) spectra of $(\text{BzTEA})_2\text{TeCl}_6$ crystals; b) Integrated PL intensity and bandwidth (FWHM) as a function of temperature	118
Figure 11	a) Arrhenius plot of natural logarithm of PL intensity against inverse temperature for broadband emission, b) fitting of the bandwidth (FWHM) as a function of temperature	119
Figure 12	Raman spectra of $(\text{BzTEA})_2\text{TeCl}_6$ crystals collected using 633 nm excitation laser source. The inset shows the low-frequency phonon modes of the Te-Cl octahedron	120
Figure 13	Lifetime decay profile of $(\text{BzTEA})_2\text{TeCl}_6$ crystals collected at low temperatures. Table lists the fitted lifetimes and their relative weights	120
Figure 14	(a) Schematic representation of the configurational coordinate diagram showing the STE-based broadband emission and thermally activated (phonon assisted) non-radiative recombination leading to thermal PL quenching in OD hybrids. LED characterization b) electroluminescence of commercial bare LED, down-converted luminescence from sample coated LED, and neat sample photoluminescence; Inset shows photographs of i) commercial bare LED and ii) sample coated down-conversion LED; c) CIE 1931 Chromaticity coordinate plot for commercial blue LED, down-conversion LED, and neat sample emission	121
Figure 15	Thermogravimetric weight loss analysis and the derivative of the weight loss curve for $(\text{BzTEA})_2\text{TeCl}_6$ crystals	123
Figure 16	Comparison of PL profile collected ($\lambda_{\text{exc}}=440$ nm) over time of ambient exposed $(\text{BzTEA})_2\text{TeCl}_6$ hybrid	123
Figure 17	Comparison of PXRD pattern (using Mo source) of as-synthesized and after one-month ambient exposure of $(\text{BzTEA})_2\text{TeCl}_6$ hybrid with that of the simulated pattern (using Mo Wavelength)	124
Figure 18	^1H NMR spectra of (a) benzyl triethylammonium chloride and (b) $(\text{BzTEA})_2\text{TeCl}_6$ product in DMSO- D_6	125

List of tables

Chapter no: table no	Table caption	page
2: Table 1	Crystal data and structure refinement for PzPbBr	32
4A: Table 1	Lifetime (μs) components and relative weights (%) for the decay profiles presented above in Figure 3	73
4A: Table 2	Lifetime (μs) components and their relative weights (%) for 3 tris Sb Yellow	89
4A: Table 3	List of estimated bond length asymmetry and bond angle variations (from ideal value) in metal halide frameworks of 1, 2, 3 as obtained from single-crystal structures	93
4A: Table 4	Comparison of Stokes shift, PL peak position and PLQY with the structure	94

Chapter 1

1.1 Introduction to halide perovskite:

The general structure of halide perovskite ABX_3 is analogous to its oxide counterpart ABO_3 where A and B are cations, O and X are anions (Figure 1). The classic example of oxide perovskite is $CaTiO_3$ named after the Russian mineralogist Lev Alekseyevich von Perovski. Later on, similar structures were also discovered e.g., $BaTiO_3$, $PbTiO_3$, $SrTiO_3$, $BiFeO_3$. Here in the structure, the B action adopts 6 fold coordination, and the A cation has 12 fold coordination¹. In the case of halide perovskite, the A-site cation can be considered by appropriately fitting in the space created by metal halide octahedra and governed by the Goldschmidt tolerance factor (t), and importantly the radii of A-site cation must satisfy the geometric condition give below

$$(R_A + R_X) = t \sqrt{2} (R_M + R_X)$$

R_A , R_M are radii of A and M Cation, R_X is the Radii of the X anion

Typically, the value of 't' should be close to 1 for a stable perovskite structure. In this regard, the A-site cation can be either inorganic (Cs, Rb, etc.) or organic (methyllummonium, formamidinium, etc.).

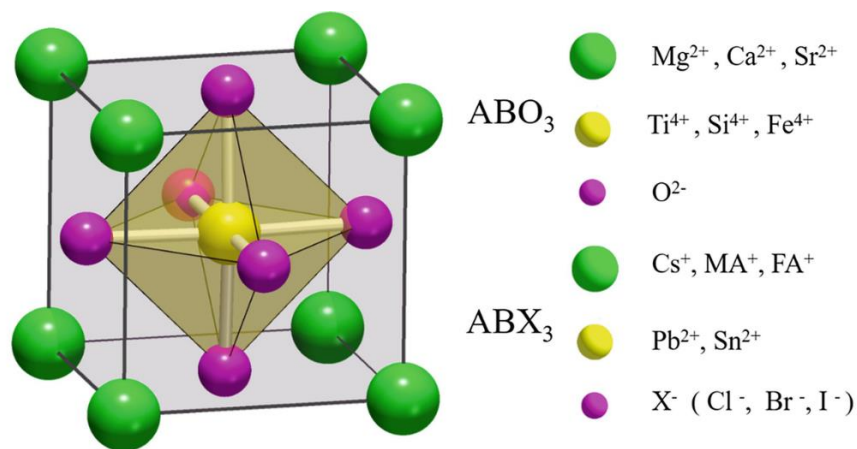


Figure 1: Structure of oxide and halide perovskite.

The structures extended over 3 dimensions and giving rise to 3-dimensional networked (DN) perovskite. The bulk phases of halide perovskite (e.g. $CsPbCl_3$) were known since 1969². Organic 'A' site cation included perovskites are known as organic-inorganic hybrid perovskite (OIHP).

The last decade has seen a meteoritic rise for hybrid perovskite after reports by Miyasaka *et al.* and Snaith *et al.* owing to their use as potential photovoltaics (PV) applications^{3,4}. Since then, the research field has gathered colossal attention and grown exponentially to the research community around the globe. The low temperature, low-cost solution processibility, high crystallinity, defect tolerance, and ease of device fabrications are the primary essential factors for choosing the materials over the conventional materials. The rapid rise of photovoltaic performance in measuring power conversion efficiency (PCE), which reached 25% for hybrid perovskite devices, is unprecedented to crystalline silicon-based technology. Studies showed that this hybrid perovskite could have other potential applications beyond solar cells, such as light-emitting diodes, photodetectors, X-ray detectors, etc.⁵⁻¹⁰ Recently, this hybrid perovskite has also emerged as a promising class of optically pumped broad light-emitting phosphors as well¹¹.

1.2 Dimensionality reduction in halide perovskite:

Confinement of electrons in different dimensions for semiconductors is the most valued avenue for getting the requisite property. Typically, in semiconductors, the confinement is achieved by considering physical dimensions and consequently gives rise to different structures such as nanoplates (2D), nanorods (1D), and quantum dots(0D)(Figure 2). In the case of halide perovskite, we can do similar electron confinements in the bulk systems without compromising the physical dimensions. Here the electrons and charge carriers were confined and controlled by the metal halide octahedral unit along different dimensions (Figure 3). Notably, the dimensionality is primarily governed by the connectivity of the metal halide octahedra over the physical dimensions¹².

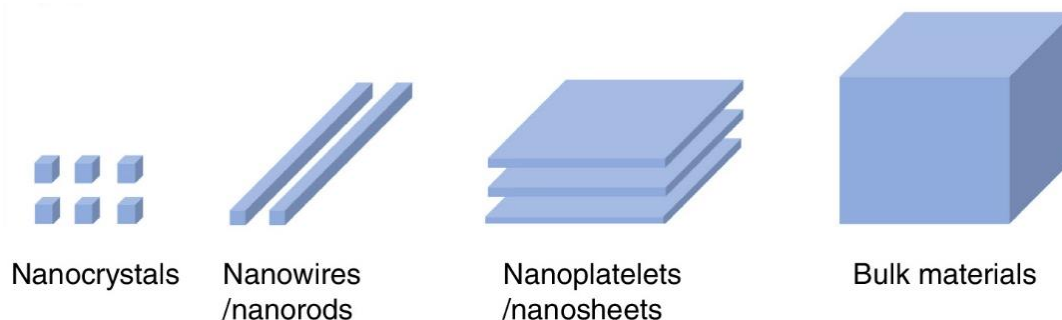


Figure 2: Dimensionality related to the material physical dimension.¹³

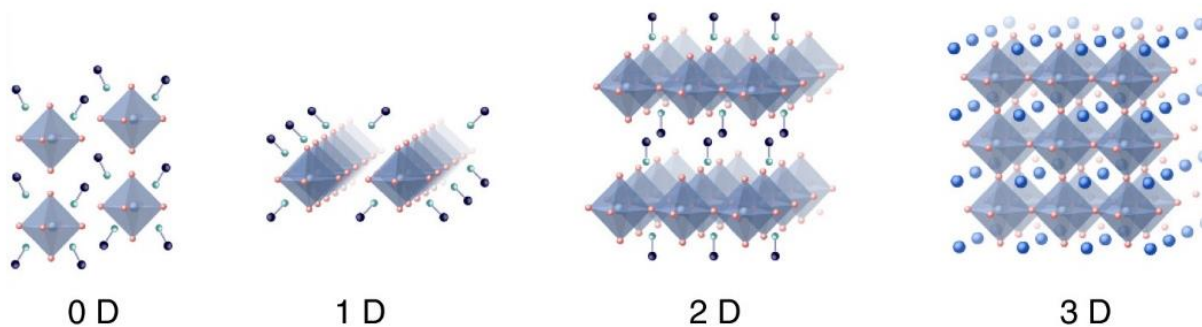


Figure 3: Dimensionality related to connectivity of metal halide unit.¹³

Typically, a 3-dimensional networked (3DN) perovskite structure is all corner connected or shared within the $[BX_6]^{4-}$ octahedra and extends over all dimensions. The A-site cation occupies the space created by the metal halide octahedra (provides overall negative charge) with appropriate valence state and overall upholds the structure with strong electrostatic interaction within themselves. Increasing the cationic size with suitable organic ammonium ion can lead to disconnection in the octahedral connections and subsequently generates lower-dimensional organic-inorganic hybrid perovskite. The 3DN perovskite¹⁴ slicing the specific crystallographic plane with bulkier organic cation will lead to 2DN perovskite. The hybrid^{9,15-21} mixture of 3DN and 2DN perovskite is often designated as quasi-2DN perovskites. The further disconnection in 2DN perovskite and can lead to the growing of octahedral units in 1DN²²⁻²⁶. For a 1D system, the connectivity can be of different types, such as corner connected, edge connected, face connected, or combinations. An isolated octahedral surrounded by organic cation in all 3 dimensions is the extreme case and abbreviated as 0DN perovskite²⁷⁻⁴⁰.

The relaxation of Goldschmidt's tolerance factor in low dimensional (LD) perovskite results in the accommodating capability of various organic amine ligands. This incorporation of various organic cations provides the ultimate compositional versatility and much more affluent than all class compounds known to date. The introduction of bulky and hydrophobic organic cation in LD perovskite improves the material stability over ambient moisture attack. The crystalline nature of LD perovskite is well preserved by the conventional low-temperature solution-based method. Device fabrication is relatively easy and scalable using spin coating, deep coating, host casting, drop-casting methods. Due to its high crystalline nature, LD perovskite has a lower ionic defect and lesser grain boundary.^{21,41} The charge transport properties are greatly improved because of

lower surface defects for these hybrids. More importantly, the optical property is highly tunable in the LD perovskite due to its diverse nature of the composition of the metal, halide, and organic cations.

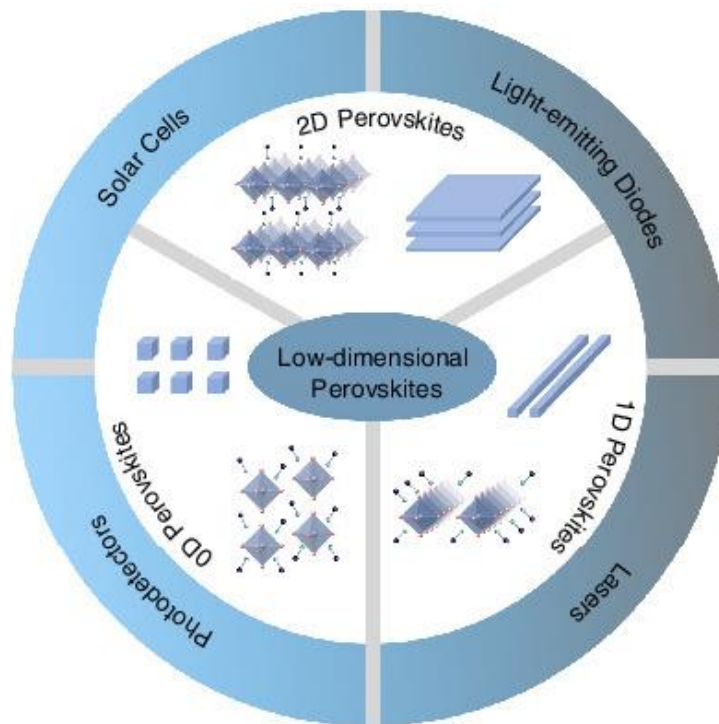


Figure 4: Applications of low dimension perovskites.¹³

For LD perovskites, due to quantum and dielectric confinements of carriers, the exciton binding emerges typically very high (hundreds of millielectronvolts). The strongly bound excitons in LD perovskites make a suitable candidate for lighting applications. On the contrary, for 3D perovskites, the exciton binding energies are typically low, suitable for solar cell applications.^{8,42,43} The dominant radiative recombination in LD perovskite will result in high photoluminescence quantum yield (PLQY), and this is highly valued for high-performance phosphors, lasers, photodetectors, solar cell, and solid-state lighting applications (Figure 4)^{10,12,43,44}

1.3 Distortion in low dimensional perovskites:

The lower structural rigidity on the metal halide octahedra in LD perovskite can give rise to distortions in their bond length and bond angles. The structural feature in the ground state, such as

bond length and bond angle, may impact optical properties. Bond angle distortion is calculated from deviation of ideal geometry (180°, 90°, etc.), and bond length distortion is calculated from the difference of highest and lowest bond lengths. Higher the deviation from the ideal condition will cause lower overlap between metal and halide atomic orbital and subsequently widens the bandgap or blue shift the absorption maxima.^{45,46} The photoluminescence efficiency and nature of emission may be correlated to MX₆ octahedral deformations from the ideal octahedral symmetry. Mathematically and quantitatively, the octahedral distortion is evaluated by octahedral angle variance σ_{oct} and octahedral elongation λ_{oct} as shown below^{12,16,45},

$$\lambda_{\text{oct}} = \frac{1}{6} \sum_{i=1}^6 (d_i/d_0)^2 \quad , \quad \sigma_{\text{oct}}^2 = \frac{1}{11} \sum_{i=1}^{12} (\alpha_i - 90)^2$$

Here, d_i are six independent metal–halide bond lengths, d_0 is the mean metal–halide bond length, and α_i are the halide-metal–halide angles.

This reveals the degree of distortion in the inorganic lattice. It was seen in literature that the distortion plays a crucial role in the generation of self-trapped excitons and leads to broad band emission^{11,20}.

1.4 Luminescence in low dimensional perovskite:

Typically lead-based halide perovskite is a direct band semiconductor where the valence band is composed of halide *p-orbital* and lead *s-orbital* while conduction band consists of lead *p-orbital*. 3DN perovskite has a higher screening effect, and due to that, the exciton binding energy is on the lower side (~50meV). Since room temperature contains ~26 meV of energy, the exciton fission is easier for 3D systems, and hence electrons and holes are separated easily, and they will be useful for solar photovoltaics. In contrast, the 2DN perovskite the exciton binding energy is more than 150 meV in most of the cases.¹⁹ This higher exciton binding energy stems from the quantum and dielectric confinement. The quantum (form inorganic lattice) and dielectric (for organic ligands) confinements cause a high *Columbic* interaction between the electron and hole. The binding energy increases to hundreds of millielectron volts. Generally, for LD perovskite, the band-to-band transition will cause a sharp and strong excitonic absorption and with a narrow photoluminescence full-width half maximum (FWHM) of 10-30 nm. Although some of the LD perovskites possess

broadband (FWHM > 100 nm) emission with highly stokes-shifted photoluminescence (>1 eV)^{9,11,16,18,19,21,39,47,48}.

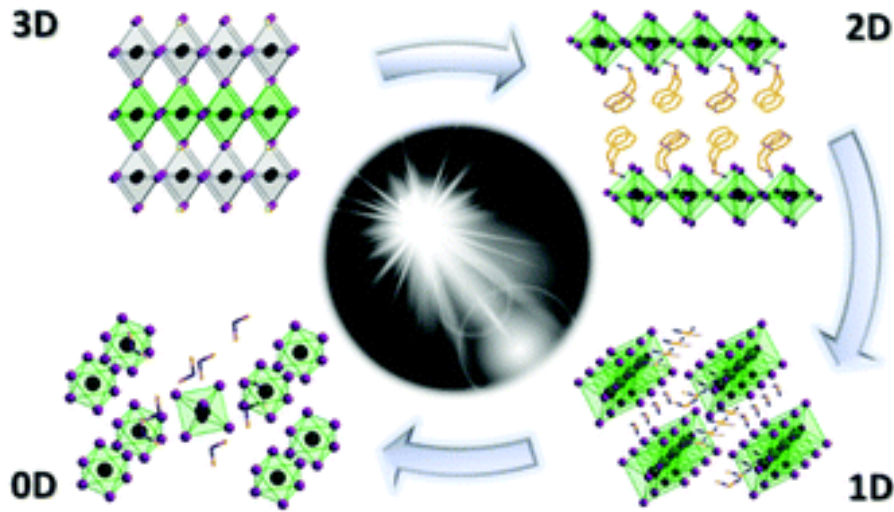


Figure 5: White light emission from halide perovskite⁴⁹.

This broadband emission is generally attributed to photo-generated intra-gap transient states, typically known as the self-trapped state (STE). It causes the widening of energy distribution among the materials. Excitonic self-trapping is boosted by deformation in lattice after photoexcitation (Figure 5). So, a higher vibration degree of freedom of the lattice will enhance the self-trapping of excitons. So, it is expected that at lower the dimension, perovskite will be more deformable upon photoexcitation, and hence more will be STE-based broadband emission. STEs are more like excited state defects and are further classified as extrinsic and intrinsic in nature. For intrinsic self-trapping, the transient lattice distortion does not require a permanent lattice defect in the material. Whereas for extrinsic self-trapping local heterogeneity in lattice and permanent defect facilitates the trapping process. Further, the structure of self-trapped electron and hole were investigated by Smith *et al.* where the localization of charges occur around the PbBr structure⁴⁵.

Excitonic self-trapping has shown some dependence on the dimensionality, connectivity, and distortion in the metal halide octahedra⁵⁰. In the case of 2D perovskites, the broadband emission is well correlated with the octahedral distortion and out-of-plane lattice distortion^{21,45,46,51}, but for 1D and 0D systems, this correlating does not seem to hold true. LD perovskite, both ‘lead-based’ and ‘lead-free’ variant exhibits a highly stoke-shifted, broadband photoluminescence with near-white light chromaticity and they are highly valued for light-emitting applications^{5,12,16, 22,23,37,50-}

⁵². Commonly available technologies for white light emission are 1) a blue LED chip coated with a yellow phosphor or a mixture of green and red phosphors, and 2) UV LED coated with multiple monochromatic blue, green, and red phosphors. Although both these methods suffer from severe limitations like a change of emission color due to the difference in material decay, efficiency loss due to self-absorption, and poor color rendition. Alongside it is seen that most LEDs are fabricated using expensive rare earth materials, and processing the materials required extreme high temperatures. This will result in an overall increase in the cost of manufacturing and fabrication of this type of technology. In specific conditions to generate broadband emission, materials require to undergo doping of metal ion and can lead to an extrinsic surface defect during the process. Considering the challenges, a suitable single phasic material that can emit all spectrum of light is of paramount importance^{16,19,51}.

1.5 Nature of luminescence:

The generation of Stoke shifted broadband emission in LD perovskite creates significant research interest due to its enabling light-emitting applications. Typically, self-trapped states are closely located to the low-lying excited state. In the case of broad emission, the FWHM and PLQY remain unchanged with respect to various physical parameters such as film, powder, bulk, nanocrystals, edge, and surface defects. Even the grinding and annealing of the bulk phased restores the emission character. The luminescence intensity increases monotonically with the increasing power of the excitation source and shows no sign of saturation.

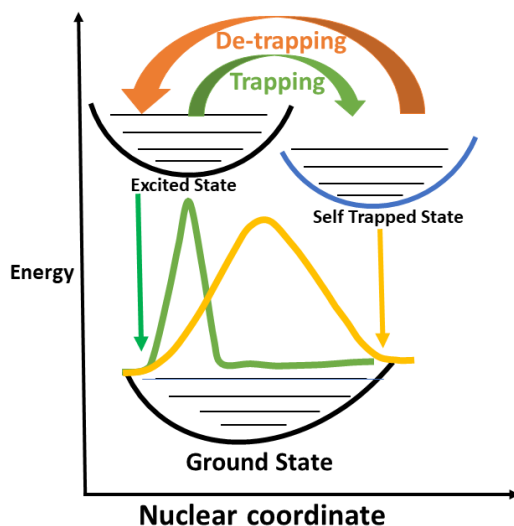


Figure 6: Energy states with nuclear coordinate.

These observations rule out the contribution of permanent defect-induced emission. In STE-based emission, electrons will hop from excited to self-trapped state and have to overcome the activation energy barrier. At room temperature, there is an existence of thermal equilibrium, which allows the trapping (excited state to self-trapped state) and detrapping (self-trapped state to excited state) to occur simultaneously (Figure 6). The detrapping possibility is reduced at lower temperatures due to high activation energy, and the self-trapped state population increases. This will lead to an increase of PL intensity. Whereas even lowering the temperature below a specific limit, the activation energy of trapping is unavailable will lead to lowering the population of STE state and consequently decrease the STE-based emission intensity. This typical behavior of temperature dependence is one of the important markers to identify STE-based broad emission. There will be the formation of multiple emissive states in LD perovskite after photoexcitation which generally dictates the broad nature, whereas for narrow emitter bleaching signature exist below excitonic absorption, evident from transient absorption studies. The excitonic self-trapping is closely related to the vibration modes of the metal-halide bond of LD perovskite²⁰. The reduced FWHM at a lower temperature is in agreement with the lower vibrational mode and associated couplings with the inorganic lattice.

1.6 Optical control/tunability with doping:

Doping of impurity ions in semiconductor materials has proved to be a unique way for the introduction of a new emission center and enables luminescence tuning⁵³⁻⁵⁵. Although doping strategy not necessarily changes the structure and fundamental photophysical property of host lattice. Doping is technologically crucial as it helps to reduce grain boundaries, decrease surface defects, enhances luminescence efficiency, and improves ambient stability, which is paramount for real-time applications⁵⁵. However, the doped system aimed to generate new properties by keeping the structure and dimension the same. Several divalent and trivalent metal ions doped in halide perovskite lattice show the success of optical tunability⁴¹. Among them, Mn⁺² ion draws considerable attention for its effective introduction of low energy emission from internal ⁴T₁ to ⁶A₁ transition, which is typically forbidden in nature. Higher exchange interaction and the presence of heavy metal are thought to be the key role player for strong luminescence. Although the Mn-centered emission wavelengths are very much dependent on the crystal field environments and

possess emission colors from green to red⁵⁶. Mn center in tetrahedral coordination (MnX_4^{2-}) shows green emission due to lower field strength and significant distance eliminating Mn centers' spin-spin coupling. Whereas octahedral coordination (MnX_6^{2-}) shows mild orange-red emission^{63,64}. The forbiddances of d-d transition in the octahedral field give rise to lower intense emission. The dopant concentration has a dominant role to play in luminescence intensity. The luminescence intensity gradually increases with Mn dopant concentration and decreases after a threshold point is reached. This concentration-dependent luminescence is primarily due to Mn-Mn clustering or coupling at higher concentrations⁵⁷. Also, reducing the Mn-Mn distance by increasing the dopant concentration can cause Red Shift in emission wavelength. So, both the crystal field strength and formation of the Mn-Mn pair may cause the color tunability. Alongside, Mn doping in ABF_3 ($\text{A} = \text{K}^+$; $\text{B} = \text{Mg}^{2+}, \text{Zn}^{2+}$) shows NIR emission and anti-ferromagnetic super exchange interaction within Mn^{2+} dimers⁵⁸. Excitation spectra confirm this variable emission wavelength which is originated from Mn centers. So overall, the luminescence property of the Mn center has a direct relation with the concentration of dopant and crystal field strengths.

Mn^{+2} ion-doped in 3DN halide perovskite has shown much success and proves its potential for lighting applications. The defect tolerance of trap state, tunability of bandgap, and energy transfer possibility for host lattice helps in the energy transfer from host to dopant Mn site and eventually leads to high luminescence⁵³. Many authors have reported the suitability of band energies and transfer of electrons from free excitons (FEs) to Mn center for CsPbCl_3 perovskite. Recently, the $\sim 600\text{nm}$ centered ${}^4\text{T}_1$ to ${}^6\text{A}_1$ orange-red emission reached $\sim 60\%$ quantum efficiency. Compared to 3DN perovskite low dimensional perovskite (2D, 1D, 0D) will be more suitable for doping due to their characteristic strongly bound excitons⁶¹. The quantum and dielectric confinement give rise to high exciton binding energy and enhance energy transfer from host to dopants. At present, the doping strategy for tuning the optical property is mainly concentrated in 3D and 2D systems^{55,60}. Nevertheless, doping induced synergistic emission from STEs, FEs, and Mn center and leading to broadband white light emission is still a challenge. The 'lead-free' low-dimensional system doped with Mn^{+2} ion is still in its incipient stage and needs to be explored further.

1.7 Scope of the thesis:

In the current scenario, LD perovskite (0D, 1D, 2D) composed of variable halide and ammonium ligand shows promising results in self-trapped mediated broad emission^{11,19,51}. There is much progress in answering the origin of photoluminescence property in LD perovskite, but the relation of light emission with perovskite structural feature is still unexplored. Broadly, this thesis aims to answer and understand the underlying principle for designing a perovskite structure and its relation to the optical property. Especially for 2D perovskites, the broad emission can be correlated to octahedra distortion and out-of-plane lattice distortion. 1D perovskites are different from the others in terms of their connections (edge share, face share, corner share, and combinations). Literature indicates that in a 1D structure, the optical property may have significant dependence on the connectivity mode. Reports suggested that edge-sharing connectivity will play a pivotal role in directing broadband emission. However, there are variations found in the same family. So, further validation is required to get the generality of the hypothesis. Doping can be a good choice for getting an additional level of optical control, although the bond energies for a 2D system preclude the success of the approach.

2D perovskite possesses higher binding energy in excitons because of that it possesses a high coulombic attraction of the electron and hole, and doping will be significantly important because there is a possibility of an energy transfer from a strongly bound exciton to dopant center. As mentioned above, expected scientific outcomes are primarily dealt with lead-based LD perovskites. However, considering toxicity and low to modest quantum efficiency in most reports, it prohibits its practical applications. For 'lead-free' perovskites, antimony and tellurium would be immensely interesting and relevant in keeping the ns^2 electronic configuration. Some of the antimony-based perovskites showed near unity luminescence values but the structure-property relation is still ambiguous. Typically, antimony perovskites are generally crystalizing in various possible polyhedral units. The main unanswered questions for antimony-based systems are 1) is there any correlation between the luminescence properties and the geometric structure/distortion of the metal-halide unit?. Moreover, 2) How does the presence/absence of distortion be related - PLQY and Stoke shift of the emission band? Finding a linear correlation in antimony-based perovskite may be difficult due to various polyhedral structures. In this regard, tellurium-based perovskite will be suitable because it primarily adopts octahedral geometry. On the other hand, all

the reported literature on tellurium-based perovskite has shown very poor photoluminescence makes then good for scientific study but bad for practical applications. So, the major concern lies in understanding the photophysical behavior of Pb-free perovskite with efficient luminescence. Through my thesis, I aim to address these issues and discussed them in detail in the working chapters.

1.8 Thesis objective:

- a) The primary objective of the thesis is to understand the nature of luminescence in 'Pb' and 'Pb-free' perovskite systems.
- b) Look for the structure-property correlation in a 'lead-free' zero-dimensional perovskite system.
- c) Exploration the tellurium-based perovskite with substantial room temperature STE based luminescent broadband emission.
- d) Optical flexibility by doping of metal ion in host lower dimensional perovskite system.
- e) Exploring the effect of connectivity vs. broadband self-trapped emission (STE) in Pb-based 1D perovskite. The probable factor in the contribution of broadband STE emission.

1.9 Thesis outline:

This thesis is divided into 5 chapters.

The 1st chapter provides the introduction of perovskite, dimensionality reduced structure, and photophysical property. This chapter also highlights the importance and reason behind broad emission in LD perovskites. Here we have briefly discussed the optical tunability in terms of doping of metal ion in the host matrix. 'lead-free' perovskite for efficient luminescence material was also introduced in the chapter. The chapter highlights the notable efforts by others in understanding photophysical behavior for LD perovskites.

The 2nd chapter deals with my effort in understanding the structure, connectivity, and photophysical properties of lead-based 1D perovskite. The study shows that 1D lead-based purely conner shared contorted structure can have comparable (with respect to best report in literature) efficient STE-based broad band emission at room temperature.

Anupam Biswas, Rangarajan Bakthavatsalam, Samir R. Shaikh, Aparna Shinde, Amruta Lohar, Satyam Jena, Rajesh G. Gonnade, and Janardan Kundu: Efficient Broad-Band Emission from Contorted Purely Corner-Shared One Dimensional (1D) Organic Lead Halide Perovskite, *Chem. Mater.* **2019**, *31*, 2253–2257.

The 3rd chapter is about doping-induced broadband emission in 2D lead-based perovskite. Here we present the 1st successful effort (best of our knowledge) of Mn²⁺ ion doping in butylammonium lead bromide (2D) and open up of internal ⁴T₁ to ⁶A₁ forbidden transition visible by intense orange emission (~600nm).

Anupam Biswas, Rangarajan Bakthavatsalam, Janardan Kundu: Efficient Exciton to Dopant Energy Transfer in Mn²⁺ Doped(C₄H₉NH₃)₂PbBr₄ 2D Layered Perovskites *Chem. Mater.*, **2017** *29*, 7816-7825.

The 4th chapter discusses the importance of structure-distortion parameter in governing photophysical properties of 'Pb-free' perovskite. Here we have tried to address the issue with antimony and tellurium-based zero-dimensional perovskite systems.

Anupam Biswas, Rangarajan Bakthavatsalam, Vir Bahadur, Chinmoy Biswas, Bhupendra P Mali, Sai Santosh Kumar Raavi, Rajesh G Gonnade and Janardan Kundu: Lead-free Zero Dimensional Tellurium (IV) Chloride-Organic Hybrid with Strong Room Temperature Emission as Luminescent Material, *J. Mater. Chem. C*, **2021**,*9*, 4351-4358.

Anupam Biswas, Rangarajan Bakthavatsalam, Bhupendra P Mali, Vir Bahadur, Chinmoy Biswas, Sai Santosh Kumar Raavi, Rajesh G Gonnade and Janardan Kundu: The metal halide structure and the extent of distortion control the photo-physical properties of luminescent zero dimensional organiantimony (III) halide hybrids, *J. Mater. Chem. C*, **2021**,*9*, 348-358.

The 5th chapter summarizes the thesis work with a conclusion and provides a future outlook in the research direction.

1.10 References:

- (1) Forrester, W. F.; Hinde, R. M. Crystal Structure of Barium Titanate. *Nature* **1945**, *156*, 177-177.
- (2) Natarajan, M.; Ramdas, S.; Rao, C. N. R. Antiferroelectric transition in CsPbCl₃. *Phys. Lett. A* **1969**, *29*, 528.
- (3) Kojima, A.; Teshima, K.; Shirai, Y.; Miyasaka, T. Organometal Halide Perovskites as Visible-Light Sensitizers for Photovoltaic Cells. *J. Am. Chem. Soc.* **2009**, *131*, 6050-6051.
- (4) Lee, M. M.; Teuscher, J.; Miyasaka, T.; Murakami, T. N.; Snaith, H. J. Efficient Hybrid Solar Cells Based on Meso-Superstructured Organometal Halide Perovskites. *Science* **2012**, *338*, 643.
- (5) Feng, J.; Gong, C.; Gao, H.; Wen, W.; Gong, Y.; Jiang, X.; Zhang, B.; Wu, Y.; Wu, Y.; Fu, H.; Jiang, L.; Zhang, X. Single-crystalline layered metal-halide perovskite nanowires for ultrasensitive photodetectors. *Nat. Electron.* **2018**, *1*, 404-410.
- (6) Pan, W.; Wu, H.; Luo, J.; Deng, Z.; Ge, C.; Chen, C.; Jiang, X.; Yin, W.-J.; Niu, G.; Zhu, L.; Yin, L.; Zhou, Y.; Xie, Q.; Ke, X.; Sui, M.; Tang, J. Cs₂AgBiBr₆ single-crystal X-ray detectors with a low detection limit. *Nat. Photonics* **2017**, *11*, 726-732.
- (7) Leijtens, T.; Bush, K. A.; Prasanna, R.; McGehee, M. D. Opportunities and challenges for tandem solar cells using metal halide perovskite semiconductors. *Nat. Energy* **2018**, *3*, 828-838.
- (8) Tsai, H.; Nie, W.; Blancon, J.-C.; Stoumpos, C. C.; Asadpour, R.; Harutyunyan, B.; Neukirch, A. J.; Verduzco, R.; Crochet, J. J.; Tretiak, S.; Pedesseau, L.; Even, J.; Alam, M. A.; Gupta, G.; Lou, J.; Ajayan, P. M.; Bedzyk, M. J.; Kanatzidis, M. G.; Mohite, A. D. High-efficiency two-dimensional Ruddlesden–Popper perovskite solar cells. *Nature* **2016**, *536*, 312-316.
- (9) Yangui, A.; Pillet, S.; Bendeif, E.-E.; Lusson, A.; Triki, S.; Abid, Y.; Boukheddaden, K. Broadband Emission in a New Two-Dimensional Cd-Based Hybrid Perovskite. *ACS Photonics* **2018**, *5*, 1599-1611.
- (10) Vashishtha, P.; Ng, M.; Shivarudraiah, S. B.; Halpert, J. E. High Efficiency Blue and Green Light-Emitting Diodes Using Ruddlesden–Popper Inorganic Mixed Halide Perovskites with Butylammonium Interlayers. *Chem. Mater.* **2019**, *31*, 83-89.
- (11) Cortecchia, D.; Yin, J.; Bruno, A.; Lo, S.-Z. A.; Gurzadyan, G. G.; Mhaisalkar, S.; Brédas, J.-L.; Soci, C. Polaron self-localization in white-light emitting hybrid perovskites. *J. Mater. Chem. C* **2017**, *5*, 2771-2780.

- (12) Mao, L.; Guo, P.; Kepenekian, M.; Hadar, I.; Katan, C.; Even, J.; Schaller, R. D.; Stoumpos, C. C.; Kanatzidis, M. G. Structural Diversity in White-Light-Emitting Hybrid Lead Bromide Perovskites. *J. Am. Chem. Soc.* **2018**, *140*, 13078-13088.
- (13) Zhu, P.; Zhu, J. Low-dimensional metal halide perovskites and related optoelectronic applications. *Info Mat*, *2*, 341-378.
- (14) Sun, C.; Guo, Y. H.; Han, S. S.; Li, J. Z.; Jiang, K.; Dong, L. F.; Liu, Q. L.; Yue, C. Y.; Lei, X. W. Three-Dimensional Cuprous Lead Bromide Framework with Highly Efficient and Stable Blue Photoluminescence Emission. *Angew. Chem. Int. Ed.* **2020**, *58*, 16465-16469.
- (15) Tremblay, M.-H.; Thouin, F.; Leisen, J.; Bacsá, J.; Srimath Kandada, A. R.; Hoffman, J. M.; Kanatzidis, M. G.; Mohite, A. D.; Silva, C.; Barlow, S.; Marder, S. R. (4NPEA)₂PbI₄ (4NPEA = 4-Nitrophenylethylammonium): Structural, NMR, and Optical Properties of a 3 × 3 Corrugated 2D Hybrid Perovskite. *J. Am. Chem. Soc.* **2019**, *141*, 4521-4525.
- (16) Deng, C.; Zhou, G.; Chen, D.; Zhao, J.; Wang, Y.; Liu, Q. Broadband Photoluminescence in 2D Organic-Inorganic Hybrid Perovskites: (C₇H₁₈N₂)PbBr₄ and (C₉H₂₂N₂)PbBr₄. *J. Phys. Chem. Lett.* **2020**, *11*, 2934-2940.
- (17) Straus, D. B.; Kagan, C. R. Electrons, Excitons, and Phonons in Two-Dimensional Hybrid Perovskites: Connecting Structural, Optical, and Electronic Properties. *J. Phys. Chem. Lett.* **2018**, *9*, 1434-1447.
- (18) Park, D. Y.; An, S.-J.; Lee, C.; Nguyen, D. A.; Lee, K.-N.; Jeong, M. S. Investigation of Chemical Origin of White-Light Emission in Two-Dimensional (C₄H₉NH₃)₂PbBr₄ via Infrared Nanoscopy. *J. Phys. Chem. Lett.* **2019**, *10*, 7942-7948.
- (19) Smith, M. D.; Karunadasa, H. I. White-Light Emission from Layered Halide Perovskites. *Acc. Chem. Res.* **2018**, *51*, 619-627.
- (20) Jung, M.-H. White-Light Emission from the Structural Distortion Induced by Control of Halide Composition of Two-Dimensional Perovskites ((C₆H₅CH₂NH₃)₂PbBr_{4-x}Cl_x). *Inorg. Chem.* **2019**, *58*, 6748-6757.
- (21) Dohner, E. R.; Jaffe, A.; Bradshaw, L. R.; Karunadasa, H. I. Intrinsic White-Light Emission from Layered Hybrid Perovskites. *J. Am. Chem. Soc.* **2014**, *136*, 13154-13157.
- (22) Barkaoui, H.; Abid, H.; Yangui, A.; Triki, S.; Boukheddaden, K.; Abid, Y. Yellowish White-Light Emission Involving Resonant Energy Transfer in a New One-Dimensional Hybrid Material: (C₉H₁₀N₂)PbCl₄. *J. Phys. Chem. C* **2018**, *122*, 24253-24261.

- (23) Spanopoulos, I.; Hadar, I.; Ke, W.; Guo, P.; Sidhik, S.; Kepenekian, M.; Even, J.; Mohite, A. D.; Schaller, R. D.; Kanatzidis, M. G. Water-Stable 1D Hybrid Tin(II) Iodide Emits Broad Light with 36% Photoluminescence Quantum Efficiency. *J. Am. Chem. Soc.* **2020**, *142*, 9028-9038.
- (24) Samet, A.; Triki, S.; Abid, Y. Resonantly Enhanced White-Light Emission Involving Energy and Charge Transfer in One-Dimensional Hybrid Material: (ABT)₂[PbBr₃]. *J. Phys. Chem. C* **2019**, *123*, 6213-6219.
- (25) Li, S.; Xu, J.; Li, Z.; Zeng, Z.; Li, W.; Cui, M.; Qin, C.; Du, Y. One-Dimensional Lead-Free Halide with Near-Unity Greenish-Yellow Light Emission. *Chem. Mater.* **2020**, *32*, 6525-6531.
- (26) Yuan, Z.; Zhou, C.; Tian, Y.; Shu, Y.; Messier, J.; Wang, J. C.; van de Burgt, L. J.; Kountouriotis, K.; Xin, Y.; Holt, E.; Schanze, K.; Clark, R.; Siegrist, T.; Ma, B. One-dimensional organic lead halide perovskites with efficient bluish white-light emission. *Nat. Commun.* **2017**, *8*, 14051.
- (27) Wang, Z.-P.; Wang, J.-Y.; Li, J.-R.; Feng, M.-L.; Zou, G.-D.; Huang, X.-Y. [Bmim]₂SbCl₅: a main group metal-containing ionic liquid exhibiting tunable photoluminescence and white-light emission. *ChemComm* **2015**, *51*, 3094-3097.
- (28) Zhou, C.; Lee, S.; Lin, H.; Neu, J.; Chaaban, M.; Xu, L.-J.; Arcidiacono, A.; He, Q.; Worku, M.; Ledbetter, L.; Lin, X.; Schlueter, J. A.; Siegrist, T.; Ma, B. Bulk Assembly of Multicomponent Zero-Dimensional Metal Halides with Dual Emission. *ACS Mater. Lett.* **2020**, *2*, 376-380.
- (29) Li, Z.; Li, Y.; Liang, P.; Zhou, T.; Wang, L.; Xie, R.-J. Dual-Band Luminescent Lead-Free Antimony Chloride Halides with Near-Unity Photoluminescence Quantum Efficiency. *Chem. Mater.* **2019**, *31*, 9363-9371.
- (30) Zhou, C.; Worku, M.; Neu, J.; Lin, H.; Tian, Y.; Lee, S.; Zhou, Y.; Han, D.; Chen, S.; Hao, A.; Djurovich, P. I.; Siegrist, T.; Du, M.-H.; Ma, B. Facile Preparation of Light Emitting Organic Metal Halide Crystals with Near-Unity Quantum Efficiency. *Chem. Mater.* **2018**, *30*, 2374-2378.
- (31) Zhou, C.; Lin, H.; Worku, M.; Neu, J.; Zhou, Y.; Tian, Y.; Lee, S.; Djurovich, P.; Siegrist, T.; Ma, B. Blue Emitting Single Crystalline Assembly of Metal Halide Clusters. *J. Am. Chem. Soc.* **2018**, *140*, 13181-13184.
- (32) Zhou, C.; Lin, H.; Neu, J.; Zhou, Y.; Chaaban, M.; Lee, S.; Worku, M.; Chen, B.; Clark, R.; Cheng, W.; Guan, J.; Djurovich, P.; Zhang, D.; Lü, X.; Bullock, J.; Pak, C.; Shatruk, M.; Du,

M.-H.; Siegrist, T.; Ma, B. Green Emitting Single-Crystalline Bulk Assembly of Metal Halide Clusters with Near-Unity Photoluminescence Quantum Efficiency. *ACS Mater. Lett.* **2019**, *4*, 1579-1583.

(33) Yangui, A.; Roccanova, R.; McWhorter, T. M.; Wu, Y.; Du, M.-H.; Saparov, B. Hybrid Organic–Inorganic Halides $(C_5H_7N_2)_2MBr_4$ ($M = Hg, Zn$) with High Color Rendering Index and High-Efficiency White-Light Emission. *Chem. Mater.* **2019**, *31*, 2983-2991.

(34) Chen, D.; Hao, S.; Zhou, G.; Deng, C.; Liu, Q.; Ma, S.; Wolverton, C.; Zhao, J.; Xia, Z. Lead-Free Broadband Orange-Emitting Zero-Dimensional Hybrid $(PMA)_3InBr_6$ with Direct Band Gap. *Inorg. Chem.* **2019**, *58*, 15602-15609.

(35) Song, G.; Li, M.; Yang, Y.; Liang, F.; Huang, Q.; Liu, X.; Gong, P.; Xia, Z.; Lin, Z. Lead-Free Tin(IV)-Based Organic–Inorganic Metal Halide Hybrids with Excellent Stability and Blue-Broadband Emission. *J. Phys. Chem. Lett.* **2020**, *11*, 1808-1813.

(36) Zhou, C.; Lin, H.; Tian, Y.; Yuan, Z.; Clark, R.; Chen, B.; van de Burgt, L. J.; Wang, J. C.; Zhou, Y.; Hanson, K.; Meisner, Q. J.; Neu, J.; Besara, T.; Siegrist, T.; Lambers, E.; Djurovich, P.; Ma, B. Luminescent zero-dimensional organic metal halide hybrids with near-unity quantum efficiency. *Chem. Sci.* **2018**, *9*, 586-593.

(37) Morad, V.; Yakunin, S.; Kovalenko, M. V. Supramolecular Approach for Fine-Tuning of the Bright Luminescence from Zero-Dimensional Antimony(III) Halides. *ACS Mater. Lett.* **2020**, *2*, 845-852.

(38) Febriansyah, B.; Neo, C. S. D.; Giovanni, D.; Srivastava, S.; Lekina, Y.; Koh, T. M.; Li, Y.; Shen, Z. X.; Asta, M.; Sum, T. C.; Mathews, N.; England, J. Targeted Synthesis of Trimeric Organic–Bromoplumbate Hybrids That Display Intrinsic, Highly Stokes-Shifted, Broadband Emission. *Chem. Mater.* **2020**, *32*, 4431-4441.

(39) Elleuch, S.; Lusson, A.; Pillet, S.; Boukheddaden, K.; Abid, Y. White Light Emission from a Zero-Dimensional Lead Chloride Hybrid Material. *ACS Photonics* **2020**, *7*, 1178-1187.

(40) Lin, F.; Wang, H.; Liu, W.; Li, J. Zero-dimensional ionic antimony halide inorganic–organic hybrid with strong greenish yellow emission. *J. Mater. Chem. C* **2020**, *8*, 7300-7303.

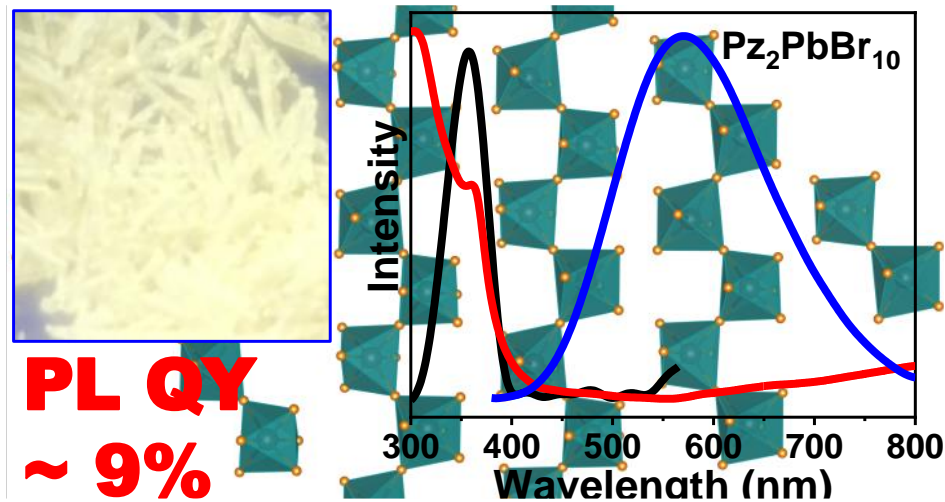
(41) Milstein, T. J.; Kroupa, D. M.; Gamelin, D. R. Picosecond Quantum Cutting Generates Photoluminescence Quantum Yields Over 100% in Ytterbium-Doped $CsPbCl_3$ Nanocrystals. *Nano Lett.* **2018**, *18*, 3792-3799.

- (42) Im, J.-H.; Jang, I.-H.; Pellet, N.; Grätzel, M.; Park, N.-G. Growth of $\text{CH}_3\text{NH}_3\text{PbI}_3$ cuboids with controlled size for high-efficiency perovskite solar cells. *Nat. Nanotechnol.* **2014**, *9*, 927-932.
- (43) Grancini, G.; Nazeeruddin, M. K. Dimensional tailoring of hybrid perovskites for photovoltaics. *Nat. Rev. Mater.* **2019**, *4*, 4-22.
- (44) Hoffman, J. M.; Che, X.; Sidhik, S.; Li, X.; Hadar, I.; Blancon, J.-C.; Yamaguchi, H.; Kepenekian, M.; Katan, C.; Even, J.; Stoumpos, C. C.; Mohite, A. D.; Kanatzidis, M. G. From 2D to 1D Electronic Dimensionality in Halide Perovskites with Stepped and Flat Layers Using Propylammonium as a Spacer. *J. Am. Chem. Soc.* **2019**, *141*, 10661-10676.
- (45) Smith, M. D.; Jaffe, A.; Dohner, E. R.; Lindenberg, A. M.; Karunadasa, H. I. Structural origins of broadband emission from layered Pb-Br hybrid perovskites. *Chem. Sci.* **2017**, *8*, 4497-4504.
- (46) Hu, T.; Smith, M. D.; Dohner, E. R.; Sher, M.-J.; Wu, X.; Trinh, M. T.; Fisher, A.; Corbett, J.; Zhu, X. Y.; Karunadasa, H. I.; Lindenberg, A. M. Mechanism for Broadband White-Light Emission from Two-Dimensional (110) Hybrid Perovskites. *J. Phys. Chem. Lett.* **2016**, *7*, 2258-2263.
- (47) Sun, C.; Guo, Y.-H.; Yuan, Y.; Chu, W.-X.; He, W.-L.; Che, H.-X.; Jing, Z.-H.; Yue, C.-Y.; Lei, X.-W. Broadband White-Light Emission in One-Dimensional Organic-Inorganic Hybrid Silver Halide. *Inorg. Chem.* **2020**, *59*, 4311-4319.
- (48) Yin, J.; Yang, H.; Fei, H. Robust, Cationic Lead Halide Layered Materials with Efficient Broadband White-Light Emission. *Chem. Mater.* **2019**, *31*, 3909-3916.
- (49) Cortecchia, D.; Yin, J.; Petrozza, A.; Soci, C. White light emission in low-dimensional perovskites. *J. Mater. Chem. C* **2019**, *7*, 4956-4969.
- (50) Biswas, A.; Bakthavatsalam, R.; Shaikh, S. R.; Shinde, A.; Lohar, A.; Jena, S.; Gonnade, R. G.; Kundu, J. Efficient Broad-Band Emission from Contorted Purely Corner-Shared One Dimensional (1D) Organic Lead Halide Perovskite. *Chem. Mater.* **2019**, *31*, 2253-2257.
- (51) Dohner, E. R.; Hoke, E. T.; Karunadasa, H. I. Self-Assembly of Broadband White-Light Emitters. *J. Am. Chem. Soc.* **2014**, *136*, 1718-1721.
- (52) Lin, H.; Zhou, C.; Tian, Y.; Besara, T.; Neu, J.; Siegrist, T.; Zhou, Y.; Bullock, J.; Schanze, K. S.; Ming, W.; Du, M.-H.; Ma, B. Bulk assembly of organic metal halide nanotubes. *Chem. Sci.* **2017**, *8*, 8400-8404.

- (53) Guria, A. K.; Dutta, S. K.; Adhikari, S. D.; Pradhan, N. Doping Mn^{2+} in Lead Halide Perovskite Nanocrystals: Successes and Challenges. *ACS Energy Lett.* **2017**, *2*, 1014-1021.
- (54) Norris, D. J.; Efros, A. L.; Erwin, S. C. Doped Nanocrystals. *Science* **2008**, *319*, 1776.
- (55) Zhou, Y.; Chen, J.; Bakr, O. M.; Sun, H.-T. Metal-Doped Lead Halide Perovskites: Synthesis, Properties, and Optoelectronic Applications. *Chem. Mater.* **2018**, *30*, 6589-6613.
- (56) Liu, W.; Lin, Q.; Li, H.; Wu, K.; Robel, I.; Pietryga, J. M.; Klimov, V. I. Mn^{2+} -Doped Lead Halide Perovskite Nanocrystals with Dual-Color Emission Controlled by Halide Content. *J. Am. Chem. Soc.* **2016**, *138*, 14954-14961.
- (57) Chen, H.-Y.; Maiti, S.; Son, D. H. Doping Location-Dependent Energy Transfer Dynamics in Mn-Doped CdS/ZnS Nanocrystals. *ACS Nano* **2012**, *6*, 583-591.
- (58) Song, E. H.; Wang, J. L.; Yu, D. C.; Ye, S.; Zhang, Q. Y. Anomalous tunable visible to near infrared emission in the Mn^{2+} -doped spinel $MgGa_2O_4$ and room-temperature upconversion in the Mn^{2+} and Yb^{3+} -codoped spinel. *J. Mater. Chem. C* **2014**, *2*, 8811-8816.
- (59) Rossi, D.; Parobek, D.; Dong, Y.; Son, D. H. Dynamics of Exciton–Mn Energy Transfer in Mn-Doped $CsPbCl_3$ Perovskite Nanocrystals. *J. Phys. Chem. C* **2017**, *121*, 17143-17149.
- (60) Parobek, D.; Roman, B. J.; Dong, Y.; Jin, H.; Lee, E.; Sheldon, M.; Son, D. H. Exciton-to-Dopant Energy Transfer in Mn-Doped Cesium Lead Halide Perovskite Nanocrystals. *Nano Lett.* **2016**, *16*, 7376-7380.
- (61) Biswas, A.; Bakthavatsalam, R.; Kundu, J. Efficient Exciton to Dopant Energy Transfer in Mn^{2+} -Doped $(C_4H_9NH_3)_2PbBr_4$ Two-Dimensional (2D) Layered Perovskites. *Chem. Mater.* **2017**, *29*, 7816-7825.

Chapter 2

Title: Structure, connectivity and photophysical properties of lead-based 1D perovskite



2.1 Introduction:

Halide perovskite has emerged to be a potential candidate for optoelectronics due to its enabling properties. Primarily halide-based perovskite structure is composed of two types of moieties: organic and inorganic. This organic-inorganic hybrid perovskite has variable binding energies for excitons which enables properties like solar cell to LEDs.¹⁻⁵ This hybrid perovskite comes with a variable tunability in terms of its dimensionality, chemical composition, phase (bulk, powder, single crystal). In the current scenario, I will be discussing the tunability of optoelectronic property in terms of the chemical composition (change of halide) and network dimensionality (3D, 2D, 1D or 0D). Generally, a three-dimensional halide perovskite has a general formula of ABX_3 (A = methylammonium, formamidinium, Cs^+ ; X = Cl^- , Br^- , I^-). Here the metal halide octahedra are connected in three dimensions, with all corners sharing inorganic counterparts. In 2D structures, the general formula can be written as L_2PbX_4 . Here the metal octahedra's are connected in corner-sharing and within inorganic layers bulky organic (ammonium and phosphonium) ligands. Further reduction in dimensionality will lead to 1D structure where it is primarily governed by the nature of connectivity. Depending on the connectivity like face shared, edge shared, corner shared, or combination can give rise to 1D chain flat or contorted. For 1D structure, the metal octahedra are isolated and surrounded by large or bulky organic ligands. The enormous diversity in the connectivity mode-driven structure in bulk or nano regime is the new and exciting

frontier of material science. This motivates us to investigate the diversity and correlation in the halide perovskite.⁶⁻⁸

The lower-dimensional lead-based perovskite (2D and 1D) structure shows a huge interest among the researcher due to its broad band emission at room temperature, which enables the protentional application in solid-state lighting. There are reports for 2D lead-based perovskite, either flat or contorted, exhibit broad band emission with PLQY ~9%. In the case of 2D perovskite, the broad band emissions are well correlated to metal halide octahedral distortion and out-of-plane lattice distortion. It was observed that the distortions would cause excited state defects and are formed due to the deformability of lattice under photoexcitation. This deformable lattice will further act as a trap site for the generated excitons. Generated excitons under photoexcitation are called self-trapping of excitons (STEs) in perovskite lattice and are mediated through exciton-phonon coupling. However, the generation of STEs is not limited to 2D structure, and it very much evident in 1D Pb-based perovskite. Evidently, the self-trapping of excitons becomes easier in the 1D system because of the higher vibrational degrees of freedom.⁹⁻¹¹ This will enable to have more deformable after photoexcitation and subsequently enhances the self-trapping of excitons.¹³⁻¹⁵ The exciton-phonon interaction strength is higher in low dimensional 1D system, which will make a better-suited material for stronger broad-band emission with higher PLQY than the 2D perovskite system. So, in summary, for 1D system we would expect higher PLQY due to higher electron-phonon coupling due to an increase in vibration degree of freedom from 2D to 1D⁹. Interestingly within the family of 1D perovskites, we see a notable difference in PLQY. 1D perovskite featuring edge sharing metal halide octahedra with high PL QY~20%¹⁶ was reported by Yuan et al. Later on, Mao et al. show a combining edge-and corner-sharing double chains single corner-sharing chains that exhibits broad-band emission with modest PL QY ~12%⁸. The reports highlight the necessity of connectivity in the metal halide octahedra in dictating the photophysical property. However, the difference in PLQY might depend on the structure or connectivity of metal halide octahedra. The reports suggested the octahedra connectivity mode to edge-sharing motif would be necessary to realize strong and efficient broad-band STE emission with high PLQY. The unavailability of correlation suggests the design mechanism to achieve STE base broad band emission with high PLQY in 1D system is still unanswered. The suggestion of connectivity mode in deciding the tunability with high PLQY requires further validation. If the edge-sharing connectivity is the primary reason for high PLQY, then it would be reflected in other 1D

perovskites as well. To add that there are very few reports are on purely corner shared 1D perovskites and all of them show weak/narrow emission¹⁷⁻²⁰. All this study indicates that the octahedral connectivity mode might affect the broad band emission. So, in order to rationalize the role played by connectivity mode in dictating the PLQY of the STE emission, we need to investigate the pure corner shared 1D perovskite in order to draw some significant conclusions.

2.2 Materials:

Lead (II) bromide (99%), Lead (II) chloride (99%), Hydrochloric acid (37%) were purchased from Sigma Aldrich. Dimethyl sulfoxide (DMSO), Dichloromethane (DCM, anhydrous), 1-(2-Aminoethyl) piperazine, and Hydrobromic acid (47%) were purchased from TCI Chemicals. All chemicals were used as purchased without further purification.

2.3 Synthesis:

** For simplicity 1-(2-Aminoethyl) piperazine was abbreviated as Pz in the rest of the discussion.*

2.3.A Synthesis of powdered PzPbBr 1D Perovskites:

For the preparation of powdered (Pz)₂PbBr₁₀ perovskite, 1 mmol (365 mg) of PbBr₂ was dissolved in 3 mL of hydrobromic acid. To this, 1 mmol (140 μL) 1-(2-Aminoethyl) piperazine was added drop by drop. The solution turns turbid white immediately after addition and precipitates into white perovskite powder gradually. The resulting precipitate was washed with diethyl ether three times and dried under a vacuum at 60°C for further recrystallization.

2.3.B Synthesis of Single Crystals of PzPbBr 1D Perovskites:

For the synthesis of single crystals of (Pz)₂PbBr₁₀ perovskite, 2 mmol (730 mg) of PbBr₂ was dissolved in 10 mL of hydrobromic acid. To this transparent solution, 2 mmol (280 μL) 1-(2-Aminoethyl) piperazine was added in a dropwise manner. When the solution becomes turbid white, it was heated at 170 °C in an oil bath for 30 minutes under observation till the solution was clear. It was then allowed to cool naturally while still in oil bath. The natural drop in temperature leads to the formation of colourless bar-shaped crystal visible in the mother liquor. The crystals were filtered using a vacuum pump and washed repeatedly with dichloromethane for further characterization.

2.3.C Synthesis of Single Crystals of PzPbCl 1D Perovskites:

Powdered (Pz)₂PbCl₁₀ perovskite was prepared by dissolving 1 mmol (278 mg) of PbCl₂ in 5 mL of hydrochloric acid (37%) followed by dropwise addition of 1 mmol (140 μL) 1-(2-Aminoethyl) piperazine. The obtained powder was filtered using a vacuum pump and washed 3 times with diethyl ether. For recrystallization of synthesised perovskite considerable amount was dissolved in dimethyl sulfoxide by heating at 150 °C. The solution was cooled naturally and kept in ambient atmosphere for several days to grow single crystals. The obtained single crystals were washed repeatedly with diethyl ether for further analysis.

2.3.D Synthesis of Single Crystals of PzPbBr_{1-x}Cl_x 1D Perovskites:

For synthesis of mixed halide perovskite single crystals, 0.5 mmol (183 mg) of PbBr₂ was dissolved in a mixture of hydrobromic acid and hydrochloric acid with varying ratio 3:1, 1:1 and 1:3 respectively keeping the total acid volume 20 mL, To that solution mixture, 0.5 mmol (70 μL) of 1-(2-Aminoethyl) piperazine was added in dropwise manner. After a few minutes the whole solution becomes white turbid which was then heated in a pre-heated oil bath at 210°C till transparent solution. Then the clear solution was cooled slowly inside oil bath which give rise to mixed halide perovskite crystals. The obtained crystals were filtered using a vacuum pump and washed repeatedly with dichloromethane for further characterization.

2.4 Characterization technique:

UV-Vis Absorbance was performed in a Shimadzu UV-VIS-NIR3600Plus spectrometer. Steady State PL and lifetime was measured using an Edinburgh FS5 spectrophotometer. PXRD patterns were recorded using a PANalytic X'Pert Pro using Copper Ka radiation ($\lambda=1.5406 \text{ \AA}$). TGA measurements were performed using a TAG system (Mettler-Toledo, Model TGA/SDTA851e) and samples were heated in the range of 25-800°C at a heating rate of 5°C/min under nitrogen atmosphere. Raman spectroscopy was performed using a Renishaw InVia Raman spectrometer with an excitation laser at 633nm. Absolute quantum yield measurements were carried out in a Horiba JOBIN YVON Fluoromax-4 spectrometer with a calibrated integrating sphere attachment. Low-temperature PL measurements were performed on a homebuilt PL set up consisting of an

excitation monochromator (Jobin Yvon Triax 180), an emission monochromator (Jobin Yvon iHR 320) and photomultiplier tube (PMT) as the detector with xenon lamp (450 W).

Single crystals X-ray intensity data measurements of compounds AB_280818 (PzPbBr) and AB_190918 (PzPbCl) were carried out on a Bruker D8 VENTURE Kappa Duo PHOTON II CPAD diffractometer equipped with Incoatech multilayer mirrors optics. The intensity measurements were carried out at 100(2) K temperature with Mo micro-focus sealed tube diffraction source ($\text{MoK}\alpha = 0.71073 \text{ \AA}$). The X-ray generator was operated at 50 kV and 1.4. A preliminary set of cell constants and an orientation matrix were calculated from three sets of 36 frames. Data were collected with ω scan width of 0.5° at different settings of φ and 2θ with a frame time of 10 secs keeping the sample-to-detector distance fixed at 5.00 cm. The X-ray data collection was monitored by APEX3 program (Bruker, 2016).¹ All the data were corrected for Lorentzian, polarization and absorption effects using SAINT and SADABS programs (Bruker, 2016).¹ Using APEX3 (Bruker) program suite, the structure was solved with the ShelXS-97 (Sheldrick, 2008)² structure solution program, using direct methods. The model was refined with version of ShelXL-2013 (Sheldrick, 2015)³ using Least Squares minimisation. All the hydrogen atoms were placed in a geometrically idealized position and constrained to ride on its parent atoms. An *ORTEP* III⁴ view of compounds was drawn with 50% probability displacement ellipsoids and H atoms are shown as small spheres of arbitrary radii.

References

- (1) Bruker (2016). APEX2, SAINT and SADABS. Bruker AXS Inc., Madison, Wisconsin, USA.
- (2) G. M. Sheldrick, *Acta Crystallogr.*, 2008, A64, 112.
- (3) G. M. Sheldrick, *Acta Crystallogr.*, 2015, C71, 3–8.
- (4) L. J. Farrugia, *J. Appl. Crystallogr.* 2012, 45, 849–854.

2.5 Results and Discussion:

PzPbBr was crystallized by gradual cooling of HBr solution of precursor PbBr_2 salt and 2-aminoethylpiperazine ligand heated to 100°C (Figure 1). The corresponding chloride and mixed halide version can also be prepared with a mixed solution of HBr and HCl in appropriate proportion, presented with the scheme. The details of the materials were listed above.

Reaction Scheme

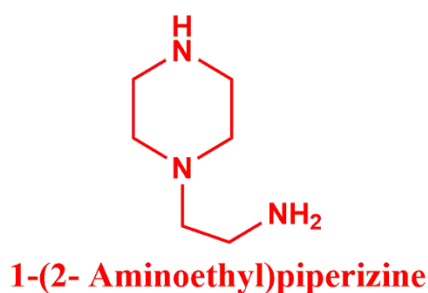
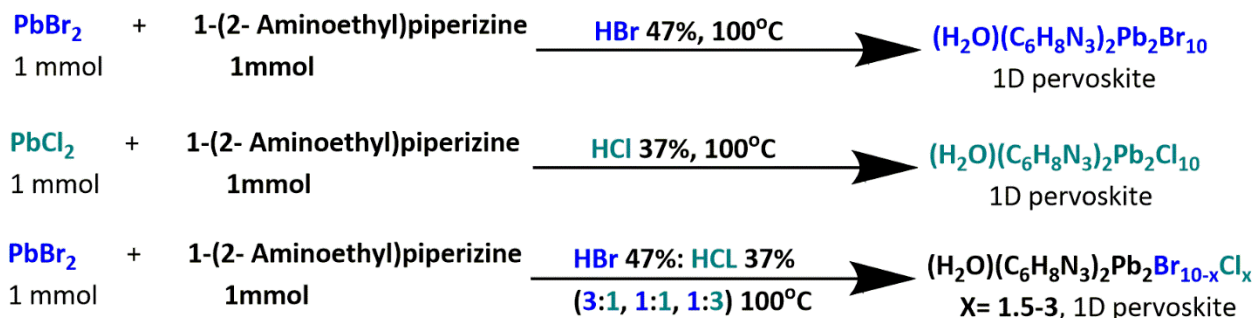


Figure 1: Represents the reaction scheme of the pure halide and mixed halide pervoskite. For the sake of simplicity $(\text{H}_2\text{O})(\text{C}_6\text{H}_8\text{N}_3)_2\text{Pb}_2\text{Br}_{10}$ is abbreviated as PzPbBr in the rest of the discussion.

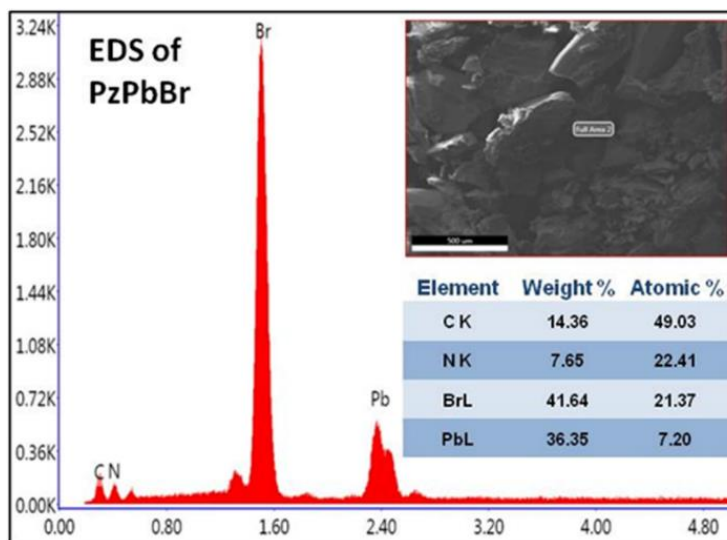


Figure 2: SEM and EDS analysis of PzPbBr

The SEM-EDS analysis confirms the presence of the constituent elements in these crystals (Figure 2).

2.5.A Optical property

Under ambient light, the crystals have a long needle shape, while under UV illumination (365 nm) they exhibit strong yellowish-white emission (Figure 3a,3b).

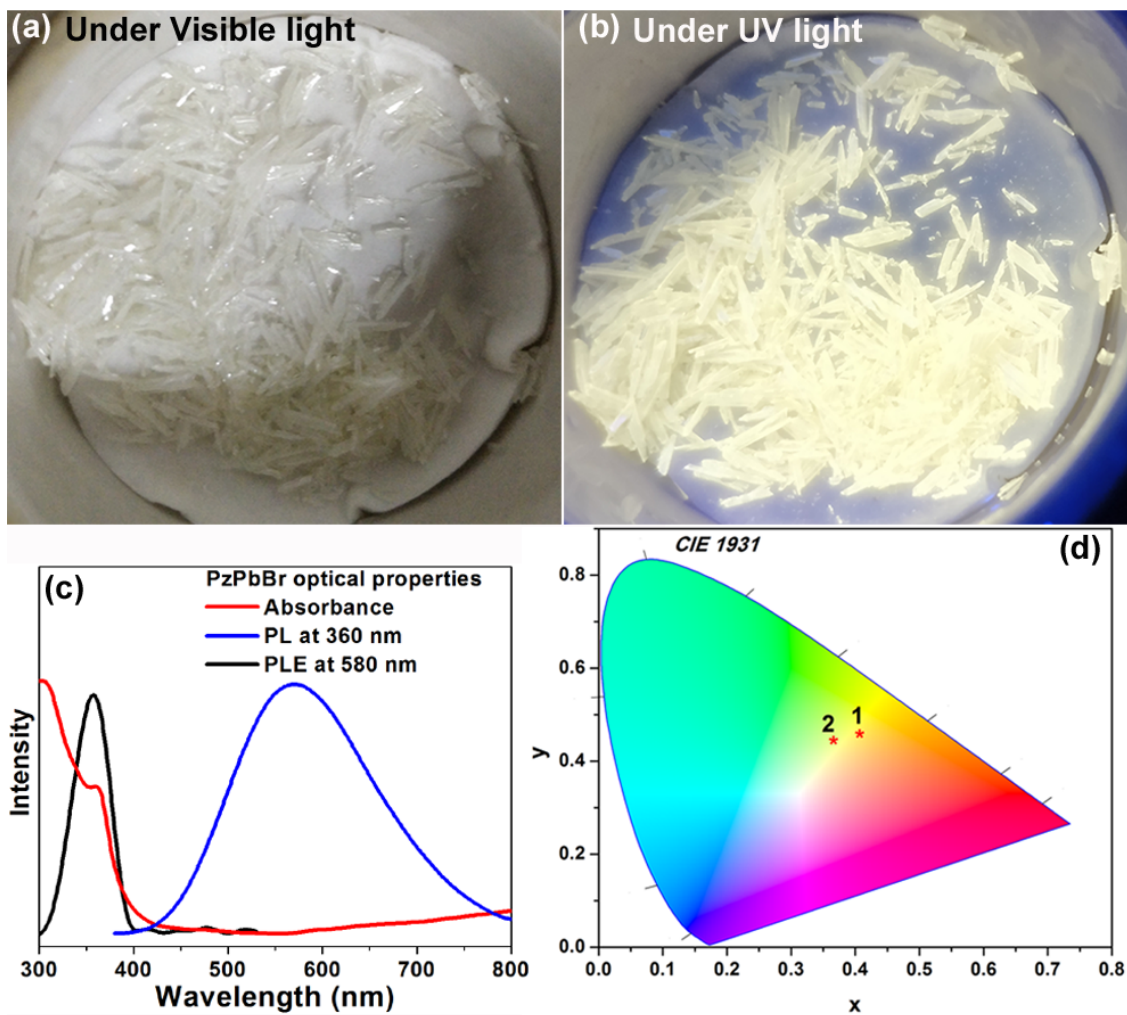


Figure 3: Photograph of single crystals of PzPbBr under (a) ambient; (b) UV light (c) optical properties (absorbance, PL, photoluminescence excitation at 580 nm); (d) CIE chromaticity coordinates for 1 (PzPbBr) and 2 (PzPbBr_xCl_{1-x}).

The optical characterization of PzPbBr, presented in Figure 3c, shows strong, Stokes shifted, and broad photoluminescence(PL) band peaked at 580 nm. The CIE chromaticity coordinate of PzPbBr is (0.41,0.47) as highlighted by 1* in Figure 3d with CCT ~ 3759 K. The photoluminescence excitation (PLE) peak at 350 nm matches well with the absorbance measured through diffuse

reflectance (Figure 3c). The match signifies that the same absorbing species is responsible for the emission.

2.5.B Nature of emission

An excitation dependent study shows an unaltered emission profile when excited within the 320-380 nm range. Moreover, the PLE profile collected across the broad emission band remains unaltered (Figure 4a, 4b).

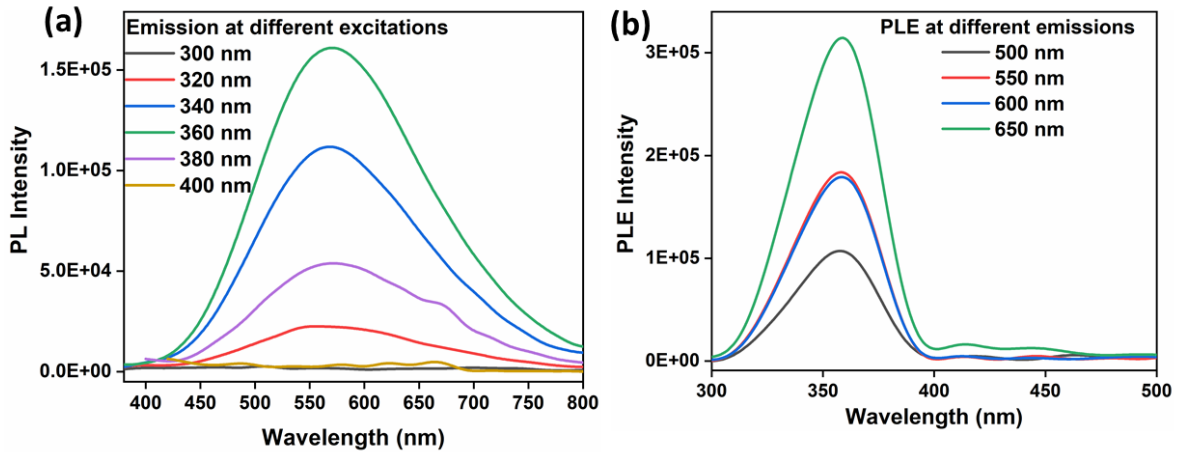


Figure 4: (a) excitation dependent emission profile; (b) photoluminescence excitation collected across broad emission band

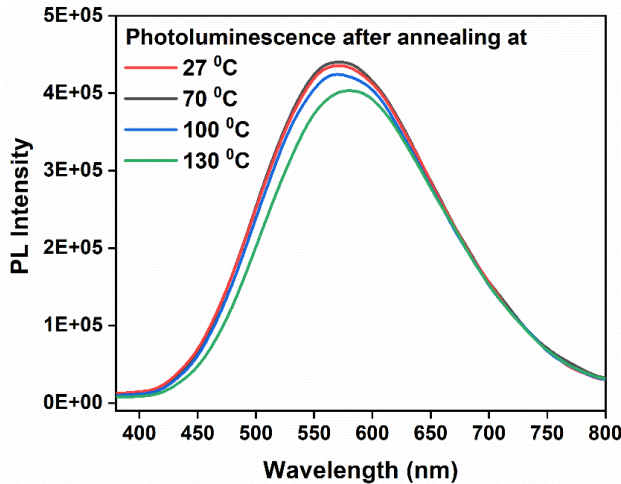


Figure 5: Effect of thermal annealing on luminescence properties

In addition, thermal annealing (Figure 5) shows minimal changes in the observed PL profile (intensity and shape). Furthermore, emission intensity is observed to increase with no signs of saturation as laser fluence is increased (Figure 6).

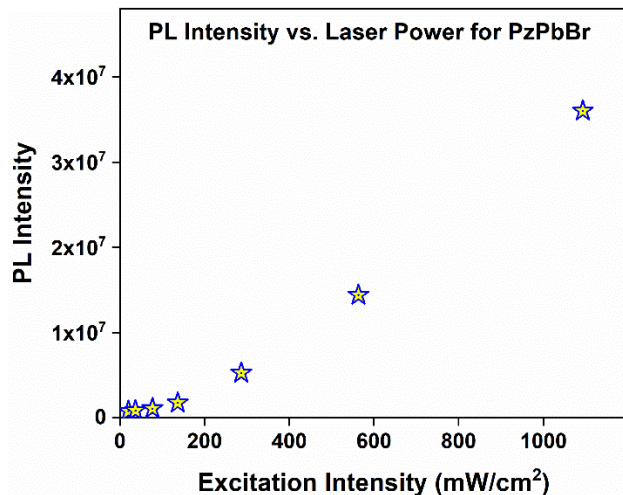


Figure 6: Intensity of broad emission increases as the excitation laser power is increased over three orders of magnitude.

All these observations suggest that the same type of emissive species that are intrinsically generated through band-edge excitation are responsible for the broad emission.⁹

Impressively, the measured room temperature absolute PL QY for PzPbBr single crystal is ~9%, comparable to the two best reports^{8,16} on 1D systems.

2.5.C Thermal stability

Thermal stability is assessed using thermogravimetric analysis (Figure 7).

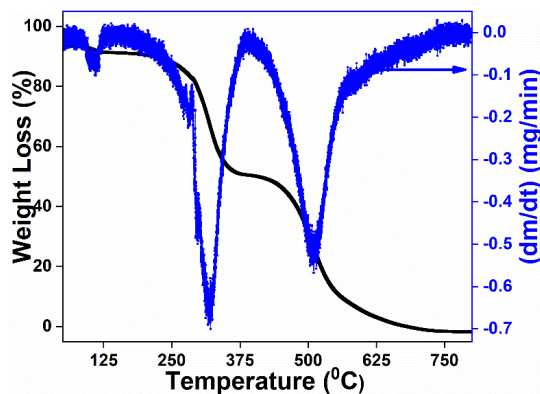


Figure 7: Thermogravimetric weight loss analysis of PzPbBr

The study shows that the crystals were stable up to 130°C. After that, there was some weight loss which was ascribed to water loss. This will be further discussed in section 2.5.G (crystal structure) Down the line at 260 °C loss is most likely due to the Pz ligand. As the ligand contains organic moieties, so degradation is reasonably possible after 200 °C. At 500 °C the weight loss corresponds to the collapse of metal halide octahedra.

2.5.D Room temperature lifetime study

Lifetime study was conducted to understand the component associated with emission decay. Time-resolved PL decay curves for single crystals of PzPbBr can be fitted to bi-exponential function with a major (96%) time component of 41 ns and a minor (4%) time component of 7 ns. These decay constants and their relative weights remain unaltered across the broad emission peak (Figure 8).

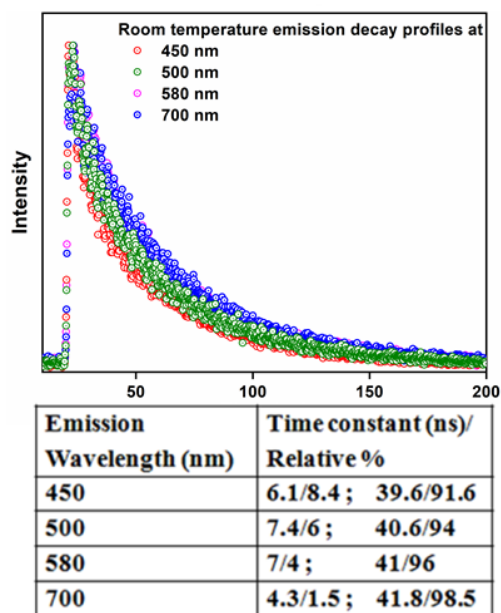


Figure 8: Room temperature time-resolved PL decay curves for PzPbBr single crystals measured across the broad emission band. Inset Table shows major and minor components of the decay time constants.

2.5.E Low-temperature luminescence and lifetime study

Low-temperature steady-state PL measurements of PzPbBr (Figure 9a, 9b) reveal the increase of PL intensity as the temperature is lowered to 125 K. With the further temperature lowering to 40 K, PL intensity starts to decrease. Such dependence of PL intensity can be ascribed to thermally activated trapping-detrapping of excitons from STE states.⁹

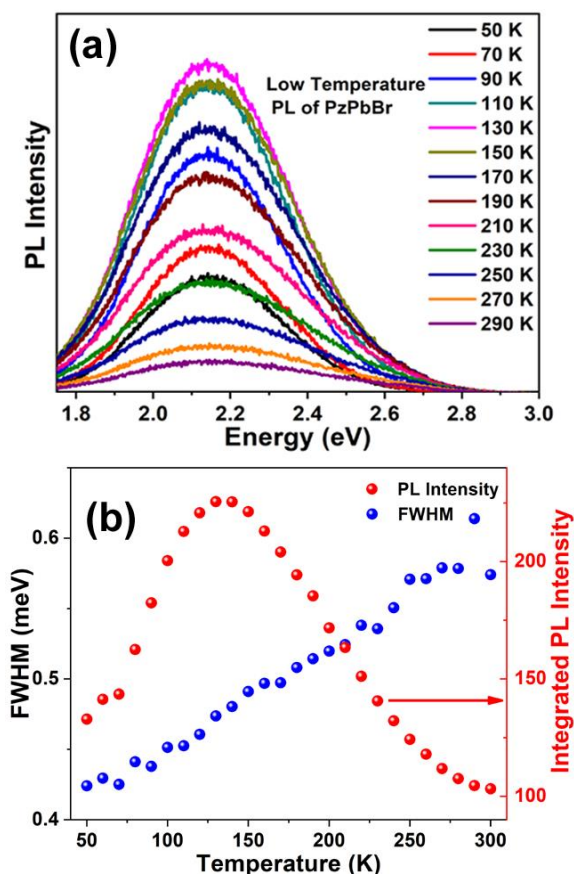


Figure 9: (a) Steady-state low-temperature PL of PzPbBr; (b) temperature dependence of PL intensity and bandwidth.

However, the dependence on the low-temperature regime can get complicated due to tunneling and defect-bound excitons.⁹ Moreover, the phonon modes (inorganic and/or organic), that couple to electronic excitation to generate STE has their own temperature dependence.²¹

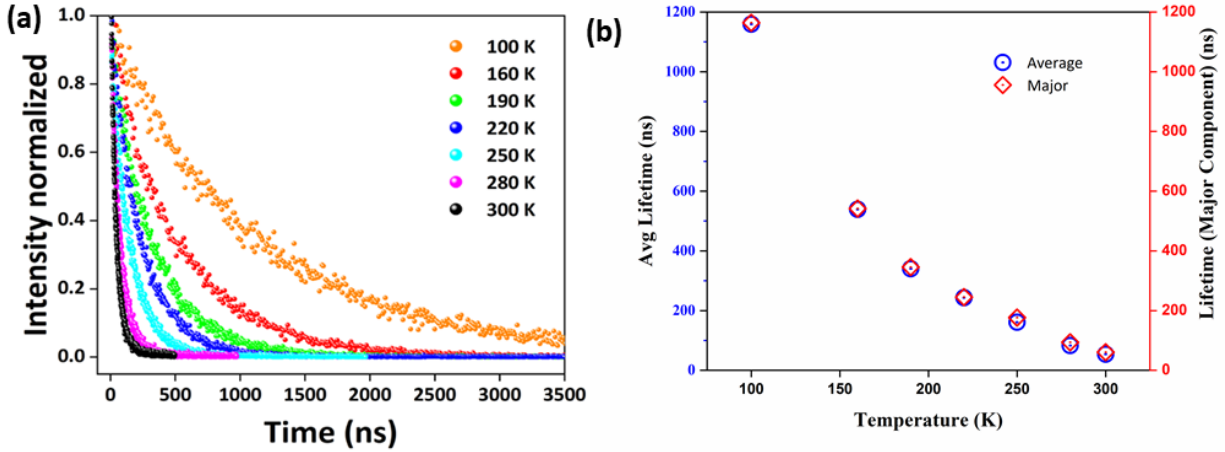


Figure 10: (a) Low-temperature lifetime; (b) average lifetime at different temperature.

The lifetime of the broad emission, as obtained from analysis of the PL decay dynamics at low temperatures, reveal that the lifetime increases the temperature is lowered from 298 K to 100 K (Figure 10). The average lifetime calculation was using the following equation.

$$Average\ Lifetime = \frac{a_1(\tau_1^2) + a_2(\tau_2^2)}{(a_1\tau_1 + a_2\tau_2)}$$

This low-temperature study suggests a thermal equilibrium between the free excitons and self-trapped excitons that govern the thermally activated trapping-detrapping from the STE states. The lifetime lengthening at low temperature is as expected due to lower thermal vibration.

1.5 F Origin of broad band

The bandwidth (FWHM) of the broad emission increases monotonically as the temperature is raised. This temperature dependence of FWHM (Γ) can be fitted to the following equation relating coupling of electronic excitations with the longitudinal optical lattice phonons²²:

$$\Gamma(T) = \Gamma_0 + \Gamma_{\text{phonon}}(e^{(E_{\text{LO}}/k_B T)} - 1)^{-1} + \Gamma_{\text{inhomo}}e^{-E_b/k_B T}$$

where, Γ_0 = FWHM at $T=0$ K, Γ_{phonon} represents electron-phonon coupling and E_{LO} represents energy of longitudinal optical phonon mode, Γ_{inhomo} represents inhomogeneous broadening while E_b is the binding energy of trapped states.

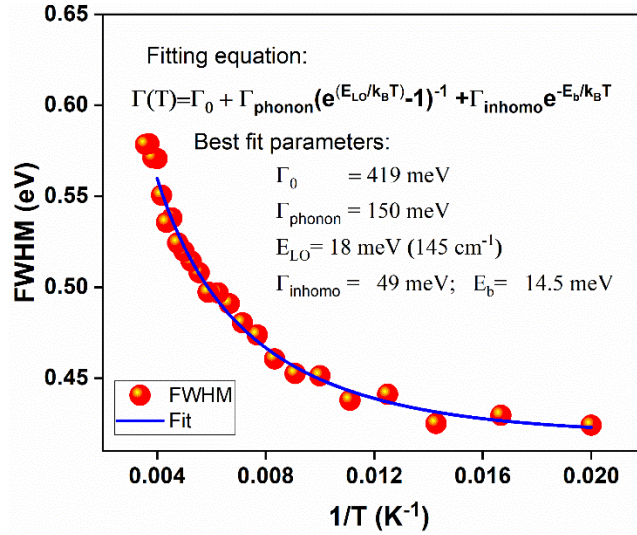


Figure 11: Fitting of FWHM as a function of Temperature with its associated parameters and fitting equation.

The fitting and its associated parameters, as shown in Figure 11, reflect strong electron-phonon coupling with $E_{LO} = 145 \text{ cm}^{-1}$, in close agreement to low-frequency Raman stretching mode of Pb-Br bonds⁸ of inorganic metal halide framework (Figure 12).

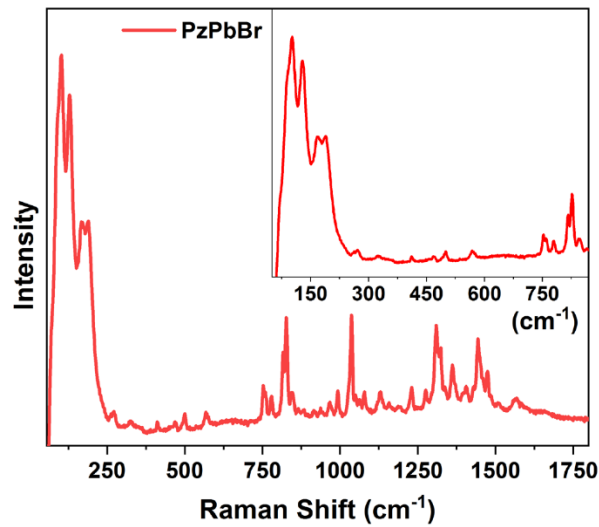


Figure 12: Raman spectra of PzPbBr perovskite crystal excited with 633 nm laser.

This suggests that the STE are localized on the metal halide octahedral framework in agreement with earlier reports on STE in 2D perovskites^{9,12} Although our results herein indicate intrinsic self-

trapping. Further detailed experiments are needed to characterize¹⁵ the nature (extrinsic vs. intrinsic) of the observed STE in this system.

2.5.G Crystal structure analysis

PzPbBr crystallizes in a monoclinic crystal system with $P2_{1/c}$ space group (Table 1, CCDC:1875387). Structure is composed of contorted 1D chains of corner-shared metal halide octahedra surrounded by ligands (Figure 13).

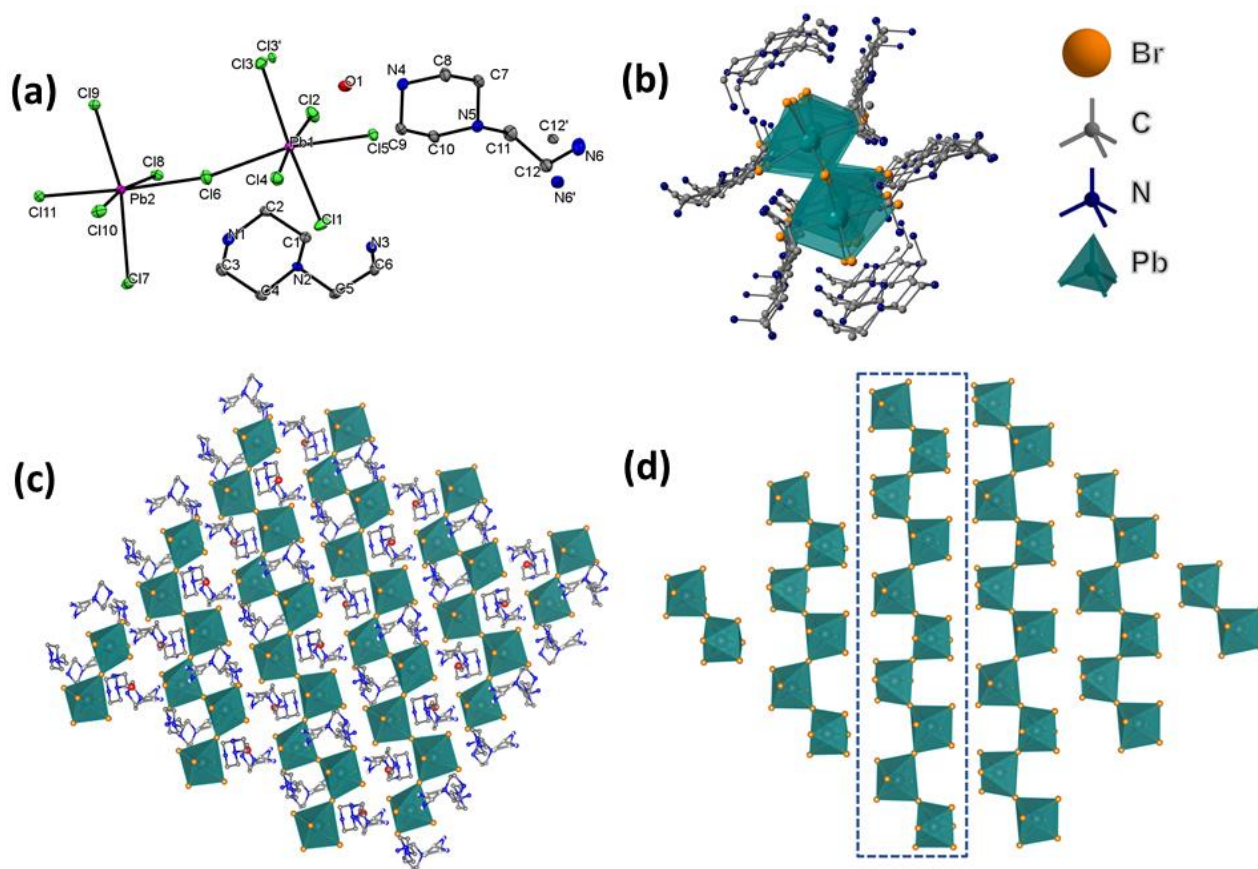


Figure 13: (a) asymmetric unit of PzPbBr; (b) sliced view highlighted the 1D contorted corner-shared structure with two octahedral unit wide chain; (c) view along c-axis; (d) clear view of the contorted 1D chain.

Table 1. Crystal data and structure refinement for PzPbBr

Identification code	mo_AB_280818_0m
Empirical formula	C ₁₂ H ₃₈ Br ₁₀ N ₆ O Pb ₂
Formula weight	1495.96

Temperature	100(2) K	
Wavelength	0.71073 Å	
Crystal system	Monoclinic	
Space group	P2 ₁ /c	
Unit cell dimensions	a = 13.7518(4) Å	α = 90°.
	b = 17.4924(6) Å	β = 96.2380(10)°.
	c = 13.7488(5) Å	γ = 90°.
Volume	3287.72(19) Å ³	
Z	4	
Density (calculated)	3.022 Mg/m ³	
Absorption coefficient	22.400 mm ⁻¹	
F(000)	2696	
Crystal size	0.200 x 0.120 x 0.080 mm ³	
Theta range for data collection	2.506 to 28.296°.	
Index ranges	-17 ≤ h ≤ 18, -23 ≤ k ≤ 23, -17 ≤ l ≤ 18	
Reflections collected	35698	
Independent reflections	8112 [R(int) = 0.0314]	
Completeness to theta = 25.242°	99.1 %	
Absorption correction	Semi-empirical from equivalents	
Max. and min. transmission	0.267 and 0.094	
Refinement method	Full-matrix least-squares on F ²	
Data / restraints / parameters	8112 / 70 / 340	
Goodness-of-fit on F ²	1.079	
Final R indices [I > 2σ(I)]	R1 = 0.0207, wR2 = 0.0395	
R indices (all data)	R1 = 0.0268, wR2 = 0.0415	
Extinction coefficient	n/a	
Largest diff. peak and hole	0.939 and -1.081 e.Å ⁻³	

The asymmetric unit (Figure 13a) has $\text{Pb}_2\text{Br}_{10}$ moiety, two ligands, and one water molecule. Strong hydrogen bonding interactions of water with bromine and nitrogen lead to a self-assembled 1D chain structure.

The powder XRD pattern compares well with the simulated XRD pattern (Figure 14). PzPbBr crystal structure displays large octahedral distortions implying a flexible structure that can support self-trapping of excitons. Distortions (quadratic elongation, bond angle variance) in $[\text{PbBr}_6]^{4-}$ octahedra, obtainable from refined crystal structure, have been previously correlated to broad-emission bandwidth for contorted 2D perovskites.^{9,12} However, for our 1D system, we do not see any such correlation. A careful examination of various other distortion parameters revealed no such correlation of the structural distortion parameters with PLQY for the reported strong, broad emitting 1D perovskites. In order to improve the CIE coordinates, $[(\text{H}_2\text{O})\text{Pz}_2\text{Pb}_2\text{Cl}_{10}]$ single crystals were synthesized (CCDC:1875386). The pure chloride variant has the same 1D corner shared structure as that of the PzPbBr perovskite.

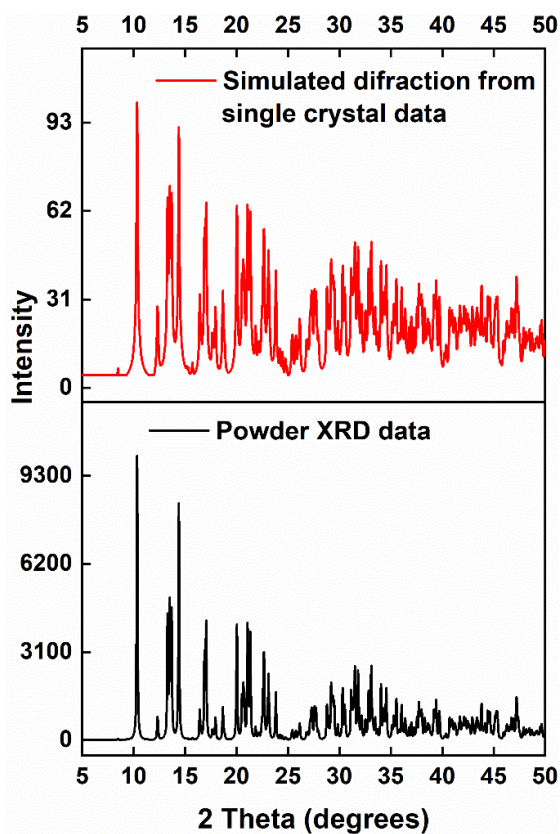


Figure 14: comparison between powder XRD pattern of PzPbBr and XRD pattern simulated from single crystal data of PzPbBr

2.5.H Mixed halide

The mixed halide perovskites $[(\text{H}_2\text{O})\text{Pz}_2\text{Pb}_2\text{Br}_{10-x}\text{Cl}_x]$ with $x = 1.5 - 3$ were synthesized through halide substitution.

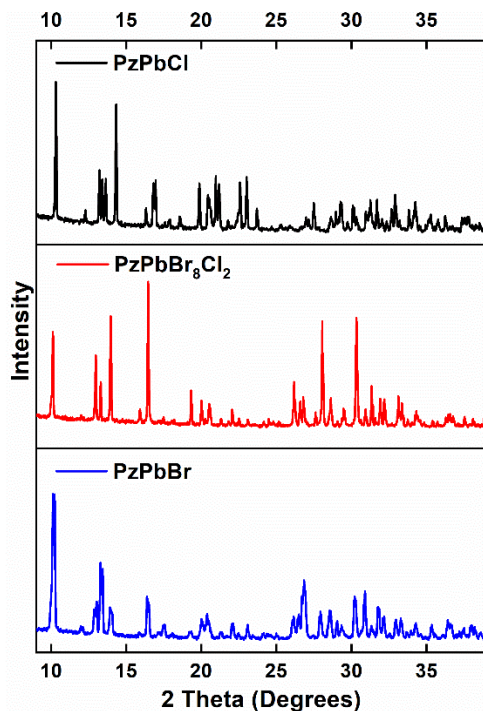


Figure 15: Comparison of XRD pattern with different halide compositions.

PXRD pattern changes with the increase in the chloride content (Figure 15). The absorption, PLE, and PL show systematic blue-shift with increasing chloride content (Figure 16). Lifetime lengthening is observed for these mixed halide perovskites (Figure 16d). The mixed halide perovskite, obtained CIE coordinate, as highlighted by 2* in Figure 3d, is improved to (0.37,0.44) with high PLQY (~10%).

The emission profile of the chloride variant blue shifts, but the PLQY is ~3-4% (Figure 16). The blue shift was observed to be monotonic as it increases the chloride content in the structure. The features were consistent over the absorbance, PL, and PLE data. A decrease in a lifetime was observed with the increase of chloride ions in the structure.

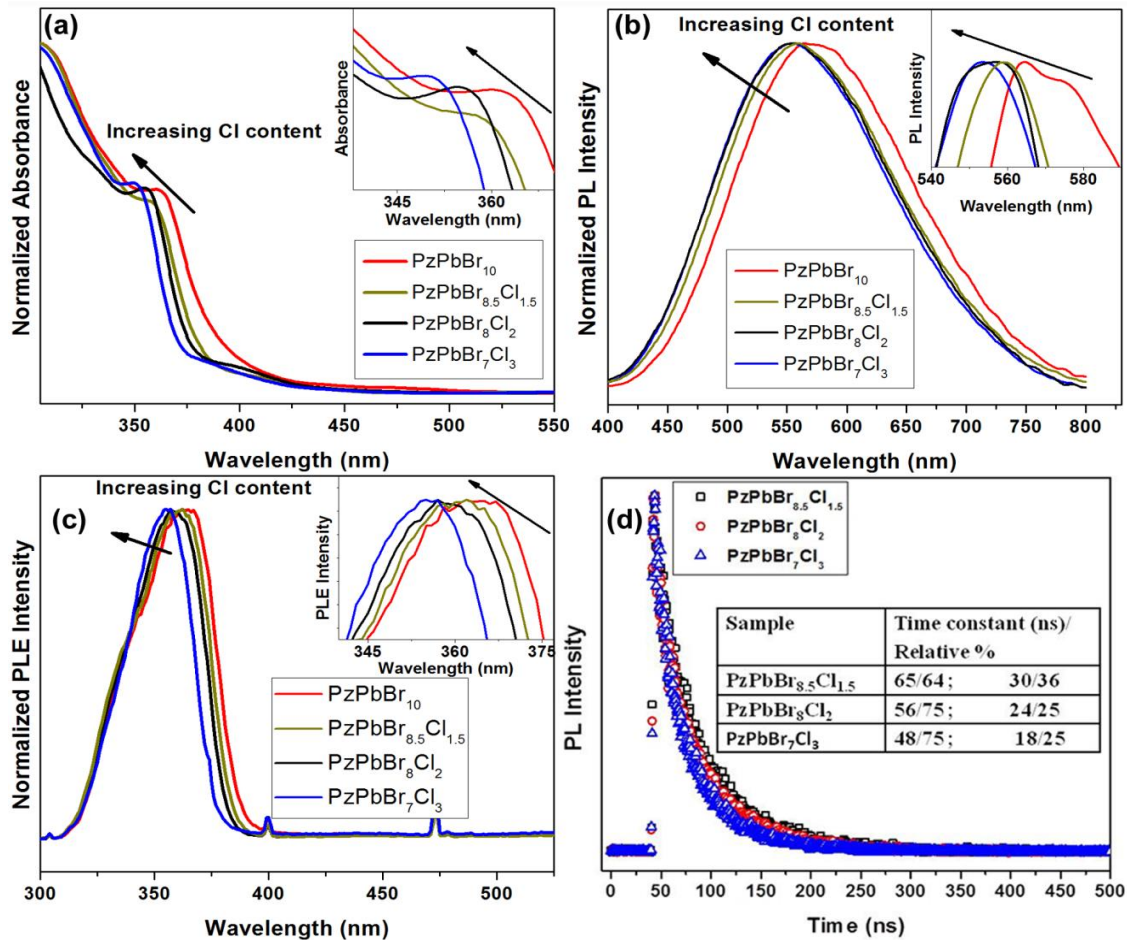


Figure 16: Comparison of (a) Absorbance; (b) PL emission; (c) PLE; (d) Lifetime analysis for PzPbBr and Br-Cl mixed halide perovskites showing blue shifted absorbance and emission with lifetime lengthening.

This halide substitution methodology provides a strong synthetic handle to further tune the emission profile (and CIE coordinates) retaining high PLQY.

2.5.I Structure-property correlation

Noteworthy, both contorted 2D perovskites and 1D perovskites are reported to support broad-band STE emission.^{8,9,12,16} Clearly, dimensionality reduction (2D → 1D) enhances broad band emission intensity.^{8,9,16} Here, we further observe that the octahedral connectivity mode and structure of the 1D chain affect the broad-band emission properties. Compared to edge shared flat 1D chain system¹⁶ or edge and corner shared flat 1D system⁸, purely corner shared contorted 1D chain structure exhibits comparable PLQY. This suggests that tuning of connectivity mode in low

dimensional perovskites is not correlated to high PLQY of broad band STE emission. In fact, 4-picolylamine based lead bromide perovskite (4AMPPbBr) with the chemical formula of $(C_6H_{10}N_2)PbBr_4$ is known to crystallize in purely edge-shared 1D structure that shows weak broad band emission.²⁰ Following this reported protocol²⁰, we have fabricated and optically characterized the 4AMPPbBr perovskite that shows very weak broad band emission. The estimated PLQY for this purely edge-shared perovskite is found to be ~0.1% for the broad emission. This again indicates that there is no observable correlation of octahedral connectivity mode with PLQY. This is further being supported by our recent report on EDHBr based perovskite that has corner shared 1D ribbon like structure with broad band emission PLQY of ~3%.²³ Interestingly, as shown in the presented PzPbX perovskite case (X=Br, Cl; both purely corner shared 1D structure), the nature of the halogen also affects the PLQY dramatically (9% for Br and 4% for Cl). Additionally, our preliminary synthetic efforts utilizing a variety of ligands show that restricting to the same 1D corner shared structure with different organic amine as the ligand drastically affects the PLQY. Hence, we strongly believe that octahedral connectivity mode is not a key role player, and it is very likely that there are many other relevant parameters (type of ligands, halides, and structure) that need to be optimized together to propose a general and rational synthetic methodology to design and fabricate low dimensional 1D perovskites with efficient broad-band STE emission. Tracing the key parameter that directs efficient, broad band STE emission in the 1D perovskites will require major and systematic synthetic efforts utilizing a variety of ligands to fabricate 1D perovskites with similar structure/connectivity mode.

2.6 Conclusions:

In conclusion, the PzPbBr, with a purely corner-sharing contorted 1D chain structure, exhibits strong room temperature yellowish-white emission with high PLQY of ~9%. Their mixed halide variants demonstrate tunable emission with high PLQY. As of yet, there is no correlation observed in terms of the structural distortion parameters (within metal octahedra and octahedral interlinkages) with the PLQY. The strong emissive properties of corner shared PzPbBr and weakly emitting properties of edge shared 4AMPPbBr perovskites highlight that connectivity mode tuning is not responsible for shaping the PLQY of broad STE emission band. In summary, the nature of the ligand, halogen type, and structure (contorted vs flat) together would play a decisive role in determining the PLQY of STE emission in 1D perovskites. This implicates further experimental

probing that is required by focusing efforts on synthesizing a wide range of broad emitting low dimensional perovskites utilizing a variety of ligands and halides. There is work underway where other 1D and 0D structure of Pb-based perovskite and help to draw the correlation of structure-property,

2.7 References:

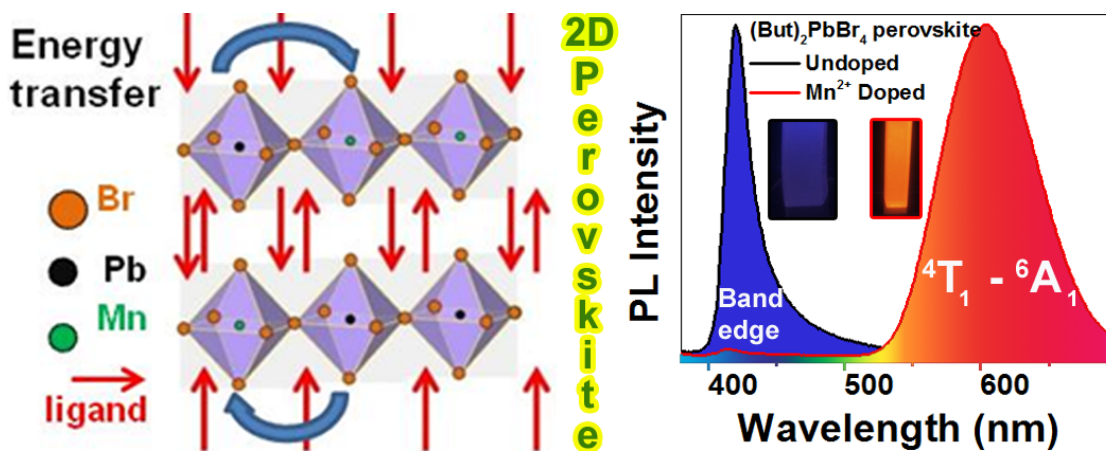
- (1) Li, W.; Wang, Z.; Deschler, F.; Gao, S.; Friend, R. H.; Cheetham, A. K. Chemically diverse and multifunctional hybrid organic–inorganic perovskites. *Nat. Rev. Mater.* **2017**, *2*, 16099.
- (2) Tan, H.; Jain, A.; Voznyy, O.; Lan, X.; de Arquer, F. P. G.; Fan, J. Z.; Quintero-Bermudez, R.; Yuan, M.; Zhang, B.; Zhao, Y.; Fan, F.; Li, P.; Quan, L. N.; Zhao, Y.; Lu, Z.-H.; Yang, Z.; Hoogland, S.; Sargent, E. H. Efficient and stable solution-processed planar perovskite solar cells via contact passivation. *Science* **2017**, *355*, 722-726.
- (3) Stoumpos, C. C.; Kanatzidis, M. G. The Renaissance of Halide Perovskites and Their Evolution as Emerging Semiconductors. *Acc. Chem. Res.* **2015**, *48*, 2791-2802.
- (4) Stranks, S. D.; Snaith, H. J. Metal-halide perovskites for photovoltaic and light-emitting devices. *Nat. Nanotechnol.* **2015**, *10*, 391-402.
- (5) Wang, N.; Cheng, L.; Ge, R.; Zhang, S.; Miao, Y.; Zou, W.; Yi, C.; Sun, Y.; Cao, Y.; Yang, R.; Wei, Y.; Guo, Q.; Ke, Y.; Yu, M.; Jin, Y.; Liu, Y.; Ding, Q.; Di, D. Y., L.; Xing, G.; Tian, H.; Jin, C.; Gao, F.; Friend, R. H.; Wang, J.; Huang, W. Perovskite light-emitting diodes based on solution-processed self-organized multiple quantum wells. *Nat. Photonics* **2016**, *10*, 699-704.
- (6) Lin, H.; Zhou, C.; Tian, Y.; Siegrist, T.; Ma, B. Low-Dimensional Organometal Halide Perovskites. *ACS Energy Lett.* **2018**, *3*, 54-62.
- (7) Saidaminov, M. I.; Mohammed, O. F.; Bakr, O. M. Low-Dimensional-Networked Metal Halide Perovskites: The Next Big Thing. *ACS Energy Lett.* **2017**, *2*, 889-896.
- (8) Mao, L.; Guo, P.; Kepenekian, M.; Hadar, I.; Katan, C.; J.; E.; Schaller, R. D.; Stoumpos, C. C.; Kanatzidis, M. G. Structural Diversity in White-Light-Emitting Hybrid Lead Bromide Perovskites. *J. Am. Chem. Soc.* **2018**, *140*, 13078-13088.
- (9) Smith, M. D.; Karunadasa, H. I. White-Light Emission from Layered Halide Perovskites. *Acc. Chem. Res.* **2018**, *51*, 619-627.

- (10) Mao, L.; Wu, Y.; Stoumpos, C. C.; Wasielewski, M. R.; Kanatzidis, M. G. White-Light Emission and Structural Distortion in New Corrugated Two-Dimensional Lead Bromide Perovskites. *J. Am. Chem. Soc.* **2017**, *139*, 5210-5215.
- (11) Cortecchia, D.; Yin, J.; Bruno, A.; Lo, S.-Z. A.; Gurzadyan, G. G.; Mhaisalkar, S. G.; Brédas, J.-L.; Soci, C. Polaron self-localization in white-light emitting hybrid perovskites. *J. Mater. Chem. C* **2017**, *5*, 2771–2780.
- (12) Cortecchia, D.; Neutzner, S.; Srimath Kandada, A. R.; Mosconi, E.; Meggiolaro, D.; De Angelis, F.; Soci, C.; Petrozza, A. Broadband Emission in Two-Dimensional Hybrid Perovskites: The Role of Structural Deformation. *J. Am. Chem. Soc.* **2017**, *139*, 39–42.
- (13) McCall, K. M.; Stoumpos, C. C.; Kostina, S. S.; Kanatzidis, M. G.; Wessels, B. W. Strong Electron–Phonon Coupling and Self-Trapped Excitons in the Defect Halide Perovskites $A_3M_2I_9$ ($A = Cs, Rb$; $M = Bi, Sb$). *Chem. Mater.* **2017**, *29*, 4129–4145.
- (14) Zheng, W.; Huang, P.; Gong, Z.; Tu, D.; Xu, J.; Zou, Q.; Li, R.; You, W.; Bünzli, J. C. G.; Chen, X. Near-Infrared-Triggered Photon Upconversion Tuning in All-Inorganic Cesium Lead Halide Perovskite Quantum Dots. *Nat. Commun.* **2018**, *9*, 3462.
- (15) Yu, J.; Kong, J.; Hao, W.; Guo, X.; He, H.; Leow, W. R.; Liu, Z.; Cai, P.; Qian, G.; Li, S.; Chen, X.; Chen, X. Broadband Extrinsic Self-Trapped Exciton Emission in Sn-Doped 2D Lead-Halide Perovskites, *Adv. Mater.* **2018**, *31*, 1806385.
- (16) Yuan, Z.; Zhou, C.; Tian, Y.; Shu, Y.; Messier, J.; Wang, J. C.; van de Burgt, L. J.; Kountouriotis, K.; Xin, Y.; Holt, E.; Schanze, K.; Clark, R.; Siegrist, T.; Ma, B. One-dimensional organic lead halide perovskites with efficient bluish white-light emission. *Nat. Commun.* **2017**, *8*, 14051.
- (17) Williams, R. T.; Song, K. S. The self-trapped exciton. *J. Phys. Chem. Solids* **1990**, *51*, 679-716.
- (18) Ishida, K. Self-trapping dynamics of excitons on a one-dimensional lattice. *Z. Phys. B Con. Mat.* **1997**, *102*, 483-491.
- (19) Mousdis, G. A.; Gionis, V.; Papavassiliou, G. C.; Raptopoulou C. P.; Terzis, A. Preparation, structure and optical properties of $[CH_3SC(=NH_2)NH_2]_3PbI_5$, $[CH_3SC(=NH_2)NH_2]_4Pb_2Br_8$ and $[CH_3SC(=NH_2)NH_2]_3PbCl_5 \cdot CH_3SC(=NH_2)NH_2Cl$. *J. Mater. Chem.*, **1998**, *8*, 2259-2262.
- (20) Li, Y.; Zheng, G.; Lin, C.; Lin, J. Synthesis, structure and optical properties of different dimensional organic-inorganic perovskites. *Solid State Sci.* **2007**, *9*, 855-861.

- (21) Thirumal, K.; Chong, W. K.; Xie, W.; Ganguly, R.; Muduli, S. K.; Sherburne, M.; Asta, M.; Mhaisalkar, S.; Sum, T. C.; Soo, H. S.; Mathews, N. Morphology-Independent Stable White-Light Emission from Self-Assembled Two-Dimensional Perovskites Driven by Strong Exciton–Phonon Coupling to the Organic Framework. *Chem. Mater.* **2017**, *29*, 3947-3953.
- (22) Viswanath, A. K.; Lee, J. I.; Kim, D.; Lee, C. R.; Leem, J. Y. Exciton-Phonon Interactions, Exciton Binding Energy, and Their Importance in the Realization of Room-Temperature Semiconductor Lasers Based on GaN. *Phys. Rev. B* **1998**, *58*, 16333.
- (23) Haris, M. P. U.; Bakthavatsalam, R.; Shaikh, S.; Kore, B. P.; Moghe, D.; Gonnade, R. G.; Sarma, D. D.; Kabra, D.; Kundu, J. Synthetic Control on Structure/Dimensionality and Photophysical Properties of Low Dimensional Organic Lead Bromide Perovskite. *Inorg. Chem.* **2018**, *57*, 13443-13452.

Chapter 3

Title: Dopant induced broadband emission in 2D lead-based perovskite



3.1 Introduction:

Lead trihalide based 3D perovskite materials (APbX₃ with A= Cs, Methylammonium; X=Cl, Br, I) have attracted phenomenal research interest due to their intriguing applications in high efficiency solar cells, color tunable & narrow line-width light emitting diodes (LEDs), lasers, and photodetectors.¹⁻⁷ Such materials have recorded >20% solar cell efficiency and is believed to set a new paradigm for renewable energy sources due to their superior charge carrier mobilities and low density of mid-gap trap states, and defect tolerant nature.⁸ Currently, the development of 3D APbX₃ based materials for illumination and display applications due to their enabling optical properties (tunable band edge emission, narrow line-width, high PL quantum yield, and fast radiative decay rates) is attracting active research interest.⁹⁻¹³ Very recently, many have reported on providing an additional level of control on the optoelectronic properties of these 3D perovskite materials by deliberately introducing impurity ions in the form of dopants.¹⁴⁻²⁰ Specifically, doping Mn²⁺ ions directly into 3D APbCl₃ nanocrystals have met with great success unraveling interesting physical phenomena due to the energy transfer process from the host semiconductor to dopant Mn²⁺ ions.^{14-16, 18} Strong exchange interactions between the d electrons of Mn²⁺ and charge carriers of the host semiconductor facilitates such energy transfer. Along with the remnant band-edge photoluminescence, a new emission channel at ~590 nm, which is typically a forbidden internal ⁴T₁ to ⁶A₁ transition of Mn²⁺ dopant, becomes active with high luminescence efficiency. Impact excitation of the impurity ion by the optically excited charge carriers of the host semiconductor

activates this forbidden internal transition. Consequently, photoluminescence spectra show emission peaks due to band edge emission and/or yellow-orange Mn^{2+} emission with different timescales of PL decay (band edge: nanosecond, Mn^{2+} emission: milliseconds). Notably, APbCl_3 systems have been directly doped with Mn^{2+} ions successfully while the same strategy does not seem to work for APbBr_3 systems.^{14, 16, 18} This has been ascribed to the higher bond strength of the Pb-Br than Mn-Br bonds. Thermodynamics of the bond energy precludes successful direct doping of Mn^{2+} ions at the Pb sites in the case of APbBr_3 nanocrystals.¹⁴ In order to fabricate Mn^{2+} doped APbBr_3 nanocrystals, an anion exchange strategy has been utilized on Mn^{2+} doped APbCl_3 nanocrystals as the starting material.^{14, 16} The current research activity on 3D APbX_3 based materials (undoped; doped) has shown great potential for applications in LEDs, sensitized solar cells, luminescent solar concentrators, biomedical imaging, and phosphorescence biosensing.²¹⁻²⁴ However, the 3D APbX_3 based material typically has low exciton binding energies.²⁵ In contrast, 2D layered lead halide-based perovskites are excellent candidates as active materials for LED applications due to their characteristic strongly bound excitons with high binding energies even at room temperature and fast radiative decay rates.²⁵⁻²⁸ Such 2D layered perovskites can be utilized as semiconductor host materials for energy transfer to appropriately chosen organic ligands as the acceptor moieties.^{27, 29-31} To note, 2D layered perovskites, with the general formula $(\text{L})_2(\text{L}')_n\text{Pb}_n\text{X}_{3n+1}$, can be thought of as derived from 3D APbX_3 lattice by slicing along $\langle 100 \rangle$ direction. Here L is an alkyl ammonium ligand, and the variable n represents the number of the metal cation layers sandwiched between the two organic dielectric layers. For $n = 1$, the structure represents quantum well with one atomic layer of $[\text{PbX}_4]^{2-}$ separated by organic chains, in which the adjacent layers are held together by weak van der Waals forces. The bulk phase of $n=1$ 2D layered perovskites represents a multiple quantum well structures wherein the inorganic plane consisting of corner shared metal halide octahedra networked in 2 dimensions are separated by organic chain layers. This organic layer acts as a dielectric spacer confining the inorganic excitons within the metal plane, isolating the 2D quantum wells in each layer from the electronic coupling. The quantum and dielectric confinement lead to high exciton binding energies, high oscillator strengths, and fast radiative decay rates in these 2D layered perovskites.^{27, 28, 32-34} Hence, these materials are believed to be highly beneficial for applications in LEDs and displays.

With the current interest in the perovskite materials for solar cell applications, research on 2D perovskite materials has seen an incredible resurgence. Low dimensional perovskites are now

considered to be the new frontier that deserves special attention for optoelectronic applications.³⁵ In this chapter, I have demonstrated $(\text{C}_4\text{H}_9\text{NH}_3)_2\text{PbBr}_4$ based bulk 2D layered perovskites as an active semiconductor host material for energy transfer to incorporate Mn^{2+} impurity ions for the development of high efficiency phosphor materials for LED applications. Mn^{2+} incorporated 2D layered perovskite bulk material is demonstrated to be synthesized in a simple and scalable methodology that can be effectively translated for the development of pure color LEDs. To explore the feasibility, we took lead butyl ammonium bromide as host material for doping. For simplicity of annotation and brevity, bulk 2D layered host perovskite material, $(\text{C}_4\text{H}_9\text{NH}_3)_2\text{PbBr}_4$, will be referred to as $(\text{But})_2\text{PbBr}_4$ while the Mn^{2+} incorporated into the host $(\text{C}_4\text{H}_9\text{NH}_3)_2\text{PbBr}_4$ perovskite will be referred to as $\text{Mn}^{2+}:(\text{But})_2\text{PbBr}_4$ throughout the rest of this chapter.

3.2 Materials:

Butylammonium bromide (BABr) was purchased from Great Cell Solar. HBr was purchased from TCI Chemicals. The salt lead bromide (PbBr_2), dimethylformamide (DMF), and manganese bromide (MnBr_2) were procured from Sigma Aldrich. All of the chemicals were utilized as such without any purification.

3.3 Synthesis:

Synthesis of all materials and subsequent down converted LED were described below.

3.3.A Synthesis of $\text{C}_4\text{H}_9\text{NH}_3\text{Br}$ (Butyl ammonium lead bromide)

In a 250 ml round bottom flask, 10 ml of Butyl amine and 25ml of methanol was added, stirred and maintained at 0 °C using an ice bath. 10 ml of concentrated HBr was added drop-wise to the above solution after which the ice bath was removed. The mixture was stirred at room temperature for 3 hours. Rotary evaporator was used at 70 °C to remove the methanol and water. The crude oil-like product was washed repeatedly with diethyl ether and finally recrystallized from a mixed solvent of diethyl ether and ethanol. After filtration, the white solid was collected and dried at 60°C in a vacuum oven for 24 hours.

3.3.B Synthesis of single crystals of $(\text{C}_4\text{H}_9\text{NH}_3)_2\text{PbBr}_4$ 2D layered perovskite

For the preparation of single crystals of $(\text{C}_4\text{H}_9\text{NH}_3)_2\text{PbBr}_4$, $\text{C}_4\text{H}_9\text{NH}_3\text{Br}$ (308 mg, 2 mmol), PbBr_2 (367 mg, 1 mmol) and 2 drops of HBr aqueous solution were dissolved in 2 mL DMF solvent

which was heated to 90 °C. To this hot clear solution toluene is added just up until the solution starts turning turbid. The heating is removed and the solution is allowed to cool naturally. This leads to the formation of plate like white crystals in copious amounts. After 3 hours, the supernatant liquid is removed and the crystals are repeatedly washed using acetone, and THF. The crystals are filtered and dried under vacuum at 60 °C for overnight.

3.3.C Synthesis of Mn²⁺ doped (C₄H₉NH₃)₂PbBr₄ 2D layered perovskite

A desired amount of the above crystals of (C₄H₉NH₃)₂PbBr₄ was mixed with MnBr₂ (amount of Mn salt being added is with respect to number of mole percent of Pb) in an Agate Mortar and Pestle. The powders are ground homogeneously for more than 15 minutes. This finely ground powder is then added to glass vial and was heated at 125 °C in an oven for an hour. The sample was allowed to cool naturally and was used further for characterization.

3.4 Characterization methods:

Transmission electron microscopy (TEM) images were collected using Tecnai T20 TEM operating at an accelerating voltage of 200 kV. Powder x-ray diffraction (XRD) patterns were recorded using a PAN analytical X'Pert Pro equipped with Cu K α radiation ($\lambda = 1.5406$ Å). Steady state PL measurements were performed utilizing PTI QM 400 fluorometer. PL decay dynamics were recorded using FLS 980 (Edinburgh Instruments) using microsecond flash lamp with power 100 W. For Mn emission decay dynamics, the sample was excited at 300 nm using microsecond flash lamp, whereas, excitonic PL decay was recorded using 340 nm picosecond pulsed LED laser source. PL quantum yield for Mn emission was measured against R6G dye. Absorbance measurements were performed using a Shimadzu UV-3600 plus UV-Vis-NIR spectrophotometer. Thermogravimetric analysis (TGA) measurements were recorded using Mettler Toledo TGA/SDTA851e. The samples were heated in the range of 30-800 °C at the heating rate of 5 °C/min. For measurement of luminance and CIE color chromaticity coordinates of the LED, Konica-Minolta chromameter CS-200 was utilized.

3.5 Results and Discussions:

Single crystals of $(\text{But})_2\text{PbBr}_4$ host material was synthesized by slow cooling of hot solution of stoichiometric amounts of PbBr_2 and $((\text{C}_4\text{H}_9\text{NH}_3)\text{Br}$ in DMF/toluene mixture with 2-3 drops of concentrated HBr aqueous solution.²⁶ In order to incorporate optically active Mn^{2+} impurity ions into the fabricated 2D layered host material, simple solid-state grinding of single crystals of $(\text{But})_2\text{PbBr}_4$ and MnBr_2 in the desired ratio is performed, followed by an hour of annealing at 125 °C. The starting crystals of the host material and Mn^{2+} incorporated 2D layered perovskite products are abbreviated as $(\text{But})_2\text{PbBr}_4$ and $\text{Mn}^{2+}:(\text{But})_2\text{PbBr}_4$ respectively. The discussion on the obtained results is discussed in the rest of the chapter.

3.5.A Optical Property

UV-Vis absorption measurement of $(\text{But})_2\text{PbBr}_4$ crystals show a broad absorption band centered at 410 nm. Steady-state photoluminescence measurement of the host material shows a strong and narrow (FWHM: 20 nm) blue emission peak at 420 nm when excited at 360 nm above the band edge (Figure 1).

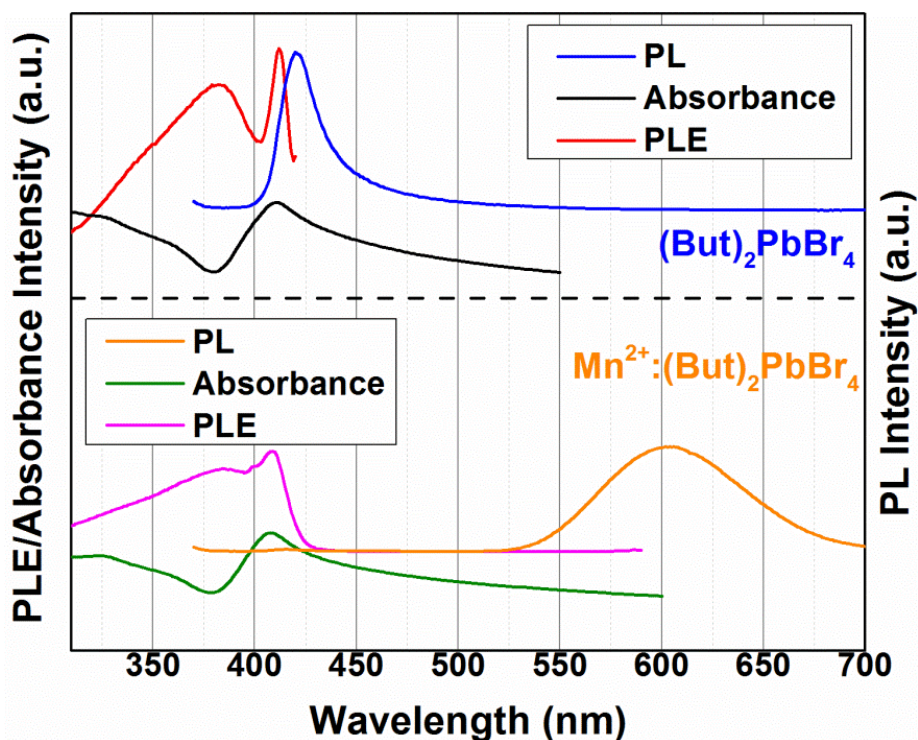


Figure 1: Absorbance, PL, and PLE spectra for the undoped (top) and doped 2D perovskite.

The photoluminescence excitation (PLE) spectra collected at 425 nm shows excitonic absorption feature at 410 nm with very small stokes shift (Figure 1). The excitation spectra are characterized by a sharply rising threshold region occurring near the absorption edge of the host bulk $(\text{But})_2\text{PbBr}_4$ material. The resemblance of the absorption band with the PLE spectra of the bulk host material for the blue emission signifies that the blue emission is due to the formation of electron-hole pairs in the host semiconductor material (Figure 2 image).

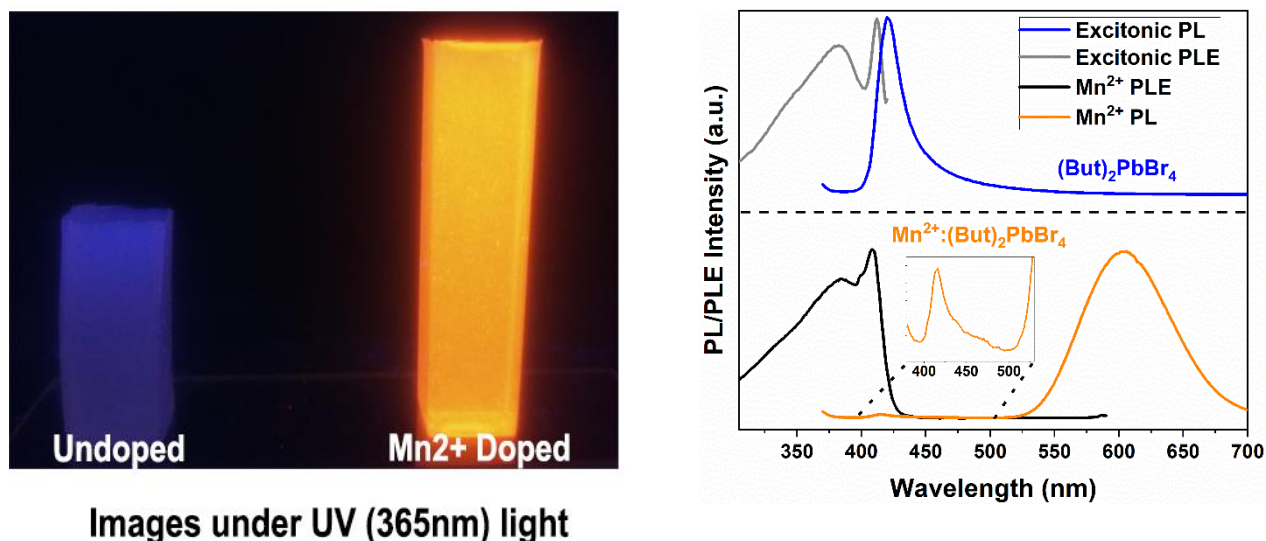


Figure 2: Left-image of host and Mn^{2+} doped system. Right-optical properties of Mn^{2+} doped (bottom) and undoped (top) host material showing the PL and PLE for the band edge and Mn^{2+} emission.

Interestingly, the photoluminescence spectra of the $\text{Mn}^{2+}:(\text{But})_2\text{PbBr}_4$ sample show a very weak emission band at 420 nm (Figure 2). Additionally, a broad emission peak (FWHM = 80 nm), centered at ~600 nm, is observed in the PL spectra (Figure 2). This peak is attributable to the Mn^{2+} $d-d$ emission corresponding to the forbidden ${}^4\text{T}_1 \rightarrow {}^6\text{A}_1$ internal transition. Such transitions are known to be universally broad in II-VI systems both in bulk or nanostructured morphologies.^{36, 37} Importantly, the PLE spectra collected at 600 nm (Figure 1,2) shows features that resemble very closely to that of the PLE spectra of the host material without any Mn^{2+} ions. Moreover, the excitation spectra here is characterized by a sharply rising threshold region occurring near the absorption band edge of $\text{Mn}^{2+}:(\text{But})_2\text{PbBr}_4$ material (Figure 1). This signifies that the 600 nm Mn^{2+} emission is sensitized by band edge absorption of the host semiconductor material. This, in turn,

clearly indicates efficient energy transfer mechanism from the host perovskite to the closely located Mn^{2+} ions incorporated into the host semiconductor material. The excitation-dependent PL spectra (Figure 3) indicate that the dual emission peaks (very weak band edge and strong Mn^{2+} luminescence) have no shift by altering the excitation wavelength from 340 to 400 nm.

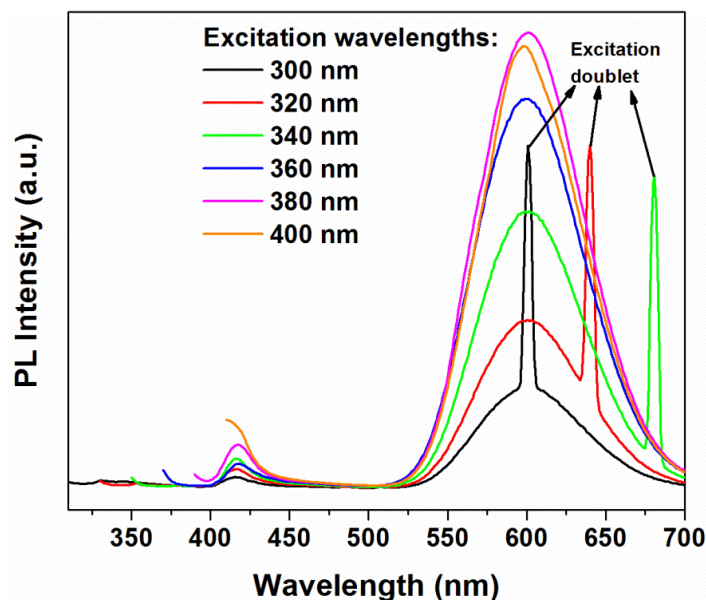


Figure 3: Excitation dependent PL spectra of the doped 2D perovskite

This independence of the PL spectra on excitation wavelength confirms the single source of the dual emission, namely, the exciton of the host bulk 2D layered perovskite. The presence of strong Mn^{2+} luminescence, sensitized by the host bulk perovskite, signifies that the incorporated Mn^{2+} ions act as efficient energy acceptor, out-competing various other non-radiative relaxation pathways. Qualitatively, the efficiency of energy transfer from the exciton to the Mn^{2+} ions, as manifested in the form of Mn^{2+} luminescence band, is governed by the interplay of two opposing phenomena: i) spin-spin exchange coupling between the charge carriers of the semiconductor host material and the Mn^{2+} ions; and ii) inherent forbidden nature of the internal d-d transition of Mn^{2+} ions due to weak transition dipoles. The observed strong Mn^{2+} luminescence suggests the presence of sufficiently strong exchange coupling between the charge carriers of the host and the Mn^{2+} *d* electrons.

3.5.B Effect of dopant concentration

The effect of varying the input Mn concentration (with respect to the number of moles of Pb) on the luminescence intensity of the Mn^{2+} emission band was also performed. The actual amount of Mn^{2+} ion that was going in the structure was less than 2% in most of the cases and seen by ICP analysis.

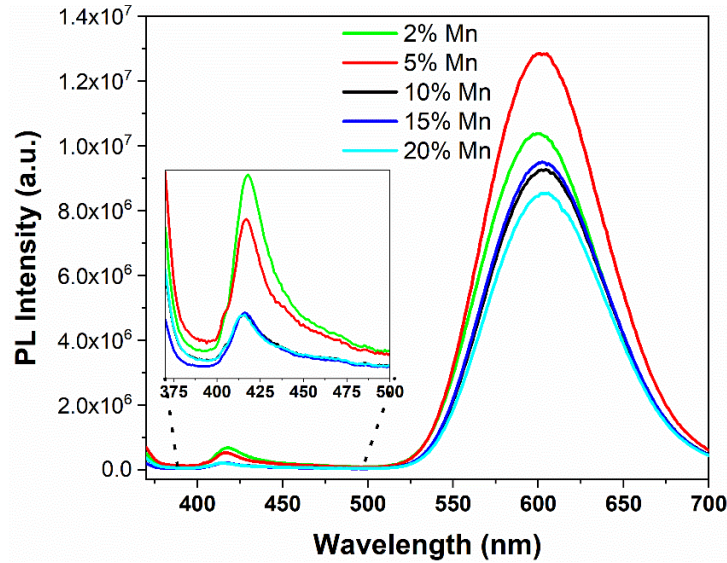


Figure 4: Dopant concentration-dependent PL spectra

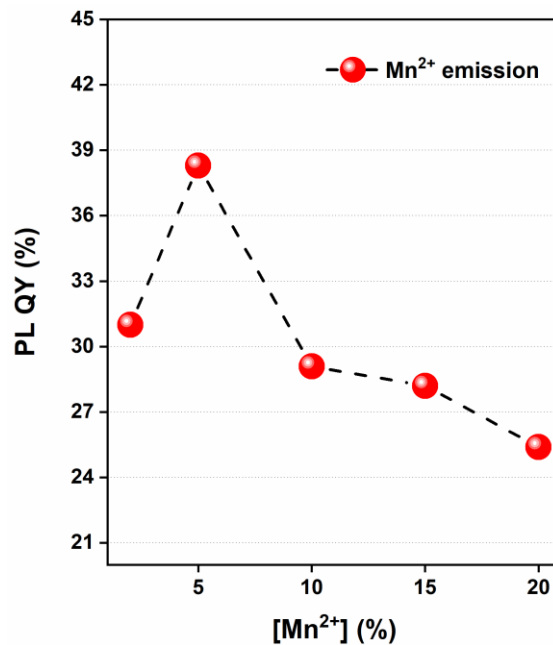


Figure 5: Dopant concentration-dependent quantum yield of Mn^{2+} emission (QY_{Mn})

With the increase of the concentration of Mn from 2% to 5%, Mn^{2+} PL emission becomes stronger, followed by a gradual decrease of the Mn^{2+} PL intensity as the Mn concentration increases from 10% to 20%. For all of these cases, a very weak band edge persists. The calculated quantum yield for Mn^{2+} emission, QY_{Mn} , for the different Mn concentrations is shown in Figure 5, which clearly shows that the values of QY_{Mn} initially rises and then gradually declines with the increase in the Mn concentration. The initial rise of the QY_{Mn} is due to increased number of luminescent centers acting as acceptors for the energy transferred from the band edge exciton. However, with the further increase in the Mn^{2+} concentration, the PL efficiency decreases due to interaction between neighboring Mn^{2+} ions. In this scenario, a radiation less resonance energy transfer can occur between closely placed Mn^{2+} ions.³⁶ This leads to decrease of luminescence quantum efficiency as observed here. The highest QY_{Mn} of 37% is obtained for samples with 10% Mn (feed amount with respect to Pb) incorporation with overall yellow-orange colored emission. It is important to note that the QY_{Mn} values obtained for the different Mn concentrations (2% - 20 %) explored here are all above 24 % and represents a very strong luminescence efficiency. The observed high QY_{Mn} in these doped materials could be due to the utilization of host material with strong quantum confinement that boosts sp-d carrier exchange interaction thereby increasing the energy transfer efficiency between the host and the dopant ions. However, with the attempted further increase of the Mn concentration, the products show qualitatively the same spectral features but with low QY_{Mn} values. This is likely due to the formation of surface or internal defects in the host semiconductor material. Hence, we restrict ourselves with low Mn^{2+} concentration regime samples (2% - 20%) for this study.

3.5.C Effect of thermal annealing on PL properties

Noteworthy here is the fact that $\text{Mn}^{2+}:(\text{But})_2\text{PbBr}_4$ samples are prepared by solid-state grinding followed by one hour of annealing at 125 °C. This annealing step turns out to be very critical in successfully incorporating the Mn^{2+} ions into the host lattice and thereby engineering its optical properties. Hence, temperature-dependent annealing studies were performed for the host $(\text{But})_2\text{PbBr}_4$ and $\text{Mn}^{2+}:(\text{But})_2\text{PbBr}_4$ material.

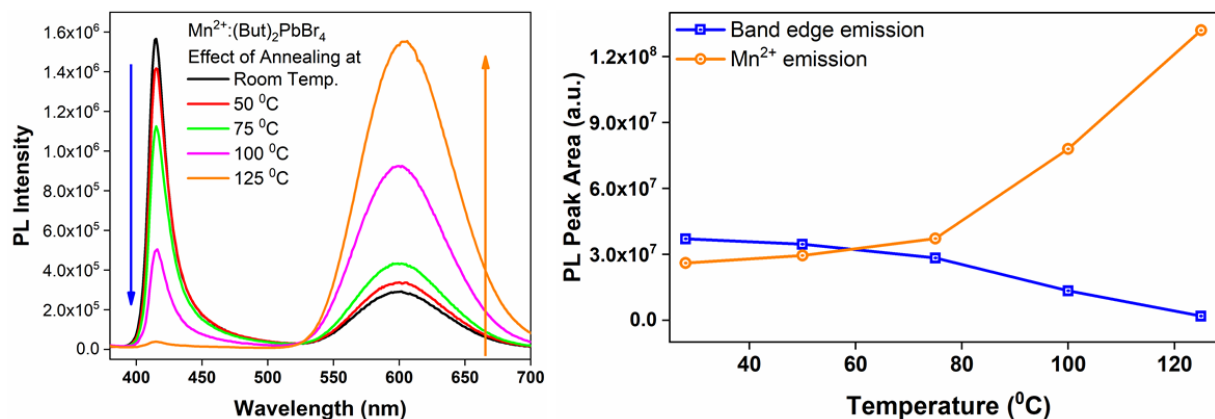


Figure 6: Band edge PL decreases and dopant emission increases as annealing temperature is increased. Increased doping of host due to increased thermal diffusion

In Figure 6 we see the PL properties of the $\text{Mn}^{2+}:(\text{But})_2\text{PbBr}_4$ sample annealed at different temperatures. PL spectra clearly show that when the sample is annealed at room temperature, there is a dominant band edge blue emission with a weak orange-yellow Mn^{2+} emission peak. As this annealing temperature is progressively increased, the band edge blue emission intensity decreases strongly. More interestingly, the orange-yellow Mn^{2+} emission peak intensity gradually intensifies. When annealed at 100 °C, the Mn^{2+} emission peak is observed to be stronger than the band edge emission. For 125 °C annealing temperature, the band edge emission is seen to be suppressed heavily while the Mn^{2+} emission peak is the strongest mode observed. Figure 6 also shows the integrated peak area for the band edge and Mn^{2+} emission as a function of annealing temperatures. It is clear from the figure that as the annealing temperature is increased, the band edge emission gets progressively suppressed while the Mn^{2+} emission enhances strongly. This implies that the energy transfer from the host to the Mn^{2+} luminescent centers becomes more efficient as the sample is annealed at progressively higher temperatures. This could be due to the increased extent of Mn^{2+} incorporation into the host lattice sites due to increased thermal diffusion of the dopant ions.

3.5.D Lifetime study

The PL lifetimes of the host $(\text{But})_2\text{PbBr}_4$ and $\text{Mn}^{2+}:(\text{But})_2\text{PbBr}_4$ samples were measured using time-resolved PL spectroscopy.

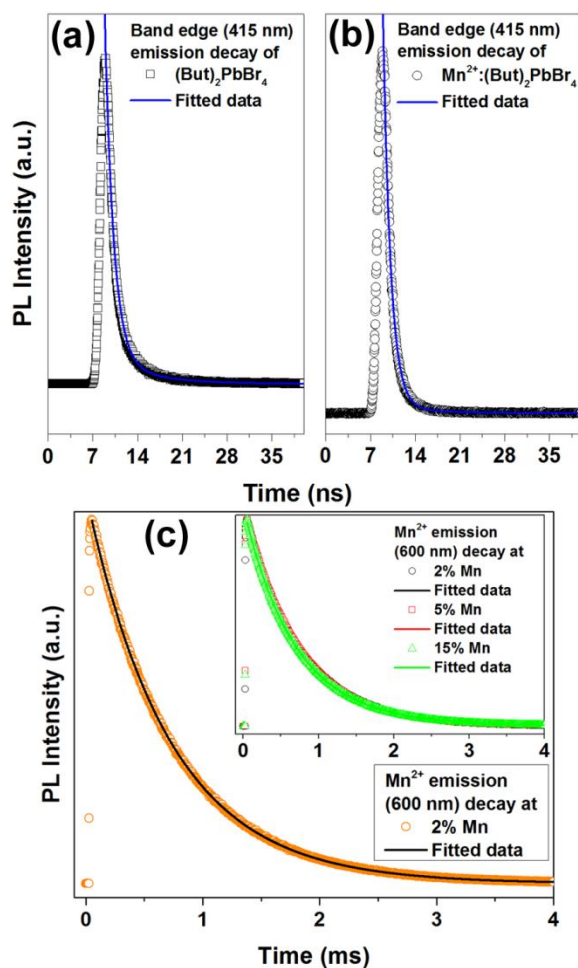


Figure 7: PL decay dynamics of (a) undoped host sample; (b) doped sample for the band edge emission; (c) doped sample for the Mn^{2+} emission with inset showing the same at different dopant concentrations.

For the $(\text{But})_2\text{PbBr}_4$ host material, the band edge PL decay curve (Figure 7a) shows a bi-exponential fit with lifetimes of 1.4 ns (73% contribution) and 6.5 ns (27% contribution), which are in close agreement to the reported data.²⁶ Interestingly, for $(\text{But})_2\text{PbBr}_4$ and Mn^{2+} samples, two very different lifetimes are observed. For this, the band edge PL decay curve (Figure 7) shows a bi-exponential fit with lifetimes of 1.2 ns (90% contribution) and 6.3 ns (10% contribution). For the Mn^{2+} emission band, the lifetime data can be fitted to a mono-exponential decay curve with a long lifetime of 740 μs . This long lifetime is due to the forbidden nature of the $^4\text{T}_1$ to $^6\text{A}_1$ internal Mn^{2+} transition and contribution due to neighboring Mn^{2+} - Mn^{2+} clustering interaction.³⁶ Varying the Mn^{2+} concentration in the range of 2% - 15% does not seem to have a significant influence on

the lifetime of this Mn^{2+} d electron emission, as shown in the inset of Figure 7c. The observed Mn^{2+} emission lifetime of $\sim 740 \mu s$ is shorter than the typical $1300 \mu s$ lifetime of isolated Mn^{2+} doped in perovskite^{15-18, 36} or in II-VI⁴¹⁻⁴³ quantum dot systems. This lifetime shortening indicates dipole-dipole interaction between neighboring Mn^{2+} - Mn^{2+} ions of a cluster residing in the host perovskite.

3.5.E Morphology and elemental composition

The morphological characterization of the bulk host material was performed using TEM/EDS elemental mapping, which confirms the sheet-like 2D morphology of the micro-particles with chemical composition showing the presence of Pb and Br (atomic % of Pb: Br =17:83), in consonance to reported data.²⁶ The elemental mapping shows the homogeneous presence of constituent elements (Figure 8). The morphology analysis of the Mn^{2+} : (But)₂PbBr₄ samples, using TEM/EDS elemental mapping, reveals 2D sheet-like morphology of the micro-particles.

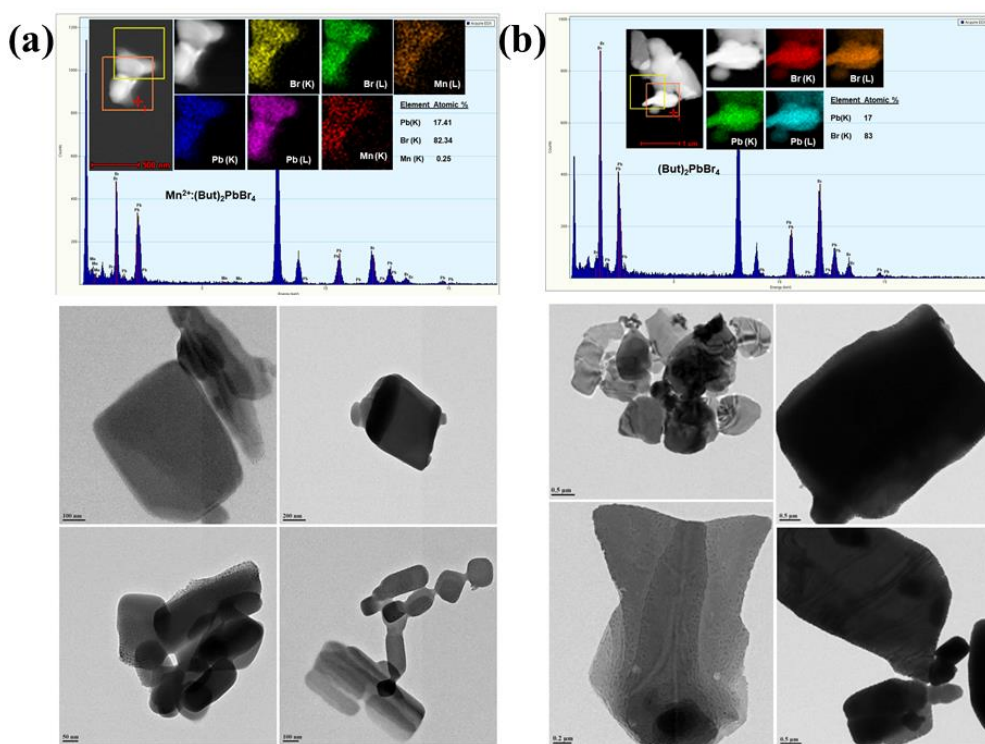


Figure 8: TEM and Elemental mapping a) for (But)₂PbBr₄ and b) Mn^{2+} :(But)₂PbBr₄ samples.

The EDS analysis clearly confirms the presence of Mn^{2+} ions in the samples (Figure 8a). Elemental mapping shows the homogeneous distribution of Pb, Br, and Mn as the constituting elements.

3.5.F Thermal stability

TGA data for the host $(\text{But})_2\text{PbBr}_4$ and $\text{Mn}^{2+}:(\text{But})_2\text{PbBr}_4$ sample were recorded (Figure 9) and presents very similar weight loss characteristics. The TGA data analysis for the host material shows two major weight loss peaks:

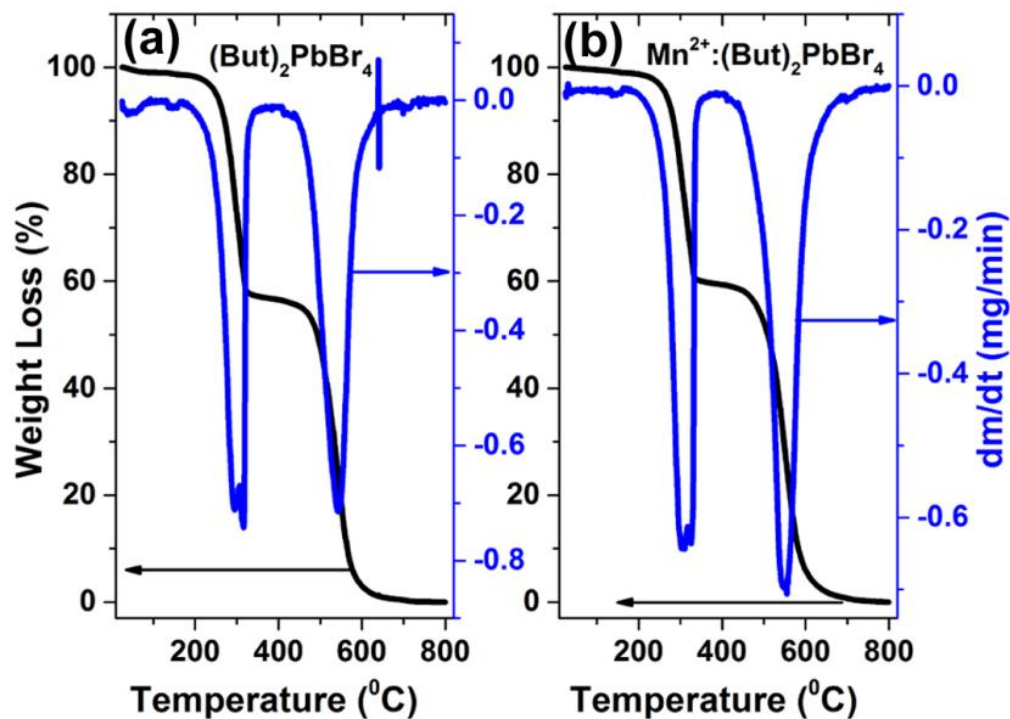


Figure 9: TGA for the a) undoped and b) doped 2D perovskite.

The loss of the butyl ammonium bromide ligand of 45% at 315 °C, and the other related to the release of inorganic lead bromide of 55% at 550 °C (Figure 9a). Similarly, for the $\text{Mn}^{2+}:(\text{But})_2\text{PbBr}_4$ sample, loss of the butyl ammonium bromide ligand of 42% at 321 °C, and another related to the release of inorganic lead bromide of 58% at 555 °C is observed (Figure 9b). The observed weight loss ratio of organic to inorganic component for the $(\text{But})_2\text{PbBr}_4$ and $\text{Mn}^{2+}:(\text{But})_2\text{PbBr}_4$ sample suggests approximately 2:1 molar ratio between the organic and inorganic components, a feature of the 2D layered perovskite materials. Such TGA analysis, confirming the approximate chemical composition in the 2D layered perovskite, is in consonance to existing reports.^{26, 38, 39}

3.5.G Nature of doping

X-ray diffraction studies characterized the location of Mn site in the doped system. XRD characterization of the host $(\text{But})_2\text{PbBr}_4$ and the $\text{Mn}^{2+}:(\text{But})_2\text{PbBr}_4$ sample is shown in Figure 10.

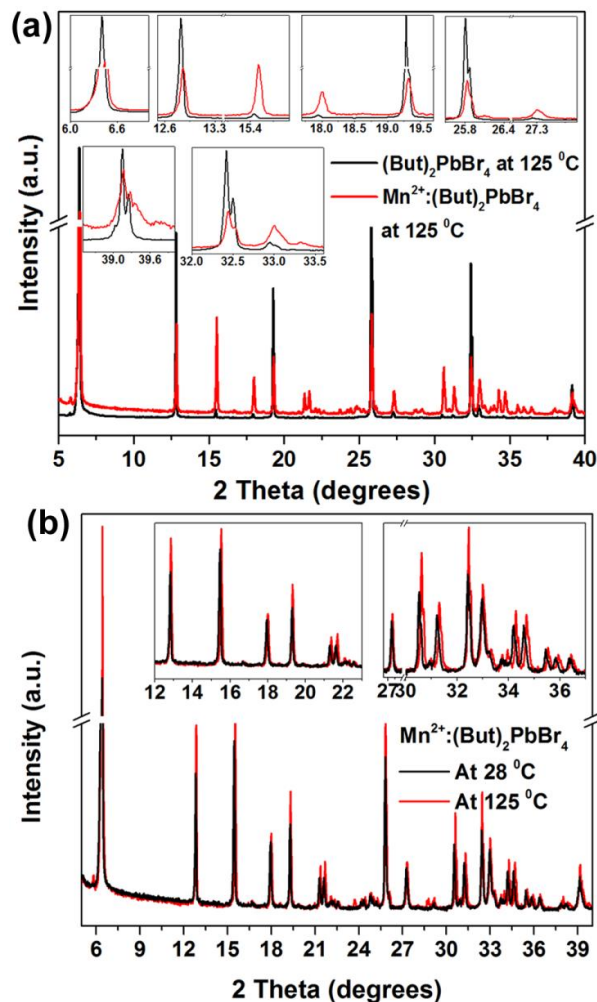


Figure 10: XRD pattern of (a) undoped and doped material both annealed at 125°C with a magnified view as insets; (b) doped material annealed at 28°C and 125°C with a magnified view as insets.

The as-prepared single crystals of the host material show an XRD pattern that is in excellent agreement with the prior report.²⁶ The 125°C heated sample was used to give a better understanding of the occurrence of doping. Interestingly, the XRD pattern of the $\text{Mn}^{2+}:(\text{But})_2\text{PbBr}_4$ sample is structurally very similar to the XRD pattern of the host $(\text{But})_2\text{PbBr}_4$ sample (Figure 10). A more careful examination of the XRD patterns reveals that the peak positions of the

$\text{Mn}^{2+}:(\text{But})_2\text{PbBr}_4$ sample have monotonically shifted to higher angles compared to that of the host material (Figure 10b). This observed shift of the XRD peak positions indicates toward successful incorporation of Mn^{2+} ions into the lattice of the host material. The increase of the 2θ values is consistent with lattice contraction due to the substitution of Pb^{2+} ions (ionic radius 1.33\AA) with smaller Mn^{2+} ions (ionic radius 0.97\AA).⁴⁰ The decrease of the cation size, due to substitutional doping shifts the XRD pattern towards higher 2θ values. In order to understand this enhanced energy transfer efficiency achievable at high-temperature annealing conditions, we have performed the XRD analysis. Figure 10b shows the comparison of the XRD pattern of $(\text{But})_2\text{PbBr}_4$ (black trace) and $\text{Mn}^{2+}:(\text{But})_2\text{PbBr}_4$ (red trace) sample, both annealed at $125\text{ }^\circ\text{C}$, with insets showing the magnified view of the patterns. This clearly shows that the XRD peaks have shifted to higher angle values confirming the incorporation of Mn^{2+} dopants into the crystal lattice of the host semiconductor. Figure 10b compares the XRD patterns of the room temperature and 125°C annealed sample of $\text{Mn}^{2+}:(\text{But})_2\text{PbBr}_4$. This clearly shows that for the $\text{Mn}^{2+}:(\text{But})_2\text{PbBr}_4$ samples, the XRD peak positions of the $125\text{ }^\circ\text{C}$ annealed sample have a notable shift to higher angles compared to room temperature annealed sample.

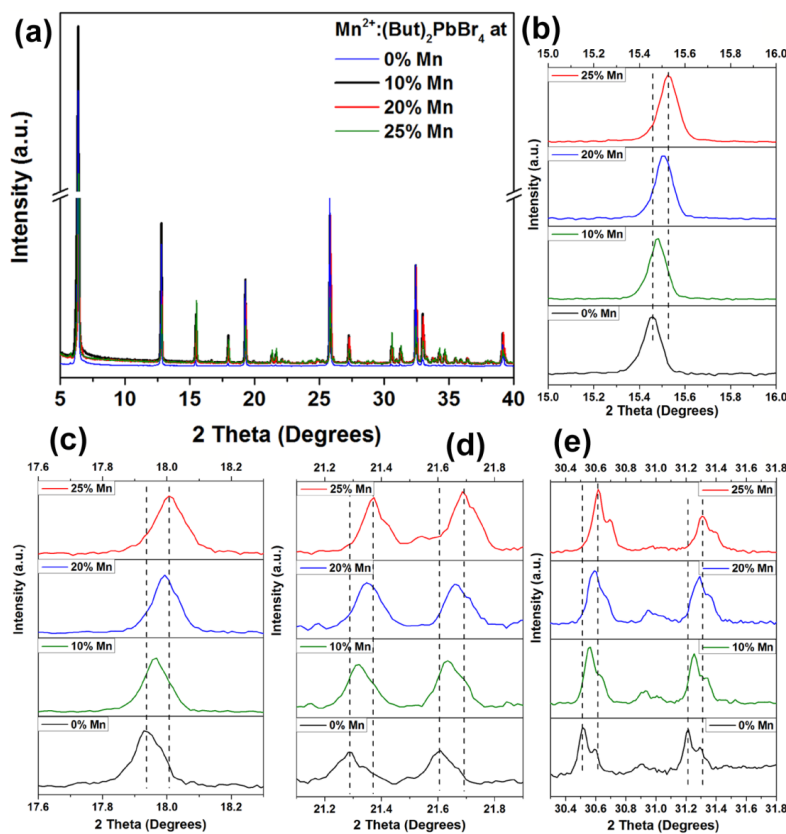


Figure 11; XRD pattern of (a) doped material at different dopant concentrations with their magnified views (b-e)

This indicates that thermal diffusion of the Mn^{2+} ions into the crystal lattice of the host material occurs strongly when annealed at elevated temperatures. This increased extent of doping the host material under high-temperature annealing conditions provides more acceptor Mn^{2+} ions for enhanced energy transfer to occur. XRD analysis of $\text{Mn}^{2+}:(\text{But})_2\text{PbBr}_4$ samples, annealed at 125 °C, with varying Mn^{2+} dopant concentration has also been performed. Figure 11 shows the XRD patterns at different Mn^{2+} concentrations (0, 10, 20, 25 % Mn^{2+}). A magnified view of the XRD patterns is shown in Figure 11 b-d for clarity. It is evident from the XRD analysis that the peak positions monotonically shift towards higher angles as Mn^{2+} dopant concentration is increased. This again indicates progressively higher substitutional Mn^{2+} doping of host perovskites as the concentration of the input Mn^{2+} ions is increased. This increased doping causes an enhancement of the energy transfer efficiency and helps boost the PLQY_{Mn} .

It is important to note here that the Mn^{2+} emission from these doped samples arises from the host's energy transfer to the closely located dopant ions. Besides substitutional doping, acceptor Mn^{2+} ions can also undergo clustering residing inside the host perovskite material. Given the solid-state grinding method of doping, it is very likely that Mn^{2+} clusters can form that can act as acceptors. The observed XRD peak shifts confirm substitutional doping at the octahedral sites. However, this does not preclude the presence of Mn^{2+} ions clustered inside the host perovskite. Irrespective of whether the acceptor Mn^{2+} ions are isolated or clustered, they act as efficient acceptor of energy from the photoexcited charge carriers of the host material and show strong orange emission with high quantum yield, feature that could be exploited for their utility as color converting materials for LEDs.

Simple solid-state mechano-chemical synthesis of bulk APbBr_3 (A= Cs, MA) perovskites and their nanoparticles has been successfully demonstrated wherein the A-X, and Pb-X precursor powders are ground homogeneously at room temperature for the addition reaction.⁴⁵ Noteworthy, Mn^{2+} doping is achieved here by a simple solid-state grinding, and thermal annealing process wherein the Pb^{2+} ions are exchanged with the dopant Mn^{2+} ions. This thermally activated cation exchange on the octahedral sites leads to the formation of solid solutions. Typically, cation exchange/diffusion in 3D AMX_3 system is known to be very slow with high activation energy due

to lack of interstitial sites.⁴⁶ Anion exchange, on the other hand, is very efficient and fast due to the low activation energy of formation and diffusion of anion vacancy. This low activation energy supports presence of anion vacancy in the bulk 3D perovskites.^{47, 48} Under these conditions, a simple solid state grinding and thermal annealing shows strong evidence of substitutional doping of the host perovskite by the Mn^{2+} dopant ions. It is very likely in our case here that anion exchange precedes the cation exchange event. The utilized metal bromide dopant precursor (MnBr_2) for bromide-based host perovskite has important benefit of having the same anion that can exploit the formation and diffusion of halide vacancy in the host material leading to exchange of Pb^{2+} ions with the Mn^{2+} ions for the formation of doped material. The mechanism of doping is shown in the schematic diagram (Figure 12).

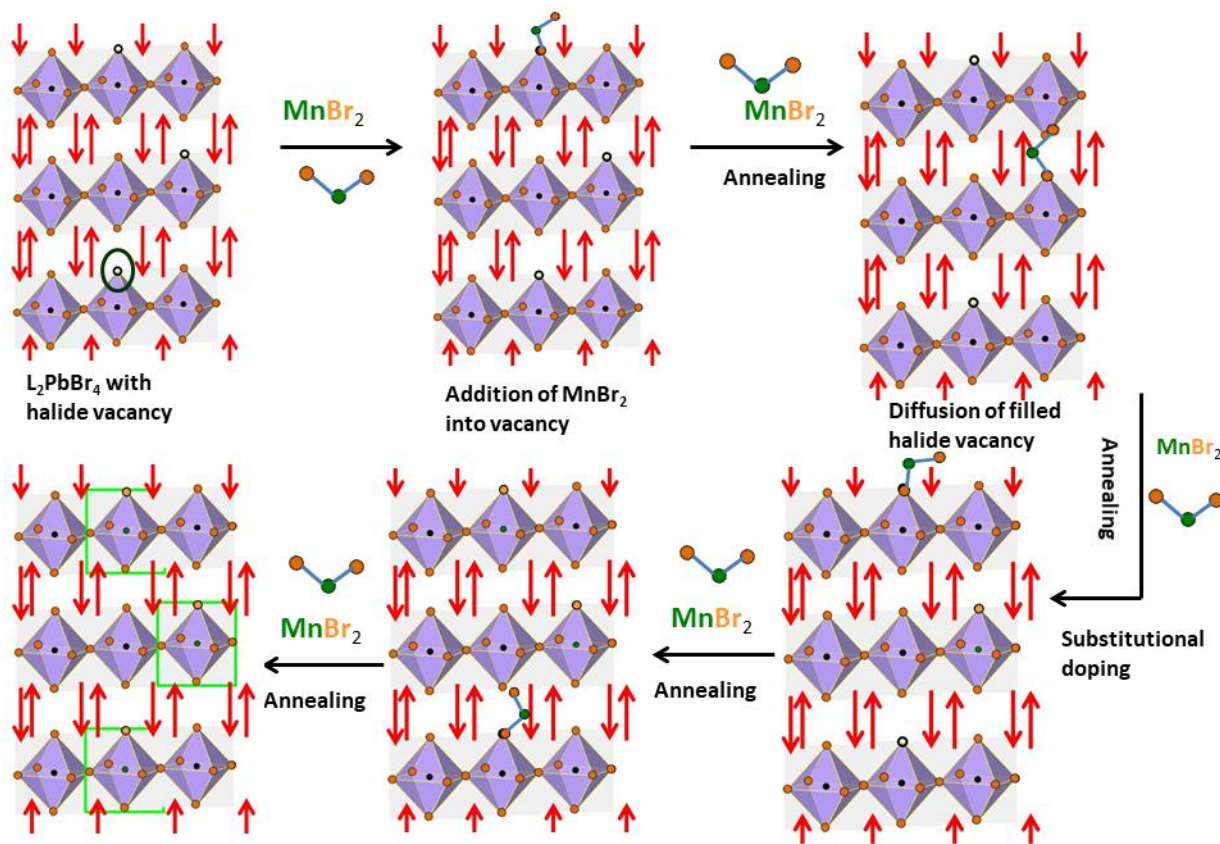


Figure 12: The mechanism of substitutional doping

The MnBr_2 precursor binds to the existing halide vacancy in the host material as a molecular unit, incorporating MnBr_2 in the host lattice. This filling of the halide vacancy releases energy due to the formation of bond between incoming Br and the host lattice without necessarily breaking the

Mn-Br bond. Further, during the thermal annealing step, energy is supplied for diffusion of this halide vacancy and breaking the Pb-Br bond in the host lattice. This allows quick exchange of the Pb^{2+} ions with the Mn^{2+} dopant ions inside the host lattice, leading to solid solution formation. Such a mechanistic pathway for doping is consistent with observing XRD peak shifts to higher angles for exclusively annealed samples at higher temperatures.

3.6 Conclusions:

2D layered bulk perovskite semiconductor with multiple quantum well structures has been successfully utilized as a host material for doping Mn^{2+} ions in a facile and scalable methodology. Successful incorporation of Mn^{2+} dopants into the host crystal lattice was demonstrated using Photoluminescence excitation spectra and XRD analysis. These Mn^{2+} doped samples exhibit a weak band edge emission (~ 420 nm) with a strong Mn^{2+} emission band (~ 600 nm). The calculated quantum yield for Mn^{2+} emission is found to be greater than $\sim 24\%$ across samples with different Mn^{2+} dopant concentrations. Here, the strongly bound excitons with fast radiative decay rates for the bulk 2D layered host material has been exploited for achieving high PL quantum yield for the Mn^{2+} emission. These Mn^{2+} doped samples show efficient energy transfer from photoexcited host excitons to the dopant ions. The resultant strong yellow-orange emission is attributed to the spin forbidden internal transition of the d electrons of Mn^{2+} ions (${}^4\text{T}_1 \rightarrow {}^6\text{A}_1$). The enabling properties of the Mn^{2+} doped samples (high quantum yield, stability against ambient moisture, facile and scalable synthesis) suggest great potential for these materials as down-conversion based phosphor materials for LED applications.

3.7 References:

- (1) Liu, M.; Johnston, M. B.; Snaith, H. J. Efficient planar heterojunction perovskite solar cells by vapour deposition. *Nature* **2013**, *501*, 395–398.
- (2) Shi, D.; Adinolfi, V.; Comin, R.; Yuan, M.; Alarousu, E.; Buin, A.; Chen, Y.; Hoogland, S.; Rothenberger, A.; Katsiev, K.; Losovyj, Y.; Zhang, X.; Dowben, P. A.; Mohammed, O. F.;

Sargent, E. H.; Bakr, O. M. Solar cells. Low trap-state density and long carrier diffusion in organolead trihalide perovskite single crystals. *Science* **2015**, *347*, 519–522.

(3) Nie, W.; Tsai, H.; Asadpour, R.; Blancon, J.-C.; Neukirch, A. J.; Gupta, G.; Crochet, J. J.; Chhowalla, M.; Tretiak, S.; Alam, M. A.; Wang, H.-L.; Mohite, A. D. Solar cells. High-efficiency solution-processed perovskite solar cells with millimeter-scale grains. *Science* **2015**, *347*, 522–525.

(4) Jeon, N. J.; Noh, J. H.; Yang, W. S.; Kim, Y. C.; Ryu, S.; Seo, J.; Seok, S. I. Compositional engineering of perovskite materials for high performance solar cells. *Nature* **2015**, *517*, 476–480.

(5) Tan, Z.-K.; Moghaddam, R. S.; Lai, M. L.; Docampo, P.; Higler, R.; Deschler, F.; Price, M.; Sadhanala, A.; Pazos, L. M.; Credgington, D.; Hanusch, F.; Bein, T.; Snaith, H. J.; Friend, R. H. Bright light-emitting diodes based on organometal halide perovskite. *Nat. Nanotechnol.* **2014**, *9*, 687–692.

(6) Xing, G.; Mathews, N.; Lim, S. S.; Yantara, N.; Liu, X.; Sabba, D.; Grätzel, M.; Mhaisalkar, S.; Sum, T. C. Low-temperature solution processed wavelength-tunable perovskites for lasing. *Nat. Mater.* **2014**, *13*, 476–480.

(7) Zhu, H.; Fu, Y.; Meng, F.; Wu, X.; Gong, Z.; Ding, Q.; Gustafsson, M. V.; Trinh, M. T.; Jin, S.; Zhu, X. Y. Lead halide perovskite nanowire lasers with low lasing thresholds and high quality factors. *Nat. Mater.* **2015**, *14*, 636–642.

(8) Yang, W. S.; Noh, J. H.; Jeon, N. J.; Kim, Y. C.; Ryu, S.; Seo, J.; Seok, S. I. High-performance photovoltaic perovskite layers fabricated through intramolecular exchange. *Science* **2015**, *348*, 1234–1237.

(9) Cho, H.; Jeong, S.-H.; Park, M.-H.; Kim, Y.-H.; Wolf, C.; Lee, C.-L.; Heo, J. H.; Sadhanala, A.; Myoung, N.; Yoo, S.; Im, S. H.; Friend, R. H.; Lee, T.-W. Overcoming the Electroluminescence Efficiency Limitations of Perovskite Light-Emitting Diodes. *Science* **2015**, *350*, 1222–1225.

(10) Wang, H.-C.; Lin, S.-Y.; Tang, A.-C.; Singh, B. P.; Tong, H.-C.; Chen, C.-Y.; Lee, Y.-C.; Tsai, T.-L.; Liu, R.-S. Mesoporous Silica Particles Integrated with All-Inorganic CsPbBr₃ Perovskite Quantum-Dot Nanocomposites (MP-PQDs) with High Stability and Wide Color Gamut Used for Backlight Display. *Angew. Chem., Int. Ed.* **2016**, *55*, 7924–7929.

- (11) Pathak, S.; Sakai, N.; Wisnivesky Rocca Rivarola, F.; Stranks, S. D.; Liu, J.; Eperon, G. E.; Ducati, C.; Wojciechowski, K.; Griffiths, J. T.; Haghighirad, A. A.; Pellaroque, A.; Friend, R. H.; Snaith, H. J. Perovskite Crystals for Tunable White Light Emission. *Chem. Mater.* **2015**, *27*, 8066–8075.
- (12) Song, J.; Li, J.; Li, X.; Xu, L.; Dong, Y.; Zeng, H. Quantum Dot Light-Emitting Diodes Based on Inorganic Perovskite Cesium Lead Halides (CsPbX₃). *Adv. Mater.* **2015**, *27*, 7162–7167.
- (13) Weidman, M. C.; Goodman, A. J.; Tisdale, W. A. Colloidal Halide Perovskite Nanoplatelets: An Exciting New Class of Semiconductor Nanomaterials. *Chem. Mater.* **2017**, *29*, 5019–5030.
- (14) Liu, W.; Lin, Q.; Li, H.; Wu, K.; Robel, I.; Pietryga, J. M.; Klimov, V. I. Mn²⁺-Doped Lead Halide Perovskite Nanocrystals with Dual-Color Emission Controlled by Halide Content. *J. Am. Chem. Soc.* **2016**, *138*, 14954–14961.
- (15) Parobek, D.; Roman, B. J.; Dong, Y.; Jin, H.; Lee, E.; Sheldon, M.; Son, D. H. Exciton-to-Dopant Energy Transfer in Mn-Doped Cesium Lead Halide Perovskite Nanocrystals. *Nano Lett.* **2016**, *16*, 7376–7380.
- (16) Mir, W. J.; Jagadeeswararao, M.; Das, S.; Nag, A. Colloidal Mn-Doped Cesium Lead Halide Perovskite Nanoplatelets. *ACS Energy Lett.* **2017**, *2*, 537–543.
- (17) Liu, H.; Wu, Z.; Shao, J.; Yao, D.; Gao, H.; Liu, Y.; Yu, W.; Zhang, H.; Yang, B. CsPb_xMn_{1-x}Cl₃ Perovskite Quantum Dots with High Mn Substitution Ratio. *ACS Nano* **2017**, *11*, 2239–2247.
- (18) Guria, A. K.; Dutta, S. K.; Adhikari, S. D.; Pradhan, N. Doping Mn²⁺ in Lead Halide Perovskite Nanocrystals: Successes and Challenges. *ACS Energy Lett.* **2017**, *2*, 1014–1021.
- (19) Begum, R.; Parida, M. R.; Abdelhady, A. L.; Murali, B.; Alyami, N. M.; Ahmed, G. H.; Hedhili, M. N.; Bakr, O. M.; Mohammed, O. F. Engineering Interfacial Charge Transfer in CsPbBr₃ Perovskite Nanocrystals by Heterovalent Doping. *J. Am. Chem. Soc.* **2017**, *139*, 731–737.
- (20) van der Stam, W.; Geuchies, J. J.; Altantzis, T.; van den Bos, K. H. W.; Meeldijk, J. D.; Van Aert, S.; Bals, S.; Vanmaekelbergh, D.; de Mello Donega, C. Highly Emissive Divalent-Ion-Doped Colloidal CsPb_{1-x}M_xBr₃ Perovskite Nanocrystals through Cation Exchange. *J. Am. Chem. Soc.* **2017**, *139*, 4087–4097.

- (21) Santra, P. K.; Kamat, P. V. Mn-Doped Quantum Dot Sensitized Solar Cells: A Strategy to Boost Efficiency over 5%. *J. Am. Chem. Soc.* **2012**, *134*, 2508–2511.
- (22) He, Y.; Wang, H.-F.; Yan, X.-P. Exploring Mn-Doped ZnS Quantum Dots for the Room-Temperature Phosphorescence Detection of Enoxacin in Biological Fluids. *Anal. Chem.* **2008**, *80*, 3832–3837.
- (23) Erickson, C. S.; Bradshaw, L. R.; McDowall, S.; Gilbertson, J. D.; Gamelin, D. R.; Patrick, D. L. Zero-Reabsorption Doped-Nanocrystal Luminescent Solar Concentrators. *ACS Nano* **2014**, *8*, 3461–3467.
- (24) Yu, J. H.; Kwon, S.-H.; Petrášek, Z.; Park, O. K.; Jun, S. W.; Shin, K.; Choi, M.; Park, Y. I.; Park, K.; Na, H. B.; Lee, N.; Lee, D. W.; Kim, J. H.; Schwille, P.; Hyeon, T. High-resolution three-photon biomedical imaging using doped ZnS nanocrystals. *Nat. Mater.* **2013**, *12*, 359–366.
- (25) Yuan, M.; Quan, L. N.; Comin, R.; Walters, G.; Sabatini, R.; Voznyy, O.; Hoogland, S.; Zhao, Y.; Beauregard, E. M.; Kanjanaboos, P.; Lu, Z.; Kim, D. H.; Sargent, E. H. Perovskite energy funnels for efficient light-emitting diodes. *Nat. Nanotechnol.* **2016**, *11*, 872–877.
- (26) Dou, L.; Wong, A. B.; Yu, Y.; Lai, M.; Kornienko, N.; Eaton, S. W.; Fu, A.; Bischak, C. G.; Ma, J.; Ding, T.; Ginsberg, N. S.; Wang, L.-W.; Alivisatos, A. P.; Yang, P. Atomically thin two-dimensional organic-inorganic hybrid perovskites. *Science* **2015**, *349*, 1518–1521.
- (27) Cheng, Z.; Lin, J. Layered organic–inorganic hybrid perovskites: structure, optical properties, film preparation, patterning and templating engineering. *Cryst. Eng. Comm.* **2010**, *12*, 2646–2662.
- (28) Mitzi, D. B. Templating and structural engineering in organic–inorganic perovskites. *J. Chem. Soc., Dalton Trans.* **2001**, 1–12.
- (29) Mitzi, D. B. Synthesis, structure, and properties of organic–inorganic perovskites and related materials. *Prog. Inorg. Chem.* **1999**, *48*, 1–121.
- (30) Braun, M.; Tuffentsammer, W.; Wachtel, H.; Wolf, H. C. Tailoring of energy levels in lead chloride based layered perovskites and energy transfer between the organic and inorganic planes. *Chem. Phys. Lett.* **1999**, *303*, 157–164.
- (31) Li, Y. Y.; Lin, C. K.; Zheng, G. L.; Cheng, Z. Y.; You, H.; Wang, W. D.; Lin, J. Novel (110)-Oriented Organic–Inorganic Perovskite Compound Stabilized by N-(3-Aminopropyl) imidazole with Improved Optical Properties. *Chem. Mater.* **2006**, *18*, 3463–3469.

- (32) Braun, M.; Tuffentsammer, W.; Wachtel, H.; Wolf, H. C. Pyrene as emitting chromophore in organic–inorganic lead halide-based layered perovskites with different halides. *Chem. Phys. Lett.* **1999**, *307*, 373–378.
- (33) Mitzi, D. B.; Feild, C. A.; Harrison, W. T. A.; Guloy, A. M. Conducting tin halides with a layered organic-based perovskite structure. *Nature* **1994**, *369*, 467–469.
- (34) Kawano, N.; Koshimizu, M.; Sun, Y.; Yahaba, N.; Fujimoto, Y.; Yanagida, T.; Asai, K. Effects of Organic Moieties on Luminescence Properties of Organic–Inorganic Layered Perovskite-Type Compounds. *J. Phys. Chem. C* **2014**, *118*, 9101–9106.
- (35) Ishihara, T.; Takahashi, J.; Goto, T. Exciton state in two dimensional perovskite semiconductor $(\text{C}_{10}\text{H}_{21}\text{NH}_3)_2\text{PbI}_4$. *Solid State Commun.* **1989**, *69*, 933–936.
- (36) Saidaminov, M. I.; Mohammed, O. F.; Bakr, O. M. Low- Dimensional-Networked Metal Halide Perovskites: The Next Big Thing. *ACS Energy Lett.* **2017**, *2*, 889–896.
- (37) Goede, O.; Heimbrod, W. Optical Properties of (Zn, Mn) and (Cd, Mn) Chalcogenide Mixed Crystals and Superlattices. *Phys. Status Solidi B* **1988**, *146*, 11–62.
- (38) Moriwaki, M. M.; Becker, W. M.; Gebhardt, W.; Galazka, R. R. Study of the 2.0-eV photoluminescence band in $\text{Cd}_{1-x}\text{Mn}_x\text{Te}$ semiconductor alloys. *Phys. Rev. B: Condens. Matter Mater. Phys.* **1982**, *26*, 3165–3171.
- (39) Beaulac, R.; Archer, P. I.; Ochsenein, S. T.; Gamelin, D. R. Mn^{2+} -Doped CdSe Quantum Dots: New Inorganic Materials for Spin- Electronics and Spin-Photonics. *Adv. Funct. Mater.* **2008**, *18*, 3873–3891.
- (40) Nag, A.; Chakraborty, S.; Sarma, D. D. To Dope Mn^{2+} in a Semiconducting Nanocrystal. *J. Am. Chem. Soc.* **2008**, *130*, 10605–10611.
- (41) Tanaka, K.; Takahashi, T.; Kondo, T.; Umeda, K.; Ema, K.; Umebayashi, T.; Asai, K.; Uchida, K.; Miura, N. Electronic and Excitonic Structures of Inorganic–Organic Perovskite-Type Quantum-Well Crystal $(\text{C}_4\text{H}_9\text{NH}_3)_2\text{PbBr}_4$. *Jpn. J. Appl. Phys.* **2005**, *44*, 5923–5932.
- (42) Wang, Q.; Zhang, X.; Jin, Z.; Zhang, J.; Gao, Z.; Li, Y.; Liu, S. F. Energy-Down-Shift CsPbCl_3 : Mn Quantum Dots for Boosting the Efficiency and Stability of Perovskite Solar Cells. *ACS Energy Lett.* **2017**, *2*, 1479–1486.
- (43) Yuan, Z.; Shu, Y.; Tian, Y.; Xin, Y.; Ma, B. A facile one-pot synthesis of deep blue luminescent lead bromide perovskite microdisks. *Chem. Commun.* **2015**, *51*, 16385–16388.

- (44) Gonzalez-Carrero, S.; Mínguez Espallargas, G.; Galian, R. E.; Pérez-Prieto, J. Blue luminescent organic lead bromide perovskites: Highly dispersible and photostable materials. *J. Mater. Chem. A* **2015**, *3*, 14039–14045.
- (45) Shannon, R. D. A. Revised Effective Ionic-Radii and Systematic Studies of Interatomic Distances in Halides and Chalcogenides. *Acta Crystallogr., Sect. A: Cryst. Phys., Diffr., Theor. Gen. Crystallogr.* **1976**, *32*, 751–767.
- (46) Magana, D.; Perera, S. C.; Harter, A. G.; Dalal, N. S.; Strouse, G. F. Switching-On Super para magnetism in Mn/CdSe Quantum Dots. *J. Am. Chem. Soc.* **2006**, *128*, 2931–2939.
- (47) Norris, D. J.; Yao, N.; Charnock, F. T.; Kennedy, T. A. High- Quality Manganese-Doped ZnSe Nanocrystals. *Nano Lett.* **2001**, *1*, 3–7.
- (48) Stowell, C. A.; Wiacek, R. J.; Saunders, A. E.; Korgel, B. A. Synthesis and Characterization of Dilute Magnetic Semiconductor Manganese-Doped Indium Arsenide Nanocrystals. *Nano Lett.* **2003**, *3*, 1441–1447.
- (49) Nag, A.; Sapra, S.; Nagamani, C.; Sharma, A.; Pradhan, N.; Bhat, S. V.; Sarma, D. D. A Study of Mn²⁺ Doping in CdS Nanocrystals. *Chem. Mater.* **2007**, *19*, 3252–3259.
- (50) Jana, A.; Mittal, M.; Singla, A.; Sapra, S. Solvent-free, mechanochemical syntheses of bulk trihalide perovskites and their nanoparticles. *Chem. Commun.* **2017**, *53*, 3046–3049.
- (51) Walsh, A.; Scanlon, D. O.; Chen, S.; Gong, X. G.; Wei, S.-H. Self-regulation mechanism for charged point defects in hybrid halide perovskites. *Angew. Chem., Int. Ed.* **2015**, *54*, 1791–1794.
- (52) Buin, A.; Pietsch, P.; Xu, J.; Voznyy, O.; Ip, A. H.; Comin, R.; Sargent, E. H. Materials Processing Routes to Trap-Free Halide Perovskites. *Nano Lett.* **2014**, *14*, 6281–6286.

Chapter 4

Title: Importance of structure-distortion parameter in governing photophysical properties of 'Pb-free' perovskite.

Lead-based low dimension perovskite has shown significant success in terms of broadband emission. Although Pb-based perovskite has tremendous success, the potential threat to nature cannot be overshadowed. Along with that, the quantum yield of these systems is low to modest in most cases. An alternative would be lead-free perovskite keeping the same ns^2 electronic configuration.

We need to keep in mind that the lead-free perovskite system should have appreciably high PLQY. In this regard, the potential alternative would be Sb^{3+} , Te^{4+} , Sn^{2+} , Bi^{3+} etc. This working chapter will discuss the effort on antimony and tellurium based zero-dimension structures, which are highly luminescence at room temperature. Furthermore, later down the line discusses the structure-property correlation in the systems.

The chapter is divided into 2 parts.

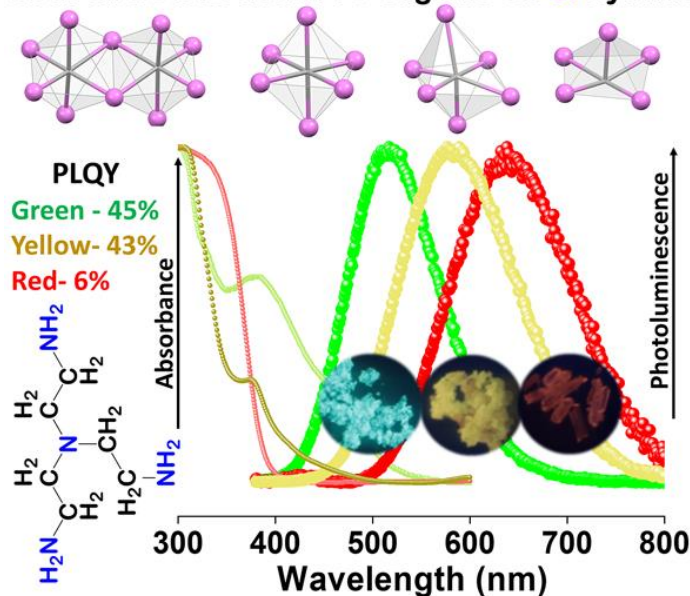
Part 4A: Luminescent 0D organic-inorganic Antimony (III) hybrid.

Part 4B: Luminescent 0D organic-inorganic Tellurium (IV) hybrid.

Chapter 4A

Title: Luminescent 0D organic-inorganic Antimony (III) hybrid

Structure/Distortion in 0D Organic-Sb Cl Hybrids



4.1 Introduction:

Recently, *low dimensional* organic-metal halide hybrids (OMHH) have emerged as a new class of material with exquisite properties enabling optoelectronic applications in photovoltaics and solid-state lighting.¹⁻⁶ Dimensionality in such organic-metal halide hybrid materials refer to the electronic dimensionality/networked structure of the constituent metal halide inorganic unit (*i.e.* 2D, 1D, 0D). For zero-dimensional (0D) variants of such materials, the semiconducting metal halide unit is isolated and surrounded by organic ligands. Photo-excitation of such low dimensional hybrids leads to the generation of strongly bound excitons confined within the metal halide unit.⁷ *Strong* electron-phonon coupling in such materials allows transient localization of the charge carriers (electrons, holes) in the metal halide unit by introducing local distortions of the lattice. The *self-trapped excitons* (STEs), thus produced, lead to phonon emissions that alter the energy of the photoluminescence (PL) emission. This primarily leads to the Stokes shifted broad band visible emission.⁸⁻¹² Various factors that govern the PL emission energy and photoluminescence quantum yield (PLQY) of such broad band emission are not clearly understood.^{1, 13-15} However, it is generally observed that PLQY tends to be enhanced as the dimensionality is lowered.^{2, 14, 16} Typical lead halide based low dimensional (2D, 1D, 0D) hybrids have been reported corroborating to the

STE based broad band emission with modest/high PLQY.¹⁷ Noteworthy, for a given metal ion, the accessibility of the desired dimensionality in such systems is largely dictated by choice of halides, organic ligands, and experimental reaction conditions.^{15, 18, 19}

The toxicity²⁰ of Pb(II) has instigated many research initiatives for the development of the lead free variant of low dimensional OMHH materials.²¹⁻²³ Suitable replacements for Pb²⁺ ion in such hybrids must retain the ns^2 electronic configuration of the valence shell that has been touted as the key role player in conferring enabling properties to the lead based low dimensional hybrids.²⁴ Recently, Sb³⁺ and Bi³⁺ ions, that are less susceptible to oxidation while retaining the ns^2 valence electronic configuration have been introduced as a replacement for Pb²⁺ ions.^{7, 25-27} There have been few reports on low dimensional Sb(III) chloride-based organic hybrids with strong, long-lived, stokes shifted, and broad band STE-based ambient emission.^{7, 26-32} Interestingly, all of these 0D antimony chloride hybrids show triplet STE-based broad band emission with high/modest PLQY. They all demonstrate the structural commonality of having an individual metal-halide unit ([SbCl₅]²⁻, [SbCl₆]³⁻) that is completely isolated from each other and is surrounded by the respective organic ligands. The quadrangular pyramidal metal halide unit in these reports have Sb-Cl equatorial bonds with very similar bond lengths and a shorter Sb-Cl axial/apical bond with low/modest variation of bond angles from their ideal values. Similar bond length and bond angle distortions are observed for the octahedral metal-halide units. Such distortion of the metal halide unit likely arises due to the presence of Sb centered stereo chemically active lone pair.^{33, 34} This might imply that the strong PL emission properties may be correlated to the ground state structure/distortion of the metal-halide unit. Antimony(III) halides are known to exist in different stoichiometric polyhedral units ([SbX₄]⁻, [SbX₅]²⁻, [SbX₆]³⁻, [Sb₂X₉]³⁻) in the solid-state.³⁵ Given the various possible polyhedral unit types in these hybrids, is there any correlation that exists between the luminescence properties and the geometric structure/distortion of the metal-halide unit? How does the presence/absence of distortion in metal-halide unit affect the PLQY and Stokes shift of the emission band? Research efforts aimed to answer these questions (tunability of metal halide unit structure: octahedral or quadrangular pyramidal, and factors that affect emissive properties) are of current importance.^{29, 36-38} In an effort to demonstrate structural tunability (octahedral, quadrangular pyramidal) and to rationalize the photo-physical origins of the observed emissive properties, I have synthesized various Sb(III) chloride 0D hybrids utilizing a *common* organic ligand and have analyzed for correlation between the specific structural features of metal-

halide unit and their luminescence properties. Here, I have utilized Tris(2-aminoethyl) amine ligand to synthesize the chlorinated zero-dimension perovskite.

The common ligand was utilized to synthesize different 0D hybrids, and for simplicity, abbreviated as tris Sb green, tris Sb red, and tris Sb yellow (in the rest of the chapter). The chemical formula is given below

1 $[(C_6H_{22}N_4)_2 (Sb_2Cl_{10}) (SbCl_6) (Cl)_2 (H_3O)].(3H_2O)$; *tris Sb Green*);

2 $[(C_6H_{22}N_4)_2 (SbCl_6)_2 (Cl)_2].3(H_2O)$; *tris Sb Red*);

3 $[(C_6H_{22}N_4)_4 (SbCl_6)_3 (Cl)_7].4(H_2O)$; *tris Sb Yellow*);

4.2 Materials:

Antimony (III) Oxide (99%), Hydrochloric acid (37%) and Acetone were purchased from Sigma Aldrich. Tris(2-aminoethyl)amine was purchased from TCI Chemicals. Diethyl ether was purchased for HiMedia. All chemicals were used as purchased without further purification.

4.3 Synthesis:

4.3.A Synthesis of powdered **1** *tris Sb Green*

To prepare **1** *tris Sb Green* powder sample, 0.1 mmol (29.1 mg) of Antimony (III) Oxide was dissolved in 5 mL of hydrochloric acid. To this, 0.1 mmol (14.6 mg) Tris(2-aminoethyl) amine was added. The solution turns turbid white after some time. The resulting precipitate is filtered and washed with diethyl ether repeatedly and dried in a vacuum for further characterization.

4.3.B Synthesis of Single Crystals of **1** *tris Sb Green*

To obtain single crystals of **1** *tris Sb Green*, the same reaction procedure was followed with the following details: 0.1 mmol (29.1 mg) of Antimony (III) Oxide was dissolved in 5 mL of hydrochloric acid. To this, 0.1 mmol (14.6 mg) Tris(2-aminoethyl) amine was added. The resultant mixture was heated in a preheated oil bath at 60 °C till dissolution. The solution is slowly cooled to obtain white crystals. Crystallization led to plate-shaped pale yellow crystals, which appear bright green under UV (365 nm) light. The crystals were filtered using a vacuum pump and washed repeatedly with acetone and diethyl ether for further characterization.

4.3.C Synthesis of Single Crystals of **2** *tris Sb Red*

In order to synthesize single crystals of **2** *tris Sb Red*, the same procedure was followed as for **1** described above. However, the oil bath temperature was set to 120 °C for dissolving the crystal and cooled naturally to room temperature. After cooling needle-shaped colorless crystals formed which emits red color under UV (365 nm) light. Here we have used same filtration and washing as mentioned above.

4.3.D Synthesis of powdered **3** *tris Sb Yellow*

To prepare **3** *tris Sb Yellow* powder sample, 0.1 mmol (29.1 mg) of Antimony (III) Oxide was dissolved in 5 mL of hydrochloric acid. To this, 1 mmol (146 mg) Tris(2-aminoethyl) amine was added. The solution turns turbid white after some time. The precipitate appears bright yellow under UV(365nm) light.

4.3. E Synthesis of Single Crystals of **3** *tris Sb Yellow*

To obtain single crystals of **3** *tris Sb Yellow*, 1: 10 equivalent metal vs ligand ratio was used. Typically for reaction 0.1 mmol (29.1 mg) of Antimony (III) Oxide was dissolved in 5 mL of hydrochloric acid. To this, 1 mmol (146 mg) Tris(2-aminoethyl) amine was added. The resultant mixture was kept in a preheated oil bath at 120 °C till dissolution. The solution is slowly cooled to room temperature to obtain crystals. Crystallization led to cube-shaped pale yellow crystals, which appear bright yellow under UV (365 nm) light. The crystals were filtered using a vacuum pump and washed repeatedly with acetone and diethyl ether for further characterization.

4.4 Characterization methods:

UV-Vis Absorbance was performed in a Shimadzu UV-VIS-NIR3600Plus spectrometer. Steady State PL and lifetime was measured using an Edinburgh FS5 spectrophotometer. TGA measurements were performed using a TAG system (Mettler-Toledo, Model TGA/SDTA851e) and samples were heated in the range of 25 - 800 °C at a heating rate of 5 °C/min under nitrogen atmosphere. ¹H NMR spectra were recorded on Bruker A-400 MHz system using DMSO-d₆ as the solvent at room temperature. Powder X-ray diffraction (XRD) patterns were recorded using a PANalytical X'Pert Pro equipped with Cu K α radiation ($\lambda = 1.5406$ Å). Absolute quantum yield measurements were carried out in a Horiba JOBIN YVON Fluoromax-4 spectrometer with a

calibrated integrating sphere attachment. Scanning Electron Microscopy (SEM) imaging and mapping were performed by Zeiss™ Ultra Plus field-emission scanning electron microscope. X-ray photoelectron spectroscopy (XPS) characterization was performed with ESCALab spectrometer having Al K α X-ray source ($h\nu=1486.6$ eV) operating at 150 W using a Physical Electronics 04-548 dual Mg/Al anode and in a UHV system with base pressure of $\leq 5 \times 10^{-9}$ Torr. Low temperature PL of the crystals was performed using an Edinburgh FLS1000 photoluminescence spectrometer, attached with Optistat DN cryostat and the temperature was controlled using Mercury iTC temperature controller (Oxford instruments). The sample was excited using a xenon lamp and emission was collected from 320 nm to 800 nm. Single crystals X-ray intensity data measurements of compounds **1** and **2** were carried out on a Bruker D8 VENTURE Kappa Duo PHOTON II CPAD diffractometer.

4.5 Results and Discussions:

Antimony(III)chloride OD hybrids were synthesized utilizing Sb₂O₃ and Tris(2-aminoethyl)amine as the ligand in concentrated HCl acid. Extensive details of the utilized synthetic conditions are provided in the experimental section (section 4.3).

4.5.A Optical Property

The temperature variation gives rise to two different types of UV emissive crystal, so initially we proceed to characterize them. Product **1** *tris Sb Green* shows *strong, green* emission while **2** *tris Sb Red* sample shows *weak, red* emission when viewed inside UV chamber. Optical properties of **1** *tris Sb Green*, presented in Figure 1, show strong and broad photoluminescence (PL) emission band centered at 517 nm with full width at half maximum (FWHM) of ~ 110 nm. The photoluminescence excitation (PLE) spectra, collected at 530 nm, match well with the absorption spectra showing multiple features in 300 - 400 nm range. The estimated “Stokes shift” (difference between the peak positions of PL and PLE) is ~ 165 nm. The photoluminescence quantum yield (PLQY) for **1** *tris Sb Green* is estimated to be $\sim 45\%$. On the other hand, optical properties of **2** *tris Sb Red*, presented in Figure 1b, shows weak and broad emission band centered at 638 nm with FWHM of ~ 160 nm. PLE spectra, collected at 650 nm, matches well with the absorption spectra which shows multiple features in 300 - 400 nm range. The estimated “Stokes shift” is ~ 290 nm and the PLQY for **2** *tris Sb Red* is estimated to be $\sim 6\%$.

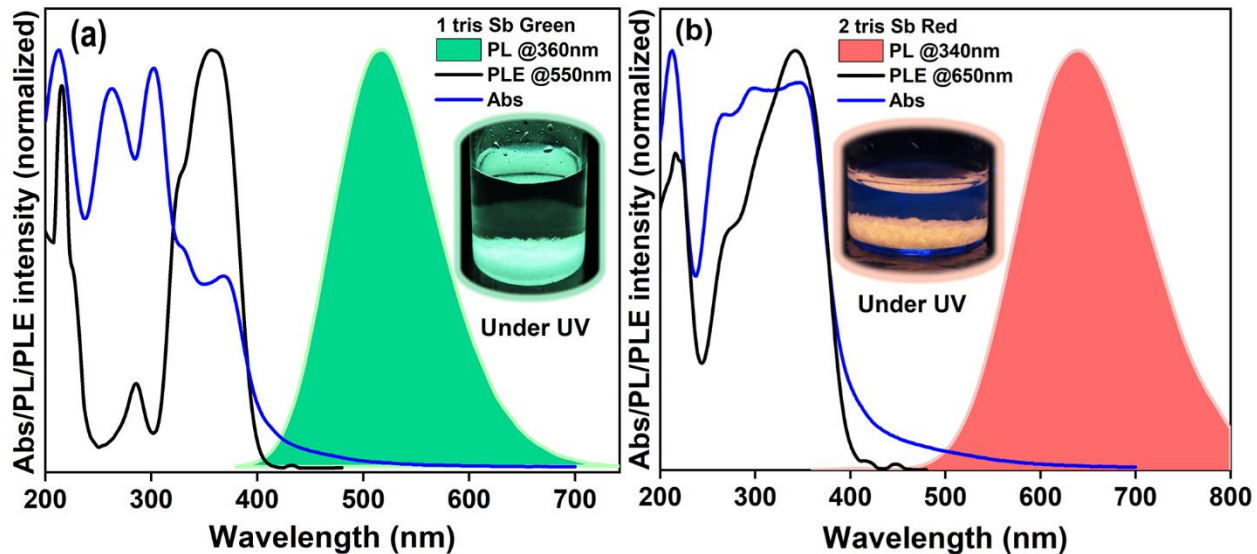


Figure 1: Absorbance (Abs), Photoluminescence (PL) and Photoluminescence excitation (PLE) spectra of a) **1 tris Sb Green**, and b) **2 tris Sb Red** single crystal samples.

The absorption features in halogen antimonite (III) systems can be attributed to the electronic transitions between the sp excited states and s^2 ground state. The observed absorbance features for products **1** and **2** can be tentatively attributed to *A* band (low energy, spin-forbidden transition $^1S_0 \rightarrow ^3P_1$), *B* band (intermediate energy, spin-forbidden transition $^1S_0 \rightarrow ^3P_2$), and *C* band (high energy, spin-allowed transition $^1S_0 \rightarrow ^1P_1$).³⁹ Rationalization of the differences in the observed PL emission peak position, Stokes shift, and PLQY for products **1** and **2** is discussed below.

4.5.B Lifetime study

The lifetime decay profiles (collected using TCSPC set up) and the extracted lifetimes across the broadband emission for **1** and **2**, as presented in Figure 2, show the dominant lifetime component of ~1 microsecond that remains unchanged across the emission band for **1** and **2**.

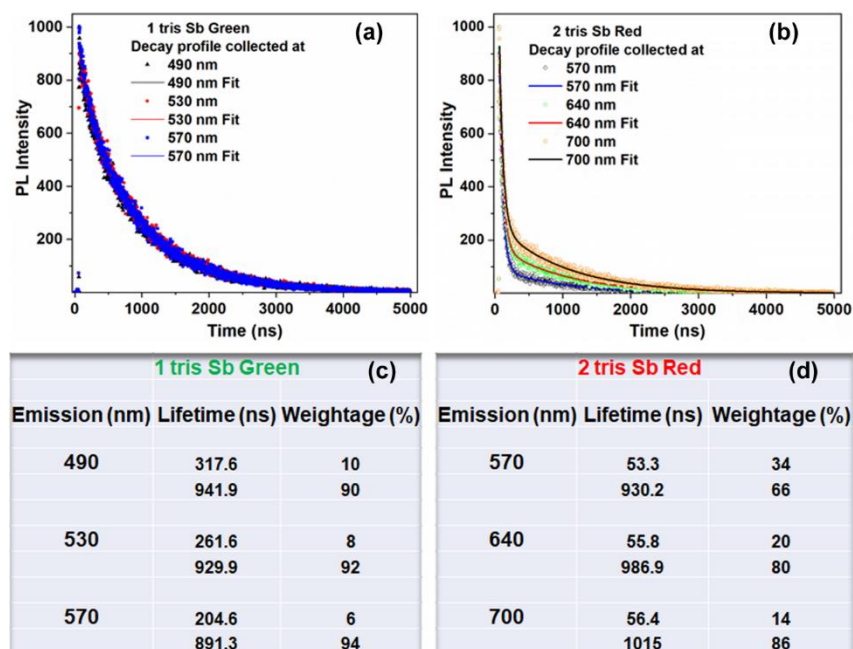


Figure 2: TCSPC Lifetime analysis for products **1 tris Sb Green** (a,c) and **2 tris Sb Red** (b,d) at room temperature across the broad band emission with estimated lifetimes in nanoseconds.

In order to better estimate the longer lifetimes, PL decay profiles were collected across the broadband utilizing a microsecond (μs) flash lamp source and are presented in Figure 3, Table 1. Clearly, lifetime components (and relative %) of 4.8 μs (73%) and 71.9 μs (27%) are observed for **1 tris Sb Green** while for **2 tris Sb Red** the lifetime components (and relative %) are 5.6 μs (90%) and 94.4 μs (10%). The observed long emission lifetime components in products **1** and **2** highlights the role played by the triplet excited state ($^3\text{P}_1$) from which the radiative emission (phosphorescence) originates.

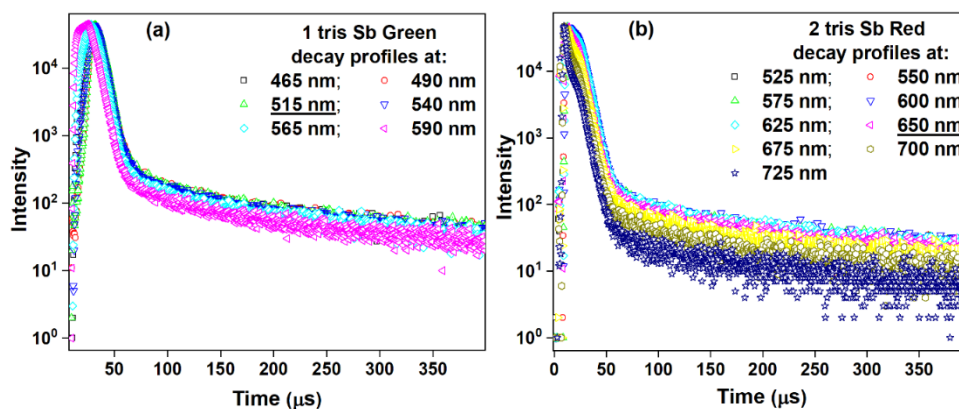


Figure 3: Lifetime decay profiles for products **1** tris Sb Green (a) and **2** tris Sb Red (b) at room temperature collected across emission band using microsecond flash lamp excitation (360 nm).

1 tris Sb Green		
Wavelength (nm)	Life time (μs) (at room temp.)	Relative %
465	4.88	69.99
	77.1	30.01
490	4.91	76.98
	71.61	23.02
515	4.77	72.55
	71.9	27.45
540	4.89	73.32
	73.8	26.68
565	5.01	80.57
	79.4	19.43
590	5.25	86.14
	85.1	13.86

2 tris Sb Red		
Wavelength (nm)	Life time (μs) (at room temp.)	Relative %
525	5.6	90.04
	92.7	9.96
550	5.61	90.81
	90.8	9.29
575	5.62	90.77
	89.9	9.23
600	5.65	90.69

	90.5	9.31
625	5.57	89.40
	92.8	10.60
650	5.66	90.68
	94.4	9.32
675	5.63	90.15
	90.7	9.85
700	5.68	90.74
	90.4	9.26
725	5.68	89.20
	96.3	10.80

Table 1: Lifetime (μs) components and relative weights (%) for the decay profiles presented above in Figure 3.

4.5.C Nature of emission

Given the broad nature of the PL emission peak for both **1** and **2**, it is important to decipher if defect emission leads to the observed broad emission bandwidth. Dependence of the emission band shape/profile on excitation wavelength was studied for products **1** and **2** as presented in Figure 4. The PL emission band shape/profile remains unchanged for products **1** and **2** (albeit with a concomitant change in PL intensity) as across the excitation wavelength range of 320 – 380 nm. PLE spectra collected across the broad emission band of products **1** and **2** (Figure 4) also remain unchanged.

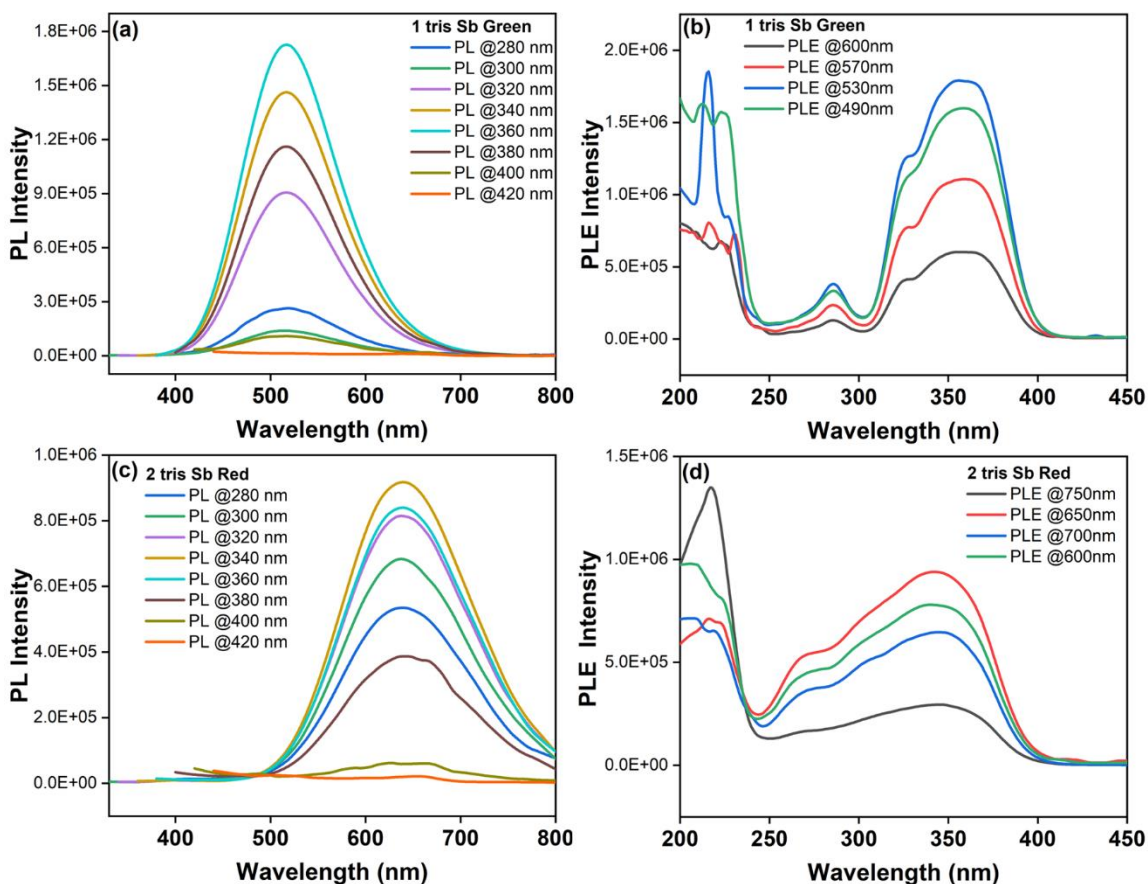


Figure 4: Dependence of photoluminescence (PL) on excitation wavelength and photoluminescence excitation (PLE) spectrum collected across the broad PL peak for a) **1 tris Sb Green**, and b) **2 tris Sb Red** powder samples.

These observations suggest that unique emissive species are responsible for the broad emission in products **1** and **2** and very likely do not involve extrinsic defects. Further, PL/PLE studies were performed for products **1** and **2**, wherein the single-crystal samples were ground (Figure 5). If defects are the cause for the broad band emission, sample grinding will cause substantial change of the PL/PLE profile.¹⁰ However, no changes in the PL/PLE band profile for both the products were observed when the samples were ground thoroughly as shown in Figure 5. Also, the ground samples of both the products were annealed at different temperatures, followed by their PL/PLE characterizations, as shown in Figure 5.

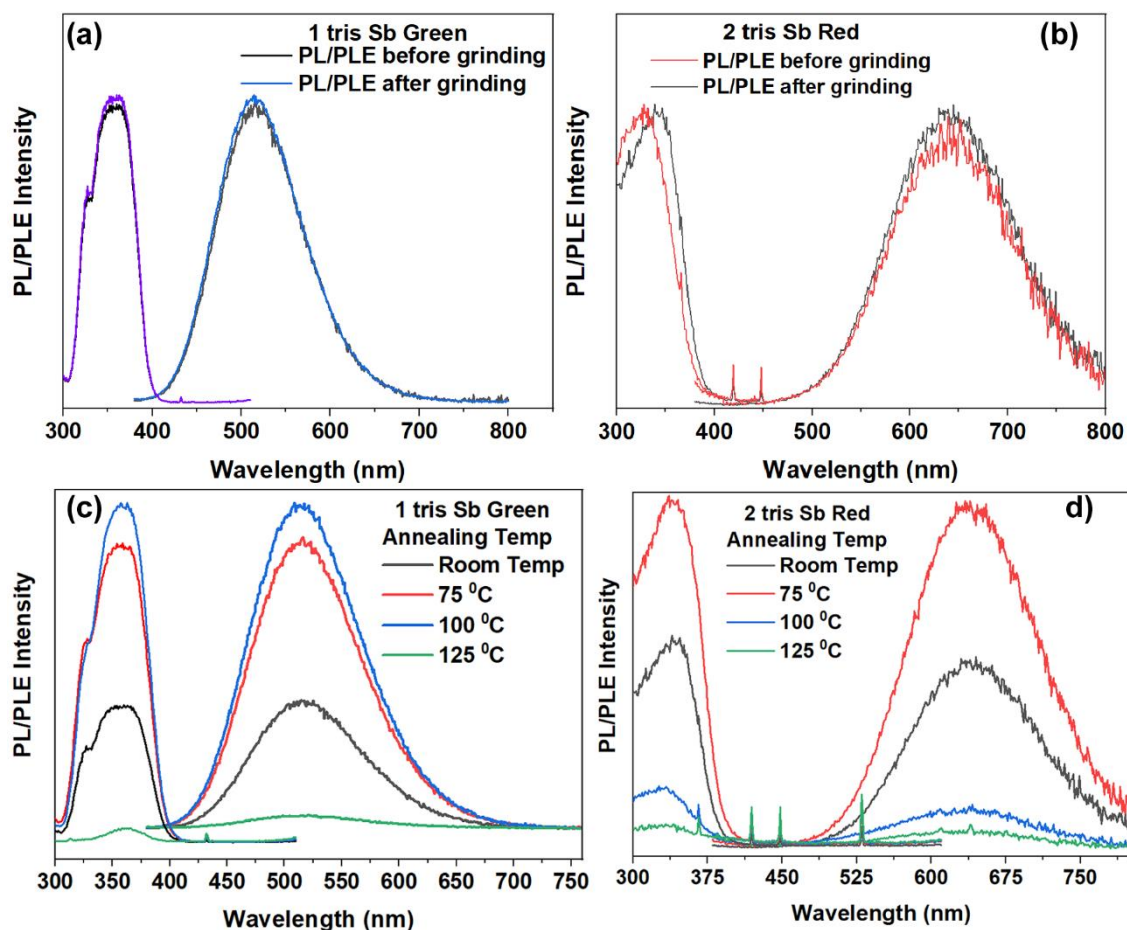


Figure 5: PL/PLE of **1** tris Sb Green and **2** tris Sb Red samples upon a-b) room temperature grinding (10 mins, mortar-pestle) and c-d) annealing of the ground powders at different temperatures. The drastic drop of PL/PLE intensity for **1** and **2** at around 100 °C is related to the loss of solvent (water) molecules integral to the stability of the structure of the products through a network of hydrogen bonding.

Again, no changes in the PL/PLE band profile are observed (albeit with a concomitant change in PL intensity @ 100-120 °C attributed to solvent loss as discussed in thermal analysis and crystal structure part). These observations clearly suggest that the broad emission is not due to the presence of the defects in products **1** and **2** and is due to the presence of unique emissive species that lead to intrinsic broadband emission.

4.5.D Low-temperature photoluminescence

Low-temperature PL measurements were carried out to gain further insight to the phonon-assisted radiative recombination of STEs leading to the broad band emission in **1** and **2**. Steady-state photoluminescence spectra were collected over the temperature range of 300 – 77 K, as shown in Figure 6.

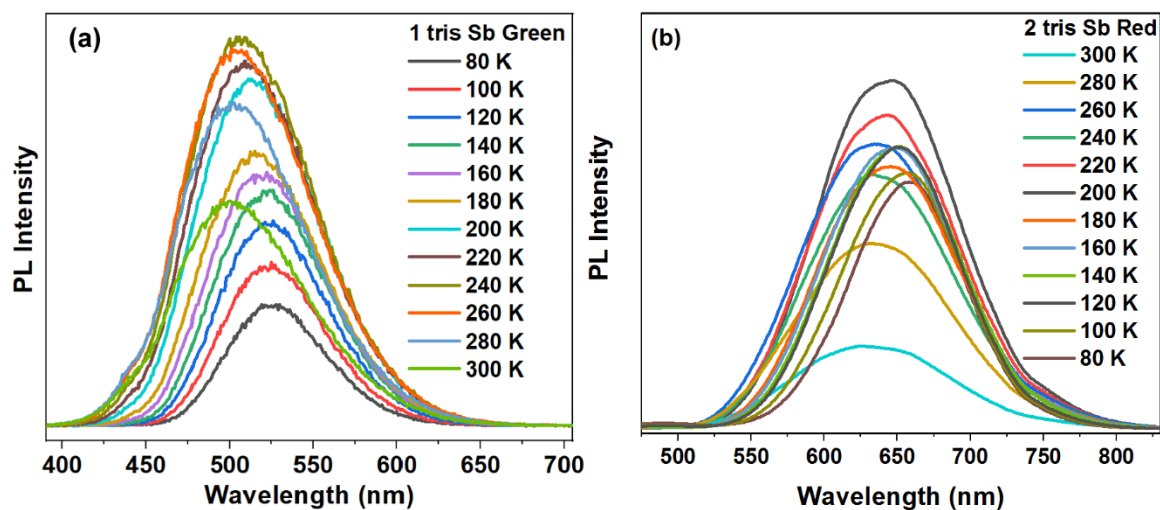


Figure 6: Low-temperature photoluminescence spectra of a) **1** tris Sb Green and b) **2** tris Sb Red powder samples excited at 370 nm and 350 nm respectively using a μ s flash lamp.

Integrated PL peak area and FWHM are calculated for both products (**1,2**) and are presented in Figure 7. For both products, the PL intensity is initially observed to increase, reaching maxima (\sim 230 K) followed by a decrease as the temperature is lowered (to 80 K). Such dependence of PL intensity can be ascribed to thermally activated trapping–detrapping of excitons from STE states.¹⁰ However, the dependence in the low-temperature regime can get complicated due to tunneling and defect bound excitons.¹⁰ Moreover, the phonon modes that couple to electronic excitation to generate STE have their own temperature dependence.⁴⁰ Bandwidth (FWHM) of the broad emission of **1** and **2** is observed to decrease monotonically as the temperature lowered. As the temperature is lowered, fewer phonon modes are thermally accessible to couple to the STEs assisting radiative recombination, thereby reducing the bandwidth of the PL emission.

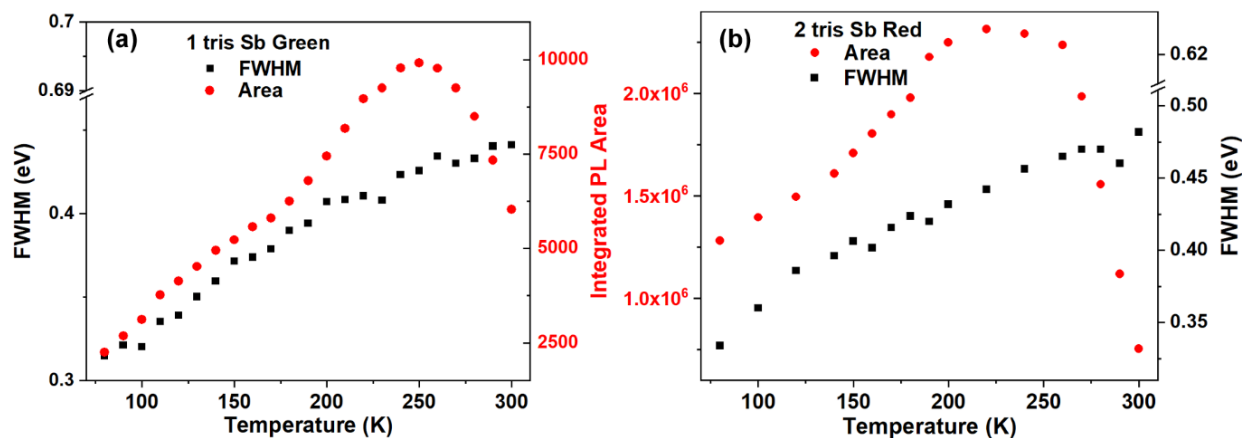


Figure 7: Integrated PL peak area and FWHM of the broad PL peak for a) *1 tris Sb Green*, and b) *2 tris Sb Red* powder samples as a function of temperature (300 – 80 K).

This could suggest thermal equilibrium between the triplet excitons and self-trapped excitons that governs the thermally activated trapping of triplet excitons in the STE states. These results indicate intrinsic broadband STE based emission in accord with many other reports on low dimensional organic-inorganic (Sb, Pb, Sn) hybrids showing broadband emission.^{7, 10, 14, 27, 28, 36, 41, 42} Further detailed experiments and analysis are needed to characterize⁴³ the nature of the STE in these systems.

4.5.E X-ray diffraction study

A clear understanding of the structure of the obtained products can potentially provide insight to the PL peak positions (green vs. red), large Stokes shift, and markedly different PLQY of **1** and **2**. Figure 3 shows the overview of the single-crystal structure of the products **1** (CCDC#2017736), **2** (CCDC#2017737). Both the products are zero-dimensional in nature wherein the organic ligands surround the metal halide unit (Figure 8). **1 tris Sb Green** crystallized in triclinic centrosymmetric space group *P*-1 containing one ligand (C₆H₂₂N₄ with +4 charge), one unit of SbCl₅ (with -2 charge), ½ unit of SbCl₆ (-1.5 charge), one Cl anion (-1 charge), one water molecule, and one H_{2.5}O molecule (+1/2 charge) in the asymmetric unit. The H atom of the charged water molecule (H_{2.5}O) which is located at the inversion center (0.5, 0.5, 0.5) and shared between the two water molecules which are related by inversion symmetry across the inversion center. The moiety formula of **1 tris Sb green** is represented as: [(C₆H₂₂N₄)₂ (Sb₂Cl₁₀) (SbCl₆) (Cl)₂ (H₃O)].(3H₂O). Structure of *1 tris Sb Green*, is composed of two basic building units of antimony chloride

framework: isolated **octahedron** and isolated edge shared **octahedra** (Figure 9b-c). In the isolated octahedral, Sb1 atom occupies a special position (0.5, 1.0, 1.0) across the inversion center and hence only half SbCl_6 moiety is present in the asymmetric unit and other half unit is generated by inversion operation, whereas the other SbCl_5 moiety generates an edge-shared dimeric octahedral unit by inversion operation. These metal halide units, periodically embedded in the organic ligand matrix, also incorporate solvent water molecules. The crystal structure is governed by strong $\text{N-H}\cdots\text{Cl}$ hydrogen bonding interactions engaging the ligand N-H moieties and Cl atoms (Figure 8).The view of the molecular packing down the b-axis shows the layered assembly of the ligand molecules along the a-axis, which accommodate the octahedra and the edge-shared dimeric octahedral units between its layers alternately parallel to the c-axis.

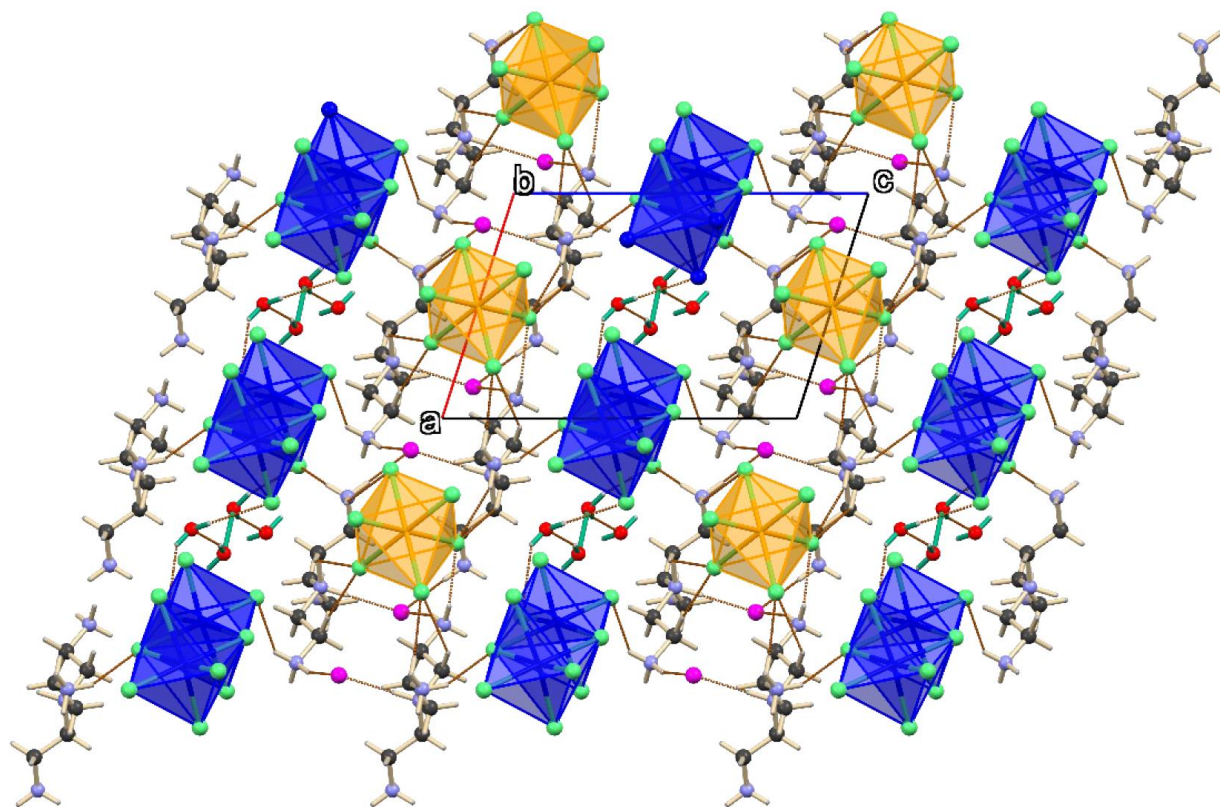


Figure 8 a): A view of the molecular packing down the b-axis in crystals of **1** (*tris Sb Green*) showed the associations of the metal halide, organic ligands, and water molecules.

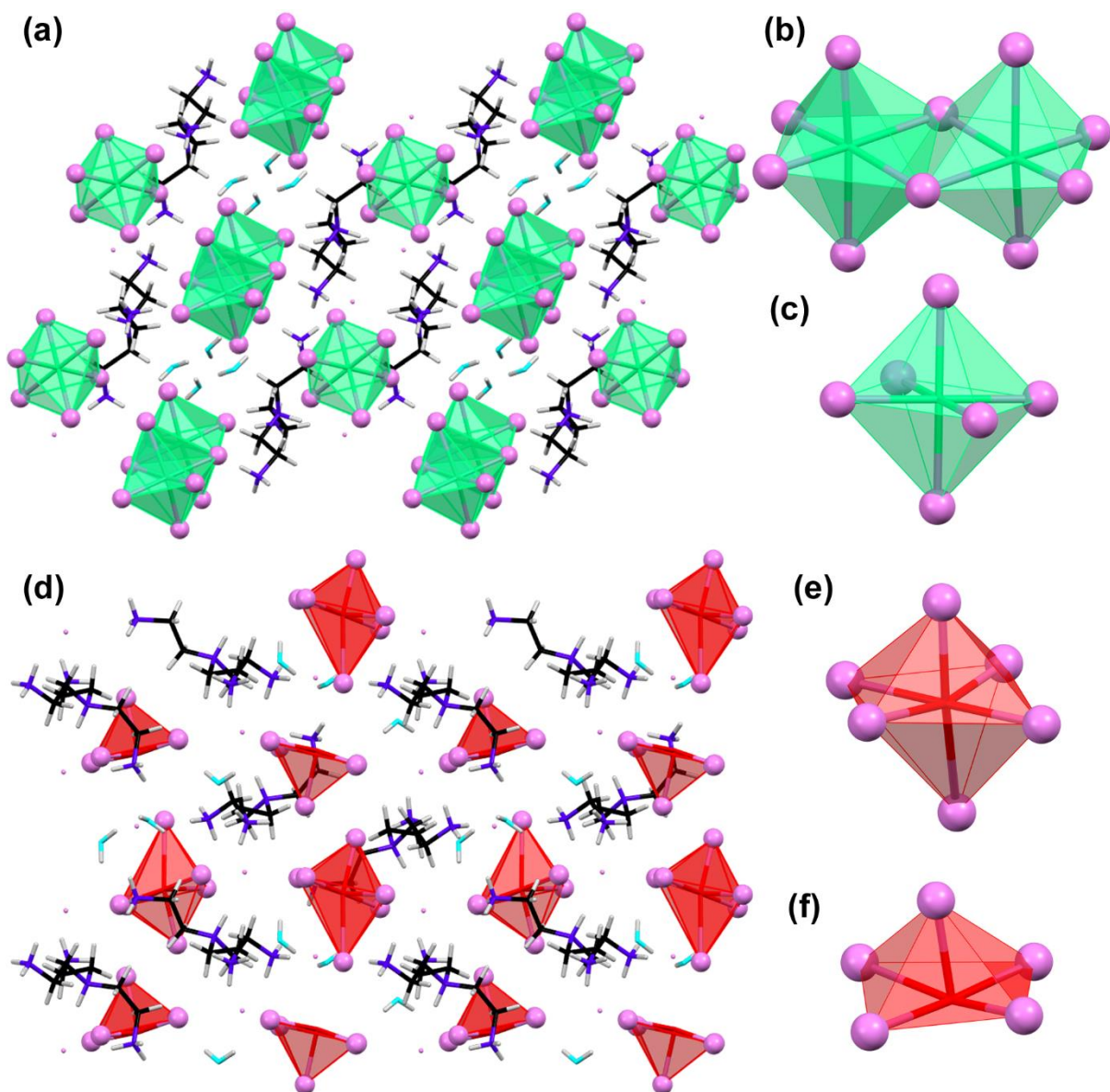


Figure 9: Single crystal structures of zero-dimensional chloro antimonite (III) – organic hybrids for (a-c) **1 tris Sb Green**, and (d-f) **2 tris Sb Red** respectively. Shown also are the metal halide units (octahedra, dimer octahedra for **1 tris Sb Green**; distorted octahedra and distorted pyramid for **2 tris Sb Red**) for both the products.

The arrangement of the neighboring edge-shared dimeric octahedral units along the channel encapsulates the water molecules between them which interact with these metal halide units through O–H···Cl hydrogen bonding interactions. Conversely, the non-bonded Cl ions are located in the space between the two octahedral units along the channel parallel to the a-axis and forms a

N–H \cdots Cl hydrogen bond with the ammonium protons. These strong hydrogen bonding interactions govern the crystal packing and play a crucial role in optoelectronic responses. The extent of distortion (bond lengths, bond angles) in the monomeric and dimeric octahedra was estimated for **1** *tris Sb green*. The monomeric octahedron is almost undistorted with very similar Sb–Cl bond lengths (largest difference in Sb–Cl bond length = 0.01 Å, largest deviation of the Cl–Sb–Cl bond angle from the ideal value = 31°). The edge shared dimeric octahedron with six different Sb–Cl bond lengths shows slight distortions (largest difference in Sb–Cl bond length = 0.6 Å, largest deviation of the Cl–Sb–Cl bond angle from the ideal value = 6°). Such distortions are not unexpected in the edge shared (μ -Cl) dimeric octahedral metal halide unit. The phase purity of **1** was verified using the powder X-ray diffraction (PXRD) patterns, which matched well with the simulated ones in terms of the single-crystal X-ray data (Figure 11)

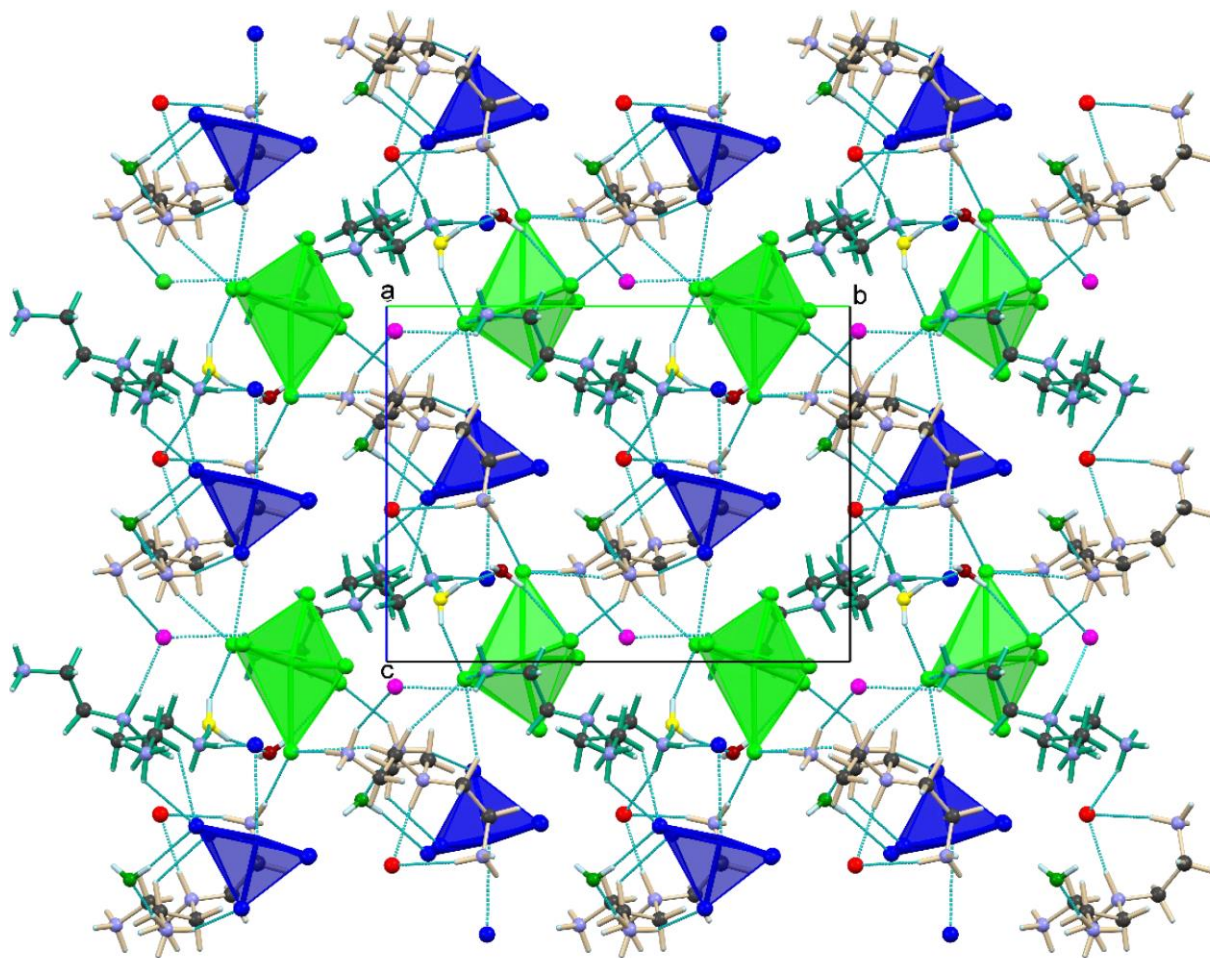


Figure 10: A view of the molecular packing down the a-axis in crystals of **2** (*tris Sb Red*) showing the associations of the metal halide, organic ligands, and water

Product 2 tris Sb Red crystallizes in a monoclinic chiral space group $P2_1$ containing two ligands (tetra positive), two $[\text{SbCl}_6]^{3-}$ anions, two $[\text{Cl}]^-$ anions, and three H_2O molecules in the asymmetric unit having the formula $[(\text{C}_6\text{H}_{22}\text{N}_4)_2 (\text{SbCl}_6)_2 (\text{Cl})_2].3(\text{H}_2\text{O})$. Structure of 2 is composed of two basic building units of antimony chloride unit: isolated heavily distorted octahedron and isolated heavily distorted quadrangular pyramid (Figure 9e-f). The quadrangular pyramid has the sixth coordination by a distant Cl atom (3.156 Å) as highlighted in Figure 9f. The isolated very distorted octahedron with a lengthened apical Sb–Cl bond length (3.042 Å) may also be thought of as a distorted ‘quadrangular pyramidal’ structure. Such long Sb–Cl bond distances are not uncommon and have been attributed to the secondary bonding interaction.⁴⁴ These distortions highlight the site asymmetry in the coordination environment of the hexacoordinated Sb motifs. These metal halide units are again periodically embedded in the inert matrix of the organic ligand incorporating water molecules forming the 0D structure. The view of the molecular packing down the a-axis revealed the layered arrangement of both metal halides parallel to the b-axis which are embedded between the channels formed by symmetry independent organic ligands. The respective layers of metal halides are arranged alternately along the c-axis. The crystal structure is stabilized by strong intermolecular $\text{N}-\text{H}\cdots\text{Cl}$ hydrogen bonding interactions engaging ammonium H-atoms of the organic ligand and Cl atoms (of metal halides) or Cl ions (Figure 10). The three water molecules also form strong H-bonding interactions ($\text{O}-\text{H}\cdots\text{Cl}$ and $\text{N}-\text{H}\cdots\text{O}$) involving Cl atoms and ammonium protons of metal halides and organic ligands, respectively. The water molecules also interact with each other through $\text{O}-\text{H}\cdots\text{O}$ hydrogen bonds. The extent of distortion in the heavily distorted octahedron and the extremely distorted octahedron was estimated for 2 tris Sb red. The heavily distorted octahedron shows high site asymmetry with six different Sb–Cl bond lengths (largest difference in Sb–Cl bond length = 0.6 Å, largest deviation of the Cl–Sb–Cl bond angle from ideal value = 23°), thereby approaching a ‘quadrangular pyramidal’ structure. The extremely distorted octahedron shows extreme site asymmetry with very different Sb–Cl bond lengths (largest difference in Sb–Cl bond length = 0.45 Å, largest deviation of Cl–Sb–Cl bond angle from the ideal value = 101). The ‘apical’ Sb–Cl bond length in this unit is 2.448 Å. The phase purity of 1 and 2 was confirmed using the PXRD patterns which matched well with the simulated ones in terms of the single-crystal X-ray data as shown in Figure 11.

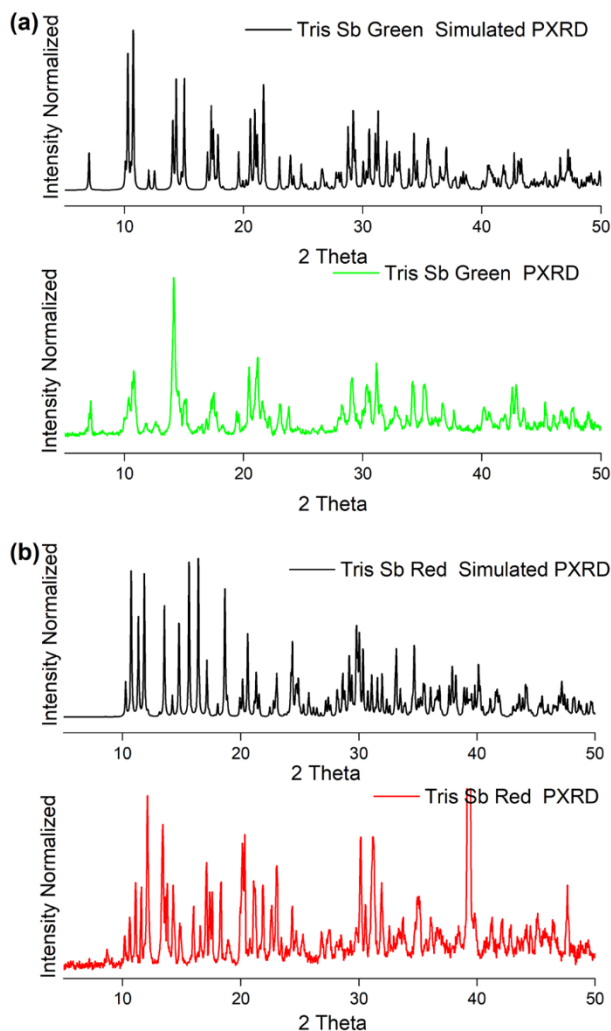


Figure 11: Comparison of the PXR D pattern with the simulated pattern from the single crystal structure data for a) **1** tris Sb Green, b) **2** tris Sb Red

4.5.F Structure-property correlation in **1** tris Sb Green & **2** tris Sb Red

Comparing the above-estimated ground state structural distortions of the photoactive metal halide units reveals that average distortion is appreciably higher in **2** tris Sb Red and is relatively lower in **1** tris Sb Green. In essence, **1** tris Sb Green has undistorted Octahedral metal halide units, while **2** tris Sb Red has distorted quadrangular pyramid units. The presence of the common organic ligand in **1** and **2** allows us to perform a structure-property-mechanism correlation that can provide us with deeper understanding of the crucial factors that control their photo-physical properties. Understandably, the extent of distortion and ground state structure affects Stokes shifts and PL emission energies. It is clear from Figure 1 that both products (**1**, **2**) show large Stokes Shift

implying strong structural reorganization in the excited state (3P_1). The observed Stokes shift is much higher for 2 tris Sb Red (~290 nm) than that of 1 tris Sb Green (~165 nm) suggesting stronger excited state reorganization for 2 than 1. Hence, Stokes shift depends not only on the ground state structure (and its distortion) but also on structure in the excited state of the metal halide unit. Within the theoretical framework of ns^2 metal ions, as proposed by Blasse et al., the luminescence properties are directly related to the structure and the extent of distortion of the ns^2 metal-halide unit.⁴⁴⁻⁴⁶ Upon photo-excitation of these ns^2 metal-halide units, the ground state s^2 configuration will transform into a sp excited state with higher symmetry.^{39,44} Gaining this structural symmetry due to photo-excitation from the distorted ground state structure results in the observed Stokes shift. Clearly, ground state structural distortion in 2 tris Sb Red is relatively higher than in 1 tris Sb Green and is in accord with the observed larger Stokes shift in the former. Similar approach has been successfully utilized by Blasse et al. for ns^2 metal ions doped in host lattices that show large Stokes shifts if the metal ions occupy off-center positions in large interstices as these ions can move towards the center in the excited state thereby gaining symmetry.⁴⁴ The difference in the PL emission energies (peak position) for the two products (1, 2) can again be rationalized in terms of the ground state structure. Typically, the structures of these s^2 metal halide units are affected by the presence of metal centered, stereo chemically active lone pair. However, s^2 complexes with six coordination number have octahedral geometry and appear as an exception from the VSEPR model.^{39,47} For complexes with coordination number lower than six are in general agreement with the VSEPR model and show distortions/asymmetry in their structures due to the stereochemical activity of lone pair.^{39,48,49} These considerations are also applicable to halogen antimonite(III) polyhedral units here that constitute the photoactive building units for products 1, 2. For 1 tris Sb green, metal halide coordination sphere has octahedral geometry with slight differences in the Sb-Cl bond lengths (undistorted octahedron and distorted dimeric octahedra). However, for 2 tris Sb Red, the metal halide coordination sphere has quadrangular pyramidal structure with modest differences in the Sb-Cl bond lengths (quadrangular pyramid and distorted octahedron structure that approaches quadrangular pyramidal structure). Clearly, the 'effective' interaction strength of Cl- anions (3s, 3p orbitals) with the Sb^{3+} (5s, 5p orbitals) metal ion will be stronger for 1 tris Sb Green (less bond length distorted Octahedral structure) than 2 tris Sb Red (more bond length distorted quadrangular pyramidal structure) due to the degree of asymmetry in the metal-halide coordination environment. Symmetrically stronger 'effective' interaction between the metal and

halide in 1 will lead to higher energy gap between the HOMO and LUMO. Asymmetric and weaker metal halide interaction in 2 will result in a smaller energy difference between the HOMO and LUMO (qualitative molecular orbital diagram for octahedral and square pyramidal structural cases are shown in Figure 12).

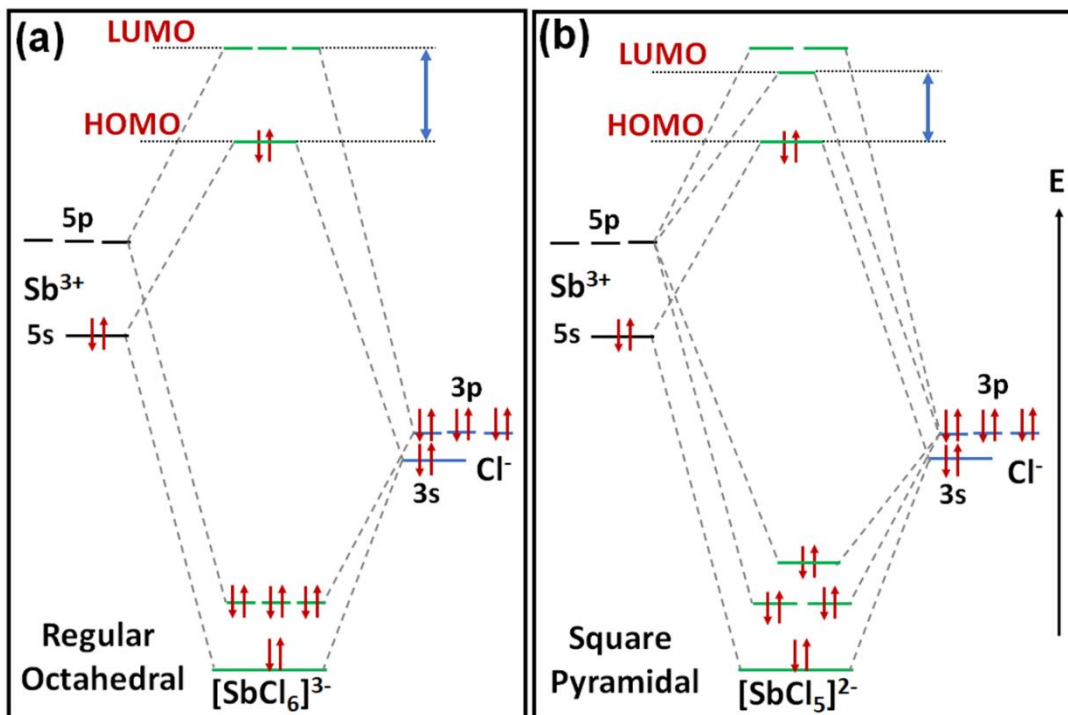


Figure 12: Qualitative molecular orbital diagram of (a) octahedral and (b) square pyramidal metal-halide framework and the associated change in the energy gap between the HOMO and LUMO that manifests as PL emission energy difference between the two structures.

Hence, it is anticipated that 1 tris Sb Green, with symmetrical octahedral structure, would have high energy PL emission (LUMO→HOMO) peak while 2 tris Sb Red, with asymmetric quadrangular pyramidal structure will emit at lower energies. This is in qualitative agreement with the observed high energy PL emission peak of 1 tris Sb Green ($\lambda_{\text{em}} = 517 \text{ nm}$) and low energy PL emission peak of 2 tris Sb Red ($\lambda_{\text{em}} = 638 \text{ nm}$). Such ground state structure dependent molecular orbital scheme has been successfully utilized in attributing differences in the PL emission energies of $[\text{SbCl}_6]^{3-}$ and $[\text{SbCl}_4]^-$ ions in solution.³⁹ Noteworthy here, a symmetrical (undistorted) octahedral halide ligand field will lead to higher HOMO-LUMO energy gap than the energy gap in an undistorted square pyramidal ligand field. This again has a qualitative accordance with the reported low PL emission energies for many $[\text{SbCl}_5]^{2-}$ based metal halide organic 0D hybrids (with

emission energies in the orange region of 600 – 650 nm, in the solid state and higher PL emission energies in the green for $[\text{SbCl}_6]^{3-}$ based ions in solution.³⁹

The photoluminescence quantum yield (PLQY) of 1 tris Sb Green is (~45%) distinctly higher than PLQY of 2 tris Sb Red (~6%). Note that the observed PLQY for 1 tris Sb Green is lower than other literature reports^{7, 26-28} on 0D antimony chloride hybrids that have near-unity PLQY. However, a direct comparison of the PLQY of 1 tris Sb Green with these other reports, including different organic ligands might not lead to the needed understanding of the rationale behind the observed differences in their PLQY. This is due to the surrounding environment provided by the organic ligand to the photoactive metal halide unit, which can appreciably affect the PL emission intensity. There can be effective energy transfer of electron excitation from the molecular levels of the surrounding organic moiety to the $^3\text{P}_1$ luminescence level of the s^2 metal ion, thereby enhancing the PLQY.^{50, 51} ‘Loan’ of luminescence intensity from the ligands to metal has also been reported wherein ligand to metal charge transfer interactions leads to an additional thermal population of the luminescent excited state of metal ions leading to enhanced PLQY.^{52, 53} This clearly suggest the electronic contribution of the surrounding organic ligand in affecting the photoluminescence intensity in the low dimensional systems.⁵³ Interestingly, the synthetic strategy utilized here allows the crystallization of both 1 and 2 incorporating the same organic ligand. This, to a large extent, helps maintain the same electronic contribution (if any) to the metal ion, thereby similarly affecting the photoluminescence intensity from 1 and 2. Hence, the PLQY of 1 and 2 can be compared and possibly correlated to their structure/distortion to gain some insight into the observed differences in their PLQY. This effort of finding any existent correlation between structure/distortion and PLQY is extremely important for further design and synthesis of broad band, lead-free emitters and is reported for the first time here for Sb halide based 0D perovskite. Although there have been few reports on antimony chloride-based 0D hybrids that show near-unity PLQY but none of the reports provide any insight into the observed PL peak position and the observed high PLQY. The commonality in all of these high PLQY low dimensional antimony chloride-based hybrids is the presence of isolated, almost undistorted metal halide unit (particularly SbX_5 unit).^{7, 26-28}

Moreover, antimony chloride-based low dimensional hybrids with polymeric metal halide units (showing distortions) have low/modest emission strength.^{50, 51, 54} In the present comparison of PLQY of 1 and 2, metal halide polyhedral units for 1 (isolated octahedra, dimer octahedra) show

small distortions while metal halide polyhedral units for 2 (octahedra and quadrangular pyramid) show relatively higher distortions (Table 3). Survey of the existing literature on antimony chloride-based low dimensional materials, revealing that the isolated undistorted monomeric units demonstrate high emission intensities, suggest the importance of distortions in affecting the PLQY.^{50-53, 55} Clearly, the extent of distortion in 1 is relatively lower than the distortion in 2. This implies a correlation of the structure/distortion with the PLQY for the 0D Sb halide-based hybrids. Noteworthy, the presence of distorted dimer octahedra (plausibly suppressing PLQY) along with almost undistorted octahedra (plausibly enhancing PLQY) in 1 shows higher PLQY than 2 having all isolated monomeric units (plausibly enhancing PLQY) with heavy distortions (plausibly suppressing PLQY). This again indicates the important role played by structural distortions in the ground state. The presence of the dimer octahedra with some distortions in 1 can then explain the observed lower than unity PLQY which is in accord with earlier reports⁵¹ on low dimensional antimony chloride hybrids with dimeric/polymeric metal halide units. The observed correlation of the structure/distortion with the PLQY could be rationalized in terms of photoexcitation of ns^2 metal ions transiting from the ground state to the excited state having higher symmetry. Hence, the smaller the distortions in the ground state structure of the metal halide polyhedral unit, the lower the amount of electronic excitation energy that will be utilized in the process of excited-state structural reorganization. This will minimize non-radiative losses of the electronic excitation energy, thereby enhancing the possibility of stronger luminescence. The above-proposed rationalization providing insight to the experimentally observed correlation between structure/distortion and PLQY for 0D antimony chloride-based hybrids is by no means universal and needs to be further tested/verified. In order to clearly understand the role of distortion in affecting PLQY, we have designed and synthesize different structures of antimony chloride-based 0D hybrids by altering the ligand concentration in the later part of the study.

4.5.G Effect of ligand concentration

The successfully modified synthetic strategy allows crystallizing 0D hybrids with isolated monomeric metal-halide unit (albeit with a mixture of octahedral and pyramidal units). This is achieved by increasing the metal to ligand ratio to 1: 10 as detailed in the experimental section. The obtained product, 3 tris Sb Yellow, appears to emit bright yellow light when viewed inside UV chamber. Steady-state optical characterization of 3 tris Sb Yellow, as shown in Figure 13,

reveals a strong, broad yellow emission band centered at 580 nm with full width at half maximum (FWHM) of ~140 nm. The PLE spectra, collected at 580 nm, match well with the absorption spectra showing multiple features in 300 - 400 nm range.

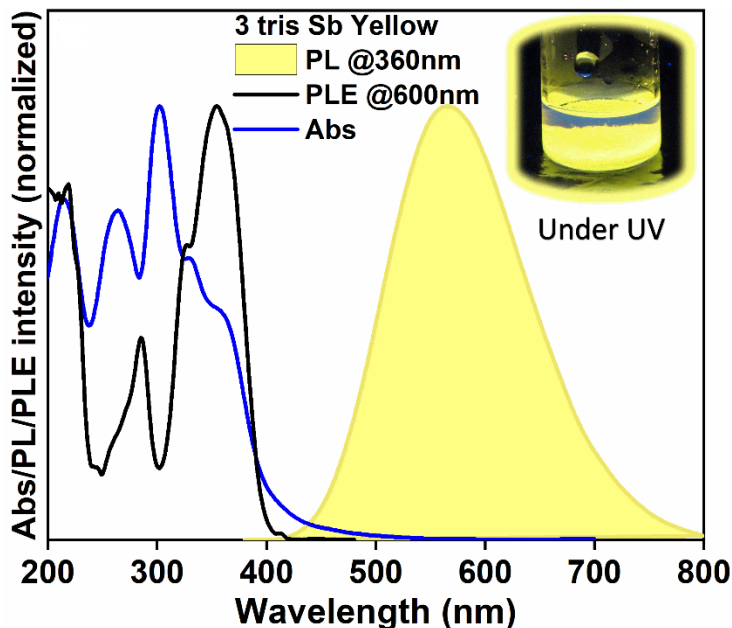


Figure 13: Optical and structural characterization of *3 tris Sb yellow*-(a) Absorbance (Abs), Photoluminescence (PL), and Photoluminescence excitation (PLE) spectra

The estimated “Stokes shift” is ~200 nm and the PLQY for *3 tris Sb Yellow* is estimated to be ~43%.

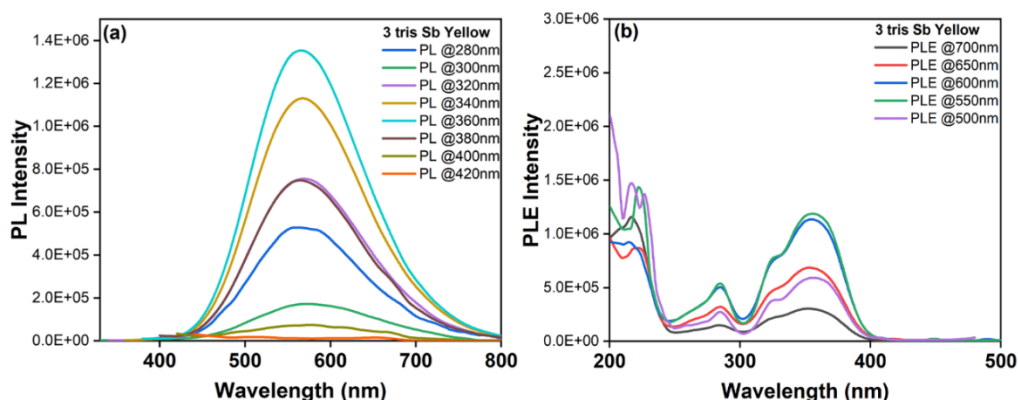


Figure14: Dependence of photoluminescence (PL) on excitation wavelength and photoluminescence excitation (PLE) spectrum collected across the broad PL peak for *3 tris Sb Yellow* powder samples

The broad yellow emission profile remains unchanged as the excitation wavelength is changed. Further, the PLE profile remains unchanged across the broad band emission (Figure 14).

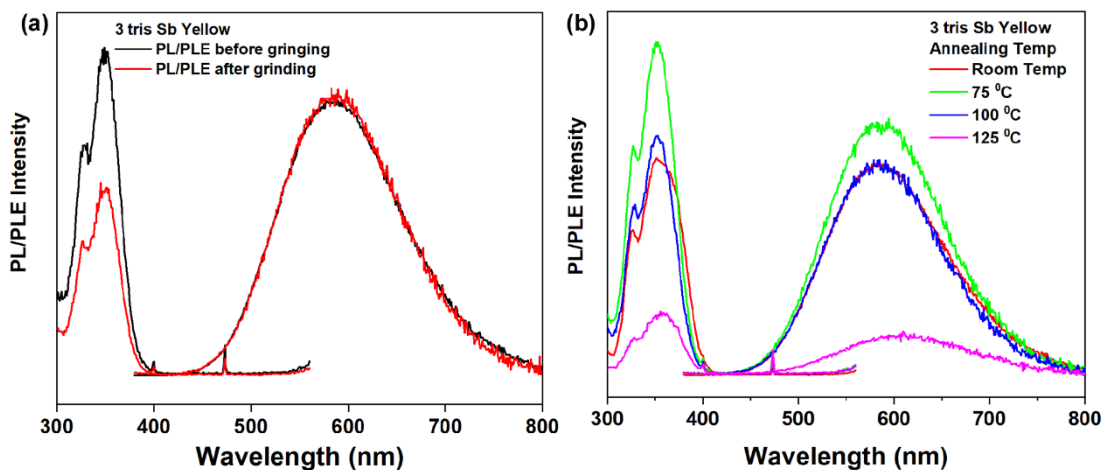


Figure 15: Dependence of PL and PLE on a) grinding and b) annealing for 3 tris Sb Yellow powder samples.

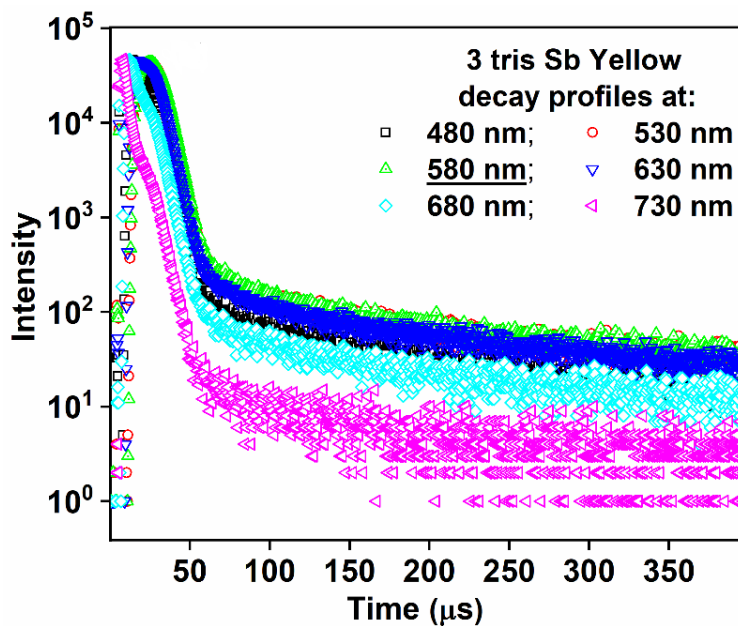


Figure 16: Lifetime decay profiles collected across the yellow emission band using microsecond flash lamp excitation (360 nm).

The PL and PLE profile remains unchanged upon solid-state grinding and annealing (Figure 15). Moreover, analysis of the collected decay profiles across the broad emission band of 3 tris Sb Yellow, as presented in Figure 16, provides lifetime components (and relative %) of 5.2 μs (85%) and 84.6 μs (15%) that largely remains unchanged across the emission band. (Table 2).

Tris Sb Yellow		
Wavelength (nm)	Life time (microseconds)	Relative %
480	5.18	82.59
	92.05	17.41
530	5.25	84.97
	87.20	15.03
580	5.20	83.90
	84.6	16.10
630	5.28	84.68
	89.39	15.32
680	5.52	89.46
	93.51	10.54
730	5.67	91.37
	97.91	8.63

Table 2: Lifetime (μs) components and their relative weights (%) for 3 tris Sb Yellow

This indicates the presence of unique emissive species responsible for the observed phosphorescence in 3 tris Sb Yellow. Notably, PL emission energy of 3 tris Sb yellow sample represent an intermediate value when compared to that of 1 tris Sb Green and 2 tris Sb Red while the PLQY value is close to that of 1 tris Sb Green

4.5.H Crystal structure of 3 tris Sb Yellow

Single crystal structure of 3 tris Sb Yellow (CCDC #2017738) belongs to triclinic space group P-1.

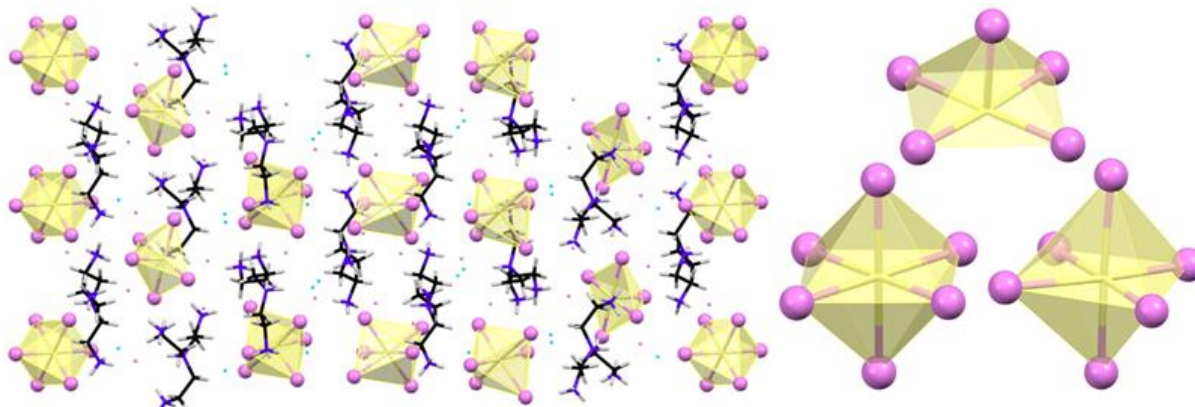


Figure 17: An overview of single crystal structure of 0D 3 tris Sb Yellow product and metal halide units (distorted quadrangular pyramid, octahedra, and distorted octahedra) comprising the 0D structure.

It contains four ligands (tetra positive), two units of half of $[\text{SbCl}_6]^{3-}$ anion, two units of $[\text{SbCl}_6]^{3-}$ anion, seven $[\text{Cl}]^-$ anions, and four $[\text{H}_2\text{O}]$ molecules in the asymmetric unit leading to $[(\text{C}_6\text{H}_{22}\text{N}_4)_4(\text{SbCl}_6)_3(\text{Cl})_7].4(\text{H}_2\text{O})$ as the formula moiety (Figure 17)). Two of the Sb atoms of $\frac{1}{2}$ units of $[\text{SbCl}_6]^{3-}$ anion occupy a special position (inversion center), Sb1 (0.0, 0.5, 0.0) and Sb2 (0.0, 0.5, 0.5), hence only half unit is present in the asymmetric unit and the other half is generated by inversion operation. Structure of 3 is composed of isolated octahedra, and isolated quadrangular pyramid as the basic building units. These metal halide units are periodically embedded in the organic ligand matrix, wherein water molecules are also incorporated.

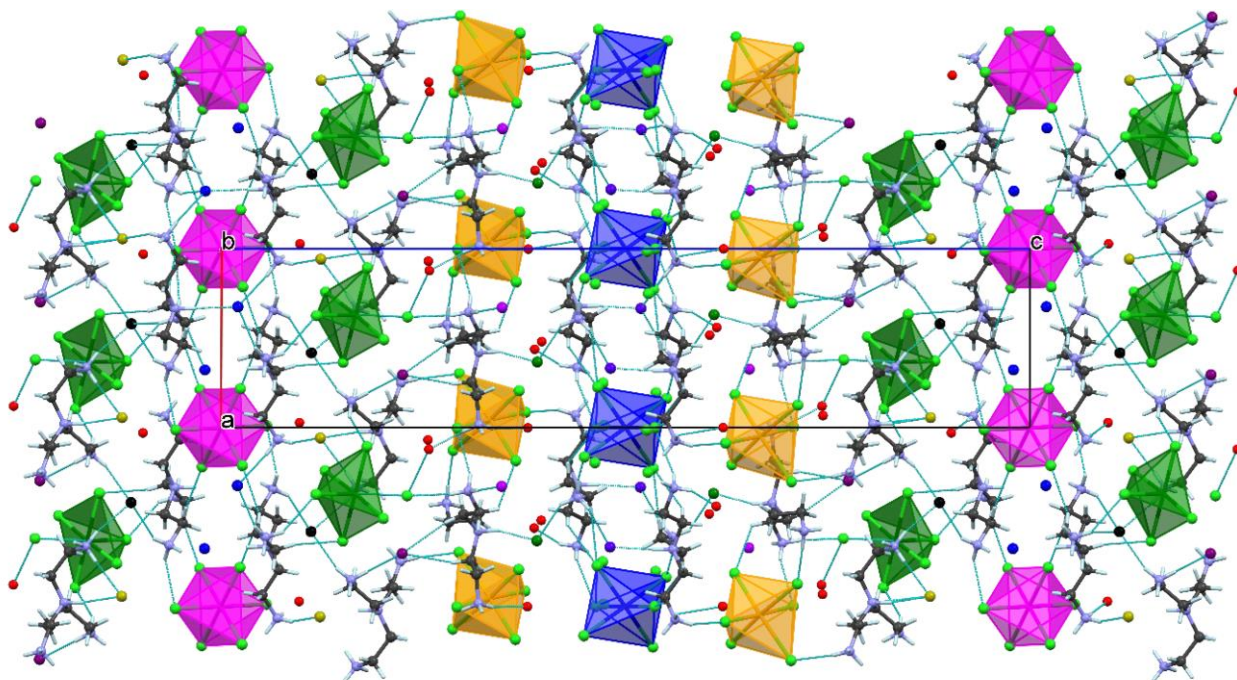


Figure 18: A view of the molecular packing down the b-axis in crystals of **3** (*tris Sb Yellow*) showing the associations of the metal halide, organic ligands, and water molecules

These water molecules create hydrogen bonding network with metal halide unit and organic ligands. There are strong hydrogen bonding interactions between the ammonium head group protons with the halides and the water oxygen atom throughout the structure (Figure 18). In addition to the presence of slightly distorted quadrangular pyramid, the crystal structure shows two types of isolated octahedron- one that is almost undistorted and the other with slight distortions. The undistorted octahedron has very similar Sb-Cl bond lengths (largest difference in Sb-Cl bond length = 0.028 Å, largest deviation of the Cl-Sb-Cl bond angle from ideal value = 3°). The distorted octahedron has six different Sb-Cl bond lengths (largest difference in Sb-Cl bond length = 0.46 Å, largest deviation of the Cl-Sb-Cl bond angle from ideal value = 4.6°). The distorted quadrangular pyramid has the sixth coordination by a distant Cl atom (3.06 Å). This quadrangular pyramidal unit has five different Sb-Cl bond lengths (largest difference in Sb-Cl bond length = 0.21 Å, largest deviation of Cl-Sb-Cl bond angle from ideal value = 3.2°). The apical Sb-Cl bond length here is 2.452 Å.

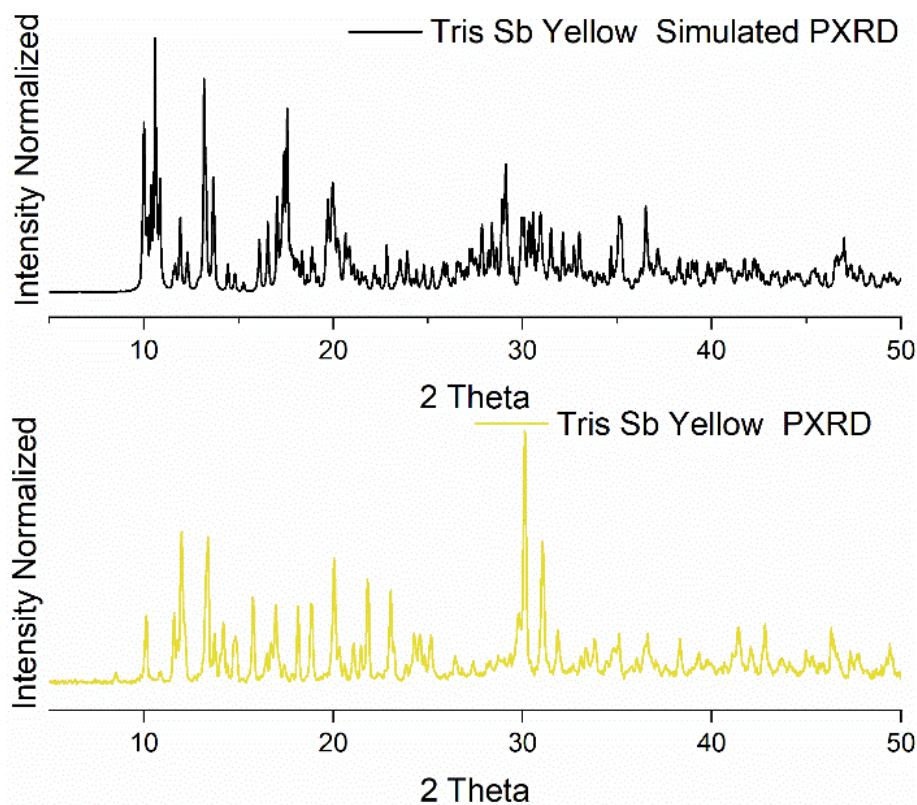


Figure 19: Comparison of the PXR D pattern with the simulated pattern from the single crystal structure data for 3 tris Sb Yellow sample.

The phase purity of 3 tris Sb Yellow was verified using the PXR D patterns which matched well with the simulated ones from the single-crystal X-ray data as shown in Figure 19

4.5.I Generality of structure-property relation

Now, the pertinent question here is can we utilize the same structure/distortion correlation to understand the observed photo-physical properties for 3 tris Sb Yellow? Such rationalization would then fall in-line with the proposition made for products 1 and 2 and would support generality.

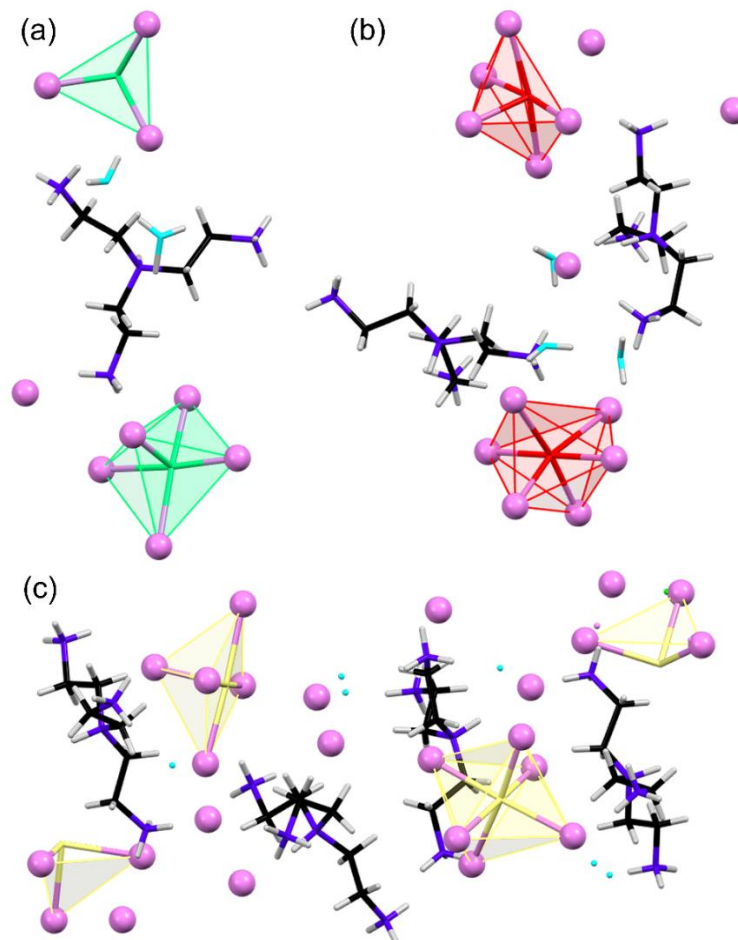


Figure 20: Structural unit of a) 1 tris SB green b) 2 tris Sb red c) 3 tris Sb yellow.

Sb-Cl polyhedral type	Bond Length Distortion	Bond Angle Distortion
<i>1 tris Sb Green</i>		
Isolated octahedral	0.01 Å	3°
Dimer octahedral	0.6 Å	6°
<i>2 tris Sb Red</i>		
Distorted octahedral	0.6 Å	23°
Quadrangular pyramid	0.45 Å	10°
<i>3 tris Sb Yellow</i>		
Octahedra	0.028 Å	3°
Distorted octahedral	0.46 Å	4.6°
Quadrangular pyramidal	0.21 Å	3.2°

*Bond Length Distortion = (highest bond length) - (lowest bond length)

#Bond Angle Distortion = $|90^\circ - (\text{Cl} - \text{Sb} - \text{Cl} \text{ bond angle})|$

Table 3: List of estimated bond length asymmetry and bond angle variations (from ideal value) in metal halide frameworks of **1**, **2**, **3** as obtained from single-crystal structures.

Sample	Stoke shift (eV)	PL peak position (nm)	PLQY
1 tris Sb Green	0.97	530	45%
2 tris Sb Red	1.9	640	6%
3 tris Sb Yellow	1.2	580	43%

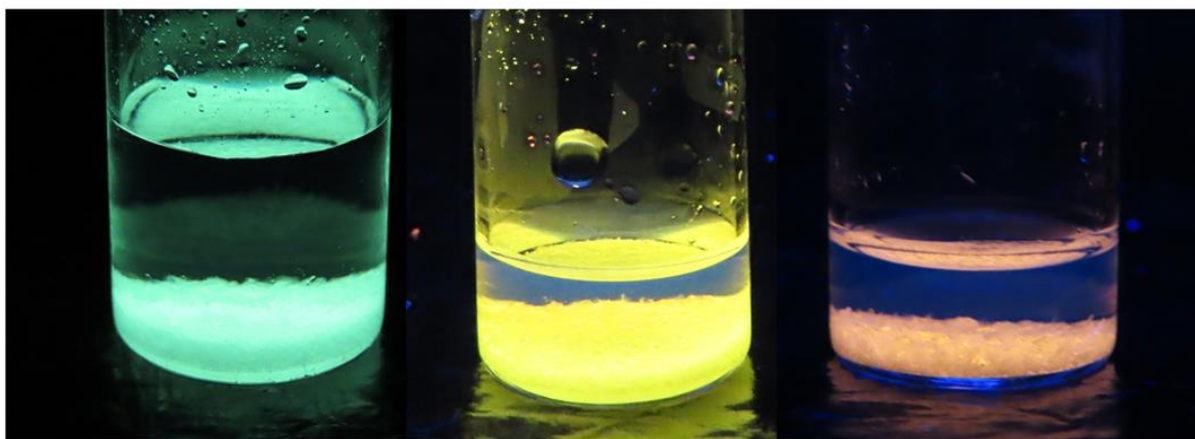
Table 4: Comparison of Stokes shift, PL peak position and PLQY with the structure

The broadband emissions in low dimensional metal halide hybrid materials have been attributed to self-trapping of excitons (STE) due to strong electron-phonon coupling that produces transiently localized charges (holes/electrons) that distort the metal halide unit. The PL emission of these self-trapped excitons is phonon assisted that broadens the radiative bandwidth.⁹ Upon photoexcitation, the low lying transient STE states can accept carriers from the excited 3P_1 state and allow slow and phonon assisted radiative decay to 1S_0 ground state thereby broadening the emission bandwidth. Necessarily, this relay of radiative decay channel leads to finite energy losses through non-radiative state hopping and accounts for finite Stokes Shift in the broad emitting low dimensional material. Importantly, this is in addition to any Stokes shift that might arise due to the changes in the excited state geometry/structure relative to the ground state structure (as discussed earlier).

A comparison of the structure/extent of distortions in the comprising metal halide units of 1 tris Sb Green, 2 tris Sb Red, and 3 tris Sb Yellow in the light of their observed photo-physical properties is crucial here. Bond length and angle distortion in the various structural units for products 1, 2, 3 (Figure 20) are calculated and presented in Table 3 shows the following order of extent of distortions- $1 \sim 3 < 2$. Qualitatively, the type of isolated metal halide polyhedra in 1 is octahedra, in 2 is quadrangular pyramid, and in 3 is a mixture of the octahedron and quadrangular pyramid. The degree of asymmetry of the coordination environment in the metal halide structural unit, as discussed earlier (MO diagram, Figure 12), largely dictates the PL emission energy with

high energy emission band for symmetric octahedral case (1 tris Sb Green) and low energy emission band for asymmetric pyramidal structure (2 tris Sb Red). Now for 3 tris Sb Yellow, the presence of mixture of octahedral and quadrangular pyramidal units would cause the PL emission band to appear in the intermediate energy range. Indeed, for 3 tris Sb Yellow, the PL band appears at energy in between the emission bands of 1 tris Sb Green and 2 tris Sb Red (Table 4). This strongly suggests the active role of metal-halide polyhedral unit structure and the degree of symmetry in metal-halide coordination environment in dictating the PL emission band position. As discussed earlier, the extent of distortion present in 1 tris Sb Green is modest and is appreciably lower when compared to that of in 2 tris Sb Red. This difference in extent of distortion reflected in the drastic difference of the observed PLQY. Interestingly, the extent of distortion present in 3 tris Sb Yellow is comparable to that of in 1 tris Sb Green (Table 3) and follows $1 \sim 3 \ll 2$. The similarity of the extent of distortion in 1 tris Sb Green and 3 tris Sb Yellow would indicate similar PLQY values much higher than that of 2 tris Sb Red. This is in accord with the measured PLQY of 3 tris Sb Yellow close to that of 1 tris Sb Green (Figure 21).

Photograph under 365 nm excited UV light



Tris Sb Green = 45% **Tris Sb Yellow = 43%** **Tris Sb Red = 6%**

Figure 21: Photographic image of the synthesized crystals under 365nm light excitation and their PLQY values written below.

Such observed correlation between the extent of distortion and PLQY clearly highlights the role of extent of distortion in affecting the photo-physical properties. The observed Stokes shifts of three products can also be then positively correlated to the extent of distortion (Stokes

shifts: 1~3<<2). Thus, the above-proposed factors (metal-halide unit structure; extent of distortion) are observed to directly impact the photo-physical properties (PL emission energy; PLQY & Stokes shift, respectively) for the different 0D Sb(III) chloride hybrids (1, 2, 3) synthesized here utilizing a common organic ligand (Table 4). Further efforts are underway to ascertain the effect of metal-halide polyhedral type and different extent of distortions in a given type of polyhedral unit on the emissive properties of 0D organic-antimony chloride hybrids.

4.5.J Thermal Stability

The thermal stability of the crystals was analyzed by TGA measurements.

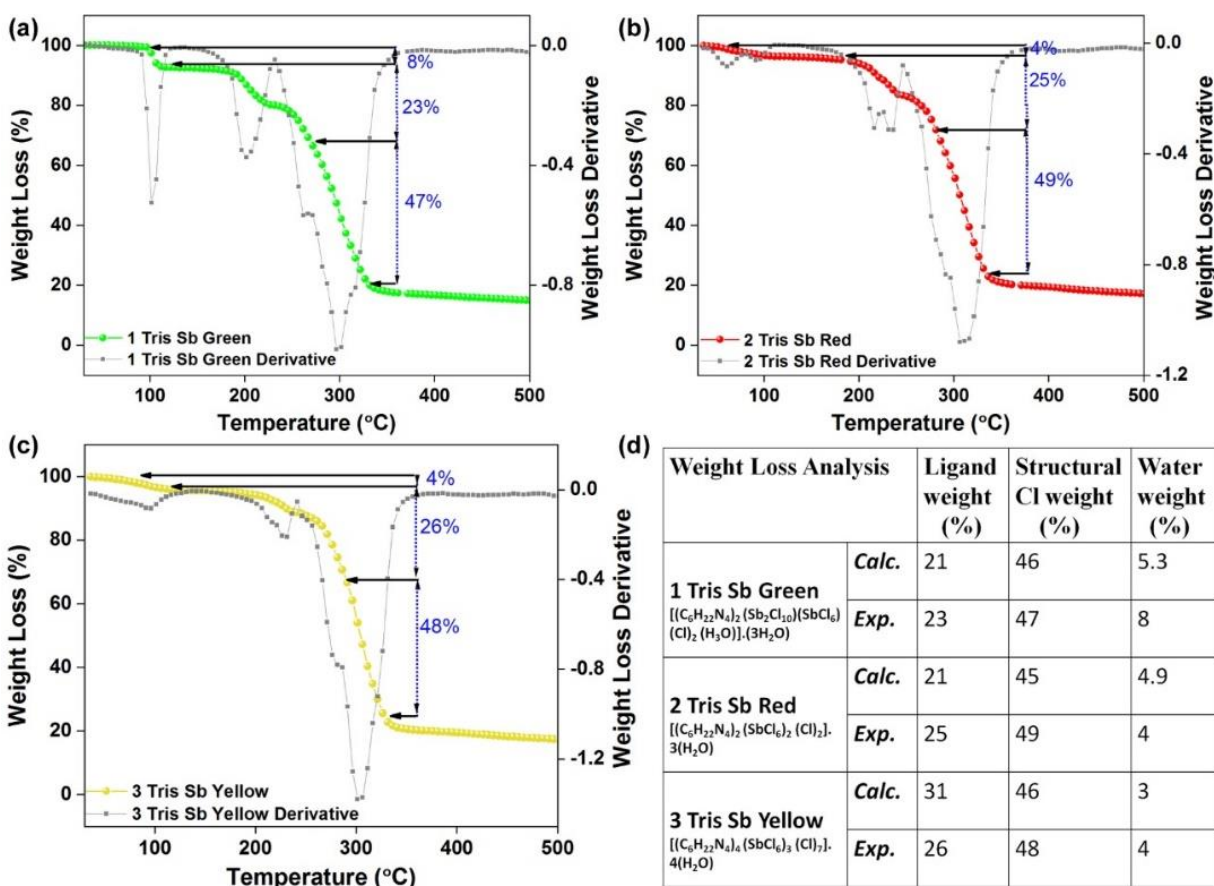


Figure 22: Thermogravimetric weight loss analysis for a) 1 tris Sb Green, b) 2 tris Sb Red, c) 3 tris Sb Yellow, d) table listing the % weight losses incurred from the plausible structural components

The loss of these water molecules at ~100 - 120 °C, as evidenced in the TGA profile (Figure 22 for all the synthesized systems, leads to a drastic loss of PL intensity of the annealed samples. This are due to the hydrogen bonding interactions between the ammonium protons with the halides and

the water Oxygen atom throughout the structures. The presence of water of crystallization in (1,2,3) allows us to assign the weight loss peaks ~ 100 °C arising due to loss of water molecules from the structures. Further, free halogens in the structures (1,2,3) allows us to tentatively attribute the weight loss at ~ 300 °C to be due to halogen loss as has been suggested in a recent report

4.5.K Phase purity

^1H NMR spectra of **1**, **2** reveal the presence of phase pure products with peaks attributed to cationic ligand moiety (Figure 21(a-d)).

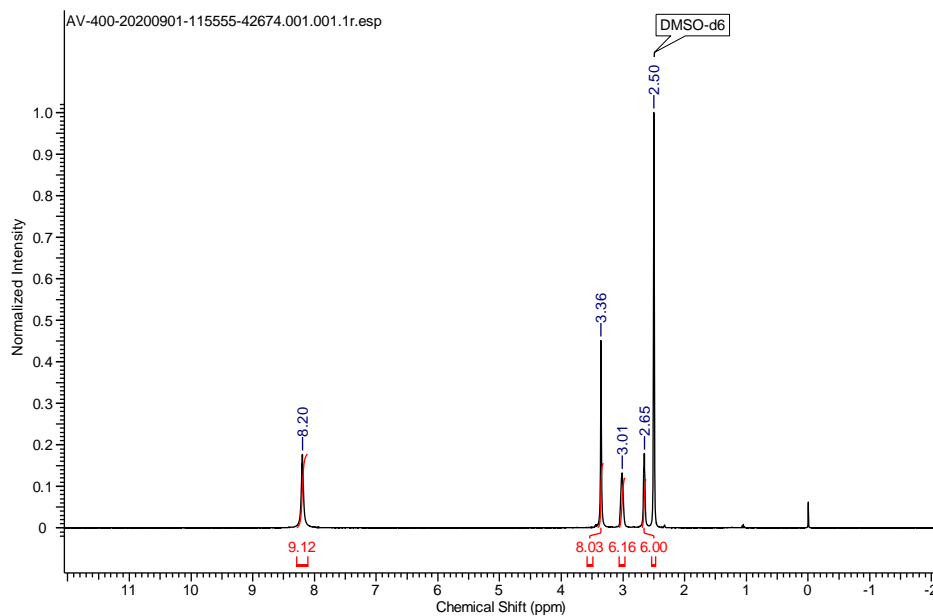


Figure 23 (a). ^1H NMR of Tris Cl salt (400 MHz, DMSO- d_6 , 298 K): δ 8.20 (br, 9H, NH_3), 3.01 (br, 6H, CH_2), 2.65 (br, 6H, CH_2) 3.36(br, 8H, H_2O) ppm.

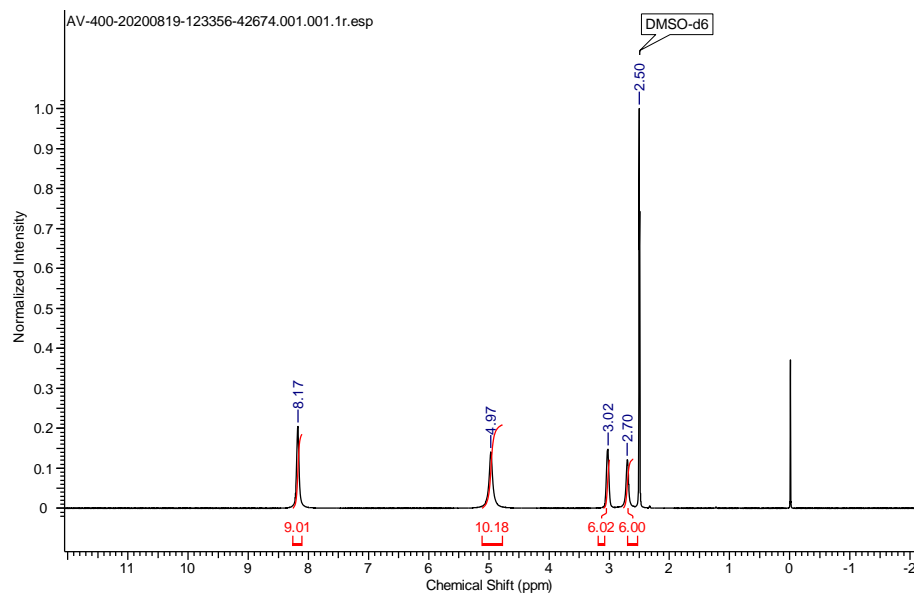


Figure 23 (b). ^1H NMR of 1 Tris Sb Green (400 MHz, DMSO- d_6 , 298 K): δ 8.17 (br, 9H, NH_3), 3.02 (br, 6H, CH_2), 2.70 (br, 6H, CH_2), 4.97 (br, 9H, H_2O & 1H, NH) ppm.

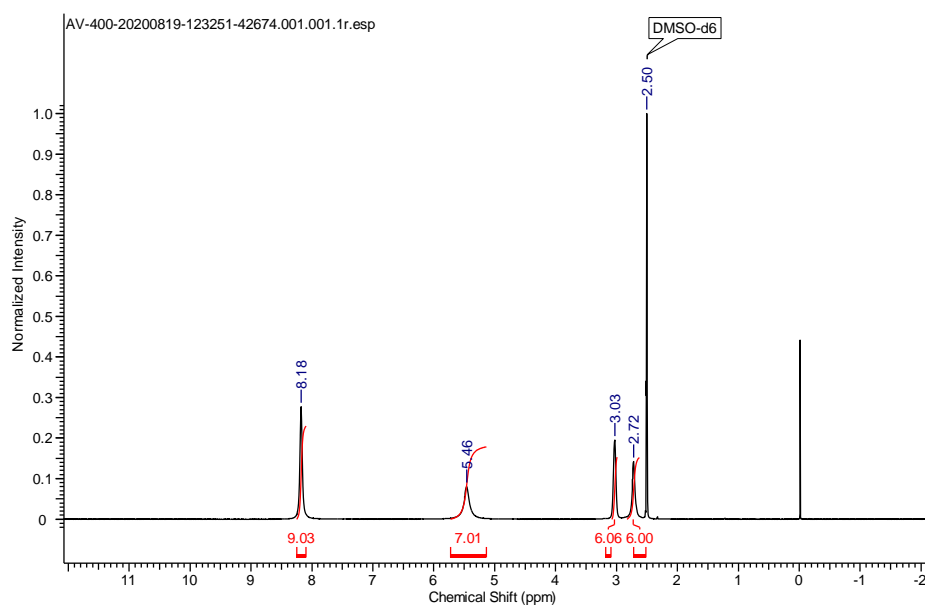


Figure 23 (c). ^1H NMR of 1 Tris Sb Red (400 MHz, DMSO- d_6 , 298 K): δ 8.18 (br, 9H, NH_3), 3.03 (br, 6H, CH_2), 2.72 (br, 6H, CH_2), 5.46 (br, 6H, H_2O & 1H, NH) ppm.

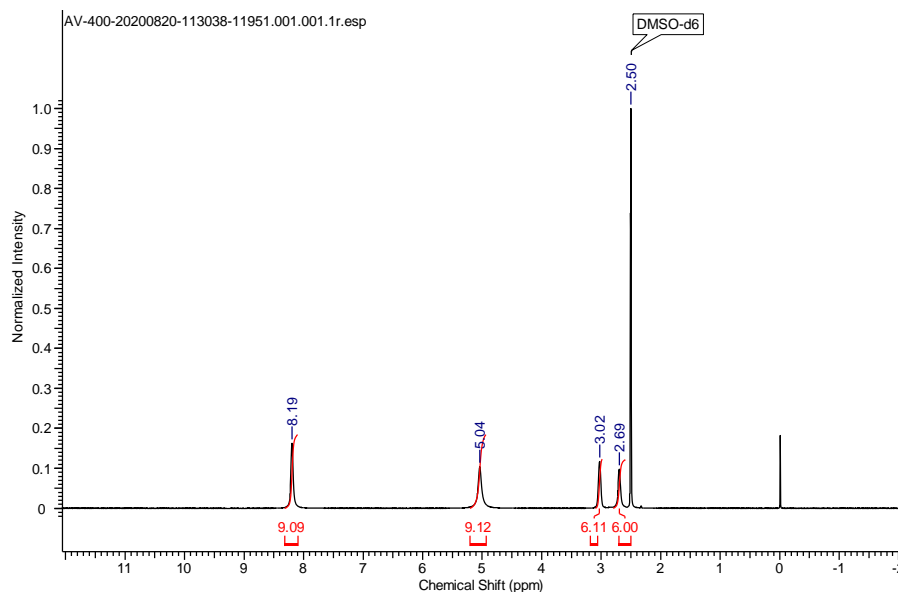


Figure 23 (d). ^1H NMR of 1 Tris Sb Yellow (400 MHz, DMSO- d_6 , 298 K): δ 8.19 (br, 9H, NH_3), 3.02 (br, 6H, CH_2), 2.69 (br, 6H, CH_2), 5.04 (br, 8H, H_2O & 1H, NH) ppm.

4.6 Conclusions:

In summary, the chapter demonstrates metal halide structural tunability (SbX_6 octahedron, SbX_5 quadrangular pyramidal, combination thereof) through synthesis of different Sb(III) chloride 0D hybrids (1, 2, 3) utilizing a common organic ligand [tris(2-aminoethyl)amine]. Crystal structure analysis reveals that the metal halide unit structure in product: i) 1 is octahedral, ii) 2 is quadrangular pyramidal, and iii) 3 is a combination of octahedra and quadrangular pyramidal. Further, structure analysis reveals that the extent of distortion of the metal halide units in these products follows: $1 \sim 3 \ll 2$. The emissive properties of these products that need rational understanding include Stokes shifted broadband visible emission with distinctly different PL emission energies (λ_{em}) and markedly different PLQY- 1: $\lambda_{\text{em}} = 517$ nm, Stokes Shift = 165 nm, PLQY = 45%; 2: $\lambda_{\text{em}} = 638$ nm, Stokes Shift = 290 nm, PLQY = 6%; 3: $\lambda_{\text{em}} = 590$ nm, Stokes Shift = 200 nm, PLQY = 43%. A structure-property correlation analysis executed here provides us with the following deeper understanding on the origins of the above emissive properties: i) qualitative molecular orbital scheme on metal halide bonding (with asymmetric metal halide coordination environment) allows rationalizing the observed PL emission energies based on the ground state structure (octahedral vs. pyramidal) of 1, 2, 3; ii) structural reorganization that

accompanies while transiting from the distorted ground state to symmetric excited 3P_1 state of Sb^{3+} ion accounts for the large Stokes shifts in the order $1 \sim 3 < 2$; iii) extent of ground-state structural distortion ($1 \sim 3 \ll 2$) is well-correlated to the PLQY ($1 \sim 3 \gg 2$). The lower (higher) extent of ground-state structural distortion would minimize (maximize) the non-radiative loss of the excitation energy in the process of excited state reorganization into a symmetric structure, thereby enhancing (suppressing) the possibility of stronger luminescence. This report demonstrates the structural tunability of the metal halide units (octahedral, pyramidal). It highlights the importance of ground-state structure/extent of distortions in affecting PL emission energies, Stokes Shifts, and PLQY for 0D antimony chloride hybrids incorporating common organic ligand.

4.7 References:

- (1) Cui, B.-B.; Han, Y.; Huang, B.; Zhao, Y.; Wu, X.; Liu, L.; Cao, G.; Du, Q.; Liu, N.; Zou, W.; Sun, M.; Wang, L.; Liu, X.; Wang, J.; Zhou, H.; Chen, Q., Locally collective hydrogen bonding isolates lead octahedra for white emission improvement. *Nat. Commun.* **2019**, *10*, 1-8.
- (2) Gautier, R.; Massuyeau, F.; Galnon, G.; Paris, M., Lead Halide Post-Perovskite-Type Chains for High-Efficiency White-Light Emission. *Adv. Mater.* **2019**, *31*, 1807383.
- (3) Lin, H.; Zhou, C.; Tian, Y.; Siegrist, T.; Ma, B., Low-dimensional organometal halide perovskites. *ACS Energy Lett.* **2017**, *3*, 54-62.
- (4) Saidaminov, M. I.; Mohammed, O. F.; Bakr, O. M., Low-Dimensional-Networked Metal Halide Perovskites: The Next Big Thing. *ACS Energy Lett.* **2017**, *2*, 889-896.
- (5) Tsai, H.; Nie, W.; Blancon, J.-C.; Stoumpos, C. C.; Asadpour, R.; Harutyunyan, B.; Neukirch, A. J.; Verduzco, R.; Crochet, J. J.; Tretiak, S.; Pedesseau, L.; Even, J.; Alam, M. A.; Gupta, G.; Lou, J.; Ajayan, P. M.; Bedzyk, M. J.; Kanatzidis, M. G.; Mohite, A. D., High-efficiency two-dimensional Ruddlesden–Popper perovskite solar cells. *Nature* **2016**, *536*, 312-316.
- (6) Zhou, C.; Lin, H.; Lee, S.; Chaaban, M.; Ma, B., Organic–inorganic metal halide hybrids beyond perovskites. *Mater. Res. Lett.* **2018**, *6*, 552-569.
- (7) Li, Z.; Li, Y.; Liang, P.; Zhou, T.; Wang, L.; Xie, R.-J., Dual-Band Luminescent Lead-Free Antimony Chloride Halides with Near-Unity Photoluminescence Quantum Efficiency. *Chem. Mater.* **2019**, *31*, 9363-9371.

- (8) Huang, K.; Rhys, A., Theory of light absorption and non-radiative transitions in F-centres. In Selected Papers Of Kun Huang: (With Commentary), *World Scientific*: **2000**, 74-92.
- (9) McCall, K. M.; Stoumpos, C. C.; Kostina, S. S.; Kanatzidis, M. G.; Wessels, B. W., Strong electron–phonon coupling and self-trapped excitons in the defect halide perovskites $A_3M_2I_9$ (A= Cs, Rb; M= Bi, Sb). *Chem. Mater.* **2017**, *29*, 4129-4145.
- (10) Smith, M. D.; Karunadasa, H., White-light emission from layered halide perovskites. *Acc. Chem. Res.* **2018**, *51*, 619-627.
- (11) Wang, X.; Meng, W.; Liao, W.; Wang, J.; Xiong, R.-G.; Yan, Y., Atomistic mechanism of broadband emission in metal halide perovskites. *J. Phys. Chem. Lett.* **2019**, *10*, 501-506.
- (12) Li, S.; Luo, J.; Liu, J.; Tang, J., Self-Trapped Excitons in All-Inorganic Halide Perovskites: Fundamentals, Status, and Potential Applications. *J. Phys. Chem. Lett.* **2019**, *10*, 1999-2007.
- (13) Shi, H.; Han, D.; Chen, S.; Du, M.-H., Impact of metal ns^2 lone pair on luminescence quantum efficiency in low-dimensional halide perovskites. *Phys. Rev. Mater.* **2019**, *3*, 034604.
- (14) Mao, L.; Guo, P.; Kepenekian, M.; Hadar, I.; Katan, C.; Even, J.; Schaller, R. D.; Stoumpos, C. C.; Kanatzidis, M. G., Structural diversity in white-light-emitting hybrid lead bromide perovskites. *J. Am. Chem. Soc.* **2018**, *140*, 13078-13088.
- (15) Biswas, A.; Bakthavatsalam, R.; Shaikh, S. R.; Shinde, A.; Lohar, A.; Jena, S.; Gonnade, R. G.; Kundu, J., Efficient Broad-Band Emission from Contorted Purely Corner-Shared One Dimensional (1D) Organic Lead Halide Perovskite. *Chem. Mater.* **2019**, *31*, 2253-2257.
- (16) Brochard-Garnier, S.; Paris, M.; Génois, R.; Han, Q.; Liu, Y.; Massuyeau, F.; Gautier, R., Screening Approach for the Discovery of New Hybrid Perovskites with Efficient Photoemission. *Adv. Funct. Mater.* **2019**, *29*, 1806728.
- (17) Cortecchia, D.; Yin, J.; Petrozza, A.; Soci, C., White light emission in low-dimensional perovskites. *J. Mater. Chem. C* **2019**, *7*, 4956-4969.
- (18) Bakthavatsalam, R.; Haris, M. P.; Shaikh, S. R.; Lohar, A.; Mohanty, A.; Moghe, D.; Sharma, S.; Biswas, C.; Raavi, S. S. K.; Gonnade, R. G.; Kundu, J., Ligand Structure Directed Dimensionality Reduction (2D→ 1D) in Lead Bromide Perovskite. *J. Phys. Chem. C* **2020**, *124*, 1888-1897.
- (19) Haris, M. P.; Bakthavatsalam, R.; Shaikh, S.; Kore, B. P.; Moghe, D.; Gonnade, R. G.; Sarma, D.; Kabra, D.; Kundu, J., Synthetic Control on Structure/Dimensionality and Photophysical

Properties of Low Dimensional Organic Lead Bromide Perovskite. *Inorg. Chem.* **2018**, *57*, 13443-13452.

(20) Fabini, D., Quantifying the Potential for Lead Pollution from Halide Perovskite Photovoltaics. *J. Phys. Chem. Lett.* **2015**, *6*, 3546-3548.

(21) Chakraborty, S.; Xie, W.; Mathews, N.; Sherburne, M.; Ahuja, R.; Asta, M.; Mhaisalkar, S. G., Rational design: a high-throughput computational screening and experimental validation methodology for lead-free and emergent hybrid perovskites. *ACS Energy Lett.* **2017**, *2*, 837-845.

(22) Slavney, A. H.; Leppert, L.; Saldivar Valdes, A.; Bartesaghi, D.; Savenije, T. J.; Neaton, J. B.; Karunadasa, H. I., Small-Band-Gap Halide Double Perovskites. *Angew. Chem. Int. Ed.* **2018**, *57*, 12765-12770.

(23) Fan, Q.; Biesold-McGee, G. V.; Ma, J.; Xu, Q.; Pan, S.; Peng, J.; Lin, Z., Lead-Free Halide Perovskite Nanocrystals: Crystal Structures, Synthesis, Stabilities, and Optical Properties. *Angew. Chem., Int. Ed.* **2020**, *59*, 1030-1046.

(24) Ganose, A. M.; Savory, C. N.; Scanlon, D. O., Beyond methylammonium lead iodide: prospects for the emergent field of ns² containing solar absorbers. *ChemComm* **2017**, *53*, 20-44.

(25) Leng, M.; Chen, Z.; Yang, Y.; Li, Z.; Zeng, K.; Li, K.; Niu, G.; He, Y.; Zhou, Q.; Tang, J., Lead-free, blue emitting bismuth halide perovskite quantum dots. *Angew. Chem. Int. Ed.* **2016**, *55*, 15012-15016.

(26) Wang, Z.-P.; Wang, J.-Y.; Li, J.-R.; Feng, M.-L.; Zou, G.-D.; Huang, X.-Y., [Bmim]₂SbCl₅: a main group metal-containing ionic liquid exhibiting tunable photoluminescence and white-light emission. *ChemComm* **2015**, *51*, 3094-3097.

(27) Zhou, C.; Lin, H.; Tian, Y.; Yuan, Z.; Clark, R.; Chen, B.; van de Burgt, L. J.; Wang, J. C.; Zhou, Y.; Hanson, K.; Meisner, Q. J.; Neu, J.; Besara, T.; Siegrist, T.; Lambers, E.; Djurovich, P.; Ma, B., Luminescent zero-dimensional organic metal halide hybrids with near-unity quantum efficiency. *Chem. Sci.* **2018**, *9*, 586-593.

(28) Zhou, C.; Worku, M.; Neu, J.; Lin, H.; Tian, Y.; Lee, S.; Zhou, Y.; Han, D.; Chen, S.; Hao, A.; Djurovich, P. I.; Siegrist, T.; Du, M.-H.; Ma, B., Facile Preparation of Light Emitting Organic Metal Halide Crystals with Near-Unity Quantum Efficiency. *Chem. Mater.* **2018**, *30*, 2374-2378.

(29) Wang, Z.; Zhang, Z.; Tao, L.; Shen, N.; Hu, B.; Gong, L.; Li, J.; Chen, X.; Huang, X.-Y. Hybrid Chloroantimonates(III): Thermally Induced Triple-Mode Reversible Luminescent

Switching and Laser-Printable Rewritable Luminescent Paper. *Angew. Chem., Int. Ed.* **2019**, *58*, 9974–9978.

(30) Chen, D.; Dai, F.; Hao, S.; Zhou, G.; Liu, Q.; Wolverton, C. M.; Zhao, J.; Xia, Z. Crystal Structure and Luminescence Properties of Lead-Free Metal Halides: $(C_6H_5CH_2NH_3)_3MBr_6$ (M = Bi and Sb). *J. Mater. Chem. C* **2020**, *8*, 7322–7329.

(31) Lin, F.; Wang, H.; Wang, L.; W.; Li, J. Zero-dimensional ionic antimony halide inorganic–organic hybrid with strong greenish yellow emission. *J. Mater. Chem. C*, **2020**, *8*, 7300-7303.

(32). Song, G.; Li, M.; Zhang, S.; Wang, N.; Gong, P.; Xia, Z.; Lin, Z. Enhancing Photoluminescence Quantum Yield in 0D Metal Halides by Introducing Water Molecules. *Adv. Funct. Mater.* **2020**, *30*, 2002468.

(33) Laurita, G.; Fabini, D. H.; Stoumpos, C. C.; Kanatzidis, M. G.; Seshadri, R., Chemical tuning of dynamic cation off-centering in the cubic phases of hybrid tin and lead halide perovskites. *Chem. Sci.* **2017**, *8*, 5628-5635.

(34) Walsh, A.; Payne, D. J.; Egdell, R. G.; Watson, G. W., Stereochemistry of post-transition metal oxides: revision of the classical lone pair model. *Chem. Soc. Rev.* **2011**, *40*, 4455-4463.

(35) Sobczyk, L.; Jakubas, R.; Zaleski, J., Self-assembly of Sb (III) and Bi (III) halo-coordinated octahedra in salts of organic cations. Structure, properties and phase transitions. *Pol. J. Chem.* **1997**, *71*, 265-300.

(36) Liu, X.; Wu, W.; Zhang, Y.; Li, Y.; Wu, H.; Fan, J., Critical Roles of High- and Low-Frequency Optical Phonons in Photodynamics of Zero-Dimensional Perovskite-like $(C_6H_{22}N_4Cl_3)SnCl_3$ Crystals. *J. Phys. Chem. Lett.* **2019**, *10*, 7586-7593.

(37). Febriansyah, B.; Borzda, T.; Cortecchia, D.; Neutzner, S.; Folpini, G.; Koh, T. M.; Li, Y.; Mathews, N.; Petrozza, A.; England, J., Metal coordination sphere deformation induced highly Stokes-shifted, ultra broadband emission in 2D hybrid lead-bromide perovskites and investigation of its origin. *Angew. Chem. Int. Ed.* **2020**, *132*, 10883-10888.

(38) Morad, V.; Yakunin, S.; Kovalenko, M., Supramolecular Approach for Fine-Tuning of the Bright Luminescence from Zero-Dimensional Antimony(III) Halides. *ACS Materials Lett.* **2020**, *2*, 845-852.

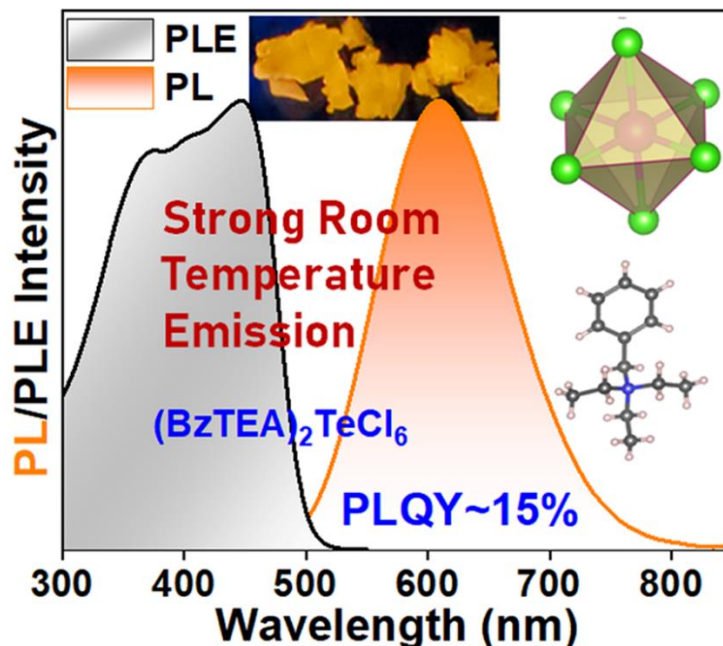
(39) Nikol, H.; Vogler, A., Photoluminescence of antimony (III) and bismuth (III) chloride complexes in solution. *J. Am. Chem. Soc.* **1991**, *113*, 8988-8990.

- (40) Thirumal, K.; Chong, W. K.; Xie, W.; Ganguly, R.; Muduli, S. K.; Sherburne, M.; Asta, M.; Mhaisalkar, S.; Sum, T. C.; Soo, H. S.; Mathews, N. Morphology-Independent Stable White-Light Emission from Self-Assembled Two-Dimensional Perovskites Driven by Strong Exciton–Phonon Coupling to the Organic Framework *Chem. Mater.* **2017**, *29*, 3947– 3953.
- (41) Yuan, Z.; Zhou, C.; Tian, Y.; Shu, Y.; Messier, J.; Wang, J. C.; Van De Burgt, L. J.; Kountouriotis, K.; Xin, Y.; Holt, E.; Schanze, K.; Clark, R.; Siegrist, T.; Ma, B., One-dimensional organic lead halide perovskites with efficient bluish white-light emission. *Nat. Commun.* **2017**, *8*, 1-7.
- (42) Zhang, B.-B.; Chen, J.-K.; Ma, J.-P.; Jia, X.-F.; Zhao, Q.; Guo, S.-Q.; Chen, Y.-M.; Liu, Q.; Kuroiwa, Y.; Moriyoshi, C.; Zhang, J.; Sun, H.-T., Antithermal Quenching of Luminescence in Zero-Dimensional Hybrid Metal Halide Solids. *J. Phys. Chem. Lett.* **2020**, *11*, 2902-2909.
- (43) Yu, J.; Kong, J.; Hao, W.; Guo, X.; He, H.; Leow, W. R.; Liu, Z.; Cai, P.; Qian, G.; Li, S.; Chen, X.; Chen, X., Broadband Extrinsic Self-Trapped Exciton Emission in Sn-Doped 2D Lead-Halide Perovskites. *Adv. Mater.* **2019**, *31*, 1806385.
- (44) Sawyer, J.F.; Gillespie, R. J.; The stereochemistry of Sb (III) halides and some related compounds . *Prog. Inorg. Chem.*, **1986**, *34*, 65–114.
- (45) Blasse, G., Luminescence of inorganic solids: from isolated centres to concentrated systems. *Prog. Solid St. Chem.* **1988**, *18*, 79-171.
- (46) Blasse, G., Luminescence of inorganic solids: trends and applications. *Rev. Inorg. Chem.* **1983**, *5*, 319-381.
- (47). Ranfagni, A.; Mugnai, D.; Bacci, M.; Viliani, G.; Fontana, M., The optical properties of thallium-like impurities in alkali-halide crystals. *Adv. Phys* **1983**, *32*, 823-905.
- (48) Bois, A. d.; Abriel, W., On the Stereochemistry of the Lone-Pair Electrons in AX₆E-Systems, IX⁺ Statically Distorted Anion in [(CH₃)₂HN(C₆H₄)NH(CH₃)₂]TeCl₆. *Z Naturforsch* **1990**, *45*, 573-578.
- (49) Ensinger, U.; Schwarz, W.; Schmidt, A., Alkylammonium-chloroantimonate (III) Struktur und Schwingungsspektren/Alkylammoniumchloroantimonates (III). Structure and Vibrational Spectra. *Z. Naturforsch. B Chem. Sci* **1983**, *38*, 149-154.
- (50) Blažič, B.; Lazarini, F., Structure of diethylammonium tetrachlorobismuthate (III). *Acta Crystallogr. C* **1985**, *41*, 1619-1621.

- (51) Mirochnik, A.; Udovenko, A.; Storozhuk, T.; Karasev, V.; Bukvetskii, B., Synthesis and luminescence of arsenic (III) and antimony (III) halide complexes with N, N'-diphenylguanidine. Crystal structures of tris (N, N'-diphenylguanidinium) hexachloro-and hexabromoarsenates (III) and-antimonates (III). *Russ. J. Coord. Chem.* **2003**, *48*, 961-971.
- (52) Sedakova, T.; Mirochnik, A.; Karasev, V., Structure and luminescence properties of antimony (III) complex compounds. *Opt Spectrosc* **2008**, *105*, 517-523.
- (53) Bely, M.; Zakharchenko, I.; Okhrimenko, B.; Skryshevsky, V., Spectra and luminescence kinetics of antimony complexes *Ukr Fiz Zh* **1980**, *25*, 1785-1788.
- (54) Petrochenkova, N.; Storozhuk, T.; Mirochnik, A.; Karasev, V., Antimony (III) complexes with quaternary ammonium bases: Synthesis, spectral, and luminescent properties. *Russ. J. Coord. Chem.* **2002**, *28*, 468-472.
- (55) Tan, Z.; Hu, M.; Niu, G.; Hu, Q.; Li, J.; Leng, M.; Gao, L.; Tang, J., Inorganic antimony halide hybrids with broad yellow emissions. *Sci. Bull.* **2019**, *64*, 904-909.
- (56) Storozhuk, T. V.; Mirochnik, A. G.; Petrochenkova, N. V.; Karasev, V. E., Sensitization of luminescence of antimony(III) in complexes with 6-methylquinoline in the spectral region of the A band. *Opt Spectrosc.* **2003**, *94*, 920-923.

Chapter 4B

Title: Luminescent 0D organic-inorganic Tellurium (IV) hybrid



4.8 Introduction:

Metal halide-organic hybrid perovskites with fascinating properties have been at the research forefront of energy related applications such as solar cells, LEDs, lasers, and photodetectors.¹⁻³ For 3D perovskites, featuring three dimensionally networked metal halide units, the photo-generated excitons are weakly bound and can diffuse in all directions within the inorganic framework with long diffusion lengths ($\sim 1 \mu\text{m}$).⁴ Organic ligand size induced dimensionality lowering (2D, 1D, 0D) restricts the exciton due to quantum and dielectric confinement with high exciton binding energies.⁵ Typically, in 0D perovskites, metal halide unit (square pyramidal, octahedral, disphenoidal) is isolated and surrounded by bulky organic ligands supporting strongly bound excitons that can relax radiatively across band edge.⁶⁻⁸ Lowered dimensionality in these materials further allows trapping of the generated excitons into the lattice sites through transient structural distortion. Such *self-trapping* of excitons⁹ is facilitated due to the soft nature of the material and strong electron-phonon coupling.¹⁰ Recombination of these self-trapped excitons (STE) lead to broad emission band with generally longer lifetimes.^{9, 11, 12} The involvement of lattice phonon modes further broadens the emission profile with an accompanying excitation energy dissipation (Stokes shift) due to the significant excited-state structural reorganization.¹³ These factors

cumulatively lead to strong, Stokes shifted, broadband emission profile in low dimensional hybrid perovskites.¹⁴ Moreover, the presence of the inorganic unit embedded within the organic ligand matrix endows environmental stability. These enabling properties have encouraged their applications in light-emitting devices, solar concentrators, and radiation detectors.¹⁴

Many low dimensional Pb(II)-halides ($6s^2$ lone pair) have been reported to show STE-based broadband white light emission properties.¹⁵ The broadband emission intensity has been correlated to the structural distortions (out of plane, in plane deformations) for the 2D Pb hybrids.¹⁵ However, no such correlation is observed to hold for 1D/0D based Pb hybrids. Nevertheless, the recent search for 'Pb free' variants has kindled immense research interest in main-group metal halides with $5s^2$ lone pairs (*viz.* Sn^{2+} , Sb^{3+}).¹⁶ Antimony (III) halide-organic 0D hybrids featuring oxidative stability, $5s^2$ electronic configuration, and isolated metal-halide units (octahedral, square pyramidal, disphenoidal, *etc.*), have been demonstrated to support efficient broadband emission with high photoluminescence quantum yield (PLQY).^{6, 7, 17-21} The broadband emission in such Sb (III) halide systems has been fully attributed to the radiative recombination of STEs originating from the excited triplet state of Sb^{3+} center ($^3\text{P}_1$) with typically longer emission lifetimes (3-10 μs).^{14, 21} There is no experimental evidence of a correlation between the structural distortions and PLQY for the 0D Sb hybrids. $5s^2$ lone pair activity-induced structure and distortion of the metal halide unit (static and/or dynamic), is *believed* to affect the luminescence properties in Sb(III) halide systems.^{14, 22} However, formulating a rational design strategy aimed to unmask the role played by Sb^{3+} $5s^2$ lone pair in shaping their luminescence properties has turned out to be challenging due to the adopted variety of isolated metal-halide unit structures (octahedral, square-pyramidal, disphenoidal). Moreover, the majority of these Sb based 0D materials lack excitation features in the visible range and necessitates them to be paired with UV LEDs (that are currently expensive and inefficient) for their application as down-conversion phosphors.¹⁴

Tellurium (IV), featuring $5s^2$ lone pair, also forms zero-dimensional hybrids with metal halide semiconducting unit dispersed in the organic ligand matrix.²³ The high charge density on Te^{4+} center supports a greater number of halide ligands and *exclusively* generates octahedral units irrespective of the counter organic cation.²⁴⁻²⁶ The most commonly adopted structure is vacancy ordered double perovskite (A_2TeX_6)^{24, 27} with almost 'regular' octahedral coordination. Given this structural simplicity (compared to Sb^{3+}), high oxidative stability, and $5s^2$ configuration (similar to Sb^{3+}) for the Te (IV) halides, it is expected that low dimensional Te(IV) halides would demonstrate

exceptional luminescence properties. The exclusive adoption of octahedral metal-halide geometry in $[\text{TeX}_6]^{2-}$ systems (unlike Sb^{3+} systems) would allow formulation of design strategy to draw any structure/distortion - PLQY correlation. Encouragingly, there have been studies on $[\text{TeX}_6]^{2-}$ hybrids that report structural²⁸⁻³² and photo-physical properties^{25, 26, 33} presenting excitation features in the visible range. Unfortunately, these $[\text{TeX}_6]^{2-}$ hybrids have not been demonstrated to be strongly emissive at room temperature as the quenching temperatures are relatively low in these compounds³⁴ and those that do emit at room temperature are very weak with low PLQYs.^{25, 26, 33} It is clear that enhancing the room temperature PLQY of $[\text{TeX}_6]^{2-}$ hybrids is of huge importance in deciphering the structure/distortion-property correlation that is currently absent for 0D metal halide hybrids (Pb, Sb, Sn). The thesis demonstrates Tellurium (IV) chloride-based zero-dimensional hybrid featuring *isolated, undistorted* $[\text{TeCl}_6]^{2-}$ *octahedral* units embedded in the organic templating ligand (benzyl triethylammonium: BzTEA) matrix that show *intrinsic, broad, yellow-orange, strong room-temperature emission* (PLQY ~ 15%) with ambient/thermal stability, and excitation feature in the visible range (445 nm) allowing for their use as potential down-conversion phosphor materials. The synthesized $(\text{BzTEA})_2\text{TeCl}_6$ product shows long-lived and broadband emission likely due to self-trapping of excitons (STEs). The emissive characteristics are observed to be independent of the particle size, surface, and other structural defects. This supports the unique and intrinsic nature of the STE-based emission. This Tellurium (IV) halide hybrid with room temperature emission and excitation band in the visible could serve as potential 'Pb-free' stable phosphor material for lighting applications as demonstrated here with a test-bed down-conversion LED architecture. Noteworthy, ambient emitting *octahedral (exclusive geometry)* $[\text{TeX}_6]^{2-}$ hybrids could further be leveraged to gain a rational understanding of structure/distortion – photophysical property correlation.

4.9 Materials:

Tellurium tetrachloride (99.99%), hydrochloric acid (37%), acetone, dimethylformamide were purchased from Sigma Aldrich. Benzyltriethylammonium Chloride (98%) was purchased from TCI Chemicals. Diethyl ether was purchased from HiMedia. All chemicals were used as purchased without further purification. For simplicity Benzyltriethylammonium Chloride is abbreviated as BzTEACl

4.10 Synthesis:

For the preparation of $(\text{BzTEA})_2\text{TeCl}_6$ crystals, 0.1 mmol (26.9 mg) of tellurium tetrachloride was dissolved in 1 mL of dimethylformamide. To this, 0.1 mmol (22.7 mg) benzyltriethylammonium chloride salt was added and dissolved. The resultant solution was used for crystallization in anti-solvent diffusion method using diethyl ether. The resulting yellow-colored crystals were filtered and washed with acetone repeatedly and dried in vacuum for further characterization. Same crystal can also be prepared using HX method wherein hydrochloric acid is used as solvent. For typical HX synthesis, 0.1 mmol (26.9 mg) of tellurium tetrachloride and 0.1 mmol (22.7 mg) benzyltriethylammonium chloride amine was dissolved in hydrochloric acid followed by heating to get a clear yellow solution followed by natural cooling to get the crystals. The crystals of the ground powders were used for further characterization.

4.11 Characterization methods:

UV-Vis Absorbance was performed in a Shimadzu UV-VIS-NIR3600Plus spectrometer. Steady State PL and lifetime was measured using an Edinburgh FS5 spectrophotometer. TGA measurements were performed using a TAG system (Mettler-Toledo, Model TGA/SDTA851e) and samples were heated in the range of 25 - 800 °C at a heating rate of 5 °C/min under nitrogen atmosphere. Absolute quantum yield measurements were carried out in a Horiba JOBIN YVON Fluoromax-4 spectrometer with a calibrated integrating sphere attachment. X-ray photoelectron spectroscopy (XPS) characterization was performed with ESCALab spectrometer having Al $K\alpha$ X-ray source ($h\nu=1486.6$ eV) operating at 150 W using a Physical Electronics 04-548 dual Mg/Al anode and in a UHV system with base pressure of $\leq 5 \times 10^{-9}$ Torr. Low temperature PL of the crystals was performed using an Edinburgh FLS1000 photoluminescence spectrometer, attached with OptistatDN cryostat and the temperature was controlled using Mercury iTC temperature controller (Oxford instruments). The sample was excited using a xenon lamp and emission was collected from 320 nm to 800 nm. Single crystals X-ray intensity data measurements of crystals were carried out on a Bruker D8 VENTURE Kappa Duo PHOTON II CPAD diffractometer. The intensity measurements were carried out with a Mo microfocus sealed tube diffraction source (Mo $K\alpha = 0.71073$ Å) at 100(2) K. The powder X-ray diffraction measurements were carried out on a Rigaku Micromax-007HF instrument (High intensity microfocus rotating anode X-ray generator)

with R-axis detector IV++ with a scanning rate of 2° $2\theta/\text{min}$ using Cu and Mo $K\alpha$ radiation. The PXRD sample was prepared by sealing 2–3 mg of finely ground powder into a Lindeman glass capillary with an inner diameter of 1 mm. Raman spectroscopic measurements were recorded at room temperature on an HR 800 Raman spectrophotometer (Jobin Yvon, Horiba, France) using monochromatic radiation (achromatic Czerny–Turner type monochromator with silver treated mirrors) emitted by a He–Ne laser (633 nm). For down-conversion LED measurements a commercially available blue LED ($\lambda_{\text{emi}}=447$ nm, FWHM=20 nm) was used. The $(\text{BzTEA})_2\text{TeCl}_6$ crystal was ground and coated on the flat surface of the commercially available blue LED for spectroscopic analysis and imaging. Further, the spectroscopic details were measured using an Edinburgh FS5 spectrophotometer and images were captured by using a digital camera (Canon PowerShot SX740 HS).

4.12 Results and Discussions:

$(\text{BzTEA})_2\text{TeCl}_6$ single crystals were synthesized by the anti-solvent diffusion method (Figure 1a). Yellow colored single crystals of $(\text{BzTEA})_2\text{TeCl}_6$ form within a day that emits intense yellow-orange light under UV illumination (Figure 1b,c).

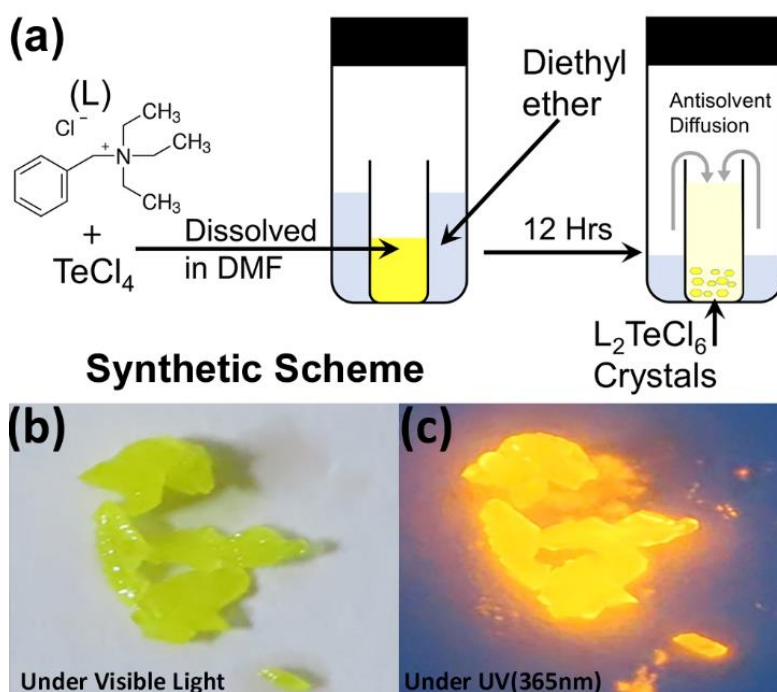


Figure 1. a) Reaction scheme (anti-solvent diffusion) utilized for the synthesis of single crystals of $(\text{BzTEA})_2\text{TeCl}_6$; photograph of the synthesized crystals at room temperature under b) visible and c) UV illumination (365nm).

4.12.A Optical property

Optical absorption characterization of the crystals (Figure 2) shows a sharply rising absorption edge (absorption onset ~ 515 nm) with absorption bands at 440 nm, 380 nm, 295 nm, and 270 nm. These absorption bands originate due to the transitions between the sp excited state and the s^2 ground state of Te(IV) center: $^1S_0 \rightarrow ^3P_1$, 3P_2 , and 1P_1 (free ion term symbols) and possibly due to ligand to metal charge transfer absorption at shorter wavelengths.¹³

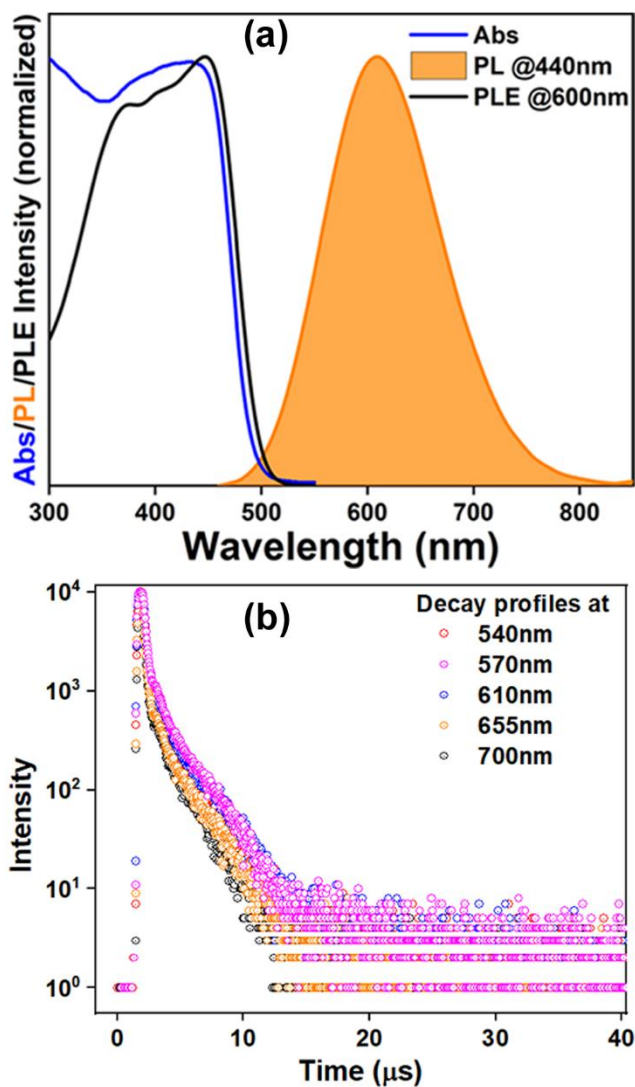


Figure 2. Optical characterization of (BzTEA)₂TeCl₆ showing a) Absorbance (Abs), Photoluminescence (PL), and Photoluminescence excitation (PLE) spectra; (b) Lifetime decay profiles collected across PL band ($\lambda_{\text{exc}}=440$ nm).

Room temperature steady-state photoluminescence (PL) characterization of the crystals (Figure 2) shows broadband (full width at half maximum: FWHM=130 nm) emission with *strong* PL peak ($\lambda_{\text{emi}}=608$ nm; $\lambda_{\text{exc}}=440$ nm). The photoluminescence excitation (PLE) spectrum of the crystals ($\lambda_{\text{emi}}=600$ nm) shows features in 300-500 nm range with a strong excitation band at 445 nm. The observed features and onset of PLE match well with the absorption spectra. The estimated Stokes shift is ~160 nm that minimizes self-reabsorption losses. The room temperature photoluminescence quantum yield (PLQY) is estimated to be 15%, attesting to the observed strong visible ambient emission. Time-resolved PL measurements (μs flash lamp source) across the broadband (decay profiles: Figure 2b, extracted lifetimes, and relative weights Figure S4, SI) of the crystals demonstrate long lifetime components [$\sim 1.1 \mu\text{s}$ (44%), $\sim 9.9 \mu\text{s}$ (56%)] in line with the exciton recombination mechanism originating from the lowest triplet state ($^3\text{P}_1 \rightarrow ^1\text{S}_0$, forbidden transition). The strong spin-orbit coupling and high Te-Cl bond covalency (~80%) can allow for appreciable relaxation of the spin forbiddances leading to strong luminescence as observed here.

4.12.B Nature of emission

Given the broad nature of the observed PL emission peak of (BzTEA)₂TeCl₆ crystals, it is important to decipher if the broadened emission is due to defect emission. The PL emission profile remains unchanged across a broad excitation range of 320 – 380 nm (Figure 3).

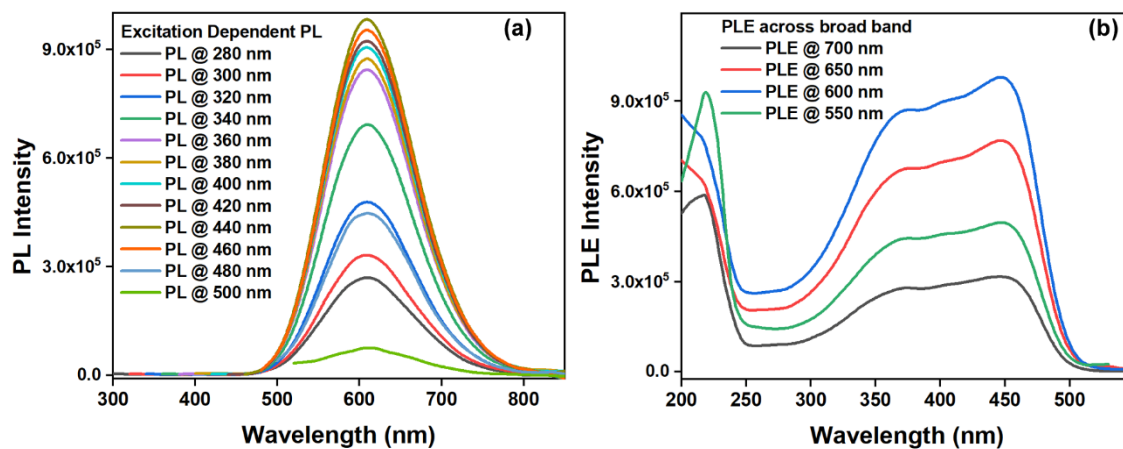


Figure 3: a) Excitation dependent a) PL and b) PLE collected across the broad emission band for $(\text{BzTEA})_2\text{TeCl}_6$ crystals.

PLE spectra collected across the broad emission band also remain unaltered. Further, PL/PLE studies were performed on ground powder samples. If defects led to broadband emission, sample grinding would cause a substantial change of the PL/PLE profile. However, no changes in the PL/PLE band profile were observed when the samples were ground (Figure 4).

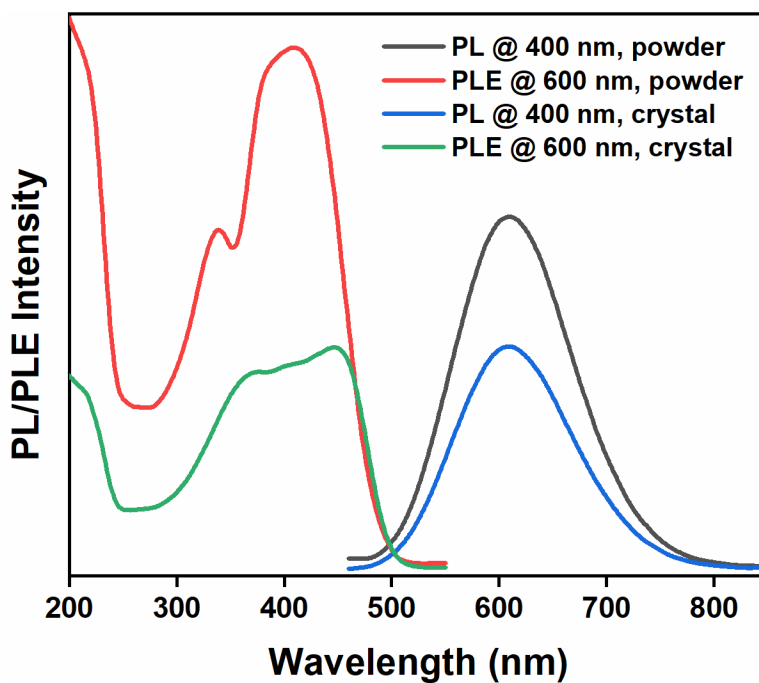


Figure 4: Comparison of the PL and PLE profile for $(\text{BzTEA})_2\text{TeCl}_6$ before and after grinding of the crystals.

Moreover, the nature of the PL/ PLE profile remains unchanged for the ground crystals when PL is collected at different excitations, and PLE is collected across the broad emission band (Figure 5).

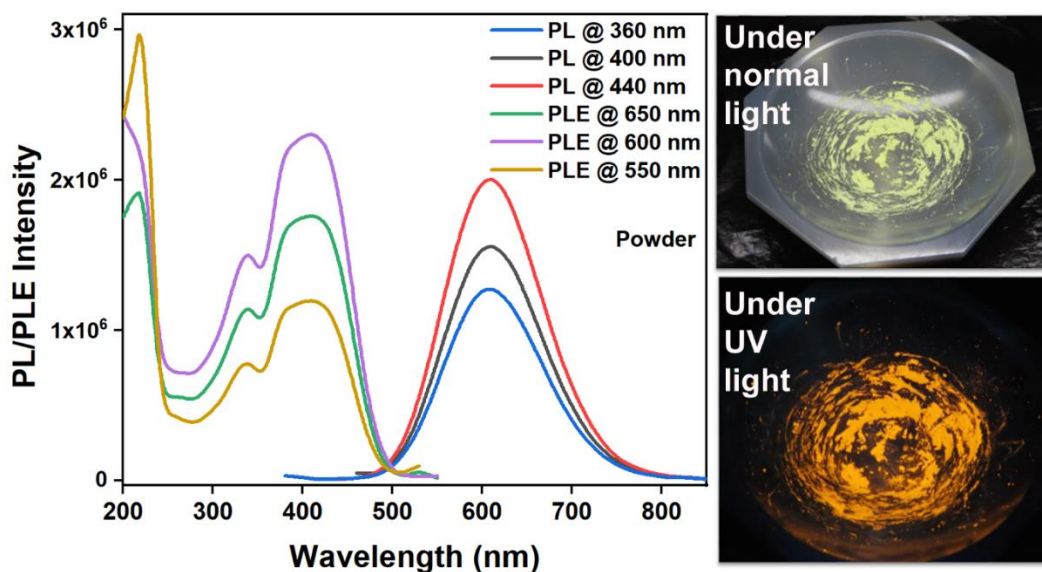


Figure 5: Comparison of the PL and PLE profile for $(\text{BzTEA})_2\text{TeCl}_6$ before and after grinding of the crystals along with their images under visible and UV light at room temperature.

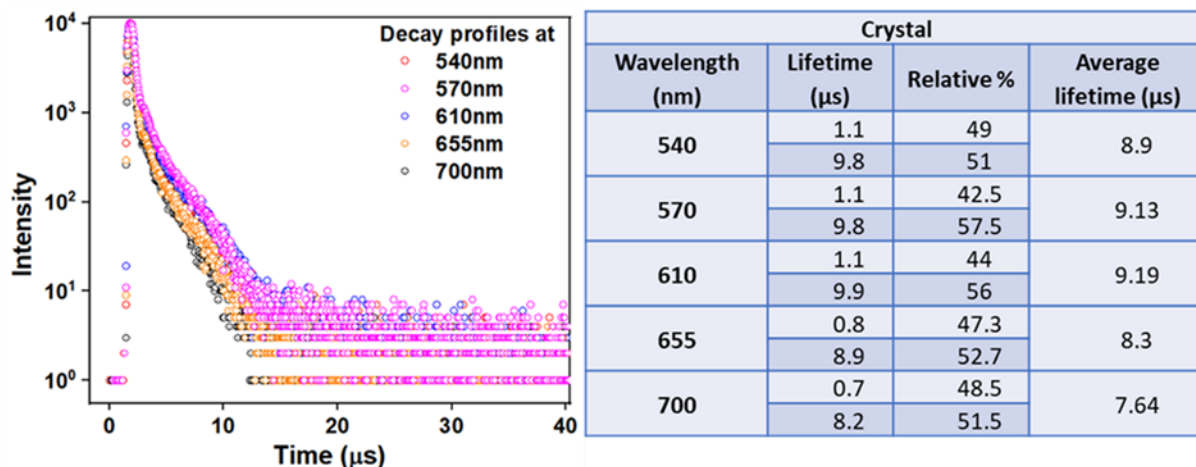


Figure 6: Decay profiles and the estimated lifetimes components along with their relative weights of $(\text{BzTEA})_2\text{TeCl}_6$ crystals excited at 440 nm.

Further, the estimated lifetime components across the broad emission band were found to remain unchanged (Figure 6). These observations suggest that unique emissive species are responsible for the broad emission and very likely do not involve extrinsic defects. Also, the crystal samples, when annealed at different temperatures, show no changes in the PL/PLE band profile (Figure 7).

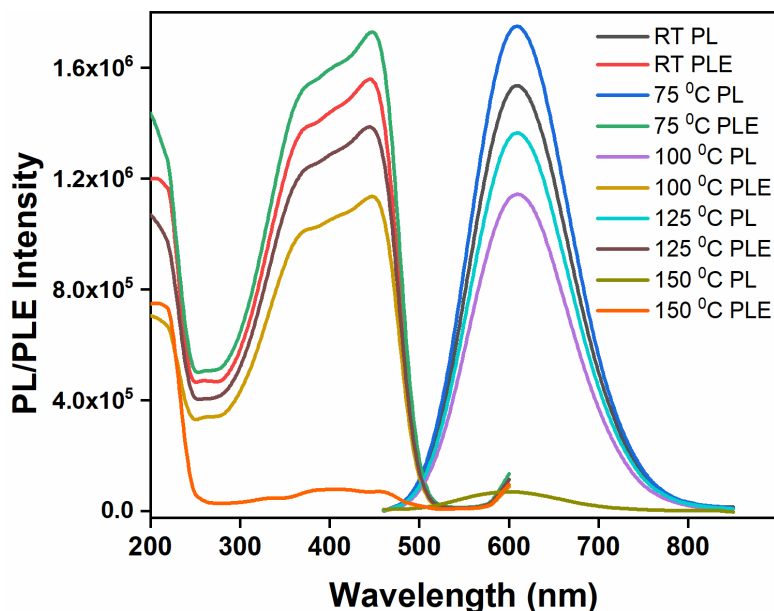


Figure 7: Effect of thermal annealing (from room temperature to 150 °C) of $(\text{BzTEA})_2\text{TeCl}_6$ crystals on the PL and PLE profiles. The excitation wavelength for PL is 445 nm, and PLE is collected at 610 nm.

These observations clearly suggest that the broad emission is not due to the presence of the defects and is due to the presence of unique emissive species that lead to intrinsic emission.

4.12.C X-ray diffraction analysis

The overview of the single crystal structure of $(\text{BzTEA})_2\text{TeCl}_6$ product (CCDC 2042525) is shown in Figure 8a. The product crystallized in monoclinic $\text{P}2_{1/n}$ space group containing one organic ligand $([\text{C}_{13}\text{H}_{22}\text{N}]^+)$ and $\frac{1}{2}$ unit of $[\text{TeCl}_6]^{2-}$ octahedron in the asymmetric unit (Figure 8)

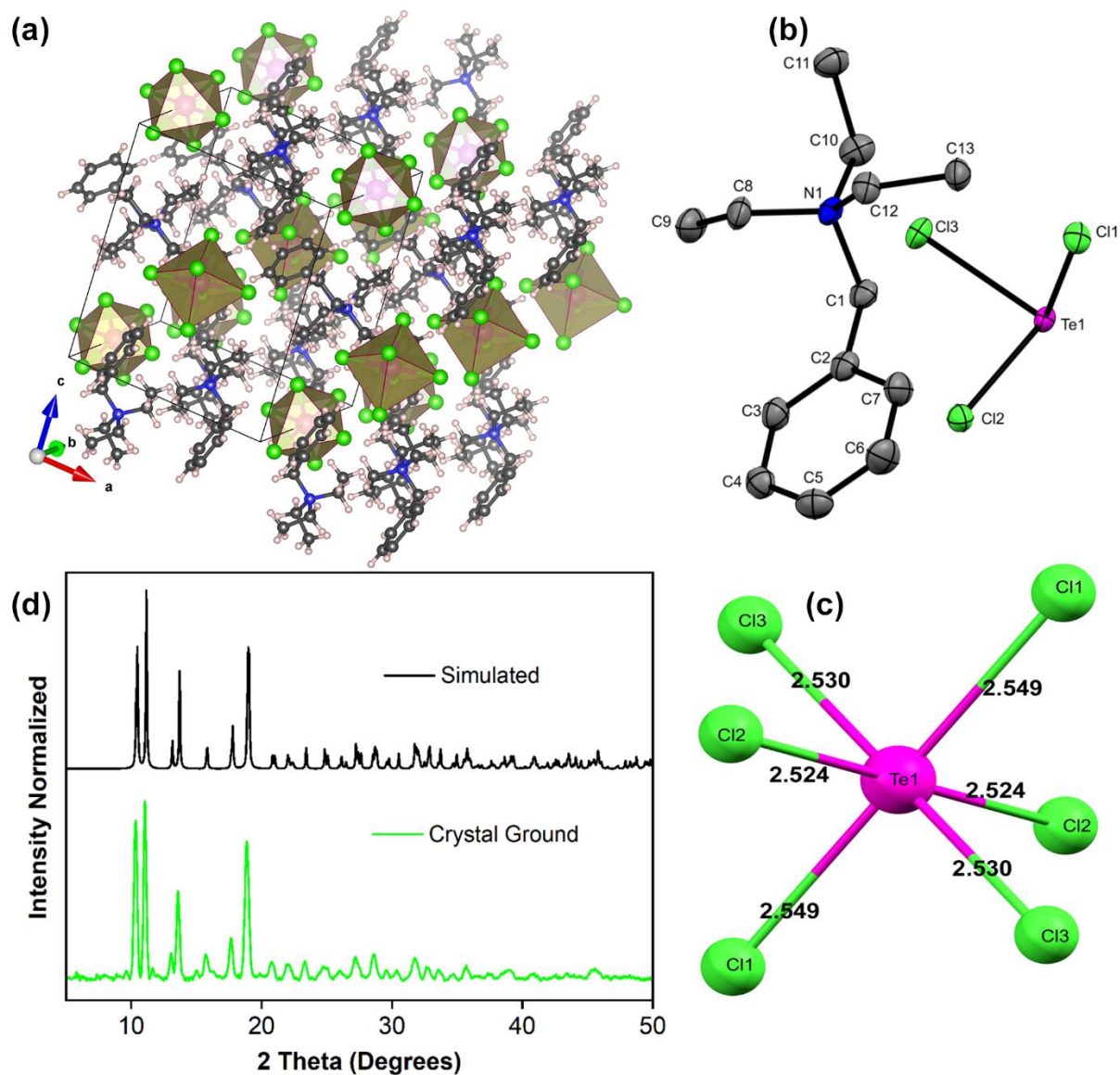
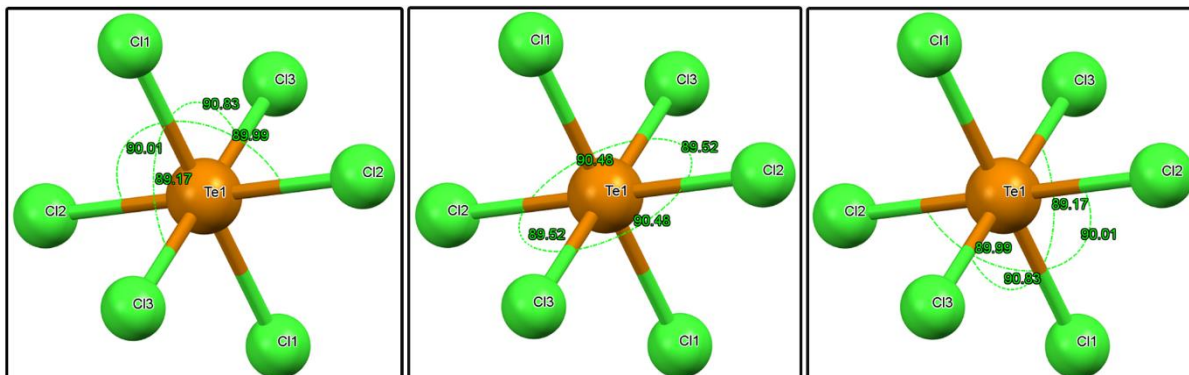


Figure 8. XRD characterization of $(\text{BzTEA})_2\text{TeCl}_6$ hybrid. Overview of the single-crystal structure (a); asymmetric unit (b); site symmetry of Metal-Halide octahedron (c); comparison of the simulated and experimental PXRD pattern using Cu source (d). H atoms are omitted in (b) for clarity.

It leads to the molecular formula of $[\text{C}_{13}\text{H}_{22}\text{N}]_2\text{TeCl}_6$. The product has isolated metal halide octahedrons periodically dispersed in the organic ligand matrix generating a zero-dimensional vacancy-ordered double perovskite structure. The inorganic unit features nearly ‘regular’ metal halide octahedron with minimal distortions (largest difference in Te-Cl bond length=0.025 Å;

largest deviation of the Cl-Te-Cl bond angle from ideal value= 0.9°; Figure 8c & 9) with quadratic elongation of 1.0001 and bond angle variance of 0.33 (degree)² attesting to the low stereochemical activity of the 5s² lone pair.



$$\lambda_{\text{oct}} = \frac{1}{6} \sum_{n=1}^6 \left[\frac{d_n - d_0}{d_0} \right]^2; \quad \sigma^2 = \frac{1}{11} \sum_{n=1}^{12} (\theta_n - 90^\circ)^2$$

Figure 9: Site symmetry of the TeCl₆ octahedron showing various bond angles. Mathematical representation of quadratic elongation (λ_{oct}) and bond angle variance (σ^2) is also shown.

A high charge on the metal center, supporting six coordination, reduces the static expression of the lone pair leading to a symmetric metal halide octahedral framework. This near-regularity of the metal halide unit leads to the observation of one broad, featureless, triplet dominated (³P_{0,1,2}) emission peak.^{13, 14} The phase purity of the product was confirmed using the powder X-ray diffraction pattern that matches well with the simulated one (Figure 8d).

4.12.D Low-temperature photoluminescence, LED measurement

The broadband emissions in low dimensional ns² metal halide hybrid materials have been attributed to the self-trapping of excitons due to strong electron-phonon coupling that produces transiently localized charges (holes/electrons) that distort the metal halide unit.¹⁴ The PL emission from these STEs is phonon assisted that broadens the radiative bandwidth.¹⁰ Upon photoexcitation, the low lying transient STE states can accept carriers from the excited ³P₁ state and allow slow, and phonon assisted radiative decay to ¹S₀ ground state, thereby broadening the emission bandwidth. Concomitantly, the carriers can undergo thermally activated non-radiative recombination that suppresses emission with a strong temperature dependence (thermal quenching

of PL due to curve crossing of excited and ground state¹⁴). Importantly, excited state reorganization in the ³P₁ state and the low-lying STE states together dictates the observed Stokes shift in the broad PL emission band.

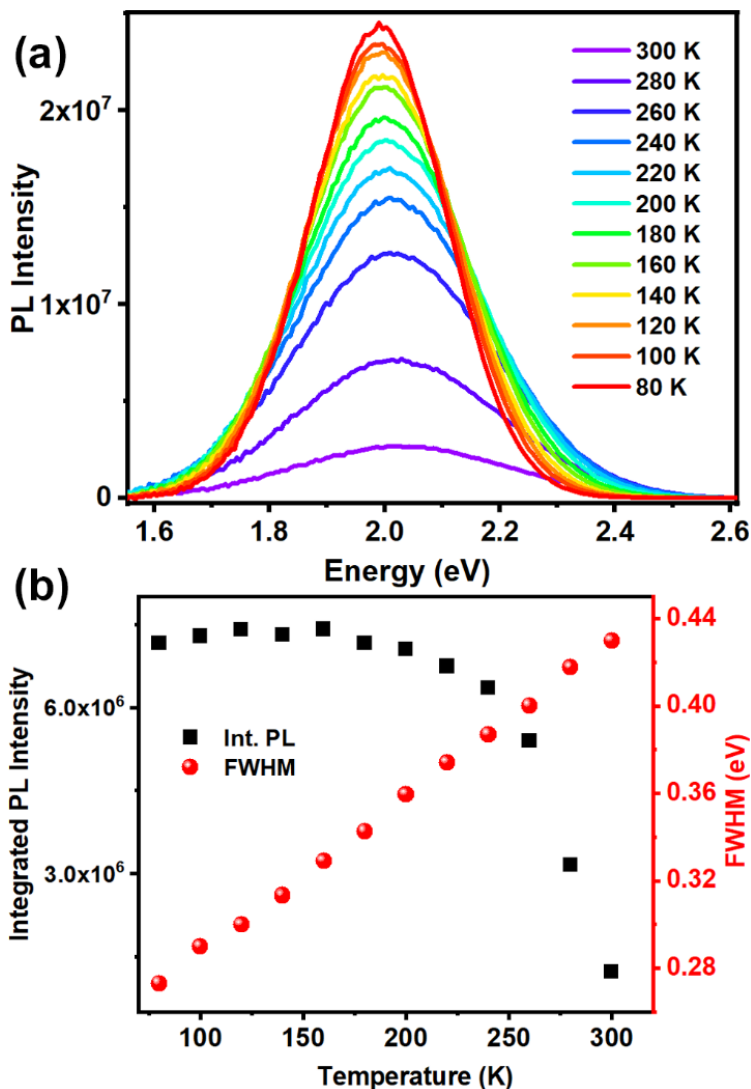


Figure 10. a) Low Temperature PL ($\lambda_{exc}=440$ nm) spectra of $(BzTEA)_2TeCl_6$ crystals; b) Integrated PL intensity and bandwidth (FWHM) as a function of temperature.

Low-temperature PL measurements were carried out to gain insight into the phonon assisted radiative recombination of STEs leading to broadband emission. Photoluminescence spectra, collected over the temperature range of 300 – 80 K (Figure 10a), show a gradual increase of the PL intensity and band narrowing as the temperature is lowered. Such changes have been generally

observed for ns² metal halide-based 0D materials.^{35, 36} Integrated PL peak area and FWHM at different temperatures is presented in Figure 10b. Observed strong PL intensity across the temperature range suggests a low activation energy downhill process of populating the low-lying STE states from the ³P₁ excited state. The decrease of the PL intensity with increase in temperature further suggests that the STE states have high self-trapping depth that allows thermally assisted de-trapping followed by fast non radiative recombination only at higher temperatures.^{8, 15, 36} Bandwidth (FWHM) of the broad emission is observed to decrease monotonically as temperature is lowered as fewer phonon modes are thermally accessible to couple to the STEs assisting radiative recombination.

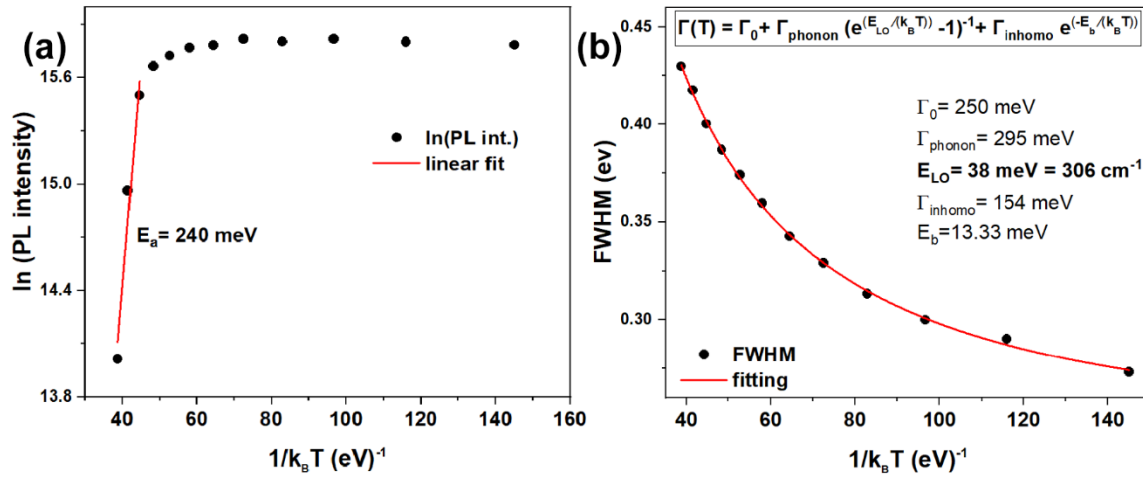


Figure 11: a) Arrhenius plot of natural logarithm of PL intensity against inverse temperature for broadband emission, b) fitting of the bandwidth (FWHM) as a function of temperature.

$$\Gamma(T) = \Gamma_0 + \Gamma_{\text{Phonon}} \left(e^{(E_{\text{LO}}/k_B T)} - 1 \right)^{-1} + \Gamma_{\text{inhomo}} e^{-E_b/k_B T}$$

This temperature dependence of FWHM (Γ) can be fitted to the following equation relating coupling of electronic excitations with the longitudinal optical lattice phonons³⁷:

where, Γ_0 =FWHM at T=0 K, Γ_{phonon} represents electron-phonon coupling and E_{LO} represents the energy of longitudinal optical phonon mode, Γ_{inhomo} represents inhomogeneous broadening while E_b is the binding energy of trapped states.

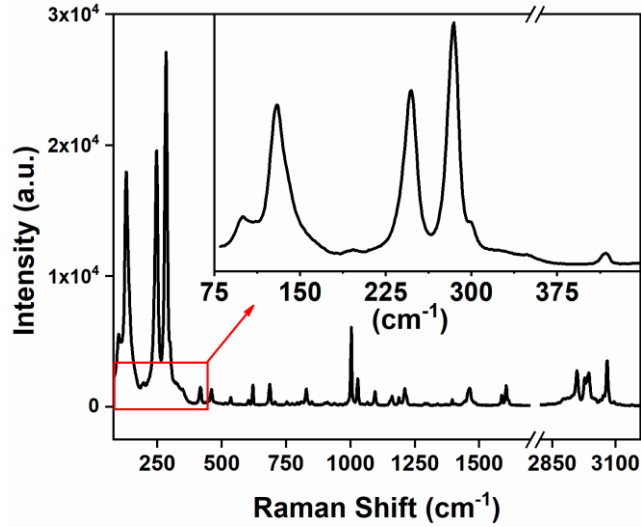


Figure 12: Raman spectra of $(\text{BzTEA})_2\text{TeCl}_6$ crystals collected using 633 nm excitation laser source. The inset shows the low-frequency phonon modes of the Te-Cl octahedron.

The fitting and its associated parameters (Figure 12) reflect strong electron-phonon coupling with $E_{L0} = 306 \text{ cm}^{-1}$, in agreement to low-frequency Raman stretching mode of Te-Cl bond^{38, 39} of inorganic metal halide framework (Figure 12). The presence of strong Te-Cl stretching Raman peaks indicates highly polarized phonon modes arising due to strong electron-phonon coupling.

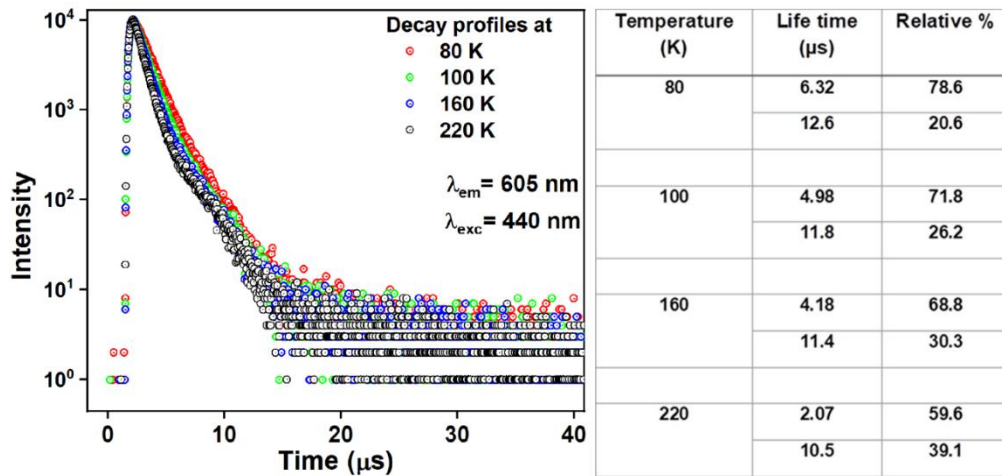


Figure 13: Lifetime decay profile of $(\text{BzTEA})_2\text{TeCl}_6$ crystals collected at low temperatures. Table lists the fitted lifetimes and their relative weights.

Time resolved PL measurements of the crystals at low temperatures (decay profiles, extracted lifetimes, and relative weights as in Figure 13 show progressive lengthening of the lifetime as temperature is lowered.

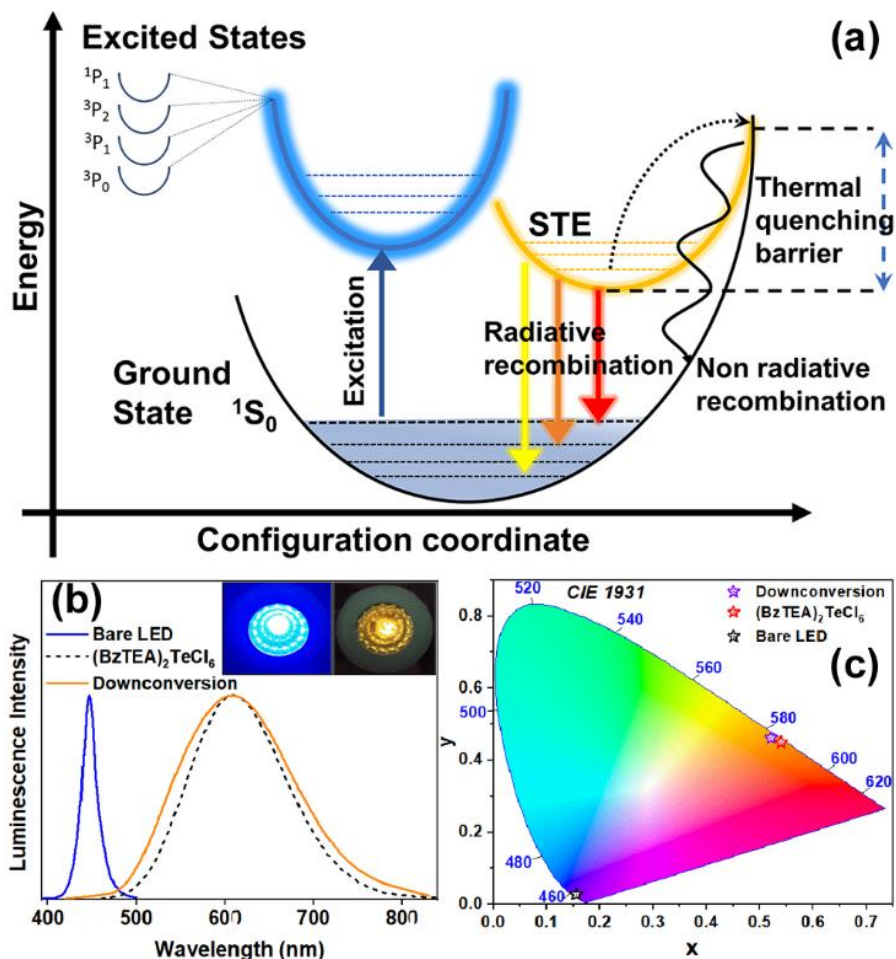


Figure 14. (a) Schematic representation of the configurational coordinate diagram showing the STE-based broadband emission and thermally activated (phonon assisted) non-radiative recombination leading to thermal PL quenching in 0D hybrids. LED characterization b) electroluminescence of commercial bare LED, down-converted luminescence from sample coated LED, and neat sample photoluminescence; Inset shows photographs of i) commercial bare LED and ii) sample coated down-conversion LED; c) CIE 1931 Chromaticity coordinate plot for commercial blue LED, down-conversion LED, and neat sample emission.

With these observations in mind, the observed photophysical properties can be rationalized in terms of a qualitative configurational coordinate diagram (Figure 14a) involving the ground state (1S_0), excited states (1P_1 , $^3P_{0,1,2}$), and the low lying self-trapped states (STEs). Following photon absorption, an electron is promoted to an excited state and, after its thermalization, is trapped in a long-lived STE state

This trapping is then followed by slow radiative recombination with broadband emission wherein the Stokes shift likely arises due to the excited state structural reorganization. A thermally activated (phonon assisted) de-trapping pathway, followed by fast non-radiative recombination process (thermal quenching due to intersection of ground and STE states), is also present and competes effectively with the radiative broadband emission at high temperatures. Clearly, the observed strong intrinsic broadband emission at room temperature (and increase of PL intensity with decreasing temperature) is due to efficient STE radiative recombination that dominates over the non-radiative, high activation energy, thermal quenching pathway. To highlight the utility of excitation features in the visible range, a proof-of-concept down-conversion LED was fabricated using a commercially available blue LED ($\lambda_{em}=447$ nm, FWHM=20 nm) as the optical source and $(BzTEA)_2TeCl_6$ hybrid as the phosphor material coated on top of the blue LED (Figure 14b, insets). Electrical biasing of the resultant LED architecture down-converts blue source light to yellow-orange phosphor light characteristic of the $(BzTEA)_2TeCl_6$ hybrid (Figure 14b). The perceived color of the light emanating from the $(BzTEA)_2TeCl_6$ hybrid, bare LED, and down-conversion LED architecture is presented in CIE 1931 chromaticity coordinate plot (Figure 14c) showing successful optical down-conversion using visible commercial LED. This, by no means, undermines the mild toxicity and rarity of elemental Tellurium for their practical applications.

4.12.E Stability & purity

To utilize the zero-dimensional $(BzTEA)_2TeCl_6$ in the practical application the stability profile was recorded. Since the structure contains organic and inorganic moiety; we would expect a step wies weight loss profile over temperature sweep. This study also provides information regarding thermal/ambient stability.

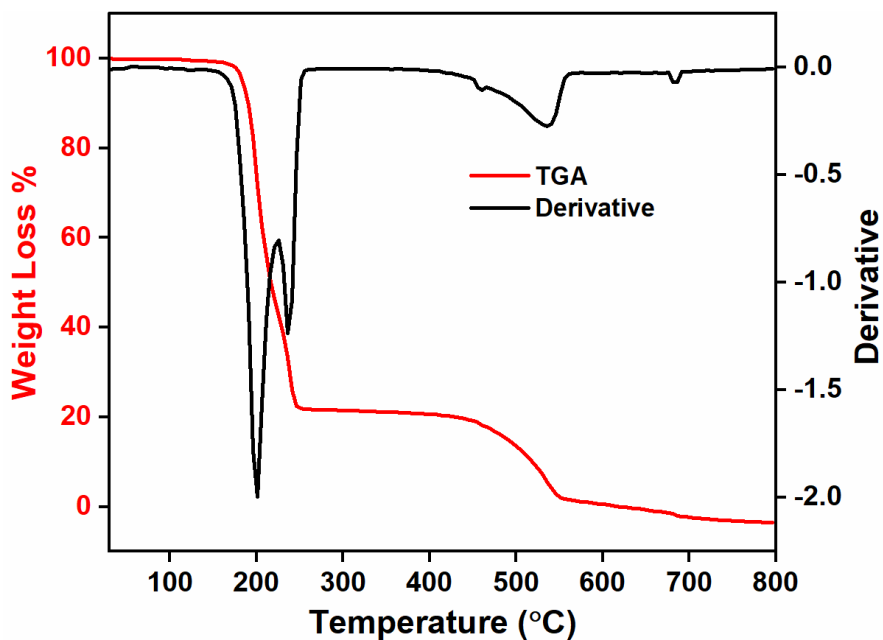


Figure 15: Thermogravimetric weight loss analysis and the derivative of the weight loss curve for $(\text{BzTEA})_2\text{TeCl}_6$ crystals.

Thermogravimetric analysis (TGA) of the product (Figure 15) demonstrates thermal stability up to 160 °C with ligand loss feature at ~200 °C and metal halide unit loss at ~500 °C.

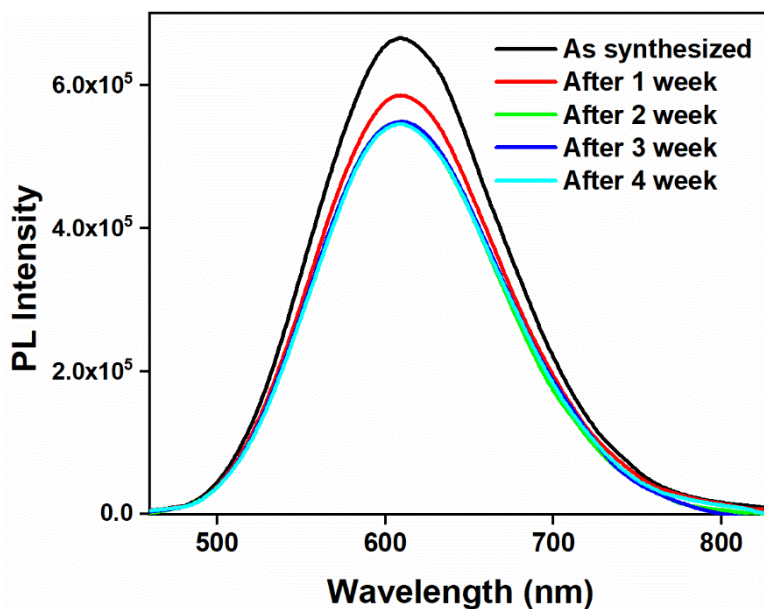


Figure 16: Comparison of PL profile collected ($\lambda_{\text{exc}}=440$ nm) over time of ambient exposed $(\text{BzTEA})_2\text{TeCl}_6$ hybrid

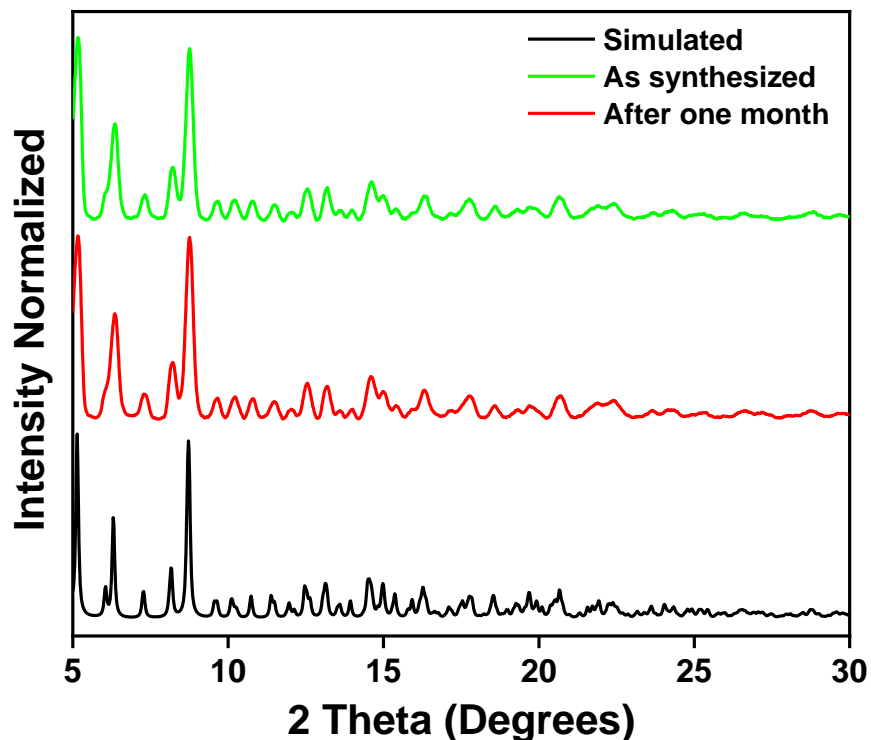


Figure 17: Comparison of PXRD pattern (using Mo source) of as-synthesized and after one-month ambient exposure of $(\text{BzTEA})_2\text{TeCl}_6$ hybrid with that of the simulated pattern (using Mo Wavelength).

The product is stable under ambient conditions over a month with a strong persistent photoluminescence (Figure 16) and no discernible changes in PXRD pattern (Figure 17).

The purity of the synthesized crystals was checked with ^1H NMR measurements (Figure 18). It was observed that all the chemical shift values match well with the number of protons in the crystal and the salt chemical composition. This also depicts the purity of the synthesized crystals.

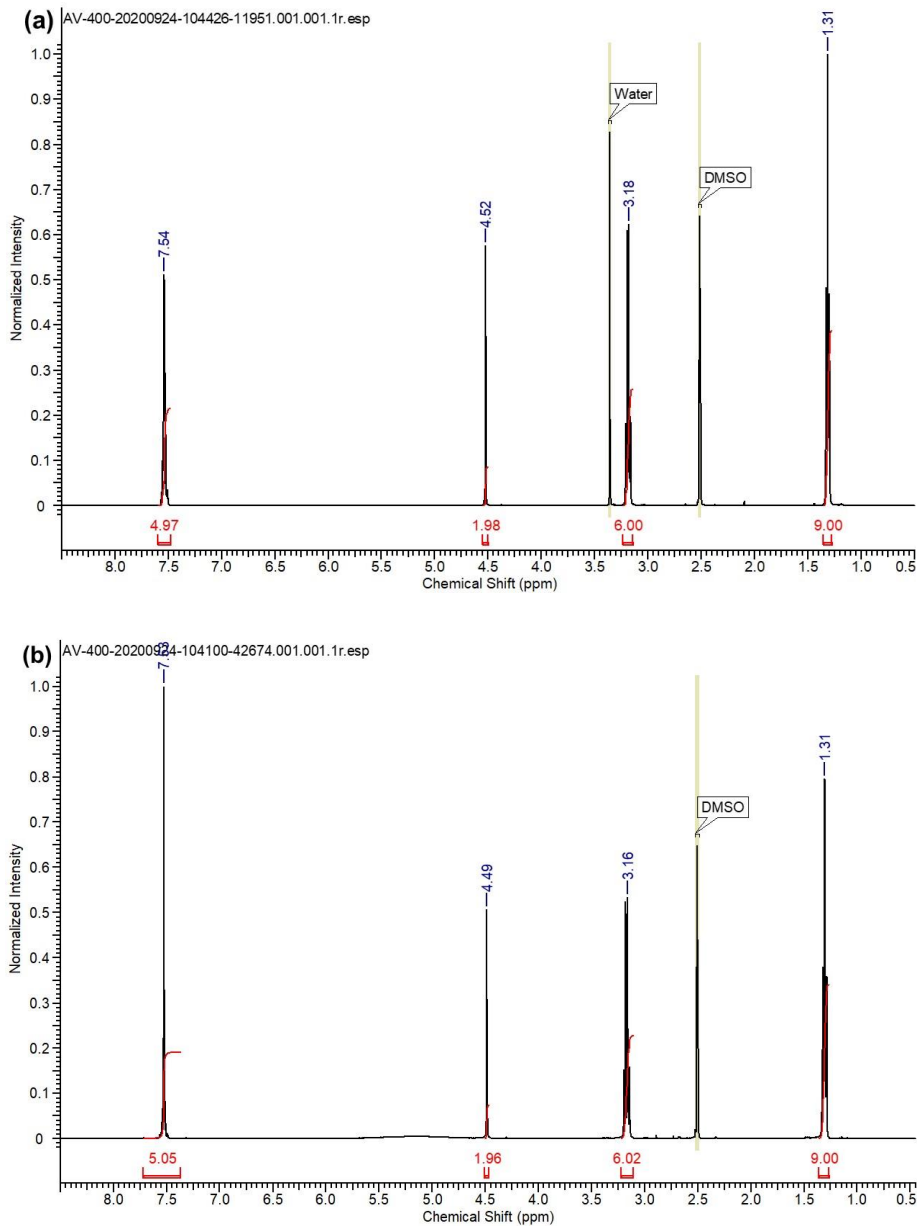


Figure 18: ^1H NMR spectra of (a) benzyl triethylammonium chloride and (b) $(\text{BzTEA})_2\text{TeCl}_6$ product in $\text{DMSO-}d_6$.

4.12.F Structure-property relation

The relevance of the current work within the premise of the burgeoning research efforts on a variety of 0D hybrids (Pb, Sn, Sb) is noted here. Synthesis of strongly emissive (at times near-unity PLQY) 0D metal halide hybrids (Sb^{3+} , Pb^{2+} , Sn^{2+}), utilizing organic counter-cationic ligands,

relies on a ‘hit-or-miss’ approach on the choice of ligand. Further, efforts on drawing any correlation between structure/distortion and PLQY for these emissive 0D hybrids (Sb, Sn) have met with limited success due to the adoption of variety of metal halide coordination geometries (octahedral, square pyramidal, disphenoidal, *etc.*) especially for Sb^{3+} 0D hybrids. This has deterred designing chemical control on PLQY for these 0D hybrids (Sb, Sn). Interestingly, Te (IV) halide hybrids, that exclusively adopt octahedral geometry irrespective of the counter cationic ligand, alleviates the above cited drawback faced by Sb(III) hybrids. Hence, $[\text{TeX}_6]^{2-}$ hybrids are apt choice for further investigation of structure/distortion-PLQY correlation studies. However, $[\text{TeX}_6]^{2-}$ hybrids typically have low PLQYs at room temperature. Encouragingly, this work demonstrates $[\text{TeX}_6]^{2-}$ a hybrid with high room temperature PLQY (~15%). By no means, the achieved PLQY for this $[\text{TeX}_6]^{2-}$ hybrid is comparable to that of Sb/Sn-based hybrids. However, the exclusivity of coordination geometry with modest ambient PLQY of $[\text{TeX}_6]^{2-}$ hybrid opens up the possibility of deciphering structure/distortion – PLQY correlation that is currently missing for the reported main group metal halide (Pb, Sb, Sn) 0D hybrids. Further work on enhancing the ambient PLQY and drawing structure-property correlation for $[\text{TeX}_6]^{2-}$ based 0D hybrids is of enormous importance and is currently underway.

4.13 Conclusions:

In conclusion, the chapter shows a successful synthesis of $(\text{BzTEA})_2\text{TeCl}_6$ zero dimensional vacancy ordered double perovskite with strong room temperature luminescence featuring octahedral Te(IV) chloride as the inorganic unit embedded in the organic ligand (benzyl triethylammonium chloride) matrix. The product shows long-lived, *intrinsic* self-trapping induced broadband, yellow-orange photoluminescence ($\lambda_{\text{emi}}=610$ nm) with high PLQY (15% at room temperature), good thermal/ambient stability, and excitation feature in the visible (~445 nm). A test-bed down-conversion LED, fabricated utilizing a *visible* commercial LED, demonstrates strong room-temperature orange down-converted emission. The exclusive adoption of ‘near’ regular octahedral structure of Te(IV)-halide unit provides a unique opportunity to unravel the role played by $5s^2$ lone pair induced distortion in shaping its luminescence properties. Further synthetic efforts on developing strongly emissive $[\text{TeX}_6]^{2-}$ hybrids utilizing a *common* templating ligand are

underway that would allow drawing discernible structure/distortion-photophysical property correlation for the 'Pb-free' 0D (Te, Sb, Sn) hybrid luminescent materials.

4.14 References:

- (1) Stoumpos, C. C.; Kanatzidis, M. G. The renaissance of halide perovskites and their evolution as emerging semiconductors, *Acc. Chem. Res.*, **2015**, *48*, 2791-2802.
- (2) Saporov, B.; Mitzi, D. B. Organic–inorganic perovskites: structural versatility for functional materials design, *Chem. Rev.*, **2016**, *116*, 4558-4596.
- (3) Stoumpos, C. C.; Malliakas, C. D.; Kanatzidis, M. G. Semiconducting tin and lead iodide perovskites with organic cations: phase transitions, high mobilities, and near-infrared photoluminescent properties, *Inorg. Chem.*, **2013**, *52*, 9019-9038.
- (4) Stranks, S. D.; Eperon, G. E.; Grancini, G.; Menelaou, C.; Alcocer, M. J. P.; Leijtens, T.; Herz, L. M.; Petrozza, A.; Snaith, H. J. Electron-hole diffusion lengths exceeding 1 micrometer in an organometal trihalide perovskite absorber *Science*, **2013**, *342*, 341-344.
- (5) Hong, X.; Ishihara, T.; Nurmikko, A. V. Dielectric Confinement Effect on Excitons in PbI₄-Based Layered Semiconductors *Phys. Rev. B: Condens. Matter Mater. Phys.* **1992**, *45*, 6961–6964.
- (6) Wang, Z. P.; Wang, J. Y.; Li, J. R.; Feng, M. L.; Zou, G. D.; Huang, X. Y. [Bmim]₂SbCl₅: a Main Group Metal-Containing Ionic Liquid Exhibiting Tunable Photoluminescence and White-Light Emission. *Chem. Commun.* **2015**, *51*, 3094– 3097.
- (7) C Zhou, C. K.; Lin, H. R.; Tian, Y.; Yuan, Z.; Clark, R.; Chen, B. H.; van de Burgt, L. J.; Wang, J. C.; Zhou, Y.; Hanson, K.; Meisner, Q. J.; Neu, J.; Besara, T.; Siegrist, T.; Lambers, E.; Djurovich, P.; Ma, B. W. Luminescent Zero-Dimensional Organic Metal Halide Hybrids with Near-Unity Quantum Efficiency. *Chem. Sci.* **2018**, *9*, 586– 593.
- (8) Benin, B. M.; Dirin, D. N.; Morad, V.; Worle, M.; Yakunin, S.; Raino, G.; Nazarenko, O.; Fischer, M.; Infante, I.; Kovalenko, M. V. Highly Emissive Self-Trapped Excitons in Fully Inorganic Zero-Dimensional Tin Halides. *Angew. Chem., Int. Ed.* **2018**, *57*, 11329– 11333
- (9) Williams, R. T.; Song, K. S. The self-trapped exciton *J. Phys. Chem. Solids*, **1990**, *51*, 679-716.

- (10) McCall, K. M.; Stoumpos, C. C.; Kostina, S. S.; Kanatzidis, M. G.; Wessels, B. W. Strong Electron–Phonon Coupling and Self-Trapped Excitons in the Defect Halide Perovskites $A_3M_2I_9$ ($A = \text{Cs, Rb}$; $M = \text{Bi, Sb}$). *Chem. Mater.* **2017**, *29*, 4129–4145.
- (11) Smith, M. D.; Jaffe, A.; Dohner, E. R.; Lindenberg, A. M. Karunadasa, H. I. Structural origins of broadband emission from layered Pb–Br hybrid perovskites, *Chem. Sci.*, **2017**, *8*, 4497–4504.
- (12) Knox, R. S. Introduction to Exciton Physics, In *Collective Excitations in Solids*, Springer, Boston, **1983**.
- (13) Vogler, A.; Nikol, H. The Structures of s^2 Metal Complexes in the Ground and sp Excited States, *Inorg. Chem.*, **1993**, *14*, 245–261.
- (14) McCall, K. M.; Morad, V.; Benin, B. M.; Kovalenko, M. V. Efficient Lone-Pair-Driven Luminescence: Structure–Property Relationships in Emissive $5s^2$ Metal Halides, *ACS Materials Lett.*, **2020**, *2*, 1218–1232.
- (15) Smith, M. D.; Karunadasa, H. I. White-Light Emission from Layered Halide Perovskites, *Acc. Chem. Res.*, **2018**, *51*, 619–627.
- (16) Xiao, Z.; Song, Z.; Yan, Y. From Lead Halide Perovskites to Lead-Free Metal Halide Perovskites and Perovskite Derivatives., *Adv. Mater.*, **2019**, *31*, 1803792.
- (17) Zhou, C.; Worku, M.; Neu, J.; Lin, H.; Tian, Y.; Lee, S.; Zhou, Y.; Han, D.; Chen, S.; Hao, A.; Djurovich, P. I.; Siegrist, T.; Du, M.-H.; Ma, B. Facile Preparation of Light Emitting Organic Metal Halide Crystals with Near-Unity Quantum Efficiency. *Chem. Mater.* **2018**, *30*, 2374–2378.
- (18) Li, Z.; Li, Y.; Liang, P.; Zhou, T.; Wang, L.; Xie, R.-J. Dual-Band Luminescent Lead-Free Antimony Chloride Halides with Near-Unity Photoluminescence Quantum Efficiency. *Chem. Mater.* **2019**, *31*, 9363–9371.
- (19) Chen, D.; Dai, F.; Hao, S.; Zhou, G.; Liu, Q.; Wolverton, C. M.; Zhao, J.; Xia, Z. Crystal Structure and Luminescence Properties of Lead-Free Metal Halides: $(\text{C}_6\text{H}_5\text{CH}_2\text{NH}_3)_3\text{MBr}_6$ ($M = \text{Bi}$ and Sb). *J. Mater. Chem. C* **2020**, *8*, 7322–7329.
- (20) Lin, F.; Wang, H.; Liu, W.; Li, J. Zero-dimensional ionic antimony halide inorganic–organic hybrid with strong greenish yellow emission, *J. Mater. Chem. C*, **2020**, *8*, 7300–7303.
- (21) Morad, V.; Yakunin, S.; Kovalenko, M. V. Supramolecular Approach for Fine-Tuning of the Bright Luminescence from Zero-Dimensional Antimony (III) Halides, *ACS Materials Lett.*, **2020**, *2*, 845–852.

- (22) Biswas, A.; Bakthavatsalam, R.; Mali, B. P.; Bahadur, V.; Biswas, C.; Raavi, S. S. K.; Gonnade, R. G.; Kundu, J. The metal halide structure and the extent of distortion control the photo-physical properties of luminescent zero dimensional organic-antimony (III) halide hybrids, *J. Mater. Chem. C*, **2021**, *9*, 348-358.
- (23) Liu, D.; Li, Q.; Zhang, Z.; Wu, K. Stable lead-free Te-based double perovskites with tunable band gaps: a first-principles study, *New J. Chem.*, **2019**, *43*, 14892-14897.
- (24) Krebs, B.; Ahlers, F.-P. Developments in Chalcogen–Halide Chemistry. *Adv. Inorg. Chem.* **1990**, *35*, 235– 317.
- (25) Sedakova, T. V.; Mirochnik, A. G.; Karasev, V. E. Structure and luminescence properties of tellurium (IV) complex compounds. *Opt. Spectrosc.* **2011**, *110*, 755 -761.
- (26) Sedakova, T. V.; Mirochnik, A. G. Luminescent and thermochromic properties of tellurium (IV) halide complexes with cesium. *Opt. Spectrosc.* **2016**, *120*, 268 -273.
- (27) Maughan, A. E.; Ganose, A. M.; Scanlon, D. O.; Neilson, R. J. Perspectives and design principles of vacancy-ordered double perovskite halide semiconductors, *Chem. Mater.*, **2019**, *31*, 1184-1195.
- (28) Kuhn, N.; Abu-Rayyan, N. A.; Eichele, K.; Piludu, C.; Steimann, M. Z. *Anorg. Allg. Chem.* **2004**, *630*, 495–497.
- (29) Ghazlen, M. H. Ben.; Bats, J. W. Bis (trimethylammonium) hexachlorotellurate (IV), *Acta Cryst.*, **1982**, *38*, 1308-1309.
- (30) Abriel, W. Symmetry rules for the stereochemistry of the lone-pair electrons in TeX_6^{2-} (X=Cl, Br, I) and the structures of 1,2-ethanediammonium hexachlorotellurate(IV) and 1,2-ethanediammonium hexachlorostannate(IV), *Acta Cryst.*, **1986**, *42*, 449-453.
- (31) Waśkowska, A.; Czapla, J. J. Z. Crystal structure of diguanidine hexachlorate tellurate (IV), *J. Alloy Compd.*, **1993**, *196*, 255-257.
- (32) Caracelli, I.; Kristallogr, Z. Crystal structure of bis(benzyltriethylammonium) hexachlorotellurate(IV), $[\text{C}_7\text{H}_7(\text{C}_2\text{H}_5)_3\text{N}]_2(\text{TeCl}_6)$, *Zeitschrift fur Kristallographie*, **2004**, *219*, 273-274.
- (33) Shen, N. N.; Cai, M. L.; Song, Y.; Wang, Z. P.; Huang, F. Q.; Li, J. R.; Huang, X. Y. Supramolecular Organization of $[\text{TeCl}_6]^{2-}$ with Ionic Liquid Cations: Studies on the Electrical Conductivity and Luminescent Properties. *Inorg. Chem.* **2018**, *57*, 5282– 5291.

- (34) Blasse, G.; Dirksen, G. J.; Abriel, W. The influence of distortion of the Te(IV) coordination octahedron on its luminescence. *Chem. Phys. Lett.* **1987**, *136*, 460–464.
- (35) Yakunin, S.; Benin, B. M.; Shynkarenko, Y.; Nazarenko, O.; Bodnarchuk, M. I.; Dirin, D. N.; Hofer, C.; Cattaneo, S.; Kovalenko, M. V. High-resolution remote thermometry and thermography using luminescent low-dimensional tin-halide perovskites. *Nat. Mater.* **2019**, *18*, 846–852.
- (36) Benin, B. M.; Dirin, D. N.; Morad, V.; Wörle, M.; Yakunin, S.; Rainò, G.; Nazarenko, O.; Fischer, M.; Infante, I.; Kovalenko, M. V. Highly Emissive Self-Trapped Excitons in Fully Inorganic Zero-Dimensional Tin Halides. *Angew. Chem., Int. Ed.* **2018**, *57*, 11329–11333.
- (37) Viswanath, A. K.; Lee, J. I.; Kim, D. C.; Lee, R. Leem, J. Y. Exciton-phonon interactions, exciton binding energy, and their importance in the realization of room-temperature semiconductor lasers based on GaN, *Phys. Rev. B: Condens. Matter Mater. Phys.* **1998**, *58*, 16333.
- (38) Ozin, G. A.; Voet, A. V., The Gas Phase Raman Spectrum and Molecular Structure of Dichlorodibromotellurium(IV) TeCl_2Br_2 . Novel Penta- and Hexa-co-ordinate Mixed Halide Anions of Tellurium (IV). Synthesis and infrared and Raman Spectra of $[\text{Et}_4\text{N}]\text{TeCl}_2\text{Br}_3$ and $[\text{Et}_4\text{N}]_2\text{TeCl}_2\text{Br}_4$, *Can. J. Chem.*, **1971**, *49*, 704-708.
- (39) Stufkens, D. J. Dynamic Jahn-Teller effect in the excited states of SeCl_6^{2-} , SeBr_6^{2-} , TeCl_6^{2-} and TeBr_6^{2-} : Interpretation of electronic absorption and Raman spectra, *Recl. Trav. Chim. Pays-Bas*, **1970**, *89*, 1185-1201.

Chapter 5

Summary and Future prospects

This thesis aims to answer the fundamental question of structure-property correlation in low dimensional halide perovskite systems both in ‘lead-based and ‘lead-free’ systems. Further tunability of optical emission was explored by introducing dopant ions in the host perovskite matrix. In Chapter 2, I have discussed the structure, connectivity, and photophysical properties of lead-based 1D perovskite in lower-dimensional halide base perovskite, the photophysical property in terms of light emission. The study here listed shows some correlation with the structural feature. As of literature, edge-sharing connectivity will play a pivotal role in high PLQY in 1D systems, and to date, all pure corner shared 1D perovskites show weak/narrow emission, making them inefficient as broadband emitters. In order to rationalize the role played by connectivity mode in dictating the PLQY of the STE emission, exploring purely corner shared and purely edge shared broad-band emitting perovskites would be immensely relevant. Our study shows that a purely corner-sharing contorted 1D chain structure exhibits strong room temperature yellowish-white emission with a high PLQY of ~9%. Their mixed halide variants demonstrate tunability in emission with varied PLQY. Our study indicates the design criteria (nature of halide, nature of ligand) and connectivity (Corner, Edge, and Face) to achieve high PLQY in 1D perovskites need further validation. So, in summary, the effect of connectivity vs. broadband self-trapped emission (STE) in low dimensional perovskite needed further investigation. In contrast, the nature of the ligand, halogen type, and structure (contorted vs. flat) together would play a decisive role in determining the PLQY of STE emission in 1D perovskites. Doping could be a potential strategy to tune the optical property, and chapter 3 discusses my dopant-induced broadband emission in 2D lead-based perovskite. Typically, manganese doping in lead-based perovskite is quite challenging because the thermodynamics of bond energies precludes successful doping as the Pb-Br bond energies are higher than the Mn-Br bond. Along with that manganese emission channel at ~590nm (4T_1 to 6A_1 transition) is forbidden and weak in nature. My study reveals that the strongly bound excitonic system can do the dopant-carrier exchange interaction and can lead to strong emissions, which are typically forbidden in nature. The 2D system is better than 3D because of its higher exciton binding energies. The barrier of bond strength, i.e., Pb-Br bond energy higher than Mn-Br bonds, can be surpassed by mechanochemical grinding of $MnBr_2$ into lead-based 2D host

perovskite matrix. As a result, the Mn-doped 2D perovskite shows enhanced energy transfer from strongly bound exciton of the host matrix to the 'd' electrons of Mn ion and results in a yellow-orange emission. The spin forbidden internal transition 4T_1 to 6A_1 is lifted by doping of heavy metal ion into the host matrix and more covalency of Mn-Br bond. As a result, in our doped system, we see the highest quantum yield of 37%. The 2D perovskite host matrix gives excellent ambient stability because of the bulky ammonium ligand. The high quantum yield of the doped system will be beneficial for color converting phosphor material and energy downshift coating for perovskite solar cells. The simplicity of the method can be utilized in large-scale production and can be effectively translated for the development of pure color phosphors. Further, the developed Mn-doped 2D perovskite is suitable for studying the exchange interaction and exploring it as a magneto-optoelectronic material.

Though the Pb-base perovskite has a tremendous success, the potential threat to nature cannot be overshadowed. Along with that, the quantum yield of these systems is low to modest in most cases. So, the alternative would be a lead-free perovskite system with appreciably high PLQY. There is quite a bit of study on the antimony-based zero-dimensional structure, and they show near-unity PLQY. Among the study, the question on structure (distortion in octahedra) vs. the optical property is mostly unanswered. In my 4th chapter, I have discussed the importance of the structure-distortion parameter in governing photophysical properties of 'Pb-free' perovskite. My study utilized a common organic ligand (electronic contribution from ligand is same throughout), metal (Sb), and halide (Cl) to demonstrate structural tunability (quadrangular pyramidal, octahedral, combination thereof) of metal halide unit in Sb (III) Cl 0D hybrids with contrasting photo-physical properties (broadband, Stokes shifted, strong/weak colored emission). By simply changing the reaction temperature and concentration of ligand, my work shows the impact on structural distortion (octahedral), ground-state structure, and consequently the emission energy correlated with the fundamental Molecular Orbital (MO) diagram and PLQY. Finding the relation between the luminescence property and structural distortion in an antimony-based system is quite challenging because it contains a huge diversity in polyhedral units ($[SbX_4]^-$, $[SbX_5]^{2-}$, $[SbX_6]^{3-}$, $[Sb_2X_9]^{3-}$). In this regard, tellurium-based perovskite would be advantageous because it primarily adopts in $[TeX_6]^{2-}$ unit (best of our knowledge). It seems tellurium halide low dimensional perovskite would be an ideal alternative to find out octahedral distortion vs luminescence property correlation. Although the major bottleneck is its PLQY which is very low in most for the reported structures

and inhibits for potential application, and also low thermal quenching (intersecting STE and ground state) barrier will lead to high non-radiative losses. To address that, I made a successful attempt to designing a high room temperature luminescence (PLQY~15%) tellurium-based zero-dimensional structure and studied ground state structure-property correlation and further work is underway. Since tellurium absorbs in the visible region (~440nm), it would be a potential alternative for visible-light-driven down conversion phosphor. Down the line, I have demonstrated the down-conversion process by coating the tellurium perovskite onto commercial blue LED.

Though there are few successes in addressing the issues, many scopes and challenges remains for low dimensional perovskite. There is no guiding principle in choosing an appropriate ligand that could give rise to high PLQY in low dimensional perovskite. We have put the 1st successful effort to have high room temperature luminescence in tellurium-based perovskite, but further synthetic efforts need to devote to developing strongly emissive $[\text{TeX}_6]^{2-}$ hybrids utilizing a common templating ligand. The structure/distortion-photophysical property correlation for the 'Pb-free' 0D (Te, Sb, Sn) hybrid luminescent materials is not fully understood. A further ambitious project will be designing luminescence 'lead-free' multi-metallic low dimensional perovskite, i.e., 2 or more metal centers in a single unit cell. This could open a new door to material design strategy and optical tunability, and I believe it would be exciting, fascinating, and challenging as well.

ABSTRACT

Name of the Student: Anupam Biswas

Faculty of Study: Chemical Science

AcSIR academic centre/CSIR Lab: CSIR-NCL, Pune

Registration No. : 10CC18A26001

Year of Submission: 2021

Name of the Supervisors:

Dr. Durba Sengupta

Dr. Janardan Kundu

Title of the thesis: Synthetic control in low dimensional 'Pb' and 'Pb-free' perovskites for rationalizing the origin of their luminescence properties

Perovskite materials has gathered a huge attention due to their enabling properties and optoelectronic applications. Perovskites in low dimension show highly tunable optical properties and this could be advantageous for light emitting devices. This thesis shows a purely corner connected 1D structure, with 9% PLQY, and further optical tuning was exhibited by changing the halide compositions. In addition, it sheds light on the importance of connectivity vs. broadband self-trapped emission and found that they were weakly correlated. In contrast, besides connectivity, factors like nature of halide, nature of the ligand, geometry (flat or contorted) will play a decisive role in directing the photoluminescence property. Apart from lead-based perovskite, this thesis explored various 'lead-free' systems, composed of antimony and tellurium. To validate the correlation of structure-property, a variety of antimony-based zero-dimensional emitting perovskite were synthesized utilizing a common organic templating ligand by varying the temperature and ligand concentration. Study indicates that the extent of distortion is well correlated with the variable PLQY, emission wavelength, and Stokes shift within the structures. This thesis also investigated a tellurium-based zero-dimensional structure, and the structure has shown a strong room temperature luminescent broadband emission with 15% PLQY. A down-conversion LED was fabricated using the tellurium-based perovskite aimed to utilize its visible light excitonic absorption at 445 nm. Doping is a well-proven strategy to tune the optical property further. Since low dimensional perovskite possesses a high exciton binding energy (>150 meV), it is suitable for a host to dopant energy transfer. This thesis shows a successful substitutional doping of Mn^{2+} ion in lead bromide-based 2D perovskite utilizing mechanochemical grinding methodology and observed $> 24\%$ PLQY across all dopant concentrations. The discussed method of doping is scalable and can be potentially applied for large-scale practical applications.

List of publication(s) in SCI Journal(s) (published & accepted) emanating from the thesis work:

1. Anupam Biswas, Rangarajan Bakthavatsalam, Vir Bahadur, Chinmoy Biswas, Bhupendra P Mali, Sai Santosh Kumar Raavi, Rajesh G Gonnade and Janardan Kundu: Lead-free Zero Dimensional Tellurium (IV) Chloride-Organic Hybrid with Strong Room Temperature Emission as Luminescent Material, *J. Mater. Chem. C*, **2021**,9, 4351-4358.
2. Anupam Biswas, Rangarajan Bakthavatsalam, Bhupendra P Mali, Vir Bahadur, Chinmoy Biswas, Sai Santosh Kumar Raavi, Rajesh G Gonnade and Janardan Kundu: The Metal Halide Structure and the Extent of Distortion Control the Photo-Physical Properties of Luminescent Zero Dimensional Organic-Antimony (iii) Halide Hybrids, *J. Mater. Chem. C*, **2021**,9, 348-358.
3. Anupam Biswas, Rangarajan Bakthavatsalam, Samir R. Shaikh, Aparna Shinde, Amruta Lohar, Satyam Jena, Rajesh G. Gonnade, and Janardan Kundu: Efficient Broad-Band Emission from Contorted Purely Corner-Shared One Dimensional (1D) Organic Lead Halide Perovskite, *Chem. Mater.*, **2019**, 31, 7, 2253–2257.
4. Anupam Biswas, Rangarajan Bakthavatsalam, Janardan Kundu: Efficient Exciton to Dopant Energy Transfer in Mn²⁺ Doped(C₄H₉NH₃)₂PbBr₄ 2D Layered Perovskites, *Chem. Mater.*, **2017**, 29, 7816-7825.

List of papers with abstract presented (oral or poster) at national or international conferences/seminars.

1. “Science day celebration 2017” held at CSIR National Chemical laboratory Pune. (Presented poster)
2. Selected and participated DST-SERB School on Advanced Functional Materials at Nano and Atomic Scale 10-28, February 2020, IIT Goa, India.

Efficient Broad-Band Emission from Contorted Purely Corner-Shared One Dimensional (1D) Organic Lead Halide Perovskite

Anupam Biswas,^{†,§} Rangarajan Bakthavatsalam,^{†,§} Samir R. Shaikh,^{†,§} Aparna Shinde,[‡] Amruta Lohar,[‡] Satyam Jena,[⊥] Rajesh G. Gonnade,^{†,§} and Janardan Kundu^{*,||}

^{||}Department of Chemistry, Indian Institute of Science Education and Research, Tirupati, Karakambadi Road, Rami Reddy Nagar, Mangalam, Tirupati, Andhra Pradesh-517507, India

[†]Physical and Materials Chemistry Division, CSIR-National Chemical Laboratory, Pune, Dr. Homi Bhabha Road, Pashan Pune, Maharashtra-411008, India

[§]Academy of Scientific and Innovative Research (AcSIR), Ghaziabad, Uttar Pradesh-201002, India

[‡]Department of Physics, Savitribai Phule Pune University, Ganeshkhind, Pune, Maharashtra-411007, India

[⊥]Department of Inorganic and Physical Chemistry, Indian Institute of Science, CV Raman Road, Bengaluru, Karnataka-560012, India

Supporting Information

Recent times have witnessed a meteoric rise of hybrid organic lead halide perovskites for their enabling properties suitable for optoelectronic applications. Their varied chemical composition, dimensionality, and phase (bulk powder/single crystals; colloidal nanoparticles; thin films) lend these materials to be highly tunable allowing their utilization for applications in solar cells and LEDs.^{1–5} Three dimensional (3D) lead halide perovskites have the general formula of APbX₃ (A = methylammonium, formamidinium, Cs⁺; X = Cl[−], Br[−], I[−]), wherein the metal halide octahedra are corner shared and interconnected in three dimensions. Low dimensional 2D perovskites have the general formula of L₂PbX₄ wherein the metal octahedra are corner shared and interconnected in two dimensions, thereby forming a layered structure separated by the bulky organic ammonium ligands (L). With further dimensionality reduction to 1D, the general formula is dictated by the connectivity mode(s) of metal halide octahedra (face shared, edge shared, corner shared, and their combinations). These low dimensional perovskites are the new frontier for materials science due to their diversity in structure and properties as governed by the underlying chemistry of their formation.^{6–8}

Generation of broad-band white-light emission at room temperature from low dimensional perovskites (2D, 1D) has been of great recent interest due to their potential applications for solid state lighting. Various contorted 2D layered perovskites were initially reported to exhibit broad-band emission^{9–11} with low/modest PLQY (<9%). For 2D perovskites, broad-band emission characteristics were correlated to distortions within the metal halide octahedra and out-of-plane lattice distortion.^{9,12} This was further correlated to generation of excited state defects that are formed due to the deformability of the lattice that acts as trap sites for the excitons.⁹ This self-trapping of excitons (STE) in the perovskite lattice is mediated through exciton–phonon coupling.^{13–15} Interestingly, this broad-band emission is not limited to 2D perovskites. Yuan et al.¹⁶ have recently reported broad-band luminescence from 1D perovskite featuring purely edge sharing metal halide octahedra with high PLQY (~20%).

Very recently, Mao et al. reported a 1D perovskite structure combining edge-and corner-sharing double chains and single corner-sharing chains that exhibits broad-band emission with modest PLQY (~12%).⁸ Exciton self-trapping becomes easier at any exciton–phonon interaction strength for low dimensional 1D systems.^{17,18} Moreover, lower dimensional structures have higher vibrational degrees of freedom and are more deformable under photoexcitation, thereby enhancing self-trapping of excitons. Clearly, 1D perovskites demonstrate stronger broad-band emission with higher PLQY than the 2D perovskites.^{8,9,16} Interestingly, within the family of a small number of reported 1D perovskites, there is a sizable difference in the reported PLQY depending upon the structure/connectivity modes of the metal halide octahedra (edge shared ~20%¹⁶ vs edge and corner shared ~12%⁸). These observations suggest that tuning the metal octahedra connectivity mode to edge sharing motif would be necessary to realize strong and efficient broad-band STE emission with high PLQY.⁸ Noteworthy here, the design criteria to achieve high PLQY for broad band STE emission in 1D perovskites is still unknown, and tunability of the connectivity mode has been suggested as design criteria that need validation. If indeed edge sharing connectivity is crucial for high PLQY in these 1D systems, then it is anticipated that many of the reported edge shared 1D perovskite that shows broad band STE emission would have high PLQY. In fact, the very few reported purely corner shared 1D perovskites, all of them show weak/narrow emission making them inefficient as broadband emitters.^{16,19} All of these observations suggest that the octahedral connectivity mode *might* affect the broad band emissive properties of these 1D materials. In order to rationalize the role played by the connectivity mode in dictating the PLQY of the STE emission, purely corner shared and purely edge shared broad-band emitting perovskites would be immensely relevant here.

Received: January 8, 2019

Revised: March 25, 2019

Published: March 26, 2019

Reported here is a new 1D perovskite, $[(\text{H}_2\text{O})-(\text{C}_6\text{H}_8\text{N}_3)_2\text{Pb}_2\text{Br}_{10}]$, further denoted as PzPbBr, with a structure composed of contorted purely corner-shared metal halide octahedra. Upon UV excitation, PzPbBr exhibits broad-band yellowish-white emission at room temperature that originates from self-trapped excitons (STE). Strikingly, the absolute PLQY for PzPbBr crystal is $\sim 9\%$ which is comparable to the best reports on STE emission in 1D systems.^{8,16} The emission profile of PzPbBr can be further tuned utilizing mixed halide variants retaining high PLQY. Observed low temperature PL properties (intensity, bandwidth) of PzPbBr can be ascribed to thermally activated trapping-detrapping of excitons between band edge and STE states and coupling of phonon modes with electronic excitation. Noteworthy observations, namely, (1) high PLQY of purely corner shared 1D structure of PzPbBr; (2) low PLQY for purely edge shared 1D 4-picolylamine based perovskite (4AMPPbBr)²⁰ estimated herein; and (3) no observable correlation of structural distortion parameters with PLQY for the reported broad emitting 1D perovskites, clearly suggest that tunability of the metal-halide octahedral connectivity mode is uncorrelated to achieving high PLQY for STE emission bands. Instead, major and systematic synthetic efforts are needed to optimize relevant parameters, viz., nature (electronic and structural) of ligands, type of halides, and structure of the perovskite (flat vs contorted), to develop design criteria to enhance broad band STE emission in low dimensional 1D perovskites.

PzPbBr is crystallized by gradual cooling of HBr solution of precursor PbBr_2 salt and 2-aminoethylpiperazine ligand heated to 180 °C (Experimental details; SI). SEM-EDS analysis confirms the presence of the constituent elements in these crystals (Figure S1a, SI). Under ambient light, the crystals have long needle shape (Figure 1a), and while under UV illumination (365 nm) they exhibit strong yellowish-white emission (Figure 1b). The optical characterization of PzPbBr, presented in Figure 1c, shows strong, Stokes shifted, and broad PL emission band peaked at 580 nm. The CIE chromaticity

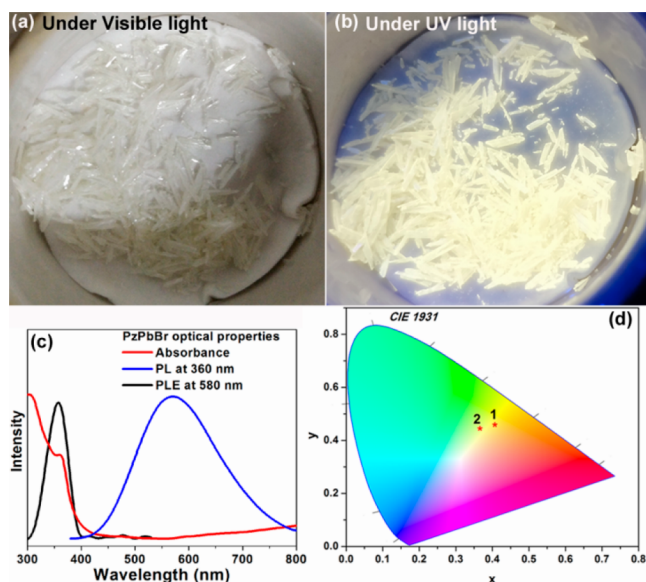


Figure 1. Photograph of single crystals of PzPbBr under (a) ambient and (b) UV light; (c) optical properties (absorbance, PL, photoluminescence excitation at 580 nm); and (d) CIE chromaticity coordinates for 1 (PzPbBr) and 2 (PzPbBr_xCl_{1-x}).

coordinate of PzPbBr is (0.41, 0.47) as highlighted by 1* in Figure 1d with CCT ~ 3759 K. The photoluminescence excitation (PLE) peak at 350 nm matches well with the absorbance measured through diffuse reflectance (Figure 1e). Figure S1b (SI) shows an unaltered emission profile when excited within the 320–380 nm range. Moreover, the PLE profile collected across the broad emission band remains unaltered (Figure S1c, SI). In addition, thermal annealing (Figure S1d, SI) shows minimal changes in the observed PL profile (intensity and shape). Furthermore, emission intensity is observed to increase with no signs of saturation as laser fluence is increased (Figure S2, SI). These observations suggest that the same type of emissive species that are intrinsically generated through band edge excitation are responsible for the broad emission.⁹ Thermal stability is assessed using thermogravimetric analysis (Figure S3a, SI). Impressively, the measured room temperature absolute PL QY for PzPbBr single crystal is $\sim 9\%$ which is comparable to the two best reports^{8,16} on 1D systems. Time resolved PL decay curves for single crystals of PzPbBr can be fitted to biexponential function with a major (96%) time component of 41 ns and a minor (4%) time component of 7 ns. These decay constants and their relative weights remain unaltered across the broad emission peak (Figure S3b; SI). The radiative decay rate is estimated to be $\sim 0.7 \times 10^7 \text{ s}^{-1}$, while the nonradiative decay rate is $\sim 2.4 \times 10^7 \text{ s}^{-1}$.

Low temperature steady state PL measurements of PzPbBr (Figure 2a,b) reveal the increase of PL intensity as temperature is lowered to 125 K. With the further temperature lowering to 40 K, PL intensity starts to decrease. Such dependence of PL intensity can be ascribed to thermally activated trapping-detrapping of excitons from STE states.⁹ However, the dependence in the low temperature regime can get complicated due to tunneling and defect bound excitons.⁹ Moreover, the phonon modes (inorganic and/or organic) that couple to electronic excitation to generate STE have their own temperature dependence.²¹ Bandwidth (fwhm) of the broad emission increases monotonically as temperature is raised. This temperature dependence of fwhm (Γ) can be fitted to the following equation relating coupling of electronic excitations with the longitudinal optical lattice phonons:²²

$$\Gamma(T) = \Gamma_0 + \Gamma_{\text{phonon}}(e^{(E_{\text{LO}}/k_{\text{B}}T)} - 1)^{-1} + \Gamma_{\text{inhomo}}e^{-E_{\text{b}}/k_{\text{B}}T}$$

where $\Gamma_0 = \text{fwhm at } T = 0 \text{ K}$, Γ_{phonon} represents electron-phonon coupling, E_{LO} represents energy of the longitudinal optical phonon mode, and Γ_{inhomo} represents inhomogeneous broadening, while E_{b} is binding energy of trapped states. The fitting and its associated parameters, as shown in Figure S4a, SI, reflects strong electron-phonon coupling with $E_{\text{LO}} = 145 \text{ cm}^{-1}$, in close agreement with the low frequency Raman stretching mode of Pb-Br bonds⁸ of inorganic metal halide framework (Figure S4b, SI). This suggests that the STE are localized on the metal halide octahedral framework in agreement with earlier reports on STE in 2D perovskites.^{9,12} In order to gain further insight into the nature of the STEs, the low temperature PL decay dynamics was analyzed. The lifetime of the broad STE emission was found to increase as the temperature is lowered from 298 to 100 K (Figure 2C; Figure S5 and Table S1, SI). This indicates thermal equilibrium between the free excitons and self-trapped excitons that governs the thermally activated trapping of free excitons in the STE states leading to the observed lengthening of the broad

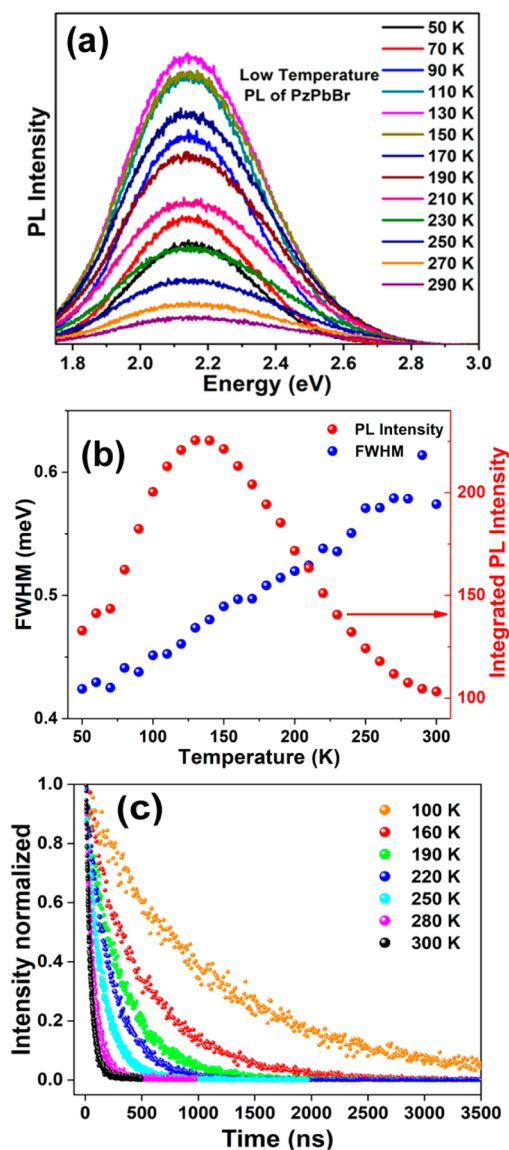


Figure 2. (a) Steady state low temperature PL of PzPbBr; (b) temperature dependence of PL intensity and bandwidth; and (c) temperature dependent lifetime of PzPbBr.

emission lifetime. Although our results herein indicate intrinsic self-trapping, further detailed experiments are needed to characterize¹⁵ the nature (extrinsic vs intrinsic) of the STE in this system.

PzPbBr crystallizes in a monoclinic crystal system with $P2_1/c$ space group (Tables S3–S5, SI; CCDC: 1875387). Structure is composed of contorted 1D chains of corner-shared metal halide octahedra surrounded by ligands (Figure 3). The asymmetric unit (Figure S6a, SI) has a $\text{Pb}_2\text{Br}_{10}$ moiety, two ligands, and one water molecule. Strong hydrogen bonding interactions of water with bromine and nitrogen leads to self-assembled 1D chain structure. The powder XRD pattern compares well with the simulated XRD pattern (Figure S6b, SI). PzPbBr crystal structure displays large octahedral distortions (Figure S6c, SI) implying a flexible structure that can support self-trapping of excitons. Distortions (quadratic elongation, bond angle variance) in $[\text{PbBr}_6]^{4-}$ octahedra, obtainable from refined crystal structure, have been previously correlated to broad-emission bandwidth for contorted 2D

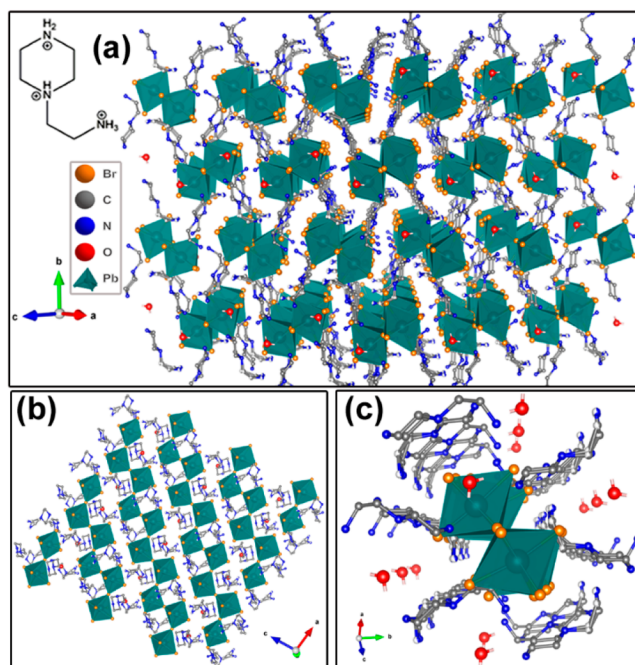


Figure 3. (a) Single crystal structure of PzPbBr with chemical formula of protonated ligand as inset; (b) top view; and (c) sliced view highlighting the 1D contorted corner-shared structure with two octahedral unit wide chains. H atoms have been omitted for clarity.

perovskites.^{9,12} However, for our 1D system we do not see any such correlation (Figure S6c, Tables S3–S5, SI). Careful examination of various other distortion parameters revealed no such correlation of the structural distortion parameters (within metal octahedra and octahedral interlinkages; see Table S2, SI) with PLQY for the reported strong broad emitting 1D perovskites.

To improve the CIE coordinates, $[(\text{H}_2\text{O})\text{Pz}_2\text{Pb}_2\text{Cl}_{10}]$ single crystals were synthesized (CCDC: 1875386 and Figure S7, Tables S6–S8, SI). The emission profile blue shifts but the PLQY is $\sim 3\text{--}4\%$ (Figure S8, SI). Further, mixed halide perovskites $[(\text{H}_2\text{O})\text{Pz}_2\text{Pb}_2\text{Br}_{10-x}\text{Cl}_x]$ with $x = 1.5\text{--}3$ were synthesized through halide substitution. The PXRD pattern changes with the increase in the chloride content (Figure S9, SI). The absorption, PLE, and PL show systematic blue-shift with increasing chloride content (Figure S10a–c; SI). Lifetime lengthening is observed for these mixed halide perovskites (Figure S10d, SI). For the $x = 2$ member of the mixed halide perovskite, the obtained CIE coordinate, as highlighted by 2* in Figure 1d, is improved to (0.37, 0.44) with high PLQY ($\sim 10\%$). This halide substitution methodology provides a strong synthetic handle to further tune the emission profile (and CIE coordinates) retaining high PLQY.

Noteworthy, both contorted 2D perovskites and 1D perovskites are reported to support broad-band STE emission.^{8,9,12,16} Clearly, dimensionality reduction (2D \rightarrow 1D) enhances broad band emission intensity.^{8,9,16} Here, we further observe that the octahedral connectivity mode and structure of the 1D chain affects the broad-band emission properties. Compared to the edge shared *flat* 1D chain system¹⁶ or edge and corner shared *flat* 1D system,⁸ purely corner shared *contorted* 1D chain structure exhibits comparable PLQY. This suggests that tuning of connectivity mode in low dimensional perovskites is not correlated to high PLQY of broad band STE emission. In fact, 4-picolyamine based lead

bromide perovskite (4AMPPbBr) with the chemical formula of $(C_6H_{10}N_2)_2PbBr_4$ is known to crystallize in a purely edge-shared 1D structure that shows weak broad band emission.²⁰ Following this reported protocol,²⁰ we have fabricated and optically characterized the 4AMPPbBr perovskite (Figure S11, SI) that shows very weak broad band emission. The estimated PLQY for this purely edge-shared perovskite is found to be $\sim 0.1\%$ for the broad emission. This again indicates that there is no observable correlation of the octahedral connectivity mode with PLQY. This is further being supported by our recent report on EDHBr based perovskite that has a corner shared 1D ribbon like structure with broad band emission PLQY of $\sim 3\%$.²³ Interestingly, as shown in the presented PzPbX perovskite case ($X = Br, Cl$), the nature of the halogen also affects the PLQY dramatically (9% for Br and 4% for Cl). Additionally, our preliminary synthetic efforts utilizing a variety of ligands show that restricting to the same 1D corner shared structure with different organic amine as the ligand drastically affects the PLQY. Hence, we strongly believe that the octahedral connectivity mode is not a key role player and it is very likely that there are many other relevant parameters (type of ligands, halides, and structure) that need to be optimized together to propose a general and rational synthetic methodology to design and fabricate low dimensional 1D perovskites with efficient broad-band STE emission. Tracing the key parameter that directs efficient, broad band STE emission in the 1D perovskites will require major and systematic synthetic efforts utilizing variety of ligands to fabricate 1D perovskites with similar structure/connectivity mode.

In conclusion, we report a new broad-band emitter, PzPbBr, with purely *corner-sharing contorted 1D* chain structure, that exhibits strong room temperature yellowish-white emission with high PLQY of $\sim 9\%$. Their mixed halide variants demonstrate tunable emission with high PLQY. Moreover, we estimated the PLQY of 4-picolylamine based purely edge shared 1D perovskite to be very low ($\sim 0.1\%$). The strong emissive properties of corner shared PzPbBr and weakly emitting properties of edge shared 4AMPPbBr perovskites highlight the fact that connectivity mode tuning is not responsible in shaping the PLQY of the broad STE emission band. We propose that nature of the ligand, halogen type, and structure (contorted vs flat) together would play a decisive role in determining the PLQY of STE emission in 1D perovskites. This implicates further experimental probing that is required by focusing efforts on synthesis of a wide range of broad emitting low dimensional perovskites utilizing a variety of ligands and halides. Toward this end, we are currently screening various ligand structures with bromide and chloride halides to fabricate lead halide based 1D broad band emissive materials.

■ ASSOCIATED CONTENT

Supporting Information

The Supporting Information is available free of charge on the ACS Publications website at DOI: 10.1021/acs.chemmater.9b00069.

Additional characterizations of compounds (PDF)

■ AUTHOR INFORMATION

Corresponding Author

*(J.K.) E-mail: janardan@iisertirupati.ac.in.

ORCID

Rangarajan Bakthavatsalam: 0000-0001-8473-8763

Rajesh G. Gonnade: 0000-0002-2841-0197

Janardan Kundu: 0000-0003-4879-0235

Notes

The authors declare no competing financial interest.

Crystallographic files for PzPbBr (CCDC: 1875387) and PzPbCl (CCDC: 1875386) through the Cambridge Crystallographic Data Centre.

■ ACKNOWLEDGMENTS

This work was financially supported by DST (Grant Nos. SB/S2/RJN-61/2013 and EMR/2014/000478) and CSIR (MLP 030326). A.B. acknowledges CSIR for Senior Research Fellowship.

■ REFERENCES

- (1) Li, W.; Wang, Z.; Deschler, F.; Gao, S.; Friend, R. H.; Cheetham, A. K. Chemically diverse and multifunctional hybrid organic-inorganic perovskites. *Nat. Rev. Mater.* **2017**, *2*, 16099.
- (2) Tan, H.; Jain, A.; Voznyy, O.; Lan, X.; García de Arquer, F. P.; Fan, J. Z.; Quintero-Bermudez, R.; Yuan, M.; Zhang, B.; Zhao, Y.; Fan, F.; Li, P.; Quan, L. N.; Zhao, Y.; Lu, Z.-H.; Yang, Z.; Hoogland, S.; Sargent, E. H. Efficient and stable solution-processed planar perovskite solar cells via contact passivation. *Science* **2017**, *355*, 722–726.
- (3) Stoumpos, C. C.; Kanatzidis, M. G. The Renaissance of Halide Perovskites and Their Evolution as Emerging Semiconductors. *Acc. Chem. Res.* **2015**, *48*, 2791–2802.
- (4) Stranks, S. D.; Snaith, H. J. Metal-halide perovskites for photovoltaic and light-emitting devices. *Nat. Nanotechnol.* **2015**, *10*, 391–402.
- (5) Wang, N.; Cheng, L.; Ge, R.; Zhang, S.; Miao, Y.; Zou, W.; Yi, C.; Sun, Y.; Cao, Y.; Yang, R.; Wei, Y.; Guo, Q.; Ke, Y.; Yu, M.; Jin, Y.; Liu, Y.; Ding, Q.; Di, D.; Xing, G.; Tian, H.; Jin, C.; Gao, F.; Friend, R. H.; Wang, J.; Huang, W.; Yang, L. Perovskite light-emitting diodes based on solution-processed self-organized multiple quantum wells. *Nat. Photonics* **2016**, *10*, 699–704.
- (6) Lin, H.; Zhou, C.; Tian, Y.; Siegrist, T.; Ma, B. Low-Dimensional Organometal Halide Perovskites. *ACS Energy Lett.* **2018**, *3*, 54–62.
- (7) Saidaminov, M. I.; Mohammed, O. F.; Bakr, O. M. Low-Dimensional-Networked Metal Halide Perovskites: The Next Big Thing. *ACS Energy Lett.* **2017**, *2*, 889–896.
- (8) Mao, L.; Guo, P.; Kepenekian, M.; Hadar, I.; Katan, C.; Even, J.; Schaller, R. D.; Stoumpos, C. C.; Kanatzidis, M. G. Structural Diversity in White-Light-Emitting Hybrid Lead Bromide Perovskites. *J. Am. Chem. Soc.* **2018**, *140*, 13078–13088.
- (9) Smith, M. D.; Karunadasa, H. I. White-Light Emission from Layered Halide Perovskites. *Acc. Chem. Res.* **2018**, *51*, 619–627.
- (10) Mao, L.; Wu, Y.; Stoumpos, C. C.; Wasielewski, M. R.; Kanatzidis, M. G. White-Light Emission and Structural Distortion in New Corrugated Two-Dimensional Lead Bromide Perovskites. *J. Am. Chem. Soc.* **2017**, *139*, 5210–5215.
- (11) Cortecchia, D.; Yin, J.; Bruno, A.; Lo, S.-Z. A.; Gurzadyan, G. G.; Mhaisalkar, S. G.; Brédas, J.-L.; Soci, C. Polaron self-localization in white-light emitting hybrid perovskites. *J. Mater. Chem. C* **2017**, *5*, 2771–2780.
- (12) Cortecchia, D.; Neutzner, S.; Srimath Kandada, A. R.; Mosconi, E.; Meggiolaro, D.; De Angelis, F.; Soci, C.; Petrozza, A. Broadband Emission in Two-Dimensional Hybrid Perovskites: The Role of Structural Deformation. *J. Am. Chem. Soc.* **2017**, *139* (1), 39–42.
- (13) McCall, K. M.; Stoumpos, C. C.; Kostina, S. S.; Kanatzidis, M. G.; Wessels, B. W. Strong Electron-Phonon Coupling and Self-Trapped Excitons in the Defect Halide Perovskites $A_3M_2I_9$ ($A = Cs, Rb; M = Bi, Sb$). *Chem. Mater.* **2017**, *29*, 4129–4145.
- (14) Zheng, W.; Huang, P.; Gong, Z.; Tu, D.; Xu, J.; Zou, Q.; Li, R.; You, W.; Bünzli, J. C. G.; Chen, X. Near-Infrared-Triggered Photon

Upconversion Tuning in All-Inorganic Cesium Lead Halide Perovskite Quantum Dots. *Nat. Commun.* **2018**, *9*, 3462.

(15) Yu, J.; Kong, J.; Hao, W.; Guo, X.; He, H.; Leow, W. R.; Liu, Z.; Cai, P.; Qian, G.; Li, S.; Chen, X.; Chen, X. Broadband Extrinsic Self-Trapped Exciton Emission in Sn-Doped 2D Lead-Halide Perovskites. *Adv. Mater.* **2018**, *31*, 1806385.

(16) Yuan, Z.; Zhou, C.; Tian, Y.; Shu, Y.; Messier, J.; Wang, J. C.; van de Burgt, L. J.; Kountouriotis, K.; Xin, Y.; Holt, E.; Schanze, K.; Clark, R.; Siegrist, T.; Ma, B. One-dimensional organic lead halide perovskites with efficient bluish white-light emission. *Nat. Commun.* **2017**, *8*, 14051.

(17) Williams, R. T.; Song, K. S. The self-trapped exciton. *J. Phys. Chem. Solids* **1990**, *51*, 679–716.

(18) Ishida, K. Self-trapping dynamics of excitons on a one-dimensional lattice. *Z. Phys. B: Condens. Matter* **1997**, *102*, 483–491.

(19) Mousdis, G. A.; Gionis, V.; Papavassiliou, G. C.; Raptopoulou, C. P.; Terzis, A. Preparation, structure and optical properties of $[\text{CH}_3\text{SC}(=\text{NH}_2)\text{NH}_2]_3\text{PbI}_5$, $[\text{CH}_3\text{SC}(=\text{NH}_2)\text{NH}_2]_4\text{Pb}_2\text{Br}_8$ and $[\text{CH}_3\text{SC}(=\text{NH}_2)\text{NH}_2]_3\text{PbCl}_5\cdot\text{CH}_3\text{SC}(=\text{NH}_2)\text{NH}_2\text{Cl}$. *J. Mater. Chem.* **1998**, *8*, 2259–2262.

(20) Li, Y.; Zheng, G.; Lin, C.; Lin, J. Synthesis, structure and optical properties of different dimensional organic-inorganic perovskites. *Solid State Sci.* **2007**, *9*, 855–861.

(21) Thirumal, K.; Chong, W. K.; Xie, W.; Ganguly, R.; Muduli, S. K.; Sherburne, M.; Asta, M.; Mhaisalkar, S.; Sum, T. C.; Soo, H. S.; Mathews, N. Morphology-Independent Stable White-Light Emission from Self-Assembled Two-Dimensional Perovskites Driven by Strong Exciton–Phonon Coupling to the Organic Framework. *Chem. Mater.* **2017**, *29*, 3947–3953.

(22) Viswanath, A. K.; Lee, J. I.; Kim, D.; Lee, C. R.; Leem, J. Y. Exciton-Phonon Interactions, Exciton Binding Energy, and Their Importance in the Realization of Room-Temperature Semiconductor Lasers Based on GaN. *Phys. Rev. B: Condens. Matter Mater. Phys.* **1998**, *58*, 16333.

(23) Haris, M. P. U.; Bakthavatsalam, R.; Shaikh, S.; Kore, B. P.; Moghe, D.; Gonnade, R. G.; Sarma, D. D.; Kabra, D.; Kundu, J. Synthetic Control on Structure/Dimensionality and Photophysical Properties of Low Dimensional Organic Lead Bromide Perovskite. *Inorg. Chem.* **2018**, *57*, 13443–13452.

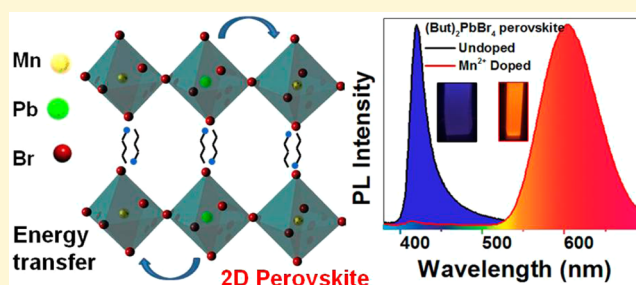
Efficient Exciton to Dopant Energy Transfer in Mn²⁺-Doped (C₄H₉NH₃)₂PbBr₄ Two-Dimensional (2D) Layered Perovskites

Anupam Biswas, Rangarajan Bakthavatsalam, and Janardan Kundu*[✉]

Physical and Materials Chemistry Division, CSIR-National Chemical Laboratory, Dr. Homi Bhabha Road, Pashan, Pune, Maharashtra India, 411008

Supporting Information

ABSTRACT: Three-dimensional ABX₃ perovskite material has attracted immense interest and applications in optoelectronic devices, because of their enabling properties. Recently, Mn²⁺ doping *directly* into APbCl₃-type three-dimensional (3D) nanocrystals, manifesting host-to-dopant energy transfer, have been reported for LED display applications. Strongly bound excitons in the doped system can enhance the dopant-carrier exchange interactions, leading to efficient energy transfer. Here, we report the simple and scalable synthesis of Mn²⁺-doped (C₄H₉NH₃)₂PbBr₄ two-dimensional (2D) layered perovskites. The Mn²⁺-doped 2D perovskite shows enhanced energy transfer efficiency from the strongly bound excitons of the host material to the *d* electrons of Mn²⁺ ions, resulting in intense orange-yellow emission, which is due to spin-forbidden internal transition (⁴T₁ → ⁶A₁) with the highest quantum yield (Mn²⁺) of 37%. Because of this high quantum yield, stability in ambient atmosphere, and simplicity and scalability of the synthetic procedure, Mn²⁺-doped 2D perovskites could be beneficial as color-converting phosphor material and as energy down-shift coating for perovskite solar cells. The newly developed Mn²⁺-doped 2D perovskites can be a suitable material to tune dopant-exciton exchange interactions to further explore their magneto-optoelectronic properties.



INTRODUCTION

Lead trihalide-based three-dimensional (3D) perovskite materials (APbX₃ with A = Cs, methylammonium; X = Cl, Br, I) have attracted phenomenal research interest, because of their intriguing applications in high-efficiency solar cells, color-tunable and narrow-line-width light-emitting diodes (LEDs), lasers, and photodetectors.^{1–7} Such materials have recorded >20% solar cell efficiency and is believed to set a new paradigm for renewable energy sources, because of their superior charge carrier mobilities and low density of midgap trap states/defect-tolerant nature.⁸ Currently, the development of 3D APbX₃-based materials for illumination and display applications, because of their enabling optical properties (tunable band edge emission, narrow line-width, high photoluminescence (PL) quantum yield, and fast radiative decay rates), is attracting active research interest.^{9–13} Very recently, many have reported on providing an additional level of control on the optoelectronic properties of these 3D perovskite materials by deliberately introducing impurity ions in the form of dopants.^{14–20} Specifically, doping Mn²⁺ ions *directly* into 3D APbCl₃ nanocrystals has had great success, with regard to unraveling interesting physical phenomena, because of the energy transfer process from the host semiconductor to dopant Mn²⁺ ions.^{14–16,18} Strong exchange interactions between the *d* electrons of Mn²⁺ and charge carriers of the host semiconductor facilitates such energy transfer. Along with the remnant band-edge photoluminescence, a new emission

channel at ~590 nm, which is typically a forbidden internal ⁴T₁-to-⁶A₁ transition of Mn²⁺ dopant, becomes active with high luminescence efficiency. Impact excitation of the impurity ion by the optically excited charge carriers of the host semiconductor activates this forbidden internal transition. Consequently, PL spectra shows emission peaks due to band edge emission and/or yellow-orange Mn²⁺ emission with different time scales of PL decay (on the scale of nanoseconds for the band edge, milliseconds for Mn²⁺ emission). Notably, APbCl₃ systems have been *directly* doped with Mn²⁺ ions successfully, while the same strategy does not seem to work for APbBr₃ systems.^{14,16,18} This has been ascribed to the higher bond strength of the Pb–Br than Mn–Br bonds. Thermodynamics of the bond energy precludes successful *direct* doping of Mn²⁺ ions at the Pb sites in case of APbBr₃ nanocrystals.¹⁴ In order to fabricate Mn²⁺-doped APbBr₃ nanocrystals, anion exchange strategy has been utilized on Mn²⁺-doped APbCl₃ nanocrystals as the starting material.^{14,16} The current research activity on 3D APbX₃-based materials (undoped and doped) has shown great potential for applications in light-emitting diodes (LEDs), sensitized solar cells, luminescent solar concentrators, biomedical imaging, and phosphorescence biosensing.^{21–24} However, the 3D APbX₃-based material typically have low exciton

Received: June 12, 2017

Revised: August 30, 2017

Published: September 11, 2017

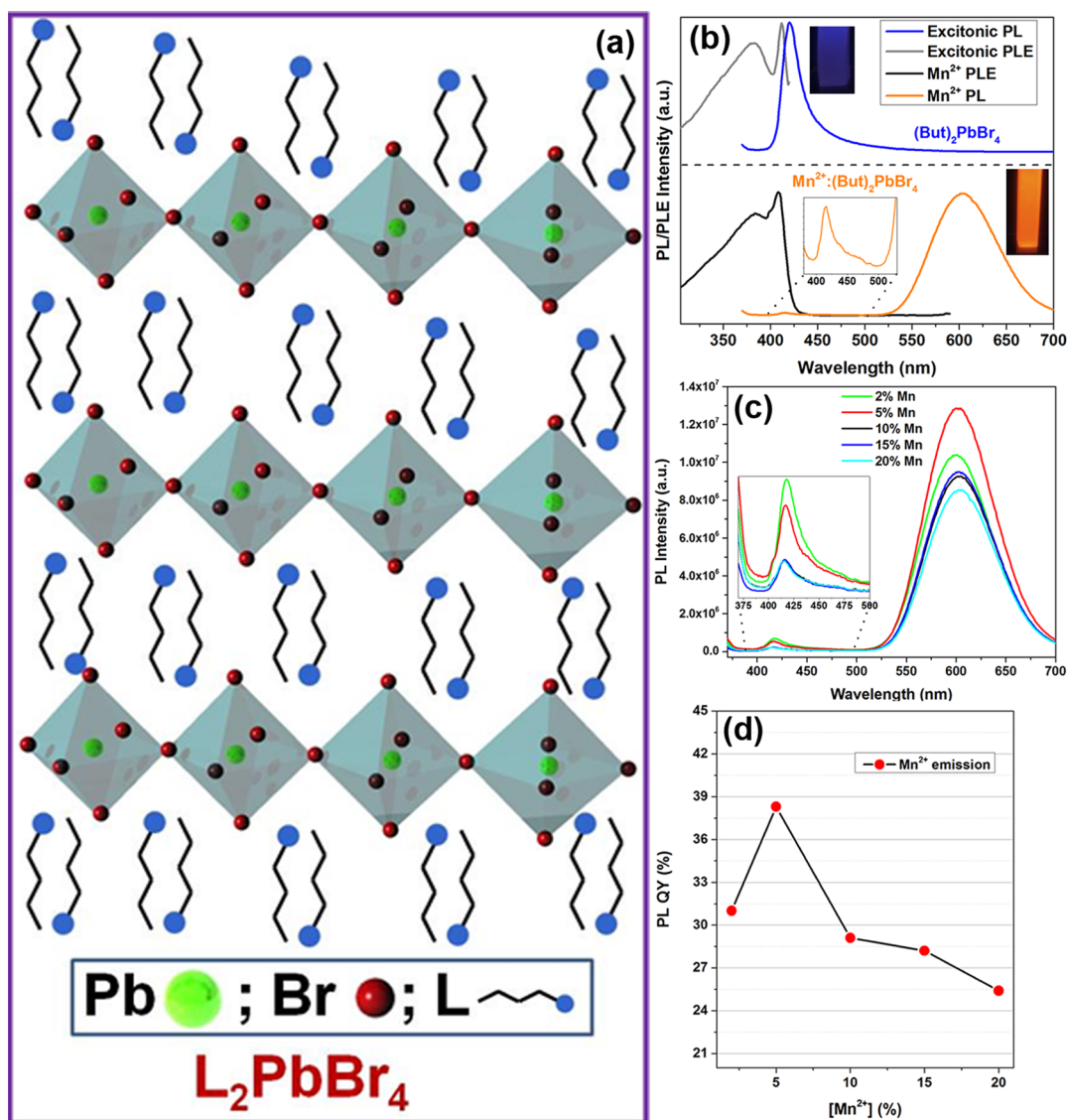


Figure 1. (a) Schematic representation of the bulk phase of $n = 1$ of $(L)_2(L')_{n-1}Pb_nX_{3n+1}$ 2D perovskite. (b) Optical properties of Mn^{2+} -doped (bottom) and undoped (top) host material showing the PL and PLE for the band edge and Mn^{2+} emission (photographs of corresponding materials under UV illumination are shown as insets). (c) Dopant input concentration-dependent PL spectra. (d) Dopant input concentration-dependent quantum yield of Mn^{2+} emission (QY_{Mn}).

binding energies.²⁵ In contrast, two-dimensional (2D) layered lead-halide-based perovskites are excellent candidates as active materials for LED applications, because of their characteristic strongly bound excitons with high binding energies, even at room temperature and fast radiative decay rates.^{25–29} Such 2D layered perovskites can be utilized as semiconductor host materials for energy transfer to appropriately chosen organic ligands as the acceptor moieties.^{27,29–32} To note, 2D layered perovskites, with the general formula $(L)_2(L')_{n-1}Pb_nX_{3n+1}$, can be thought of as being derived from 3D $APbX_3$ lattice by slicing along the $\langle 100 \rangle$ direction.²⁹ Here, L is an alkyl ammonium ligand and the variable n represents the number of the metal cation layers sandwiched between the two organic dielectric layers. For the case of $n = 1$, the structure represents a quantum well with one atomic layer of $[PbX_4]^{2-}$ separated by organic chains, in which the adjacent layers are held together by weak van der Waals forces. The bulk phase of $n = 1$ 2D layered perovskites represents a multiple quantum well structure, wherein the inorganic plane consisting of corner-sharing metal

halide octahedra networked in two dimensions are separated by organic chain layers (Figure 1a). These organic layers act as a dielectric spacer confining the inorganic excitons within the metal plane, thereby isolating the 2D quantum wells in each layer from electronic coupling.²⁹ The quantum and dielectric confinement leads to high exciton binding energies, high oscillator strengths, and fast radiative decay rates in these 2D layered perovskites.^{27–29,33–35} Hence, these materials are believed to be highly beneficial for applications in LEDs and displays. These 2D layered perovskites were heavily investigated in the early 1990s and a detailed report on their nature, properties, synthesis, and applications has been summarized by Mitzi.²⁹

With the current interest in the perovskite materials for solar cell applications, research on 2D perovskite materials has seen an incredible resurgence.²⁹ Low-dimensional perovskites are now considered to be the new frontier that deserves special attention for optoelectronic applications.³⁶ Here, we demonstrate $(C_4H_9NH_3)_2PbBr_4$ -based bulk 2D layered perovskites as

an active semiconductor host material for energy transfer to incorporated Mn^{2+} impurity ions for the development of high-efficiency phosphor materials for LED applications. Mn^{2+} -incorporated 2D layered perovskite bulk material is demonstrated to be synthesized in a simple and scalable methodology that can be effectively translated for the development of color pure LEDs. For the simplicity of annotation and brevity, bulk 2D layered host perovskite material, $(\text{C}_4\text{H}_9\text{NH}_3)_2\text{PbBr}_4$, will be referred to as $(\text{But})_2\text{PbBr}_4$ while the Mn^{2+} incorporated into the host $(\text{C}_4\text{H}_9\text{NH}_3)_2\text{PbBr}_4$ perovskite will be referred to as $\text{Mn}^{2+}:(\text{But})_2\text{PbBr}_4$ throughout the rest of this report.

RESULTS AND DISCUSSION

Experimentally, 2D platelike single crystals of $(\text{But})_2\text{PbBr}_4$ host material was synthesized by slow cooling of a hot solution of stoichiometric amounts of PbBr_2 and $(\text{C}_4\text{H}_9\text{NH}_3)\text{Br}$ in a DMF/toluene mixture with 2–3 drops of concentrated HBr aqueous solution.²⁶ In order to incorporate optically active Mn^{2+} impurity ions into the fabricated 2D layered host material, simple solid-state grinding of single crystals of $(\text{But})_2\text{PbBr}_4$ and MnBr_2 in desired ratio is performed, followed by an hour of annealing at 125 °C. The starting crystals of the host $(\text{But})_2\text{PbBr}_4$ material and the Mn^{2+} -incorporated 2D layered perovskite product ($\text{Mn}^{2+}:(\text{But})_2\text{PbBr}_4$) were extensively characterized. Ultraviolet–visible light (UV-vis) absorption measurement of the ground powder of $(\text{But})_2\text{PbBr}_4$ crystals show a broad absorption band centered at 410 nm. Steady-state PL measurement of the host material show strong and narrow (full width at half maximum (fwhm) = 20 nm) blue emission peak at 420 nm when excited at 360 nm above the band edge (Figure 1b, top). The photoluminescence excitation (PLE) spectra collected at 425 nm shows excitonic absorption feature at 410 nm with very small Stokes shift (Figure 1b, top). The excitation spectra is characterized by a sharply rising threshold region occurring near the absorption edge of the host bulk $(\text{But})_2\text{PbBr}_4$ material. The resemblance of the absorption band with the PLE spectra of the bulk host material for the blue emission signifies that the blue emission is due to the formation of electron–hole pairs in the host semiconductor material (see Figure S1 in the Supporting Information). Interestingly, the PL spectra of the $\text{Mn}^{2+}:(\text{But})_2\text{PbBr}_4$ sample shows a very weak emission band at 420 nm (Figure 1b, bottom). In addition, a broad emission peak (fwhm = 80 nm), centered at ~600 nm, is observed in the PL spectra (Figure 1b, bottom). This peak is attributable to the Mn^{2+} $d-d$ emission corresponding to the forbidden ${}^4\text{T}_1 \rightarrow {}^6\text{A}_1$ internal transition. Such transitions are known to be universally broad in II–VI systems both in bulk or nanostructured morphologies.^{37,38} Importantly, the PLE spectra collected at 600 nm (Figure 1b, bottom) shows features that very closely resemble that of the PLE spectra of the host material without any Mn^{2+} ions. Moreover, the excitation spectra here is characterized by a sharply rising threshold region occurring near the absorption band edge of $\text{Mn}^{2+}:(\text{But})_2\text{PbBr}_4$ material (see Figure S1). This clearly signifies that the 600 nm Mn^{2+} emission is sensitized by band-edge absorption of the host semiconductor material. This, in turn, clearly indicates an efficient energy transfer mechanism from the host perovskite to the closely located Mn^{2+} ions that are incorporated into the host semiconductor material. In addition, the excitation-dependent PL spectra (Figure S2 in the Supporting Information) indicate that the dual emission peaks (very weak band edge and strong Mn^{2+} luminescence) have no shift by altering the excitation wavelength from 340 nm to 400

nm. This independence of the PL spectra on excitation wavelength confirms the single source of the dual emission, namely, the exciton of the host bulk 2D layered perovskite. The presence of strong Mn^{2+} luminescence, sensitized by the host bulk perovskite, signifies that the incorporated Mn^{2+} ions act as efficient energy acceptor out-competing various other non-radiative relaxation pathways. Qualitatively, the efficiency of energy transfer from the exciton to the Mn^{2+} ions, as manifested in the form of Mn^{2+} luminescence band, is governed by the interplay of two opposing phenomena: (i) spin–spin exchange coupling between the charge carriers of the semiconductor host material and the Mn^{2+} ions; and (ii) inherent forbidden nature of the internal $d-d$ transition of Mn^{2+} ions due to weak transition dipoles.^{37,39} The observed strong Mn^{2+} luminescence suggests the presence of sufficiently strong exchange coupling between the charge carriers of the host and the Mn^{2+} d electrons.

Figure 1c shows the effect of varying the input Mn concentration (with respect to the number of moles of Pb) on the luminescence intensity of the Mn^{2+} emission band. With the increase of the input concentration of Mn from 2% (ICP value = 0.4%) to 5% (ICP value = 1.1%), Mn^{2+} PL emission becomes stronger, followed by a gradual decrease of the Mn^{2+} PL intensity as the Mn input concentration increases from 10% (ICP value = 2.1%) to 20% (ICP value = 3.7%). For all of these cases, a very weak band edge persists. The calculated quantum yield for Mn^{2+} emission (QY_{Mn}) for the different Mn concentrations is shown in Figure 1d, which clearly shows that the value of QY_{Mn} initially rises and then gradually declines with the increase in the Mn concentration. The initial increase in QY_{Mn} is due to the increased number of luminescent centers acting as acceptors for the energy transferred from the band edge exciton. However, with the further increase in the Mn^{2+} concentration, the PL efficiency decreases, because of interaction between neighboring Mn^{2+} ions in the crystal, as already reported in group II–VI semiconductor doping systems.^{18,40} In this scenario, a radiationless resonance energy transfer can occur between closely placed Mn^{2+} ions, rendering the excitation energy more mobile and amenable to be captured by centers of radiationless transitions (defects).³⁷ This leads to a decrease in Mn^{2+} luminescence quantum efficiency, as observed here. The highest QY_{Mn} (37%) is obtained for samples with 5% Mn input concentration with overall yellow-orange colored emission. It is important to note that the QY_{Mn} values obtained for the different input Mn concentrations (2%–20%) explored here are all above 24% and represents a very strong luminescence efficiency. The observed high PL QY_{Mn} in these doped materials could be due to the utilization of host material with strong confinement (exciton binding energy = 480 meV),^{36,41} which boosts sp-d carrier exchange interaction, thereby increasing the energy transfer efficiency between the host and the dopant ions. However, with the attempted further increase of the Mn concentration, the products show qualitatively the same spectral features but with low QY_{Mn} values. Hence, we restrict ourselves to low- Mn^{2+} -concentration-regime samples (2%–20%) for this study.

It is important to note that 3D nanocrystals of CsPbCl_3 nanocubes and quasi-2D nanoplates have been demonstrated to act as host material for Mn^{2+} doping.¹⁸ For such 3D or quasi-2D chloride systems, high PL QY for Mn^{2+} emission has been reported.¹⁸ The obtained PL QY_{Mn} for our case here is comparable to these earlier reports. The exciton binding energy in the reported 3D and quasi-2D systems are weak to modest

with band edge PL QY of $\sim 1\%$ (chloride systems). Moreover, these chloride perovskites are far from being stable when exposed to ambient conditions. Interestingly, the Mn^{2+} : $(\text{But})_2\text{PbBr}_4$ bulk 2D layered system presented here has a high exciton binding energy³⁶ and a low band edge PL QY (0.36%).³⁴ The presented system with such low PL QY (band edge) encouragingly shows PL QY_{Mn} values that are comparable to that of the 3D or quasi-2D systems. This indicates that the higher binding energies in this 2D system is already boosting the PL QY_{Mn} , despite a low PL QY (band edge). It is very likely that increasing this band edge PL QY for the host 2D perovskite would further increase the PL QY_{Mn} . Moreover, the presented 2D bromide perovskites in the powdered form are far more stable to ambient degradation than the corresponding quasi-2D chlorides. We have monitored the stability of the Mn^{2+} emission band for Mn-doped CsPbCl_3 quasi-2D nanoplates and Mn-doped $(\text{But})_2\text{PbBr}_4$ 2D layered perovskites. The CsPbCl_3 quasi-2D nanoplatelets were fabricated following a reported protocol.¹⁶ The percentage loss of Mn^{2+} PL band is recorded against exposure to ambient conditions over many days (see Figure S3a in the Supporting Information). It is clear from such a plot that the 80% of the Mn^{2+} emission is lost during the first 24 h of ambient exposure for quasi-2D system. After 8 days, only 10% of the Mn^{2+} emission is retained in these quasi-2D samples. This clearly shows that quasi-2D systems are highly susceptible to ambient degradation, and this observation is in agreement with the prior report.¹⁶ Encouragingly, for the $\text{Mn}:(\text{But})_2\text{PbBr}_4$ 2D layered perovskites, there is only a 10% loss of Mn^{2+} emission during the first 24 h of ambient exposure. Even after 8 days of ambient exposure, $\text{Mn}:(\text{But})_2\text{PbBr}_4$ 2D layered perovskites retain 80% of the Mn^{2+} emission. This clearly shows that $\text{Mn}:(\text{But})_2\text{PbBr}_4$ 2D layered perovskites are very stable toward exposure to ambient conditions. We have also compared the stability of the Mn^{2+} emission bands of quasi-2D nanoplatelet system and the 2D layered perovskite after repeated washing with highly polar solvent such as acetone. The percentage loss of the Mn^{2+} PL is monitored as a function of successive acetone washing steps (see Figure S3b in the Supporting Information). These experiments clearly reveal that, within two washing steps, 80% of the Mn^{2+} emission is lost for the $\text{Mn}:\text{CsPbCl}_3$ quasi-2D system. After five washing steps, the PL loss increases up to 97% for the quasi-2D system. Interestingly, for the $\text{Mn}:(\text{But})_2\text{PbBr}_4$ 2D layered perovskite here, the loss of Mn^{2+} emission is $<15\%$, even after five acetone washing steps. These stability tests clearly highlight the practical usefulness of the presented 2D layered perovskites. Moreover, the synthesis of the host and $\text{Mn}:(\text{But})_2\text{PbBr}_4$ 2D layered perovskites, presented here, is much more facile, simple, and scalable, when compared to the earlier reported 3D or quasi-2D systems. All of these features, when considered together, clearly motivate us to further investigate Mn^{2+} doping scenarios in this low-dimensional material. Currently, we are investigating the effect of utilizing a host 2D perovskite with high-band-edge PL QY that could potentially lead to even higher QY_{Mn} . Such material can have potential application as down-conversion-based phosphors for LEDs and as energy down-shift coating material that can be applied on perovskite-based solar cells for enhancing the power conversion efficiency by utilizing the UV component of the incident solar radiation.⁴² It is important to mention here that this solid-state grinding methodology for incorporating Mn^{2+} into bulk 2D layered bromide perovskite

works very well for a variety of 2D systems with different organic ligands such as

- $(\text{C}_4\text{H}_9\text{NH}_3)_2\text{PbBr}_4$, also known as (butylammonium) $_2\text{PbBr}_4$ ($(\text{But})_2\text{PbBr}_4$), as presented in this report;
- (benzylammonium) $_2\text{PbBr}_4$;
- (2-phenylethylammonium) $_2\text{PbBr}_4$; and
- (ethylenediammonium) PbBr_4 .

For all of these 2D layered perovskites, we clearly see strong Mn emission upon thermal annealing. However, similar solid-state methodology for Mn incorporation does not work for bulk/nanocrystals of the 3D CsPbBr_3 system. The observed facile incorporation of Mn^{2+} in bulk 2D systems (against 3D systems) could possibly be due to the inherent mechanical and electronic “softness” of constituent atoms of the 2D layered perovskites.²⁹ However, this requires further investigation and rationalization.

The PL lifetimes of the host $(\text{But})_2\text{PbBr}_4$ and Mn^{2+} : $(\text{But})_2\text{PbBr}_4$ samples were measured using time-resolved PL spectroscopy. For the $(\text{But})_2\text{PbBr}_4$ host material, the band edge PL decay curve (Figure 2a) shows biexponential fit with lifetimes of 1.4 ns (73% contribution) and 6.5 ns (27% contribution), which are in close agreement to the reported data.²⁶ Interestingly, for the $\text{Mn}^{2+}:(\text{But})_2\text{PbBr}_4$ samples, two very different lifetimes are observed. For this, the band-edge PL

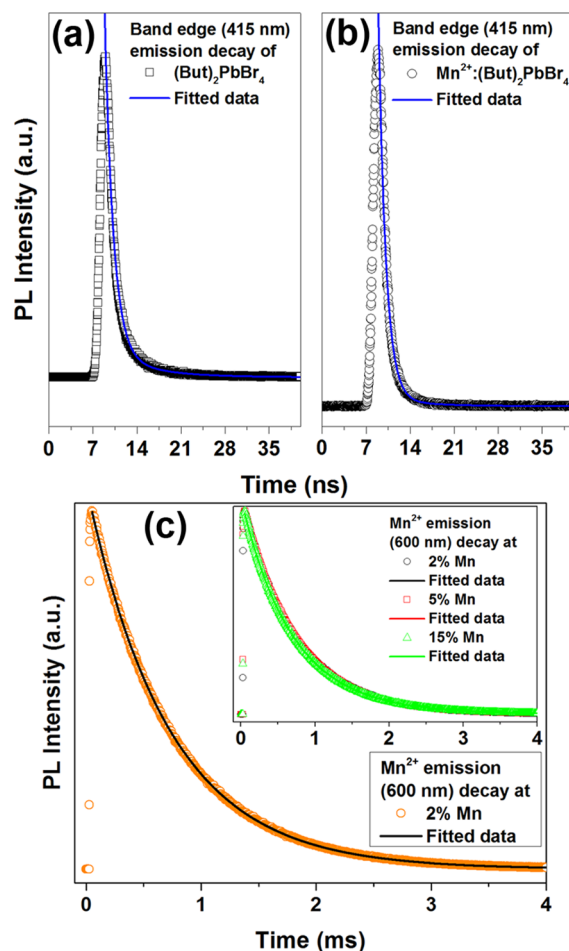


Figure 2. PL decay dynamics of (a) an undoped host sample, (b) a doped sample for the band edge emission, and (c) a doped sample for the Mn^{2+} emission (inset shows the same at different dopant concentrations).

decay curve (Figure 2b) shows a biexponential fit with lifetimes of 1.2 ns (90% contribution) and 6.3 ns (10% contribution). For the Mn^{2+} emission band, the lifetime data can be fitted to a monoexponential decay curve with a long lifetime of 740 μs (Figure 2c). This long lifetime is due to the forbidden nature of the ${}^4\text{T}_1 \rightarrow {}^6\text{A}_1$ internal Mn^{2+} transition, and the contribution due to the neighboring Mn^{2+} – Mn^{2+} clustering interaction.³⁷ Varying the Mn^{2+} concentration in the range of 2%–15% does not seem to have a significant influence on the lifetime of this Mn^{2+} d electron emission, as shown in the inset of Figure 2c and Table S1 in the Supporting Information.

Elemental analysis (carbon, hydrogen, nitrogen) of the $(\text{But})_2\text{PbBr}_4$ host material shows stoichiometric match. The morphological characterization of the host material was performed using transmission electron microscopy, coupled with energy-dispersive spectroscopy (TEM/EDS) elemental mapping (Figure S4 in the Supporting Information) which shows the bulk, irregular shaped microparticles with chemical composition, revealing the presence of Pb and Br (atomic ratio of Pb:Br = 17:83), which is consistent with the reported data.²⁶ The elemental mapping shows the homogeneous presence of constituent elements (see Figure S4). The morphology analysis of the $\text{Mn}^{2+}:(\text{But})_2\text{PbBr}_4$ samples, using TEM/EDS elemental mapping, shows the presence of bulk, irregularly shaped microparticles. The EDS analysis clearly confirms the presence of Mn^{2+} ions in the samples (Figure S5 in the Supporting Information). Elemental mapping shows the homogeneous distribution of Pb, Br, and Mn as the constituting elements (see Figure S5).

Thermogravimetric analysis (TGA) data for the host $(\text{But})_2\text{PbBr}_4$ and $\text{Mn}^{2+}:(\text{But})_2\text{PbBr}_4$ sample were recorded (Figure S6 in the Supporting Information) and presents very similar weight loss characteristics. The TGA data analysis for the host material shows two major weight loss peaks: one corresponding to the loss of the butyl ammonium bromide ligand of 45% at 315 $^\circ\text{C}$, and the other related to the release of inorganic lead bromide of 55% at 550 $^\circ\text{C}$ (see Figure S6a). Similarly, for the $\text{Mn}^{2+}:(\text{But})_2\text{PbBr}_4$ sample, a loss of the butyl ammonium bromide ligand (42% at 321 $^\circ\text{C}$) is observed, and another related to the release of inorganic lead bromide (58% at 555 $^\circ\text{C}$) is observed (see Figure S6b). The observed weight loss ratio of organic to inorganic component for the $(\text{But})_2\text{PbBr}_4$ and $\text{Mn}^{2+}:(\text{But})_2\text{PbBr}_4$ sample suggests an $\sim 2:1$ molar ratio between the organic and inorganic components, which is a feature of the 2D layered perovskite materials. Such TGA analysis, confirming the approximate chemical composition in the 2D layered perovskite, is consistent with existing reports.^{26,43,44}

XRD characterization of the host $(\text{But})_2\text{PbBr}_4$ and the $\text{Mn}^{2+}:(\text{But})_2\text{PbBr}_4$ sample is shown in Figure 3a. The as-prepared single crystals of the host material exhibit an XRD pattern that is in excellent agreement with the prior report.²⁶ Comparison of the XRD pattern between the single crystal and the ground powder of the single crystals of the host material also shows an excellent match (see Figure S7 in the Supporting Information). Interestingly, the XRD pattern of the $\text{Mn}^{2+}:(\text{But})_2\text{PbBr}_4$ sample is structurally very similar to the XRD pattern of the host $(\text{But})_2\text{PbBr}_4$ sample (see Figure 3a). A more careful examination of the XRD patterns reveal that the peak positions of the $\text{Mn}^{2+}:(\text{But})_2\text{PbBr}_4$ sample have monotonically shifted to higher angles, compared to that of the host material (Figure 3a). This observed shift of the XRD peak positions indicates successful incorporation of Mn^{2+} ions into the lattice of the

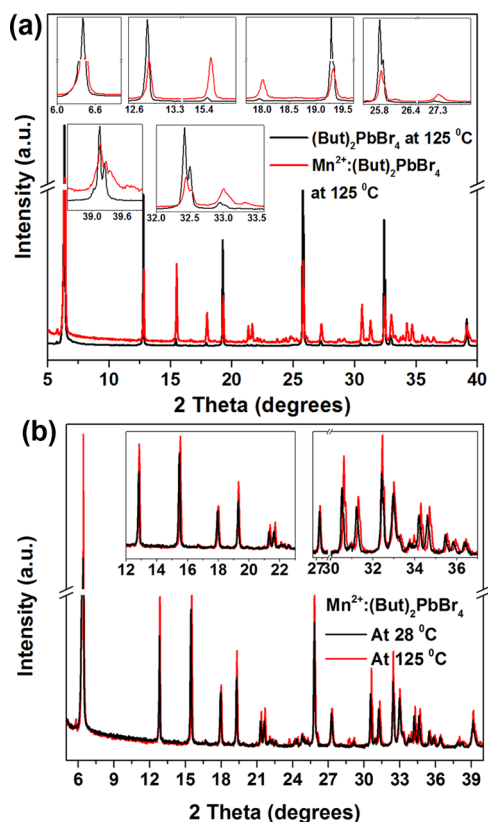


Figure 3. XRD pattern of (a) undoped and doped material both annealed at 125 $^\circ\text{C}$ (with magnified views provided as insets) and (b) doped material annealed at 28 and 125 $^\circ\text{C}$ (with magnified views provided as insets).

host material. The increase of the 2θ values is consistent with lattice contraction, because of the substitution of Pb^{2+} ions (ionic radius = 1.33 \AA) with smaller Mn^{2+} ions (ionic radius = 0.97 \AA).⁴⁵ The decrease of the cation size, due to substitutional doping, shifts the XRD pattern toward higher 2θ values.

Noteworthy here is the fact that the $\text{Mn}^{2+}:(\text{But})_2\text{PbBr}_4$ sample is prepared via solid-state grinding, followed by 1 h of annealing at 125 $^\circ\text{C}$. This annealing step turns out to be very critical in successfully incorporating the Mn^{2+} ions into the host lattice and thereby engineering its optical properties. Hence, temperature-dependent annealing studies were performed for the host $(\text{But})_2\text{PbBr}_4$ and $\text{Mn}^{2+}:(\text{But})_2\text{PbBr}_4$ material. Figure 4a shows the PL properties of the $\text{Mn}^{2+}:(\text{But})_2\text{PbBr}_4$ sample annealed at different temperatures. PL spectra (Figure 4a) clearly shows that, when the sample is annealed at room temperature, there is a dominant band-edge blue emission with a weak orange-yellow Mn^{2+} emission peak. As this annealing temperature is progressively increased, the band-edge blue emission intensity strongly decreases. More interestingly, the orange-yellow Mn^{2+} emission peak intensity gradually intensifies. When annealed at 100 $^\circ\text{C}$, the Mn^{2+} emission peak is observed to be stronger than the band-edge emission. For an annealing temperature of 125 $^\circ\text{C}$, the band-edge emission is seen to be suppressed heavily while the Mn^{2+} emission peak is the strongest mode observed. Figure 4b shows the integrated peak area for the band edge and Mn^{2+} emission, as a function of the annealing temperature. Figure 4b clearly shows that, as the annealing temperature is increased, the band-edge emission gets progressively suppressed while the Mn^{2+} emission enhances strongly. This implies that the energy transfer from

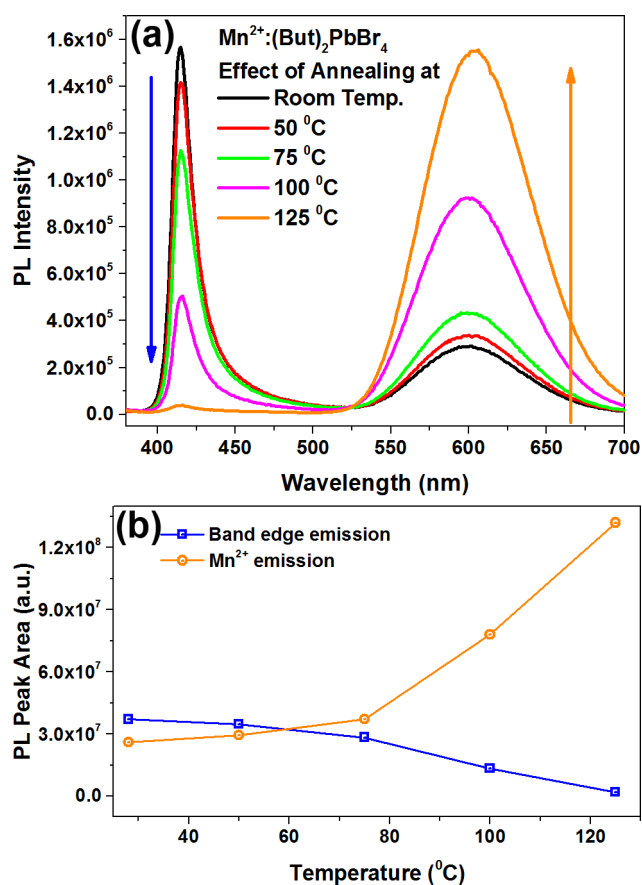


Figure 4. (a) PL spectra of doped samples annealed at progressively higher temperatures; (b) area under the band edge peak and Mn²⁺ emission peak, as a function of annealing temperature.

the host to the Mn²⁺ luminescent centers becomes more efficient as the sample is annealed at progressively higher temperatures. This could be due to increased extent of Mn²⁺ incorporation into the host lattice sites, which is due to increased thermal diffusion of the dopant ions. The PLE spectra collected at the 600 nm Mn²⁺ emission peak for different annealing temperatures is shown in Figure S8 in the Supporting Information. The nature of the PLE curve remains the same with increasing PLE intensity as the annealing temperature is increased. Also, the PLE peak presents a slight shift to shorter wavelengths (from 411 nm to 407 nm) as the annealing temperature increases. This again might indicate greater incorporation of Mn²⁺ ions into the lattice of the host perovskites when annealed at higher temperatures, which is consistent with the observed PL data. Elemental analysis for Mn²⁺ incorporated into these annealed samples through ICP was performed for two samples (each with a Mn²⁺ input concentration of 10%): one has been annealed at 75 °C and the other has been annealed at 125 °C. It is observed that amount of Mn²⁺ present in the 125 °C annealed sample is higher than that of the sample annealed at 75 °C (see Table S2 in the Supporting Information).

In order to understand this enhanced energy transfer efficiency that is achievable under high temperature annealing conditions, we have performed the XRD analysis. Figure 3a shows the comparison of the XRD pattern of (But)₂PbBr₄ (black trace) and Mn²⁺:(But)₂PbBr₄ (red trace) sample, both annealed at 125 °C, with insets showing the magnified view of the patterns. This clearly shows that the XRD peaks have

shifted to higher angle values, confirming the incorporation of Mn²⁺ dopants into the crystal lattice of the host semiconductor. Noteworthy here, the XRD patterns of the host (But)₂PbBr₄ and Mn²⁺:(But)₂PbBr₄ samples, both annealed at room temperature, are structurally identical and do not show any shifts in the peak positions (see Figure S9 in the Supporting Information). Also, the XRD patterns are identical for the host (But)₂PbBr₄ sample annealed at room temperature and at 125 °C (see Figure S10 in the Supporting Information). Figure 3b compares the XRD patterns of the room-temperature- and 125 °C-annealed sample of Mn²⁺:(But)₂PbBr₄. This clearly shows that, for the Mn²⁺:(But)₂PbBr₄ samples, the XRD peak positions of the 125 °C-annealed sample has a prominent shift to higher angles, when compared to the room-temperature-annealed sample. This indicates that thermal diffusion of the Mn²⁺ ions into the crystal lattice of the host material occurs strongly when annealed at elevated temperature. This increased extent of doping the host material under high-temperature annealing conditions provides more acceptor Mn²⁺ ions for enhanced energy transfer to occur. This is manifested in the form of intense yellow-orange emission with high QY_{Mn²⁺} as observed here.

XRD analysis of Mn²⁺:(But)₂PbBr₄ samples, annealed at 125 °C, with varying Mn²⁺ dopant concentration, has also been performed. Figure 5a shows the XRD patterns at different Mn²⁺ concentrations (0, 10, 20, 25% Mn²⁺). A magnified view of the XRD patterns is shown in Figures 5 b–d for clarity. It is evident from the XRD analysis that the peak positions monotonically shift toward higher angles as the Mn²⁺ dopant concentration is increased. This again indicates progressively higher substitutional Mn²⁺ doping of host perovskites as the concentration of the input Mn²⁺ ions is increased. This increased doping causes an enhancement of the energy transfer efficiency and helps boost the PL QY_{Mn²⁺}.

It is important to note here that the Mn²⁺ emission from these doped samples arises because of energy transfer from the host to the *closely located* dopant ions. Besides substitutional doping, acceptor Mn²⁺ ions can also undergo clustering, residing inside the host perovskite material. Given the solid-state grinding method of doping, it is very likely that Mn²⁺ clusters that can act as acceptors can form. The observed XRD peak shifts confirm substitutional doping at the octahedral sites. However, this does not preclude the presence of Mn²⁺ ions *clustered* inside the host perovskite. The observed Mn²⁺ emission lifetime of ~740 μs is shorter than the typical 1300 μs lifetime of isolated Mn²⁺ doped in perovskite^{15–18,37} or in II–VI^{46–48} quantum dot systems. This lifetime shortening indicates toward dipole–dipole interaction between neighboring Mn²⁺–Mn²⁺ ions of a cluster³⁷ residing in the host perovskite. Moreover, electron paramagnetic resonance (EPR) measurements on doped samples show some weak, partially resolved peaks superimposed on a broad background signal. These weakly resolved hyperfine splitting bands superimposed on the background broad signal indicates interaction between Mn²⁺ ions in a cluster.⁴⁹ Hence, it is very likely that clusters of Mn²⁺ ions are present, along with substitutionally doped Mn²⁺ ions in the host lattice. Irrespective of whether the acceptor Mn²⁺ ions are isolated or clustered, they act as efficient acceptors of energy from the photoexcited charge carriers of the host material and show strong orange emission with high quantum yield, which is a feature that could be exploited for their utility as color-converting materials for LEDs.

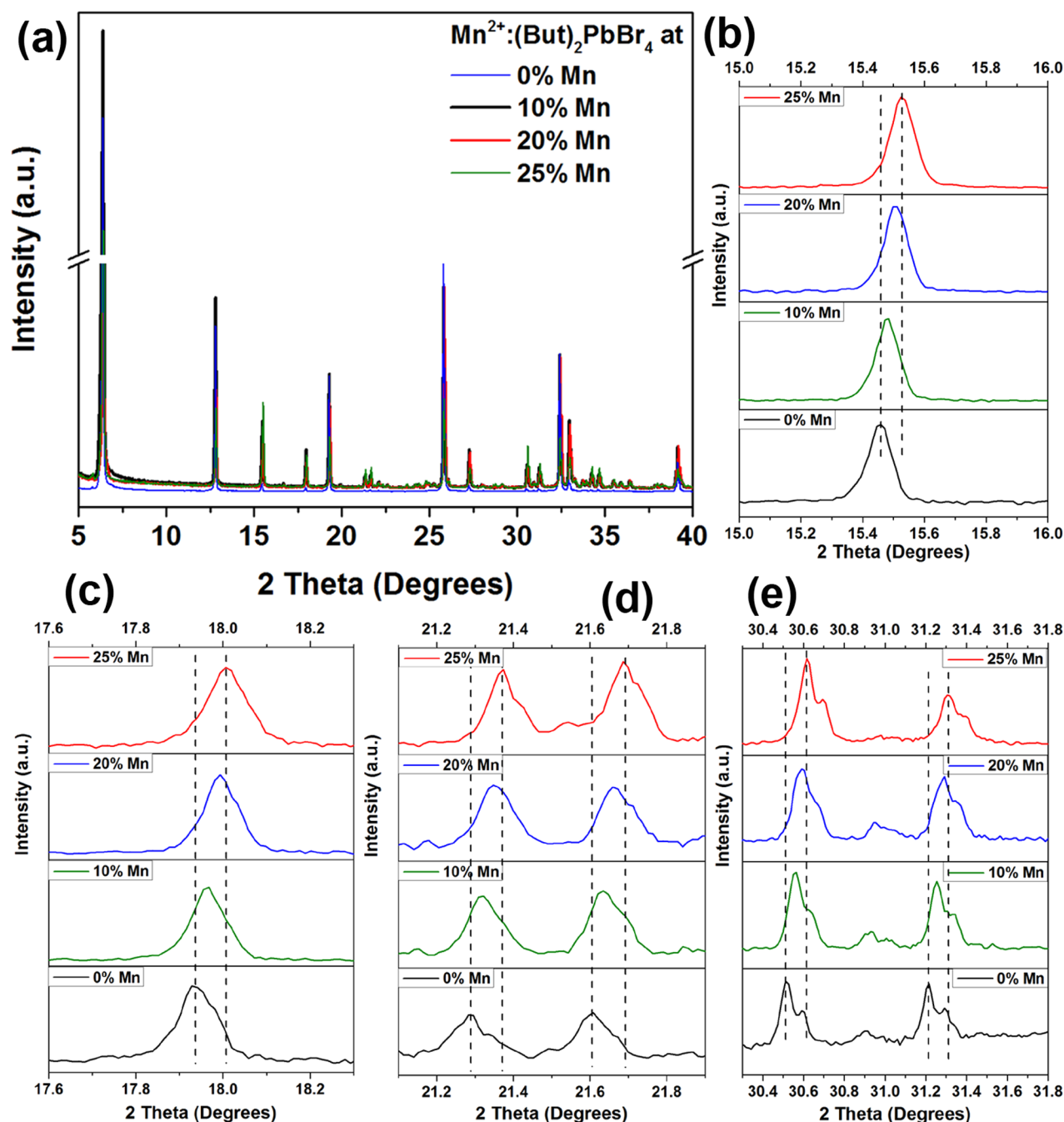


Figure 5. XRD patterns of (a) doped material at different dopant concentrations, along with their magnified views (panels (b–e)).

Simple solid-state mechanochemical synthesis of bulk APbBr_3 ($A = \text{Cs, MA}$) perovskites and their nanoparticles has been successfully demonstrated, wherein the $A\text{--}X$ and $\text{Pb--}X$ precursor powders are ground homogeneously at room temperature for the addition reaction.⁵⁰ Noteworthy, Mn^{2+} doping is achieved here via a simple solid-state grinding and thermal annealing process, wherein the Pb^{2+} ions are exchanged with the dopant Mn^{2+} ions. This thermally activated cation exchange on the octahedral sites leads to the formation of solid solutions. Typically, cation exchange/diffusion in the 3D AMX_3 system is known to be very slow with a high activation energy, because of the lack of interstitial sites.²⁰ Anion exchange, on the other hand, is very efficient and fast, because of the low activation energy of formation and diffusion of anion vacancy.

This low activation energy supports the presence of anion vacancy in the bulk 3D perovskites.^{51,52} Under these conditions, a simple solid-state grinding and thermal annealing shows strong evidence of substitutional doping of the host perovskite by the Mn^{2+} dopant ions. Here, it is very likely, in our case, that anion exchange precedes the cation exchange event. The utilized metal bromide dopant precursor (MnBr_2) for a bromide-based host perovskite has the important benefit of having the same anion that can exploit the formation and diffusion of halide vacancy in the host material, leading to an exchange of Pb^{2+} ions with the Mn^{2+} ions for the formation of doped material. The MnBr_2 precursor binds to the existing halide vacancy in the host material as a molecular unit, thereby incorporating the MnBr_2 in the host lattice. This filling of the

halide vacancy releases energy, because of the formation of a bond between the incoming Br atom and the host lattice without necessarily breaking the Mn–Br bond. Furthermore, during the thermal annealing step, energy is supplied for diffusion of this halide vacancy and breaking the Pb–Br bond in the host lattice. This allows quick exchange of the Pb^{2+} ions with the Mn^{2+} dopant ions inside the host lattice, leading to the formation of a solid solution. The existence of such mechanistic pathways for doping is consistent with the fact that we observe XRD peak shifts at higher angles for samples that were exclusively annealed at higher temperature. Recently, a similar mechanism for doping has been presented for rationalizing the cation exchange process of CsPbBr_3 nanocrystals.²⁰ Further work is underway to understand the mechanism of this doping process in greater details.

In conclusion, a 2D layered bulk perovskite semiconductor with a multiple quantum well structure has been successfully utilized as a host material for doping Mn^{2+} ions in a facile and scalable methodology. Successful incorporation of Mn^{2+} dopants into the host crystal lattice was demonstrated using PLE spectra and XRD analysis. These Mn^{2+} -doped samples exhibit a weak band-edge emission (~ 420 nm) with a strong Mn^{2+} emission band (~ 600 nm). The calculated quantum yield for Mn^{2+} emission is found to be greater than $\sim 24\%$ across samples with different Mn^{2+} dopant concentrations. Here, the strongly bound excitons with fast radiative decay rates for the bulk 2D layered host material has been exploited for achieving high PL quantum yield for the Mn^{2+} emission. These Mn^{2+} -doped samples show efficient energy transfer from photo-excited host excitons to the dopant ions. The resultant strong yellow-orange emission is attributed to the spin-forbidden internal transition of the d electrons of Mn^{2+} ions (${}^4\text{T}_1 \rightarrow {}^6\text{A}_1$). The enabling properties of the Mn^{2+} -doped samples (high quantum yield, stability against ambient moisture, facile and scalable synthesis) suggests great potential for these materials as down-conversion-based phosphor materials for LED applications and as energy down-shift coating material that can be applied on perovskite-based solar cells for enhancing the power conversion efficiency. Presented solid-state grinding methodology for Mn^{2+} doping is generally successful for a variety of bulk 2D layered perovskites that we have investigated, including (butylammonium) $_2\text{PbBr}_4$ (as showcased here), (benzylammonium) $_2\text{PbBr}_4$, and (2-phenylethylammonium) $_2\text{PbBr}_4$. To the best of our knowledge, this is the first report on Mn^{2+} doping in the multiple quantum well structure of bulk 2D layered perovskites with strongly bound excitons demonstrating efficient energy transfer and high PL QY_{Mn} . Anion exchange in these doped samples and doping other magnetic ions is being currently investigated. Future work will be on developing methodologies for utilizing colloidal 2D layered perovskites with high quantum yield as host material for doping with impurity ions in solution phase.

MATERIALS AND METHODS

Reagents. Unless otherwise stated, all of the chemicals were purchased from Sigma–Aldrich.

Synthesis of $\text{C}_4\text{H}_9\text{NH}_3\text{Br}$. In a 250 mL round-bottom flask, 10 mL of butyl amine and 25 mL of methanol was added, stirred, and maintained at 0°C , using an ice bath. Ten milliliters (10 mL) of concentrated HBr was added dropwise to the above solution, after which the ice bath was removed. The mixture was stirred at room temperature for 3 h. A rotary evaporator was used at 70°C to remove the methanol and water. The crude-oil-like product was washed repeatedly with diethyl ether and finally recrystallized from a mixed

solvent of diethyl ether and ethanol. After filtration, a white solid was collected and dried at 60°C in a vacuum oven for 24 h.

Synthesis of Single Crystals of $(\text{C}_4\text{H}_9\text{NH}_3)_2\text{PbBr}_4$ 2D Layered Host Perovskites. For the preparation of single crystals of $(\text{C}_4\text{H}_9\text{NH}_3)_2\text{PbBr}_4$, $\text{C}_4\text{H}_9\text{NH}_3\text{Br}$ (308 mg, 2 mmol), PbBr_2 (367 mg, 1 mmol) and 2 drops of HBr aqueous solution were dissolved in 2 mL of dimethylformamide (DMF) solvent which was heated to 90°C . To this hot clear solution, toluene is added just up until the solution starts to become turbid. The heating is removed and the solution is allowed to cool naturally. This leads to the formation of platelike white crystals in copious amounts. After 3 h, the supernatant liquid is removed and the crystals are repeatedly washed using acetone and tetrahydrofuran (THF). The crystals are filtered and dried under vacuum at 60°C overnight.

Synthesis of Mn^{2+} -Doped $(\text{C}_4\text{H}_9\text{NH}_3)_2\text{PbBr}_4$ 2D Layered Perovskites. A desired amount of the above crystals of $(\text{C}_4\text{H}_9\text{NH}_3)_2\text{PbBr}_4$ was mixed with MnBr_2 (amount of Mn salt being added is with respect to the mole percentage of Pb) in an agate mortar and pestle. The powders are ground homogeneously for more than 15 min. This finely ground powder is then added to a glass vial and was heated at 125°C in an oven for an hour. The sample was allowed to cool naturally and was used further for characterization.

Instruments and Procedure Utilized for Sample Characterization. Transmission electron microscopy (TEM) images were collected using a Tecnai T20 TEM system that was operating at an accelerating voltage of 200 kV. Powder X-ray diffraction (XRD) patterns were recorded using a PANalytical X'Pert Pro equipped with Cu $K\alpha$ radiation ($\lambda = 1.5406$ Å). Steady-state PL measurements were performed utilizing a PTI QM 400 fluorometer. PL decay dynamics were recorded using a fluorescence spectrometer (Edinburgh Instruments, Model FLS 980 system), using a microsecond flash lamp with a power of 100 W. For Mn emission decay dynamics, the sample was excited at 300 nm, using a microsecond flash lamp, whereas the excitonic PL decay was recorded using a 340 nm picosecond-pulsed LED laser source. PL quantum yield for Mn emission was measured against R6G dye in ethanol with QY of 95% as the standard, when excited at 360 nm. Absorbance measurements were performed using a UV-vis-NIR spectrophotometer (Shimadzu, Model UV-3600 plus). Thermogravimetric analysis (TGA) measurements were recorded using a TAG system (Mettler–Toledo, Model TGA/SDTA851e). The samples were heated in the range of 30 – 800°C at a heating rate of $5^\circ\text{C}/\text{min}$.

ASSOCIATED CONTENT

Supporting Information

The Supporting Information is available free of charge on the ACS Publications website at DOI: [10.1021/acs.chemmater.7b02429](https://doi.org/10.1021/acs.chemmater.7b02429).

Comparison of absorbance, PLE, and PL spectra; excitation of PL spectra; TEM/EDS morphology and elemental mapping; TGA data; comparison of PXRD of single crystal and ground powder of single crystal of host material; PLE (600 nm) at different annealing temperatures; XRD pattern of host and doped samples at room-temperature annealing; XRD pattern of host material annealed at room and 125°C temperature; stability test; Mn^{2+} lifetimes, ICP results (PDF)

AUTHOR INFORMATION

Corresponding Author

*E-mail: j.kundu@ncl.res.in.

ORCID

Janardan Kundu: 0000-0003-4879-0235

Notes

The authors declare no competing financial interest.

ACKNOWLEDGMENTS

The authors would like to thank Prof. S. B. Ogale, Prof. A. Das, Dr. S. B. Sukumaran, Dr. A. K. Rath, Dr. S. Basu, Dr. D. Maity, and Dr. P. Talukdar for insightful discussions. This work was supported by DST (Grant Nos. SB/S2/RJN-61/2013 and EMR/2014/000478) and CSIR-NCL start-up (Grant No. MLP030326).

REFERENCES

- (1) Liu, M.; Johnston, M. B.; Snaith, H. J. Efficient planar heterojunction perovskite solar cells by vapour deposition. *Nature* **2013**, *501*, 395–398.
- (2) Shi, D.; Adinolfi, V.; Comin, R.; Yuan, M.; Alarousu, E.; Buin, A.; Chen, Y.; Hoogland, S.; Rothenberger, A.; Katsiev, K.; Losovyj, Y.; Zhang, X.; Dowben, P. A.; Mohammed, O. F.; Sargent, E. H.; Bakr, O. M. Solar cells. Low trap-state density and long carrier diffusion in organolead trihalide perovskite single crystals. *Science* **2015**, *347*, 519–522.
- (3) Nie, W.; Tsai, H.; Asadpour, R.; Blancon, J.-C.; Neukirch, A. J.; Gupta, G.; Crochet, J. J.; Chhowalla, M.; Tretyak, S.; Alam, M. A.; Wang, H.-L.; Mohite, A. D. Solar cells. High-efficiency solution-processed perovskite solar cells with millimeter-scale grains. *Science* **2015**, *347*, 522–525.
- (4) Jeon, N. J.; Noh, J. H.; Yang, W. S.; Kim, Y. C.; Ryu, S.; Seo, J.; Seok, S. I. Compositional engineering of perovskite materials for high-performance solar cells. *Nature* **2015**, *517*, 476–480.
- (5) Tan, Z.-K.; Moghaddam, R. S.; Lai, M. L.; Docampo, P.; Higler, R.; Deschler, F.; Price, M.; Sadhanala, A.; Pazos, L. M.; Credgington, D.; Hanusch, F.; Bein, T.; Snaith, H. J.; Friend, R. H. Bright light-emitting diodes based on organometal halide perovskite. *Nat. Nanotechnol.* **2014**, *9*, 687–692.
- (6) Xing, G.; Mathews, N.; Lim, S. S.; Yantara, N.; Liu, X.; Sabba, D.; Grätzel, M.; Mhaisalkar, S.; Sum, T. C. Low-temperature solution-processed wavelength-tunable perovskites for lasing. *Nat. Mater.* **2014**, *13*, 476–480.
- (7) Zhu, H.; Fu, Y.; Meng, F.; Wu, X.; Gong, Z.; Ding, Q.; Gustafsson, M. V.; Trinh, M. T.; Jin, S.; Zhu, X. Y. Lead halide perovskite nanowire lasers with low lasing thresholds and high quality factors. *Nat. Mater.* **2015**, *14*, 636–642.
- (8) Yang, W. S.; Noh, J. H.; Jeon, N. J.; Kim, Y. C.; Ryu, S.; Seo, J.; Seok, S. I. High-performance photovoltaic perovskite layers fabricated through intramolecular exchange. *Science* **2015**, *348*, 1234–1237.
- (9) Cho, H.; Jeong, S.-H.; Park, M.-H.; Kim, Y.-H.; Wolf, C.; Lee, C.-L.; Heo, J. H.; Sadhanala, A.; Myoung, N.; Yoo, S.; Im, S. H.; Friend, R. H.; Lee, T.-W. Overcoming the Electroluminescence Efficiency Limitations of Perovskite Light-Emitting Diodes. *Science* **2015**, *350*, 1222–1225.
- (10) Wang, H.-C.; Lin, S.-Y.; Tang, A.-C.; Singh, B. P.; Tong, H.-C.; Chen, C.-Y.; Lee, Y.-C.; Tsai, T.-L.; Liu, R.-S. Mesoporous Silica Particles Integrated with All-Inorganic CsPbBr₃ Perovskite Quantum-Dot Nanocomposites (MP-PQDs) with High Stability and Wide Color Gamut Used for Backlight Display. *Angew. Chem., Int. Ed.* **2016**, *55*, 7924–7929.
- (11) Pathak, S.; Sakai, N.; Wisnivesky Rocca Rivarola, F.; Stranks, S. D.; Liu, J.; Eperon, G. E.; Ducati, C.; Wojciechowski, K.; Griffiths, J. T.; Haghighirad, A. A.; Pellaroque, A.; Friend, R. H.; Snaith, H. J. Perovskite Crystals for Tunable White Light Emission. *Chem. Mater.* **2015**, *27*, 8066–8075.
- (12) Song, J.; Li, J.; Li, X.; Xu, L.; Dong, Y.; Zeng, H. Quantum Dot Light-Emitting Diodes Based on Inorganic Perovskite Cesium Lead Halides (CsPbX₃). *Adv. Mater.* **2015**, *27*, 7162–7167.
- (13) Weidman, M. C.; Goodman, A. J.; Tisdale, W. A. Colloidal Halide Perovskite Nanoplatelets: An Exciting New Class of Semiconductor Nanomaterials. *Chem. Mater.* **2017**, *29*, 5019–5030.
- (14) Liu, W.; Lin, Q.; Li, H.; Wu, K.; Robel, I.; Pietryga, J. M.; Klimov, V. I. Mn²⁺-Doped Lead Halide Perovskite Nanocrystals with Dual-Color Emission Controlled by Halide Content. *J. Am. Chem. Soc.* **2016**, *138*, 14954–14961.
- (15) Parobek, D.; Roman, B. J.; Dong, Y.; Jin, H.; Lee, E.; Sheldon, M.; Son, D. H. Exciton-to-Dopant Energy Transfer in Mn-Doped Cesium Lead Halide Perovskite Nanocrystals. *Nano Lett.* **2016**, *16*, 7376–7380.
- (16) Mir, W. J.; Jagadeeswararao, M.; Das, S.; Nag, A. Colloidal Mn-Doped Cesium Lead Halide Perovskite Nanoplatelets. *ACS Energy Lett.* **2017**, *2*, 537–543.
- (17) Liu, H.; Wu, Z.; Shao, J.; Yao, D.; Gao, H.; Liu, Y.; Yu, W.; Zhang, H.; Yang, B. CsPb_xMn_{1-x}Cl₃ Perovskite Quantum Dots with High Mn Substitution Ratio. *ACS Nano* **2017**, *11*, 2239–2247.
- (18) Guria, A. K.; Dutta, S. K.; Adhikari, S. D.; Pradhan, N. Doping Mn²⁺ in Lead Halide Perovskite Nanocrystals: Successes and Challenges. *ACS Energy Lett.* **2017**, *2*, 1014–1021.
- (19) Begum, R.; Parida, M. R.; Abdelhady, A. L.; Murali, B.; Alyami, N. M.; Ahmed, G. H.; Hedhili, M. N.; Bakr, O. M.; Mohammed, O. F. Engineering Interfacial Charge Transfer in CsPbBr₃ Perovskite Nanocrystals by Heterovalent Doping. *J. Am. Chem. Soc.* **2017**, *139*, 731–737.
- (20) van der Stam, W.; Geuchies, J. J.; Altantzis, T.; van den Bos, K. H. W.; Meeldijk, J. D.; Van Aert, S.; Bals, S.; Vanmaekelbergh, D.; de Mello Donega, C. Highly Emissive Divalent-Ion-Doped Colloidal CsPb_{1-x}M_xBr₃ Perovskite Nanocrystals through Cation Exchange. *J. Am. Chem. Soc.* **2017**, *139*, 4087–4097.
- (21) Santra, P. K.; Kamat, P. V. Mn-Doped Quantum Dot Sensitized Solar Cells: A Strategy to Boost Efficiency over 5%. *J. Am. Chem. Soc.* **2012**, *134*, 2508–2511.
- (22) He, Y.; Wang, H.-F.; Yan, X.-P. Exploring Mn-Doped ZnS Quantum Dots for the Room-Temperature Phosphorescence Detection of Enoxacin in Biological Fluids. *Anal. Chem.* **2008**, *80*, 3832–3837.
- (23) Erickson, C. S.; Bradshaw, L. R.; McDowall, S.; Gilbertson, J. D.; Gamelin, D. R.; Patrick, D. L. Zero-Reabsorption Doped-Nanocrystal Luminescent Solar Concentrators. *ACS Nano* **2014**, *8*, 3461–3467.
- (24) Yu, J. H.; Kwon, S.-H.; Petrásek, Z.; Park, O. K.; Jun, S. W.; Shin, K.; Choi, M.; Park, Y. I.; Park, K.; Na, H. B.; Lee, N.; Lee, D. W.; Kim, J. H.; Schwill, P.; Hyeon, T. High-resolution three-photon biomedical imaging using doped ZnS nanocrystals. *Nat. Mater.* **2013**, *12*, 359–366.
- (25) Yuan, M.; Quan, L. N.; Comin, R.; Walters, G.; Sabatini, R.; Voznyy, O.; Hoogland, S.; Zhao, Y.; Beauregard, E. M.; Kanjanaboos, P.; Lu, Z.; Kim, D. H.; Sargent, E. H. Perovskite energy funnels for efficient light-emitting diodes. *Nat. Nanotechnol.* **2016**, *11*, 872–877.
- (26) Dou, L.; Wong, A. B.; Yu, Y.; Lai, M.; Kornienko, N.; Eaton, S. W.; Fu, A.; Bischak, C. G.; Ma, J.; Ding, T.; Ginsberg, N. S.; Wang, L.-W.; Alivisatos, A. P.; Yang, P. Atomically thin two-dimensional organic-inorganic hybrid perovskites. *Science* **2015**, *349*, 1518–1521.
- (27) Cheng, Z.; Lin, J. Layered organic-inorganic hybrid perovskites: structure, optical properties, film preparation, patterning and templating engineering. *CrystEngComm* **2010**, *12*, 2646–2662.
- (28) Mitzi, D. B. Templating and structural engineering in organic-inorganic perovskites. *J. Chem. Soc., Dalton Trans.* **2001**, 1–12.
- (29) Mitzi, D. B. Synthesis, structure, and properties of organic-inorganic perovskites and related materials. *Prog. Inorg. Chem.* **1999**, *48*, 1–121.
- (30) Braun, M.; Tuffentsammer, W.; Wachtel, H.; Wolf, H. C. Tailoring of energy levels in lead chloride based layered perovskites and energy transfer between the organic and inorganic planes. *Chem. Phys. Lett.* **1999**, *303*, 157–164.
- (31) Li, Y. Y.; Lin, C. K.; Zheng, G. L.; Cheng, Z. Y.; You, H.; Wang, W. D.; Lin, J. Novel (110)-Oriented Organic-Inorganic Perovskite Compound Stabilized by N-(3-Aminopropyl)imidazole with Improved Optical Properties. *Chem. Mater.* **2006**, *18*, 3463–3469.
- (32) Braun, M.; Tuffentsammer, W.; Wachtel, H.; Wolf, H. C. Pyrene as emitting chromophore in organic-inorganic lead halide-based layered perovskites with different halides. *Chem. Phys. Lett.* **1999**, *307*, 373–378.
- (33) Mitzi, D. B.; Feild, C. A.; Harrison, W. T. A.; Guloy, A. M. Conducting tin halides with a layered organic-based perovskite structure. *Nature* **1994**, *369*, 467–469.

(34) Kawano, N.; Koshimizu, M.; Sun, Y.; Yahaba, N.; Fujimoto, Y.; Yanagida, T.; Asai, K. Effects of Organic Moieties on Luminescence Properties of Organic–Inorganic Layered Perovskite-Type Compounds. *J. Phys. Chem. C* **2014**, *118*, 9101–9106.

(35) Ishihara, T.; Takahashi, J.; Goto, T. Exciton state in two-dimensional perovskite semiconductor ($C_{10}H_{21}NH_3$)₂PbI₄. *Solid State Commun.* **1989**, *69*, 933–936.

(36) Saidaminov, M. I.; Mohammed, O. F.; Bakr, O. M. Low-Dimensional-Networked Metal Halide Perovskites: The Next Big Thing. *ACS Energy Lett.* **2017**, *2*, 889–896.

(37) Goede, O.; Heimbrod, W. Optical Properties of (Zn, Mn) and (Cd, Mn) Chalcogenide Mixed Crystals and Superlattices. *Phys. Status Solidi B* **1988**, *146*, 11–62.

(38) Moriwaki, M. M.; Becker, W. M.; Gebhardt, W.; Galazka, R. R. Study of the 2.0-eV photoluminescence band in Cd_{1-x}Mn_xTe semiconductor alloys. *Phys. Rev. B: Condens. Matter Mater. Phys.* **1982**, *26*, 3165–3171.

(39) Beaulac, R.; Archer, P. I.; Ochsenein, S. T.; Gamelin, D. R. Mn²⁺-Doped CdSe Quantum Dots: New Inorganic Materials for Spin-Electronics and Spin-Photonics. *Adv. Funct. Mater.* **2008**, *18*, 3873–3891.

(40) Nag, A.; Chakraborty, S.; Sarma, D. D. To Dope Mn²⁺ in a Semiconducting Nanocrystal. *J. Am. Chem. Soc.* **2008**, *130*, 10605–10611.

(41) Tanaka, K.; Takahashi, T.; Kondo, T.; Umeda, K.; Ema, K.; Umabayashi, T.; Asai, K.; Uchida, K.; Miura, N. Electronic and Excitonic Structures of Inorganic–Organic Perovskite-Type Quantum-Well Crystal (C₄H₉NH₃)₂PbBr₄. *Jpn. J. Appl. Phys.* **2005**, *44*, 5923–5932.

(42) Wang, Q.; Zhang, X.; Jin, Z.; Zhang, J.; Gao, Z.; Li, Y.; Liu, S. F. Energy-Down-Shift CsPbCl₃:Mn Quantum Dots for Boosting the Efficiency and Stability of Perovskite Solar Cells. *ACS Energy Lett.* **2017**, *2* (7), 1479–1486.

(43) Yuan, Z.; Shu, Y.; Tian, Y.; Xin, Y.; Ma, B. A facile one-pot synthesis of deep blue luminescent lead bromide perovskite microdisks. *Chem. Commun.* **2015**, *51*, 16385–16388.

(44) Gonzalez-Carrero, S.; Mínguez Espallargas, G.; Galian, R. E.; Pérez-Prieto, J. Blue-luminescent organic lead bromide perovskites: Highly dispersible and photostable materials. *J. Mater. Chem. A* **2015**, *3*, 14039–14045.

(45) Shannon, R. D. A Revised Effective Ionic-Radii and Systematic Studies of Interatomic Distances in Halides and Chalcogenides. *Acta Crystallogr., Sect. A: Cryst. Phys., Diffraction, Theor. Gen. Crystallogr.* **1976**, *32*, 751–767.

(46) Magana, D.; Perera, S. C.; Harter, A. G.; Dalal, N. S.; Strouse, G. F. Switching-On Superparamagnetism in Mn/CdSe Quantum Dots. *J. Am. Chem. Soc.* **2006**, *128*, 2931–2939.

(47) Norris, D. J.; Yao, N.; Charnock, F. T.; Kennedy, T. A. High-Quality Manganese-Doped ZnSe Nanocrystals. *Nano Lett.* **2001**, *1*, 3–7.

(48) Stowell, C. A.; Wiacek, R. J.; Saunders, A. E.; Korgel, B. A. Synthesis and Characterization of Dilute Magnetic Semiconductor Manganese-Doped Indium Arsenide Nanocrystals. *Nano Lett.* **2003**, *3*, 1441–1447.

(49) Nag, A.; Sapra, S.; Nagamani, C.; Sharma, A.; Pradhan, N.; Bhat, S. V.; Sarma, D. D. A Study of Mn²⁺ Doping in CdS Nanocrystals. *Chem. Mater.* **2007**, *19*, 3252–3259.

(50) Jana, A.; Mittal, M.; Singla, A.; Sapra, S. Solvent-free, mechanochemical syntheses of bulk trihalide perovskites and their nanoparticles. *Chem. Commun.* **2017**, *53*, 3046–3049.

(51) Walsh, A.; Scanlon, D. O.; Chen, S.; Gong, X. G.; Wei, S.-H. Self-regulation mechanism for charged point defects in hybrid halide perovskites. *Angew. Chem., Int. Ed.* **2015**, *54*, 1791–1794.

(52) Buin, A.; Pietsch, P.; Xu, J.; Voznyy, O.; Ip, A. H.; Comin, R.; Sargent, E. H. Materials Processing Routes to Trap-Free Halide Perovskites. *Nano Lett.* **2014**, *14*, 6281–6286.

Cite this: *J. Mater. Chem. C*, 2021,
9, 348

The metal halide structure and the extent of distortion control the photo-physical properties of luminescent zero dimensional organic-antimony(III) halide hybrids†‡

Anupam Biswas,^{ab} Rangarajan Bakthavatsalam,^{ab} Bhupendra P. Mali,^{ab}
Vir Bahadur,^{ab} Chinmoy Biswas,^c Sai Santosh Kumar Raavi,^{id c}
Rajesh G. Gonnade^{id ab} and Janardan Kundu^{id *d}

Antimony(III) halide based zero dimensional hybrids have gained attention as broadband emitters. Until now, quadrangular pyramidal SbX_5 based and octahedral SbX_6 based 0D hybrids have been reported utilizing different organic ligands demonstrating some structural tunability affecting their emissive properties. Utilizing a common organic ligand, here we demonstrate the structural tunability (quadrangular pyramidal, octahedral, or a combination thereof) of the metal halide unit in $Sb(III)Cl$ 0D hybrids with contrasting photo-physical properties (broadband, Stokes shift, strong/weak colored emission). The structure–property–mechanism correlation of the synthesized compounds [**1** ($C_{12}H_{52}Cl_{18}N_8O_4Sb_3$; tris Sb green); **2** ($C_{12}H_{50}Cl_{14}N_8O_3Sb_2$; tris Sb red); **3** ($C_{24}H_{88}Cl_{25}N_{16}O_4Sb_3$; tris Sb yellow)] identifies crucial factors that control their emissive properties. The X-ray analysis reveals the structure (**1**-octahedral; **2**-quadrangular pyramidal; **3**-combination thereof) and the order of the extent of structural distortion as **1–3** \ll **2**. The metal halide coordination environment asymmetry and its structure are observed to dictate PL emission energy (**1**-green; **2**-red; **3**-yellow) as supported by a qualitative Molecular Orbital scheme. The extent of structural distortion guides the observed Stokes shifts (1–165 nm; 2–290 nm; 3–200 nm; **1–3** $<$ **2**). Interestingly, the extent of distortion is found to be well correlated with the observed PLQY (1–45%; 2–6%; 3–43%; **1–3** \gg **2**). This report clearly demonstrates the structural tunability and the effect of the metal halide unit structure/distortion in shaping the emissive properties of 0D organic $Sb(III)$ halide hybrids.

Received 20th July 2020,
Accepted 16th November 2020

DOI: 10.1039/d0tc03440a

rsc.li/materials-c

Introduction

Recently, low dimensional organic-metal halide hybrids (OMHH) have emerged as a new class of materials with exquisite properties enabling optoelectronic applications in photovoltaics and solid state lighting.^{1–6} Dimensionality in such organic–metal halide hybrid materials refers to the electronic dimensionality/networked

structure of the constituent metal halide inorganic unit (*i.e.* 2D, 1D, 0D). For zero dimensional (0D) variants of such materials, the semiconducting metal halide unit is isolated and surrounded by organic ligands. Photo-excitation of such low dimensional hybrids leads to the generation of strongly bound excitons confined within the metal halide unit.⁷ Strong electron–phonon coupling in such materials allows transient localization of the charge carriers (electrons, holes) in the metal halide unit by introducing local distortions of the lattice. The self-trapped excitons (STEs), thus produced, lead to phonon emission that alters the energy of the photoluminescence (PL) emission. This primarily leads to Stokes shifted broadband visible emission.^{8–12} Various factors that govern the PL emission energy and photoluminescence quantum yield (PLQY) of such broadband emission are not clearly understood.^{1,13–15} However, it is generally observed that the PLQY tends to be enhanced as the dimensionality is lowered.^{2,14,16} Typically, lead halide based low dimensional (2D, 1D, 0D) hybrids have been reported to manifest emissive properties corroborating to the STE based broadband emission with a modest/high

^a CSIR-National Chemical Laboratory, Pune, India^b Academy of Scientific and Innovative Research (AcSIR), Ghaziabad, India^c Indian Institute of Technology Hyderabad, Kandi, India^d Indian Institute of Science Education and Research (IISER) Tirupati, Tirupati, India. E-mail: janardan@iisertirupati.ac.in

† This paper is dedicated to all the brave individuals working tirelessly to win the battle against COVID-19 Pandemic.

‡ Electronic supplementary information (ESI) available: Experimental details and additional characterizations of compounds **1**, **2**, and **3**. CCDC Single crystal structure file for **1** (CCDC 2017736), **2** (CCDC 2017737), **3** (CCDC 2017738). For ESI and crystallographic data in CIF or other electronic format see DOI: 10.1039/d0tc03440a

PLQY.¹⁷ Noteworthy, for a given metal ion, the accessibility of a desired dimensionality in such systems is largely dictated by the choice of halides, organic ligands, and experimental reaction conditions.^{15,18,19}

The toxicity²⁰ of Pb(II) has instigated many research initiatives for the development of the lead free variant of low dimensional OMHH materials.^{21–23} Suitable replacements for Pb²⁺ ions in such hybrids must retain the ns² electronic configuration of the valence shell that has been touted as the key role player in conferring enabling properties to the lead-based low dimensional hybrids.²⁴ Recently, Sb³⁺ and Bi³⁺ ions that are less susceptible to oxidation while retaining the ns² valence electronic configuration have been introduced as replacements for Pb²⁺ ions.^{7,25–27} There have been few reports on low dimensional Sb(III) chloride based organic hybrids that have strong, long lived, Stokes shifted, and broadband STE based ambient emission.^{7,26–32} Interestingly, all of these 0D antimony chloride hybrids show triplet STE based broadband emission with a high/modest PLQY. They all demonstrate the structural commonality of having individual metal-halide units ([SbCl₅]²⁻, [SbCl₆]³⁻) that are completely isolated from each other and surrounded by the respective organic ligands. The quadrangular pyramidal metal halide unit in these reports has Sb–Cl equatorial bonds with very similar bond lengths and a shorter Sb–Cl axial/apical bond with a low/modest variation of bond angles from their ideal values. Similar bond length and bond angle distortions are observed for the octahedral metal-halide units. Such distortion of the metal halide unit likely arises due to the presence of an Sb centred stereochemically active lone pair.^{33,34} This might imply that the strong PL emission properties may be correlated to the ground state structure/distortion of the metal-halide unit. Antimony(III) halides are known to exist in different stoichiometric polyhedral units ([SbX₄]⁻, [SbX₅]²⁻, [SbX₆]³⁻, [Sb₂X₉]³⁻) in the solid state.³⁵ Given the various possible polyhedral unit types in these hybrids, is there any correlation that exists between the luminescence properties and the geometric structure/distortion of the metal-halide unit? How does the presence/absence of distortion in the metal-halide unit affect the PLQY and Stokes shift of the emission band? Research efforts aimed at answering these questions (tunability of the metal halide unit structure: octahedral or quadrangular pyramidal, and factors that affect emissive properties) are of current importance.^{29,36–38} In an effort to demonstrate structural tunability (octahedral, quadrangular pyramidal) and to rationalize the photo-physical origins of the observed emissive properties, we have synthesized various Sb(III) chloride 0D hybrids utilizing a common organic ligand and have analyzed the correlation between the specific structural features of the metal-halide unit and their luminescence properties. Here, we have utilized Tris(2-aminoethyl)amine as the common ligand to synthesize different 0D hybrids:

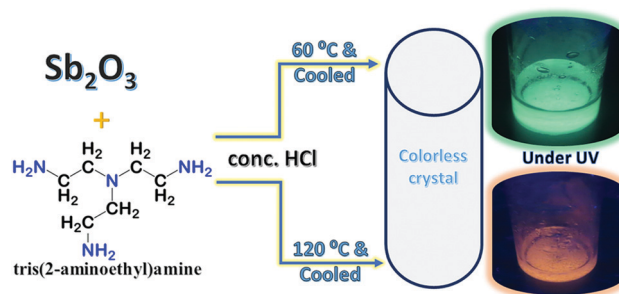
1 [(C₆H₂₂N₄)₂ (Sb₂Cl₁₀) (SbCl₆) (Cl)₂ (H₃O)]·(3H₂O); tris Sb green); **2** [(C₆H₂₂N₄)₂ (SbCl₆)₂ (Cl)₂]·3(H₂O); tris Sb red); **3** [(C₆H₂₂N₄)₄ (SbCl₆)₃ (Cl)₇]·4(H₂O); tris Sb yellow); with different structural and emissive properties. These compounds show long lived broadband emission, likely due to the self-trapping

of excitons (STEs). However, the peak of the broadband emission and their PLQYs are markedly different (**1**: green emission with PLQY ~ 45%; **2**: red emission with PLQY ~ 6%; **3**: yellow emission with PLQY ~ 43%). The single crystal structure analysis of the synthesized compounds reveals that the hybrids have different metal-halide unit structures with different extents of distortion: **1** has a combination of isolated, undistorted octahedron and distorted edge shared dimer octahedra; **2** has a combination of isolated heavily distorted octahedron and isolated heavily distorted pyramid; **3** has a combination of isolated undistorted octahedron, slightly distorted octahedron and slightly distorted quadrangular pyramid. The estimated extent of metal halide unit distortions (bond lengths, bond angles) follows: **1–3** << **2** clearly highlighting the role of the metal halide unit structural symmetry of the coordination environment (octahedron vs. quadrangular pyramid) and the absence of distortion of the metal halide unit in affecting the PL emission energy, and the PLQY of their emission, respectively. The utilized reaction chemistry here allows us to crystallize different 0D hybrids wherein any crucial electronic contribution from the organic ligand towards photoluminescence remains constant. Noteworthy, demonstrated here is structural tunability (SbX₅, SbX₆ unit) with its concomitant effect on photo-physical properties that allow us to identify the crucial role played by ground state structural symmetry and the extent of distortion of the metal halide unit in dictating their emissive properties.

Results and discussion

Antimony(III)chloride 0D hybrids were synthesized utilizing Sb₂O₃ and Tris(2-aminoethyl)amine as the ligand in concentrated HCl acid. Single crystals of **1** tris Sb green can be obtained when the reaction temperature is set at 60 °C while clear single crystals of **2** tris Sb red result when the reaction temperature is set at 120 °C (see Scheme 1). Extensive details of the utilized synthetic conditions are provided in the Experimental section.

Product **1** tris Sb green shows strong, green emission while the **2** tris Sb red sample shows weak, red emission when viewed inside the UV chamber. The presence of Sb ions in products **1**



Scheme 1 Reaction scheme utilized for the synthesis of single crystals of **1** tris Sb green and **2** tris Sb red samples wherein metal : ligand ratio = 1 : 1. The structure of the ligand is shown.

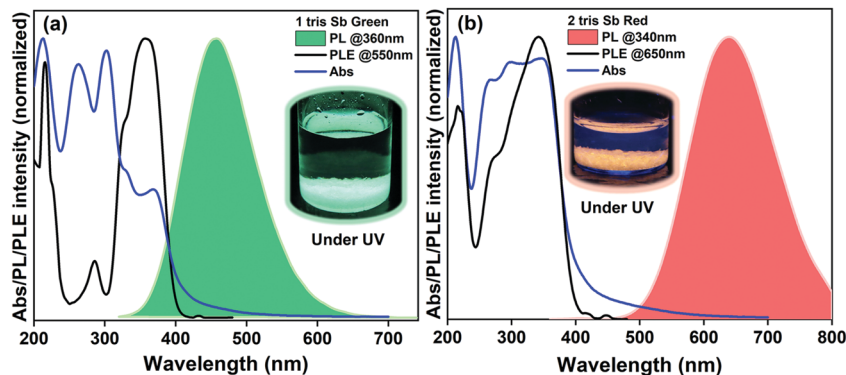


Fig. 1 Absorbance (Abs), photoluminescence (PL) and photoluminescence excitation (PLE) spectra of (a) **1** tris Sb green and (b) **2** tris Sb red single crystal samples.

and **2** was verified using SEM/EDS analysis as shown in Fig. S1, ESI.† Furthermore, XPS analysis confirms the presence of Sb(III) metal ions in **1**, **2** as shown in Fig. S2, ESI.† The ^1H NMR spectra of **1**, **2** reveal the presence of phase pure products with peaks attributed to the cationic ligand moiety (Fig. S3(a–d), ESI.†). The thermogravimetric analysis (TGA) of **1** and **2**, as shown in Fig. S4, ESI.† shows a multistep weight loss profile. Here, the onset of weight loss observed at $\sim 100^\circ\text{C}$ for both **1**, **2** is attributed to the loss of water molecules, followed by ligand loss at $\sim 200^\circ\text{C}$ and plausibly halogen loss at temperatures above 300°C (see below for a discussion on the structure of products). The optical properties of **1** tris Sb green, presented in Fig. 1a, show a strong and broad photoluminescence (PL) emission band centered at 517 nm with a full width at half maximum (FWHM) of ~ 110 nm. The photoluminescence excitation (PLE) spectra, collected at 530 nm, match well with the absorption spectra which show multiple features in the 300–400 nm range. The estimated “Stokes shift” (difference between the peak positions of PL and PLE) is ~ 165 nm. The photoluminescence quantum yield (PLQY) for **1** tris Sb green is estimated to be $\sim 45\%$. On the other hand, the optical properties of **2** tris Sb red, presented in Fig. 1b, show a weak and broad emission band centered at 638 nm with a FWHM of ~ 160 nm. The PLE spectra, collected at 650 nm, match well with the absorption spectra which show multiple features in the 300–400 nm range. The estimated “Stokes shift” is ~ 290 nm and the PLQY for **2** tris Sb red is estimated to be $\sim 6\%$.

The absorption features in halogen antimonite(III) systems can be attributed to the electronic transitions between the sp excited states and the s^2 ground state. The observed absorbance features for products **1** and **2** can be tentatively attributed to the A band (low energy, spin-forbidden transition $^1\text{S}_0 \rightarrow ^3\text{P}_1$), B band (intermediate energy, spin-forbidden transition $^1\text{S}_0 \rightarrow ^3\text{P}_2$), and C band (high energy, spin-allowed transition $^1\text{S}_0 \rightarrow ^1\text{P}_1$).³⁹ Rationalization of the differences in the observed PL emission peak position, Stokes shift, and PLQYs for products **1** and **2** is discussed below.

The lifetime decay profiles (collected using the TCSPC set-up) and the extracted lifetimes across the broadband emission for **1** and **2**, as presented in Fig. S5(a–d) (ESI.†), show a

dominant lifetime component of ~ 1 microsecond that remains unchanged across the emission band for **1** and **2**. In order to better estimate the longer lifetimes, PL decay profiles were collected across the broadband utilizing a microsecond (μs) flash lamp source and are presented in Fig. S6 and Table S1; ESI.† Clearly, lifetime components (and relative %) of $4.8 \mu\text{s}$ (73%) and $71.9 \mu\text{s}$ (27%) were observed for **1** tris Sb green while for **2** tris Sb red the lifetime components (and relative %) were $5.6 \mu\text{s}$ (90%) and $94.4 \mu\text{s}$ (10%). The observed long emission lifetime components in products **1** and **2** highlight the role played by the triplet excited state ($^3\text{P}_1$) from which the radiative emission (phosphorescence) originates (Fig. S5, S6 and Table S1; ESI.†). Given the broad nature of the PL emission band for both **1** and **2**, it is important to decipher if defect emission leads to the observed broad emission bandwidth. The dependence of the emission band shape/profile on excitation wavelength was studied for products **1** and **2** as presented in Fig. S7a and b, ESI.† The PL emission band shape/profile remains unchanged for products **1** and **2** (albeit with a concomitant change in PL intensity) as across the excitation wavelength range of 320–380 nm. The PLE spectra collected across the broad emission band of products **1** and **2** (Fig. S7a and b, ESI.†) also remain unchanged. Furthermore, the estimated lifetime components for products **1** and **2** across the broad emission band were found to remain unchanged (Fig. S5, S6 and Table S1; ESI.†). These observations suggest that unique emissive species are responsible for the broad emission in products **1** and **2** and very likely do not involve extrinsic defects. Furthermore, PL/PLE studies were performed for products **1** and **2** wherein the single crystal samples were ground. If defects are the cause for the broadband emission, sample grinding would cause a substantial change of the PL/PLE profile.¹⁰ However, no changes in the PL/PLE band profile for both the products were observed when the samples were ground thoroughly as shown in Fig. S8, ESI.† Also, the ground samples of both the products were annealed at different temperatures, followed by their PL/PLE characterizations, as shown in Fig. S8, ESI.† Again here, no changes in the PL/PLE band profile are observed (albeit with a concomitant change in PL intensity@ 100 – 120°C attributed to solvent loss as discussed later). These observations clearly

suggest that the broad emission is not due to the presence of the defects in products **1** and **2** but is due to the presence of unique emissive species that lead to intrinsic broadband emission.

The broadband emissions in low dimensional metal halide hybrid materials have been attributed to the self-trapping of excitons (STE) due to strong electron–phonon coupling that produces transiently localized charges (holes/electrons) that distort the metal halide unit. The PL emission of these self-trapped excitons is phonon assisted that broadens the radiative bandwidth.⁹ Upon photoexcitation, the low lying transient STE states can accept carriers from the excited 3P_1 state and allow slow and phonon assisted radiative decay to the 1S_0 ground state, thereby broadening the emission bandwidth. Necessarily, this relay of the radiative decay channel leads to finite energy losses through non-radiative state hopping and accounts for a finite Stokes shift in broad emitting low dimensional materials. Importantly, this is in addition to any Stokes shift that might arise due to the changes in the excited state geometry/structure relative to the ground state structure (as discussed later).

Low temperature PL measurements were carried out to gain further insights into the phonon assisted radiative recombination of STEs leading to the broadband emission in **1** and **2**. Steady state photoluminescence spectra were collected over the temperature range of 300–77 K as shown in Fig. S9, ESI.† Integrated PL peak area and FWHM were calculated for both products (**1**, **2**) and are presented in Fig. 2(a and b). For both products, the PL intensity is initially observed to increase reaching the maxima (~ 230 K), followed by a decrease, as the temperature is lowered (to 80 K). Such dependence of PL intensity can be ascribed to the thermally activated trapping–detrapping of excitons from STE states.¹⁰ However, the dependence in the low temperature regime can get complicated due to tunneling and defect bound excitons.¹⁰ Moreover, the phonon modes that couple to electronic excitation to generate STE have their own temperature dependence.⁴⁰ Bandwidths (FWHMs) of the broad emission of **1** and **2** are observed to decrease monotonically as the temperature is lowered. As the temperature is lowered fewer phonon modes are thermally accessible to couple to the STEs assisting radiative recombination, thereby reducing the bandwidth of the PL emission. Furthermore, the lifetime of the emission for both products **1** and **2** are observed to lengthen at a lower temperature (Fig. S10; ESI.†).

This could suggest thermal equilibrium between the triplet excitons and self-trapped excitons that governs the thermally activated trapping of triplet excitons in the STE states. These results cumulatively indicate intrinsic broadband STE based emission in accord with many other reports on low dimensional organic–inorganic (Sb, Pb, Sn) hybrids showing broadband emission.^{7,10,14,27,28,36,41,42} Further detailed experiments and analyses are needed to characterize⁴³ the nature of the STE in these systems.

A clear understanding of the structure of the obtained products can potentially provide an insight into the PL peak positions (green vs. red), large Stokes shift, and markedly different PLQYs of **1** and **2**. Fig. 3 shows an overview of the single-crystal structure of the products **1** (CCDC 2017736), and **2** (CCDC 2017737)† with the details of the bond angles, bond lengths, *etc.* provided in Tables S3–S8; ESI.† Both the products are zero-dimensional in nature, wherein the organic ligands surround the metal halide unit. **1** tris Sb green crystallized in a triclinic centrosymmetric space group $P\bar{1}$ containing one ligand ($C_6H_{22}N_4$ with +4 charge), one unit of $SbCl_5$ (with -2 charge), a half unit of $SbCl_6$ (-1.5 charge), one Cl anion (-1 charge), one water molecule, and one $H_{2.5}O$ molecule ($+1/2$ charge) in the asymmetric unit. The H atom of the charged water molecule ($H_{2.5}O$) is located at the inversion center (0.5, 0.5, 0.5) and shared between the two water molecules, which are related by inversion symmetry across the inversion center. The moiety formula of **1** tris Sb green is represented as $[(C_6H_{22}N_4)_2(Sb_2Cl_{10})(SbCl_6)(Cl)_2(H_3O)] \cdot (3H_2O)$. The structure of **1** tris Sb green is composed of two basic building units of the antimony chloride framework: isolated **octahedron** and isolated edge shared **octahedra** (Fig. 3b and c). In the isolated octahedron, the Sb1 atom occupies a special position (0.5, 1.0, 1.0) across the inversion center and hence only half of the $SbCl_6$ moiety is present in the asymmetric unit and the other half unit is generated by inversion operation, whereas the other $SbCl_5$ moiety generates an edge-shared dimeric octahedral unit by inversion operation. These metal halide units, periodically embedded in the organic ligand matrix, also incorporate solvent water molecules. The crystal structure is governed by strong $N-H \cdots Cl$ hydrogen bonding interactions engaging the ligand $N-H$ moieties and Cl atoms (Table S9, ESI.†). The view of the molecular packing down the *b*-axis shows the layered

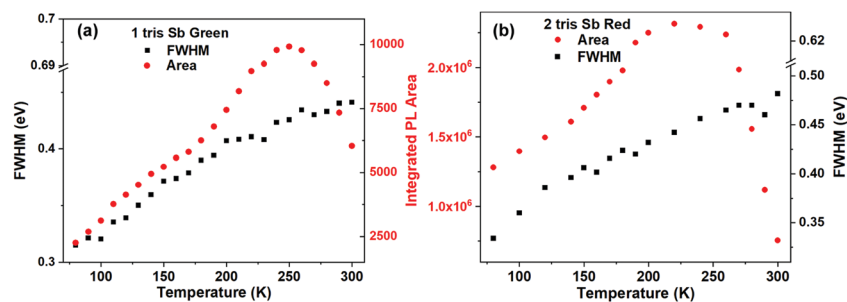


Fig. 2 Integrated PL peak area and FWHM of the broad PL peak for (a) 1 tris Sb green and (b) 2 tris Sb red powder samples as a function of temperature (300–80 K).

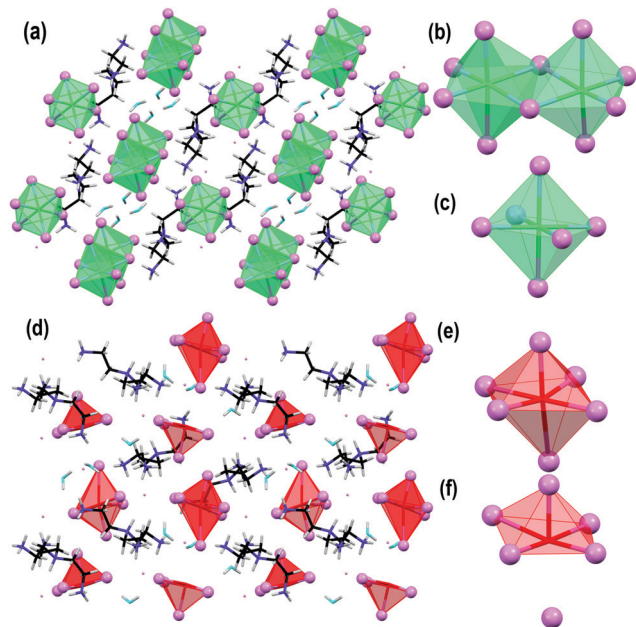


Fig. 3 Single crystal structures of zero dimensional chloro antimonite(III)-organic hybrids for (a–c) **1** tris Sb green and (d–f) **2** tris Sb red. Shown also are the metal halide units (octahedra and dimer octahedra for **1** tris Sb green; distorted octahedra and distorted pyramid for **2** tris Sb red) for both the products.

assembly of the ligand molecules along the *a*-axis, which accommodate the octahedra and the edge-shared dimeric octahedral units between its layers alternately parallel to the *c*-axis. The arrangement of the neighboring edge-shared dimeric octahedral units along the channel encapsulates the water molecules between them which interact with these metal halide units through O–H···Cl hydrogen bonding interactions (Table S9, ESI†). Conversely, the non-bonded Cl ions are located in the space between the two octahedral units along the channel parallel to the *a*-axis and forms a N–H···Cl hydrogen bond with the ammonium protons. These strong hydrogen bonding interactions govern the crystal packing (Fig. S11a, ESI†) and play a crucial role in optoelectronic responses. The loss of these water molecules at ~100–120 °C, as evidenced in the TGA profile (Fig. S4, ESI†), could be due to their encapsulation in the open channel leading to the drastic loss of the PL intensity of the annealed sample **1** (Fig. S8, ESI†). The extent of distortion (bond lengths, bond angles) in the monomeric and dimeric octahedra was estimated for **1** tris Sb green. The monomeric octahedron is almost **undistorted** with very similar Sb–Cl bond lengths (largest difference in Sb–Cl bond length = 0.01 Å, largest deviation of the Cl–Sb–Cl bond angle from the ideal value = 3°). The edge shared dimeric octahedron with six different Sb–Cl bond lengths shows slight **distortions** (largest difference in Sb–Cl bond length = 0.6 Å, largest deviation of the Cl–Sb–Cl bond angle from the ideal value = 6°). Such distortions are not unexpected in the edge shared (μ -Cl) dimeric octahedral metal halide unit. The phase purity of **1** was verified using the powder X-ray diffraction (PXRD) patterns, which matched well with the simulated ones in terms of the single-crystal X-ray data as shown in Fig. S12; ESI†.

Product **2** tris Sb red crystallizes in a monoclinic chiral space group $P2_1$ containing two ligands (tetra positive), two $[\text{SbCl}_6]^{3-}$ anions, two $[\text{Cl}]^-$ anions, and three H_2O molecules in the asymmetric unit having the formula $[(\text{C}_6\text{H}_{22}\text{N}_4)_2(\text{SbCl}_6)_2(\text{Cl})_2] \cdot 3(\text{H}_2\text{O})$. The structure of **2** is composed of two basic building units of antimony chloride with a hexa-coordinated motif: isolated *very* distorted **octahedron** and isolated extremely distorted **octahedron** (Fig. 3e and f). For the later motif, the sixth coordination site is occupied by a distant Cl atom (3.156 Å) as highlighted in Fig. 3f and may be thought of as an extremely distorted ‘quadrangular pyramidal’ unit. The isolated very distorted octahedron with a lengthened apical Sb–Cl bond length (3.042 Å) may also be thought of as a distorted ‘quadrangular pyramidal’ structure. The presence of such long Sb–Cl bond distances is not uncommon and has been attributed to the secondary bonding interaction.⁴⁴ These distortions highlight the site asymmetry in the coordination environment of the hexacoordinated Sb motifs. These metal halide units are again periodically embedded in the inert matrix of the organic ligand incorporating water molecules forming the 0D structure. The view of the molecular packing down the *a*-axis revealed the layered arrangement of both metal halides parallel to the *b*-axis which are embedded between the channels formed by symmetry independent organic ligands. The respective layers of metal halides are arranged alternately along the *c*-axis. The crystal structure is stabilized by strong intermolecular N–H···Cl hydrogen bonding interactions engaging ammonium H-atoms of the organic ligand and Cl atoms (of metal halides) or Cl ions (Fig. S11b, ESI†). The three water molecules also form strong H-bonding interactions (O–H···Cl and N–H···O) involving Cl atoms and ammonium protons of metal halides and organic ligands, respectively. The water molecules also interact with each other through O–H···O hydrogen bonds (Table S9, ESI†). The loss of the water molecules at ~100–120 °C, as evidenced in the TGA profile (Fig. S4, ESI†), leads to a drastic loss of the PL intensity of the annealed sample **2** (Fig. S8, ESI†). The extent of distortion in the heavily distorted octahedron and the extremely distorted octahedron was estimated for **2** tris Sb red. The heavily distorted octahedron shows high site asymmetry with six different Sb–Cl bond lengths (largest difference in Sb–Cl bond length = 0.6 Å, largest deviation of the Cl–Sb–Cl bond angle from ideal value = 23°), thereby approaching a ‘quadrangular pyramidal’ structure. The extremely distorted octahedron shows extreme site asymmetry with very different Sb–Cl bond lengths (largest difference in Sb–Cl bond length = 0.45 Å, largest deviation of Cl–Sb–Cl bond angle from the ideal value = 10°). The ‘apical’ Sb–Cl bond length in this unit is 2.448 Å. The phase purity of **2** was confirmed using the PXRD patterns which matched well with the simulated ones in terms of the single-crystal X-ray data as shown in Fig. S12; ESI†.

Comparison of the above estimated ground state structural distortions of the photoactive metal halide units reveals that the average distortion is appreciably higher in **2** tris Sb red and is relatively lower in **1** tris Sb green product (Fig. S13, ESI†). In essence, **1** tris Sb green has undistorted octahedral metal halide units, while **2** tris Sb red has distorted quadrangular

pyramid units. The presence of the common organic ligand in **1** and **2** allows us to perform a structure–property–mechanism correlation that can provide us with a deeper understanding of the crucial factors that control their photo-physical properties. Understandably, the extent of distortion and the ground state structure affect Stokes shifts and PL emission energies. It is clear from Fig. 1 that both products (**1**, **2**) show a large Stokes shift implying strong structural re-organization in the excited state (3P_1). The observed Stokes shift is much higher for **2** tris Sb red (~ 290 nm) than that of **1** tris Sb green (~ 165 nm) suggesting stronger excited state reorganization for **2** than that for **1**. Clearly, Stokes shift depends not only on the ground state structure (and its distortion) but also on the structure in the excited state of the metal halide unit. Within the theoretical framework of ns^2 metal ions, as proposed by Blasse *et al.*, the luminescence properties are directly related to the structure and the extent of distortion of the ns^2 metal-halide unit.^{45–47} Upon photo-excitation of these ns^2 metal-halide units, the ground state s^2 configuration is transformed into sp excited state with higher symmetry.^{39,45} Gaining this structural symmetry due to photo-excitation from the distorted ground state structure results in the observed Stokes shift. Clearly, the ground state structural distortion in **2** tris Sb red is relatively higher than that in **1** tris Sb green and is in accord with the observed larger Stokes shift in the former. A similar approach has been successfully utilized by Blasse *et al.* for ns^2 metal ions doped in host lattices that show large Stokes shifts if the metal ions occupy off-center positions in large interstices as these ions can move towards the center in the excited state, thereby gaining symmetry.⁴⁵ The difference in the PL emission energies (peak positions) for the two products (**1**, **2**) can again be rationalized in terms of the ground state structure. Typically, the structures of these s^2 metal halide units are affected by the presence of the metal centered, stereochemically active lone pair. However, s^2 complexes with a coordination number of six have octahedral geometry and appear as an exception from the VSEPR model.^{39,48} Complexes with coordination numbers lower than six are in general agreement with the VSEPR model and show distortions/asymmetry in their structures due to the stereochemical activity of the lone pair.^{39,49,50} These considerations are also applicable to halogen antimonite(III) polyhedral units here that constitute the photoactive building units for products **1**, **2**. For **1** tris Sb green, the metal halide coordination sphere has octahedral geometry with slight differences in the Sb–Cl bond lengths (undistorted octahedron and distorted dimeric octahedra). However, for **2** tris Sb red, the metal halide coordination sphere shows extreme site asymmetry ('quadrangular pyramidal' structure) with modest differences in the Sb–Cl bond lengths (both octahedral units approaching the quadrangular pyramidal structure). Clearly, the 'effective' interaction strength of Cl^- anions (3s, 3p orbitals) with the Sb^{3+} (5s, 5p orbitals) metal ion will be stronger for **1** tris Sb green (near ideal octahedral units with less bond length distortions) compared to **2** tris Sb red (heavy/extreme distortions in octahedral units that approach the 'quadrangular pyramidal' structure) due to the degree of asymmetry in the metal-halide

coordination environment. A symmetrically stronger 'effective' interaction between the metal and the halide in **1** will lead to a higher energy gap between the HOMO and LUMO. An asymmetric and weaker metal halide interaction in **2** will result in a smaller energy difference between the HOMO and LUMO (the qualitative molecular orbital diagrams for octahedral and square pyramidal structural cases are shown in Fig. S14, ESI†). Hence, it is anticipated that **1** tris Sb green, with a symmetrical octahedral structure, would display a high energy PL emission (LUMO \rightarrow HOMO) peak while **2** tris Sb red, with an asymmetric quadrangular pyramidal structure, will emit at lower energies. This is in qualitative agreement with the observed high energy PL emission peak of **1** tris Sb green ($\lambda_{em} = 517$ nm) and low energy PL emission peak of **2** tris Sb red ($\lambda_{em} = 638$ nm). Such a ground state structure dependent molecular orbital scheme has been successfully utilized in attributing differences in the PL emission energies of $[SbCl_6]^{3-}$ and $[SbCl_4]^-$ ions in solution.³⁹ It is worth noting here that a symmetrical (undistorted) octahedral halide ligand field will lead to a higher HOMO–LUMO energy gap than an undistorted square pyramidal ligand field. This again is in qualitative agreement with the reported low PL emission energies for many $[SbCl_5]^{2-}$ based metal halide organic OD hybrids (with emission energies in the orange region of 600–650 nm) in solid state and higher PL emission energies in the green region for $[SbCl_6]^{3-}$ based ions in solution.³⁹

The photoluminescence quantum yield (PLQY) of **1** tris Sb green is ($\sim 45\%$) distinctly higher than that of **2** tris Sb red ($\sim 6\%$). Note that the observed PLQY for **1** tris Sb green is lower than those reported in the literature^{7,26–28} on OD antimony chloride hybrids that have a near unity PLQY. However, a direct comparison of the PLQY of **1** tris Sb green with these other reports including different organic ligands might not lead to the required understanding of the rationale behind the observed differences in their PLQYs. This is due to the surrounding environment, provided by the organic ligand to the photoactive metal halide unit, that can appreciably affect the PL emission intensity. There can be effective energy transfer of electron excitation from the molecular levels of the surrounding organic moiety to the 3P_1 luminescence level of the s^2 metal ion, thereby enhancing the PLQY.^{51,52} 'Loan' of luminescence intensity from the ligands to the metal has also been reported wherein ligand to metal charge transfer interactions lead to additional thermal population of the luminescent excited state of metal ions leading to an enhanced PLQY.^{53,54} This clearly suggests the electronic contribution of the surrounding organic ligand in affecting the photoluminescence intensity in the low dimensional OMHH.⁵⁴ Interestingly, the synthetic strategy utilized here allows the crystallization of both **1** and **2** incorporating the same organic ligand. This, to a large extent, helps maintain the same electronic contribution (if any) to the metal ion, thereby similarly affecting the photoluminescence intensity from **1** and **2**. Hence, the PLQYs of **1** and **2** can be compared and possibly correlated to their structure/distortion to gain some insights into the observed differences in their PLQYs. This effort of finding any existent correlation between structure/distortion and PLQY is extremely

important for further design and synthesis of broadband, lead-free emitters and is reported for the first time here for Sb halide based 0D OMHH. Although there have been few reports on antimony chloride based 0D hybrids that show near unity PLQYs, none of the reports provide any insight into the observed PL peak position and the observed high PLQY. The commonality in all of these high PLQY low dimensional antimony chloride based hybrids is the presence of isolated, almost undistorted metal halide unit (particularly the SbX_3 unit).^{7,26–28}

Moreover, antimony chloride based low dimensional hybrids that have polymeric metal halide units (showing distortions) have a low/modest emission strength.^{51,52,55} In the present comparison of PLQYs of **1** and **2**, metal halide polyhedral units for **1** (isolated octahedra, dimer octahedra) show small distortions while metal halide polyhedral units for **2** (octahedra and quadrangular pyramid) show relatively higher distortions. The survey of the existing literature on antimony chloride based low dimensional materials, revealing that the isolated undistorted monomeric units demonstrate high emission intensities, suggests the importance of distortions in affecting the PLQY.^{51–54,56} Clearly, the extent of distortion in **1** is relatively lower than that in **2**. This implies a correlation of the structure/distortion with the PLQY for 0D Sb halide-based hybrids. Noteworthy, the presence of distorted dimer octahedra (plausibly suppressing the PLQY) along with almost undistorted octahedra (plausibly enhancing the PLQY) in **1** shows a higher PLQY compared to **2** having all isolated monomeric units (plausibly enhancing the PLQY) with heavy distortions (plausibly suppressing the PLQY). This again indicates the important role played by structural distortions in the ground state. The presence of the dimer octahedra with some distortions in **1** can then explain the observed lower than unity PLQY which is in accord with earlier reports⁵² on low dimensional antimony chloride hybrids with dimeric/polymeric metal halide units. The observed correlation of the structure/distortion with the PLQY could be rationalized in terms of photo-excitation of ns^2 metal ions transiting from the ground state to the excited state having higher symmetry. Hence, the smaller the distortions in the ground state structure of the metal halide polyhedra, the lower the amount of electronic excitation energy that will be utilized in the process of excited state structural reorganization. This will minimize non-radiative losses of the electronic excitation energy thereby enhancing the possibility of stronger luminescence. The above proposed rationalization providing insight to the experimentally observed correlation between structure/distortion and PLQY for 0D antimony chloride-based hybrids is by no means universal and needs to be further tested/verified. In order to clearly understand the role of distortion in affecting the PLQY, efforts are now being devoted to the design and synthesis of antimony chloride based 0D hybrids (utilizing a common organic ligand) that have only one type of isolated metal halide polyhedral unit but with different extents of distortion. This needs further exploratory synthetic efforts that are currently underway.

However, we have been successful in modifying our synthetic strategy that allows us to crystallize 0D hybrids with an

isolated monomeric metal-halide unit (albeit with a mixture of octahedral and pyramidal units). This is achieved by increasing the metal to ligand ratio to 1 : 10 as detailed in the Experimental section. The obtained product, **3** tris Sb yellow, appears to emit bright yellow light when viewed inside the UV chamber. The ^1H NMR spectra of **3** reveal the presence of phase pure products with peaks attributed to the cationic ligand moiety (Fig. S3(a–d), ESI \ddagger). The TGA data of **3**, as shown in Fig. S4, ESI \ddagger , show a multistep weight loss profile. Here, the onset of weight loss observed at ~ 100 °C for **3** is attributed to the loss of water molecules, followed by ligand loss at ~ 200 °C and plausibly halogen loss at temperatures above 300 °C. Notably, the continuous nature of the weight loss curve without clearly visible step-like features in the TGA plot for **3** and **2** might indicate the similarity of the binding interaction of the ligands and the halogens in the structures. The presence of water of crystallization in (**1**, **2**, **3**) allows us to assign the weight loss peaks at ~ 100 °C to the loss of water molecules from the structures. Furthermore, free halogens in the structures (**1**, **2**, **3**) allow us to tentatively attribute the weight loss at ~ 300 °C to be due to halogen loss as has been suggested in a recent report.³⁰ The steady state optical characterization of **3** tris Sb yellow, as shown in Fig. 4a, reveals a strong, broad yellow emission band centered at 580 nm with a full width at half maximum (FWHM) of ~ 140 nm. The PLE spectra, collected at 580 nm, match well with the absorption spectra which show multiple features in the 300–400 nm range. The estimated “Stokes shift” is ~ 200 nm and the PLQY for **3** tris Sb yellow is estimated to be $\sim 43\%$. The broad yellow emission profile remains unchanged as the excitation wavelength is changed. Furthermore, the PLE profile remains unchanged across the broadband emission (Fig. S15; ESI \ddagger). The PL and PLE profile remain unchanged upon solid state grinding and annealing (Fig. S16; ESI \ddagger). Moreover, the analysis of the collected decay profiles across the broad emission band of **3** tris Sb yellow, as presented in Fig. 4b, provides lifetime components (and relative%) of 5.2 μs (85%) and 84.6 μs (15%) that largely remain unchanged across the emission band (Table S10, ESI \ddagger). This indicates the presence of unique emissive species responsible for the observed phosphorescence in **3** tris Sb yellow. Notably, the PL emission energy of **3** tris Sb yellow sample represents an intermediate value when compared to those of **1** tris Sb green and **2** tris Sb red while the PLQY value is close to that of **1** tris Sb green.

Now, the pertinent question here is can we utilize the same structure/distortion correlation to understand the observed photo-physical properties for **3** tris Sb yellow. Such rationalization would then fall in line with the proposition made for products **1** and **2** and would support generality. The single crystal structure of **3** tris Sb yellow (CCDC 2017738) belongs to a triclinic space group $P\bar{1}$ containing four ligands (tetra positive), two units of half of the $[\text{SbCl}_6]^{3-}$ anion, two units of the $[\text{SbCl}_6]^{3-}$ anion, seven $[\text{Cl}]^-$ anions, and four $[\text{H}_2\text{O}]$ molecules in the asymmetric unit leading to $[(\text{C}_6\text{H}_{22}\text{N}_4)_4 (\text{SbCl}_6)_3 (\text{Cl})_7] \cdot 4(\text{H}_2\text{O})$ as the formula moiety (Fig. 4(c and d)). Two of the Sb atoms of the half units of the $[\text{SbCl}_6]^{3-}$ anion occupy a special

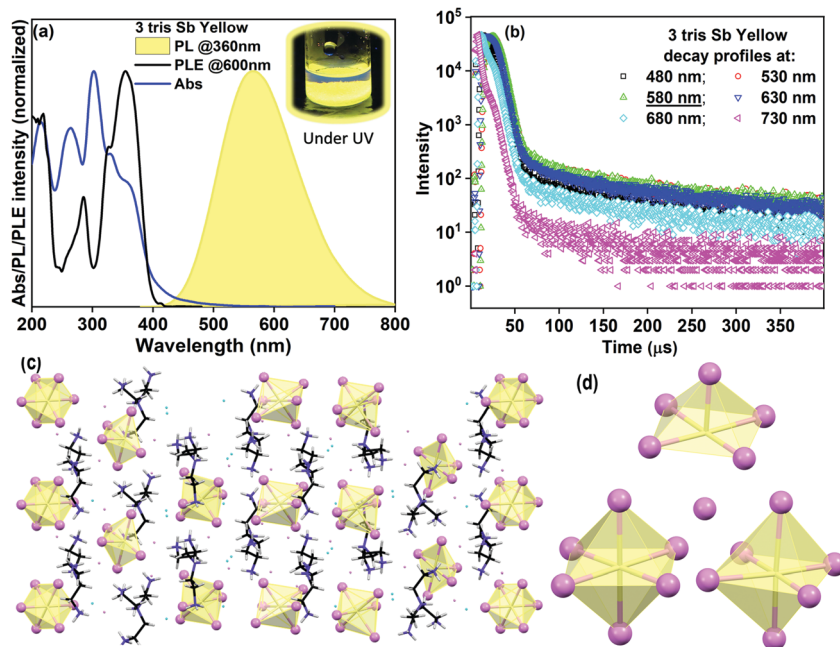


Fig. 4 Optical and structural characterization of **3** tris Sb yellow: (a) absorbance (Abs), photoluminescence (PL) and photoluminescence excitation (PLE) spectra; (b) lifetime decay profiles collected across the yellow emission band using microsecond flash lamp excitation (360 nm); (c) overview of the single crystal structure of 0D **3** tris Sb yellow product; and (d) metal halide units (distorted quadrangular pyramid, octahedra, and distorted octahedra) comprising the 0D structure.

position (inversion center), Sb1 (0.0, 0.5, 0.0) and Sb2 (0.0, 0.5, 0.5), and hence only a half unit is present in the asymmetric unit and the other half is generated by inversion operation. The structure of **3** is composed of isolated **octahedra** and an isolated heavily distorted octahedron (approaching the quadrangular pyramidal structure) as the basic building units (Fig. 4c, d and Fig. S14; ESI[†]). These metal halide units are periodically embedded in the channels of the organic ligand matrix and interact mostly with its ammonium H-atoms through N–H...Cl hydrogen bonds. The four water molecules are also encapsulated in the crystal lattice which interact with the ammonium H-atoms of the organic ligand through N–H...O hydrogen bonds (Table S9 and Fig. S11c, ESI[†]). In addition to the presence of the distorted ‘quadrangular pyramidal’ unit, the crystal structure shows two types of isolated octahedron – one that is almost undistorted and the other with slight distortions. The undistorted octahedron has very similar Sb–Cl bond lengths (largest difference in Sb–Cl bond length = 0.028 Å, largest deviation of the Cl–Sb–Cl bond angle from the ideal value = 3°). The distorted octahedron has six different Sb–Cl bond lengths (largest difference in Sb–Cl bond length = 0.46 Å, largest deviation of the Cl–Sb–Cl bond angle from the ideal value = 4.6°). The distorted ‘quadrangular pyramid’ has the sixth coordination by a distant Cl atom (3.06 Å) as highlighted in Fig. 4c and d. This ‘quadrangular pyramidal’ unit has five different Sb–Cl bond lengths (largest difference in Sb–Cl bond length = 0.21 Å, largest deviation of Cl–Sb–Cl bond angle from the ideal value = 3.2°). The ‘apical’ Sb–Cl bond length here is 2.452 Å. A detailed list of bond angles and bond lengths describing the crystal structure is provided in Tables S11–S13,

and Fig. S17, ESI[†]. Such distortions within the hexacoordinated metal halide environment depict the extent of site asymmetry. The phase purity of **3** was verified using the PXRD patterns which matched well with the simulated ones from the single-crystal X-ray data as shown in Fig. S12; ESI[†].

A comparison of the structure/extent of distortions in the comprising metal halide units of **1** tris Sb green, **2** tris Sb red, and **3** tris Sb yellow in the light of their observed photo-physical properties is crucial here. The bond length variances (λ_{oct}) of Sb–Cl and bond angle variances (σ^2) of Cl–Sb–Cl in the various structural units for products **1**, **2**, and **3** were calculated (as presented in Table S2, ESI[†]), which exhibit the following order of the extent of distortions: **1–3** \ll **2**. Qualitatively, the building unit type of isolated metal halide polyhedra in **1** is octahedra, in **2** is ‘quadrangular pyramid’, and in **3** is a mixture of octahedron and ‘quadrangular pyramid’. The degree of asymmetry of the coordination environment in the metal halide structural unit, as discussed earlier (MO diagram, Fig. S12, ESI[†]), largely dictates the PL emission energy with a high energy emission band for the symmetric octahedral case (**1** tris Sb green) and a low energy emission band for the asymmetric ‘pyramidal structure’ (**2** tris Sb red). Now, for **3** tris Sb yellow, the presence of a mixture of octahedral and ‘quadrangular pyramidal’ units would cause the PL emission band to appear in the intermediate energy range. Indeed, for **3** tris Sb yellow, the PL band appears at an energy in between the emission bands of **1** tris Sb green and **2** tris Sb red. This strongly suggests the active role of the metal-halide polyhedral unit structure and the degree of symmetry in the metal-halide coordination environment in dictating the PL emission band position.

As discussed earlier, the extent of distortion present in **1** tris Sb green is modest and is appreciably lower than that in **2** tris Sb red. This difference in the extent of distortion reflected in the drastic difference of the observed PLQY. Interestingly, the extent of distortion present in **3** tris Sb yellow is comparable to that in **1** tris Sb green (Table S2; ESI†) and follows $1-3 \ll 2$. The similarity of the extent of distortion in **1** tris Sb green and **3** tris Sb yellow would indicate similar PLQY values which are much higher than that of **2** tris Sb red. This is in accord with the measured PLQY of **3** tris Sb yellow which is close to that of **1** tris Sb green. Such observed correlation between the extent of distortion and the PLQY clearly highlights the role of the extent of distortion in affecting the photo-physical properties. The observed Stokes shifts of three products can also be then positively correlated to the extent of distortion (Stokes shifts: $1-3 \ll 2$). Thus, the above proposed factors (metal-halide unit structure; extent of distortion) are observed to directly impact the photo-physical properties (PL emission energy; PLQY and Stokes shift, respectively) for the different 0D Sb(III) chloride hybrids (**1**, **2**, **3**) synthesized here utilizing a common organic ligand. Further efforts are underway to ascertain the effect of the metal-halide polyhedral type and different extents of distortion in a given type of polyhedral unit on the emissive properties of 0D organic-antimony chloride hybrids.

Conclusion

We demonstrate metal halide structural tunability (SbX₆ octahedron, SbX₅ quadrangular pyramidal, or a combination thereof) through the synthesis of different Sb(III) chloride 0D hybrids (**1**, **2**, **3**) utilizing a common organic ligand [tris(2-aminoethyl)amine]. The crystal structure analysis reveals that the site asymmetry leads to different metal halide unit structures that may be regarded as (i) octahedral in product **1**, (ii) quadrangular pyramidal in product **2**, and (iii) a combination of octahedra and quadrangular pyramidal in product **3**. Furthermore, the structure analysis reveals that the extent of distortion of the metal halide units in these products follows the order: $1-3 \ll 2$. The emissive properties of these products that need a rational understanding include Stokes shifted broadband visible emission with distinctly different PL emission energies (λ_{em}) and markedly different PLQYs: **1**: $\lambda_{em} = 517$ nm, Stokes shift = 165 nm, PLQY = 45%; **2**: $\lambda_{em} = 638$ nm, Stokes shift = 290 nm, PLQY = 6%; and **3**: $\lambda_{em} = 590$ nm, Stokes shift = 200 nm, PLQY = 43%. A structure–property correlation analysis performed here provides us with the following deeper understanding of the origins of the above emissive properties: (i) qualitative molecular orbital scheme on metal halide bonding (with an asymmetric metal halide coordination environment) allows the observed PL emission energies to be rationalized based on the ground state structure (octahedral vs. pyramidal) of **1**, **2**, **3**; (ii) structural reorganization that accompanies while transiting from the distorted ground state to the symmetric excited ³P₁ state of Sb³⁺ ions accounts for the large Stokes shifts in the order of $1-3 < 2$; (iii) the extent of ground state structural distortion ($1-3 \ll 2$)

is well correlated to the PLQY ($1-3 \gg 2$). A lower (higher) extent of ground state structural distortion would minimize (maximize) the non-radiative loss of the excitation energy in the process of excited state reorganization into the symmetric structure, thereby enhancing (suppressing) the possibility of stronger luminescence. This report demonstrates the structural tunability of the metal halide units (octahedral, pyramidal) and highlights the importance of the ground state structure/extent of distortions in affecting PL emission energies, Stokes shifts, and PLQY for 0D antimony chloride hybrids incorporating common organic ligands.

Experimental

Materials

Antimony(III) oxide (99%), hydrochloric acid (37%) and acetone were purchased from Sigma-Aldrich. Tris(2-aminoethyl)amine was purchased from TCI Chemicals. Diethyl ether was purchased from HiMedia. All chemicals were used as purchased without further purification.

Synthesis of powdered **1** tris Sb green:

For the preparation of **1** tris Sb green powder sample, 0.1 mmol (29.1 mg) of antimony(III) oxide was dissolved in 5 mL of hydrochloric acid. To this, 0.1 mmol (14.6 mg) tris(2-aminoethyl)amine was added. The solution turned turbid white after some time. The resulting precipitate was filtered and washed with diethyl ether repeatedly and dried in vacuum for further characterization.

Synthesis of single crystals of **1** tris Sb green:

To obtain single crystals of **1** tris Sb green, the same procedure was followed with the following details: 0.1 mmol (29.1 mg) of antimony(III) oxide was dissolved in 5 mL of hydrochloric acid. To this, 0.1 mmol (14.6 mg) tris(2-aminoethyl)amine was added. The resultant mixture was heated in a preheated oil bath at 60 °C until dissolution. The solution is slowly cooled to obtain white crystals. Crystallization led to the formation of plate shaped pale yellow crystals which appear bright green under UV (365 nm) light. The crystals were filtered using a vacuum pump and washed repeatedly with acetone and diethyl ether for further characterization.

Synthesis of single crystals of **2** tris Sb red:

In order to synthesize single crystals of **2** tris Sb red, the same procedure was followed as that for **1** described above. However, the oil bath temperature was set at 120 °C for dissolving the crystal and cooled naturally to room temperature. After cooling the needle shaped colorless crystals formed which emit red color under UV (365 nm) light. Here we have used the same filtration and washing procedure as mentioned above.

Synthesis of powdered **3** tris Sb yellow

For the preparation of the **3** tris Sb yellow powder sample, 0.1 mmol (29.1 mg) of antimony(III) oxide was dissolved in 5 mL

of hydrochloric acid. To this, 1 mmol (146 mg) tris(2-aminoethyl)amine was added. The solution turned turbid white after some time. The precipitate appeared bright yellow under UV (365 nm) light.

Synthesis of single crystals of 3 tris Sb yellow

To obtain single crystals of 3 tris Sb yellow, a 1:10 equivalent metal *vs.* ligand ratio was used. Typically for the reaction 0.1 mmol (29.1 mg) of antimony(III) oxide was dissolved in 5 mL of hydrochloric acid. To this, 1 mmol (146 mg) tris(2-aminoethyl)amine was added. The resultant mixture was kept in a preheated oil bath at 120 °C until dissolution. The solution is slowly cooled to room temperature to obtain crystals. Crystallization led to the formation of cube shaped pale yellow crystals which appear bright yellow under UV (365 nm) light. The crystals were filtered using a vacuum pump and washed repeatedly with acetone and diethyl ether for further characterization.

Methods

UV-Vis absorbance was performed in a Shimadzu UV-3600 Plus UV-Vis-NIR spectrometer. Steady state PL and lifetime were measured using an Edinburgh FS5 spectrophotometer. TGA measurements were performed using a TAG system (Mettler-Toledo, Model TGA/SDTA851e) and samples were heated in the range of 25–800 °C at a heating rate of 5 °C min⁻¹ under a nitrogen atmosphere. ¹H NMR spectra were recorded on a Bruker A-400 MHz system using DMSO-d₆ as the solvent at room temperature. Powder X-ray diffraction (XRD) patterns were recorded using a PANalytical X'Pert Pro equipped with Cu K α radiation (λ = 1.5406 Å). Absolute quantum yield measurements were carried out in a Horiba JOBIN YVON Fluoromax-4 spectrometer with a calibrated integrating sphere attachment. Scanning Electron Microscopy (SEM) imaging and mapping were performed using a ZeissTM Ultra Plus field-emission scanning electron microscope. X-ray photoelectron spectroscopy (XPS) characterization was performed with an ESCALab spectrometer having an Al K α X-ray source ($h\nu$ = 1486.6 eV) operating at 150 W using a Physical Electronics 04–548 dual Mg/Al anode and in a UHV system with a base pressure of $\leq 5 \times 10^{-9}$ torr. Low temperature PL of the crystals was performed using an Edinburgh FLS 1000 photoluminescence spectrometer, attached with an OptistatDN cryostat and the temperature was controlled using a Mercury iTC temperature controller (Oxford Instruments). The sample was excited using a xenon lamp and emission was collected from 320 nm to 800 nm. Single crystal X-ray intensity measurements of compounds 1 and 2 were carried out on a Bruker D8 VENTURE Kappa Duo PHOTON II CPAD diffractometer.

Conflicts of interest

The authors declare no competing financial interest.

Acknowledgements

The authors thank Milan K Bisai (NCL Pune), Dr J. Nithyanandhan (NCL Pune), Dr S. S. Sen (NCL Pune), and

Dr R. Vaidhyathan (IISER Pune) for insightful discussion. This work was financially supported through the DST Grant No. CRG/2019/000252. A. B. and R. B. thank the CSIR for Senior Research Fellowship.

References

- 1 B.-B. Cui, Y. Han, B. Huang, Y. Zhao, X. Wu, L. Liu, G. Cao, Q. Du, N. Liu, W. Zou, M. Sun, L. Wang, X. Liu, J. Wang, H. Zhou and Q. Chen, *Nat. Commun.*, 2019, **10**, 1–8.
- 2 R. Gautier, F. Massuyeau, G. Galnon and M. Paris, *Adv. Mater.*, 2019, **31**, 1807383.
- 3 H. Lin, C. Zhou, Y. Tian, T. Siegrist and B. Ma, *ACS Energy Lett.*, 2017, **3**, 54–62.
- 4 M. I. Saidaminov, O. F. Mohammed and O. M. Bakr, *ACS Energy Lett.*, 2017, **2**, 889–896.
- 5 H. Tsai, W. Nie, J.-C. Blancon, C. C. Stoumpos, R. Asadpour, B. Harutyunyan, A. J. Neukirch, R. Verduzco, J. J. Crochet, S. Tretiak, L. Pedesseau, J. Even, M. A. Alam, G. Gupta, J. Lou, P. M. Ajayan, M. J. Bedzyk, M. G. Kanatzidis and A. D. Mohite, *Nature*, 2016, **536**, 312–316.
- 6 C. Zhou, H. Lin, S. Lee, M. Chaaban and B. Ma, *Mater. Res. Lett.*, 2018, **6**, 552–569.
- 7 Z. Li, Y. Li, P. Liang, T. Zhou, L. Wang and R.-J. Xie, *Chem. Mater.*, 2019, **31**, 9363–9371.
- 8 K. Huang and A. Rhys, *Selected Papers Of Kun Huang: (With Commentary)*, World Scientific, 2000, pp. 74–92.
- 9 K. M. McCall, C. C. Stoumpos, S. S. Kostina, M. G. Kanatzidis and B. W. Wessels, *Chem. Mater.*, 2017, **29**, 4129–4145.
- 10 M. D. Smith and H. Karunadasa, *Acc. Chem. Res.*, 2018, **51**, 619–627.
- 11 X. Wang, W. Meng, W. Liao, J. Wang, R.-G. Xiong and Y. Yan, *J. Phys. Chem. Lett.*, 2019, **10**, 501–506.
- 12 S. Li, J. Luo, J. Liu and J. Tang, *J. Phys. Chem. Lett.*, 2019, **10**, 1999–2007.
- 13 H. Shi, D. Han, S. Chen and M.-H. Du, *Phys. Rev. Mater.*, 2019, **3**, 034604.
- 14 L. Mao, P. Guo, M. Kepenekian, I. Hadar, C. Katan, J. Even, R. D. Schaller, C. C. Stoumpos and M. G. Kanatzidis, *J. Am. Chem. Soc.*, 2018, **140**, 13078–13088.
- 15 A. Biswas, R. Bakthavatsalam, S. R. Shaikh, A. Shinde, A. Lohar, S. Jena, R. G. Gonnade and J. Kundu, *Chem. Mater.*, 2019, **31**, 2253–2257.
- 16 S. Brochard-Garnier, M. Paris, R. Génois, Q. Han, Y. Liu, F. Massuyeau and R. Gautier, *Adv. Funct. Mater.*, 2019, **29**, 1806728.
- 17 D. Cortecchia, J. Yin, A. Petrozza and C. Soci, *J. Mater. Chem. C*, 2019, **7**, 4956–4969.
- 18 R. Bakthavatsalam, M. P. Haris, S. R. Shaikh, A. Lohar, A. Mohanty, D. Moghe, S. Sharma, C. Biswas, S. S. K. Raavi, R. G. Gonnade and J. Kundu, *J. Phys. Chem. C*, 2020, **124**, 1888–1897.
- 19 M. P. Haris, R. Bakthavatsalam, S. Shaikh, B. P. Kore, D. Moghe, R. G. Gonnade, D. Sarma, D. Kabra and J. Kundu, *Inorg. Chem.*, 2018, **57**, 13443–13452.
- 20 D. Fabini, *J. Phys. Chem. Lett.*, 2015, **6**, 3546–3548.

- 21 S. Chakraborty, W. Xie, N. Mathews, M. Sherburne, R. Ahuja, M. Asta and S. G. Mhaisalkar, *ACS Energy Lett.*, 2017, **2**, 837–845.
- 22 A. H. Slavney, L. Leppert, A. Saldivar Valdes, D. Bartesaghi, T. J. Savenije, J. B. Neaton and H. I. Karunadasa, *Angew. Chem., Int. Ed.*, 2018, **57**, 12765–12770.
- 23 Q. Fan, G. V. Biesold-McGee, J. Ma, Q. Xu, S. Pan, J. Peng and Z. Lin, *Angew. Chem., Int. Ed.*, 2020, **59**, 1030–1046.
- 24 A. M. Ganose, C. N. Savory and D. O. Scanlon, *Chem. Commun.*, 2017, **53**, 20–44.
- 25 M. Leng, Z. Chen, Y. Yang, Z. Li, K. Zeng, K. Li, G. Niu, Y. He, Q. Zhou and J. Tang, *Angew. Chem., Int. Ed.*, 2016, **55**, 15012–15016.
- 26 Z.-P. Wang, J.-Y. Wang, J.-R. Li, M.-L. Feng, G.-D. Zou and X.-Y. Huang, *Chem. Commun.*, 2015, **51**, 3094–3097.
- 27 C. Zhou, H. Lin, Y. Tian, Z. Yuan, R. Clark, B. Chen, L. J. van de Burgt, J. C. Wang, Y. Zhou, K. Hanson, Q. J. Meisner, J. Neu, T. Besara, T. Siegrist, E. Lambers, P. Djurovich and B. Ma, *Chem. Sci.*, 2018, **9**, 586–593.
- 28 C. Zhou, M. Worku, J. Neu, H. Lin, Y. Tian, S. Lee, Y. Zhou, D. Han, S. Chen, A. Hao, P. I. Djurovich, T. Siegrist, M.-H. Du and B. Ma, *Chem. Mater.*, 2018, **30**, 2374–2378.
- 29 Z. Wang, Z. Zhang, L. Tao, N. Shen, B. Hu, L. Gong, J. Li, X. Chen and X. Huang, *Angew. Chem., Int. Ed.*, 2019, **58**, 9974–9978.
- 30 D. Chen, F. Dai, S. Hao, G. Zhou, Q. Liu, C. Wolverton, J. Zhao and Z. Xia, *J. Mater. Chem. C*, 2020, **8**, 7322–7329.
- 31 F. Lin, H. Wang, W. Liu and J. Li, *J. Mater. Chem. C*, 2020, **8**, 7300–7303.
- 32 G. Song, M. Li, S. Zhang, N. Wang, P. Gong, Z. Xia and Z. Lin, *Adv. Funct. Mater.*, 2020, **30**, 2002468.
- 33 G. Laurita, D. H. Fabini, C. C. Stoumpos, M. G. Kanatzidis and R. Seshadri, *Chem. Sci.*, 2017, **8**, 5628–5635.
- 34 A. Walsh, D. J. Payne, R. G. Egdell and G. W. Watson, *Chem. Soc. Rev.*, 2011, **40**, 4455–4463.
- 35 L. Sobczyk, R. Jakubas and J. Zaleski, *Pol. J. Chem.*, 1997, **71**, 265–300.
- 36 X. Liu, W. Wu, Y. Zhang, Y. Li, H. Wu and J. Fan, *J. Phys. Chem. Lett.*, 2019, **10**, 7586–7593.
- 37 B. Febriansyah, T. Borzda, D. Cortecchia, S. Neutzner, G. Folpini, T. M. Koh, Y. Li, N. Mathews, A. Petrozza and J. England, *Angew. Chem., Int. Ed.*, 2020, **132**, 10883–10888.
- 38 V. Morad, S. Yakunin and M. Kovalenko, *ACS Mater. Lett.*, 2020, **2**, 845–852.
- 39 H. Nikol and A. Vogler, *J. Am. Chem. Soc.*, 1991, **113**, 8988–8990.
- 40 K. Thirumal, W. K. Chong, W. Xie, R. Ganguly, S. K. Muduli, M. Sherburne, M. Asta, S. Mhaisalkar, T. C. Sum, H. S. Soo and N. Mathews, *Chem. Mater.*, 2017, **29**, 3947–3953.
- 41 Z. Yuan, C. Zhou, Y. Tian, Y. Shu, J. Messier, J. C. Wang, L. J. Van De Burgt, K. Kountouriotis, Y. Xin, E. Holt, K. Schanze, R. Clark, T. Siegrist and B. Ma, *Nat. Commun.*, 2017, **8**, 1–7.
- 42 B.-B. Zhang, J.-K. Chen, J.-P. Ma, X.-F. Jia, Q. Zhao, S.-Q. Guo, Y.-M. Chen, Q. Liu, Y. Kuroiwa, C. Moriyoshi, J. Zhang and H.-T. Sun, *J. Phys. Chem. Lett.*, 2020, **11**, 2902–2909.
- 43 J. Yu, J. Kong, W. Hao, X. Guo, H. He, W. R. Leow, Z. Liu, P. Cai, G. Qian, S. Li, X. Chen and X. Chen, *Adv. Mater.*, 2019, **31**, 1806385.
- 44 J. F. Sawyer and R. J. Gillespie, *Prog. Inorg. Chem.*, 1986, **34**, 65–114.
- 45 G. Blasse, *Prog. Solid State Chem.*, 1988, **18**, 79–171.
- 46 G. Blasse, *Rev. Inorg. Chem.*, 1983, **5**, 319–381.
- 47 A. Ranfagni, D. Mugnai, M. Bacci, G. Viliani and M. Fontana, *Adv. Phys.*, 1983, **32**, 823–905.
- 48 A. d. Bois and W. Abriel, *Z. Naturforsch.*, 1990, **45**, 573–578.
- 49 U. Ensinger, W. Schwarz and A. Schmidt, *Z. Naturforsch., B: Chem. Sci.*, 1983, **38**, 149–154.
- 50 B. Blažič and F. Lazarini, *Acta Crystallogr., Sect. C: Cryst. Struct. Commun.*, 1985, **41**, 1619–1621.
- 51 A. Mirochnik, A. Udovenko, T. Storozhuk, V. Karasev and B. Bukvetskii, *Russ. J. Coord. Chem.*, 2003, **48**, 961–971.
- 52 T. Sedakova, A. Mirochnik and V. Karasev, *Opt. Spectrosc.*, 2008, **105**, 517–523.
- 53 M. Bely, I. Zakharchenko, B. Okhrimenko and V. Skryshevsky, *Ukr. Fiz. Zh.*, 1980, **25**, 1785–1788.
- 54 N. Petrochenkova, T. Storozhuk, A. Mirochnik and V. Karasev, *Russ. J. Coord. Chem.*, 2002, **28**, 468–472.
- 55 Z. Tan, M. Hu, G. Niu, Q. Hu, J. Li, M. Leng, L. Gao and J. Tang, *Sci. Bull.*, 2019, **64**, 904–909.
- 56 T. V. Storozhuk, A. G. Mirochnik, N. V. Petrochenkova and V. E. Karasev, *Opt. Spectrosc.*, 2003, **94**, 920–923.

Cite this: *J. Mater. Chem. C*, 2021,
9, 4351

Lead-free zero dimensional tellurium(IV) chloride-organic hybrid with strong room temperature emission as a luminescent material†

Anupam Biswas,^{ab} Rangarajan Bakthavatsalam,^{ab} Vir Bahadur,^{ab}
Chinmoy Biswas,^c Bhupendra P. Mali,^{ab} Sai Santosh Kumar Raavi,^{cd}
Rajesh G. Gonnade^{ab} and Janardan Kundu^{ab*}

Despite the current progress in 'Pb-free' low dimensional main group metal halide based luminescent materials, it is challenging to synthesize Te(IV) halide hybrids with strong ambient emission with excitation features in the visible range as efficient and stable phosphors for potential lighting applications. Reported here is a (benzyltriethylammonium)₂TeCl₆ zero dimensional hybrid material with excitation features in the visible range and strong room temperature, broadband, intrinsic luminescence (PLQY ~15%) arising due to self-trapped excitons (STEs). Furthermore, a proof-of-concept LED architecture demonstrates successful optical down-conversion with a visible light excitation source. Here, exclusive adoption of a 'regular' octahedral Te(IV)-halide unit structure with minimal static distortion provides a unique opportunity to unmask the role played by 5s² lone pair electrons in shaping the emissive properties. This effort may open up new avenues towards unravelling the role of lone pair stereoactivity in controlling the PLQY in low dimensional hybrids that has proven to be challenging for the reported (Sb, Sn) based low dimensional 5s² metal halide hybrid materials.

Received 7th December 2020,
Accepted 15th February 2021

DOI: 10.1039/d0tc05752e

rsc.li/materials-c

Introduction

Metal halide-organic hybrid perovskites with fascinating properties have been at the research forefront of energy related applications such as solar cells, LEDs, lasers, and photodetectors.^{1–3} For 3D perovskites, featuring three dimensional networked metal halide units, the photo-generated excitons are weakly bound and can diffuse in all directions within the inorganic framework with long diffusion lengths (~1 μm).⁴ Organic ligand size induced dimensionality lowering (2D, 1D, 0D) restricts the exciton due to quantum and dielectric confinement with high exciton binding energies.⁵ Typically, in 0D perovskites, the metal halide unit (square pyramidal, octahedral,

disphenoidal) is isolated and surrounded by bulky organic ligands supporting strongly bound excitons that can relax radiatively across the band edge.^{6–8} Lowered dimensionality in these materials further allows trapping of the generated excitons into the lattice sites through transient structural distortion. Such self-trapping of excitons⁹ is facilitated due to the soft nature of the material and strong electron-phonon coupling.¹⁰ Recombination of these self-trapped excitons (STE) leads to a broad emission band with generally longer lifetimes.^{9,11,12} The involvement of lattice phonon modes further broadens the emission profile with an accompanying excitation energy dissipation (Stokes shift) due to the significant excited state structural reorganization.¹³ These factors cumulatively lead to a strong, Stokes shifted, broad band emission profile in low dimensional hybrid perovskites.¹⁴ Moreover, the presence of the inorganic unit embedded within the organic ligand matrix endows environmental stability. These enabling properties have encouraged their applications in light emitting devices, solar concentrators, and radiation detectors.¹⁴

Many low dimensional Pb(II)-halides (6s² lone pair) have been reported to show STE based broadband white light emission properties.¹⁵ The broadband emission intensity has been correlated to the structural distortions (out of plane, in plane deformations) for the 2D Pb hybrids.¹⁵ However, no such correlation is observed to hold for 1D/0D based Pb hybrids. Nevertheless, the recent search for 'Pb free' variants has

^a CSIR-National Chemical Laboratory, Pune, India^b Academy of Scientific and Innovative Research (AcSIR), Ghaziabad, India^c Indian Institute of Technology Hyderabad, Kandi, India^d Indian Institute of Science Education and Research (IISER) Tirupati, Tirupati, India. E-mail: janardan@isertirupati.ac.in

† Electronic supplementary information (ESI) available: Single crystal structure experimental details, XPS, NMR, Tauc Plot, optical characterization, lifetime decay profiles, structural distortion parameters, single crystal data with various bond angles and bond lengths, grinding and annealing photophysical characterization, Raman spectra, fitting of low temperature PL data, configuration coordinate diagram, TGA data, and stability data. CCDC 2042525. For ESI and crystallographic data in CIF or other electronic format see DOI: 10.1039/d0tc05752e

kindled immense research interest in main-group metal halides with $5s^2$ lone pairs (*viz.* Sn^{2+} , Sb^{3+}).¹⁶ Antimony(III) halide-organic 0D hybrids featuring oxidative stability, $5s^2$ electronic configuration, and isolated metal-halide units (octahedral, square pyramidal, disphenoidal, *etc.*), have been demonstrated to support efficient broadband emission with high photoluminescence quantum yield (PLQY).^{6,7,17–21} The broad band emission in such Sb(III) halide systems has been fully attributed to the radiative recombination of STEs originating from the excited triplet state of the Sb^{3+} centre ($^3\text{P}_1$) with typically longer emission lifetimes (3–10 μs).^{14,21} There is no experimental evidence of a correlation between the structural distortions and PLQY for the 0D Sb hybrids. $5s^2$ lone pair activity induced structure and distortion of the metal halide unit (static and/or dynamic), is believed to affect the luminescence properties in Sb(III) halide systems.^{14,22} However, formulating a rational design strategy aimed to unmask the role played by the Sb^{3+} $5s^2$ lone pair in shaping their luminescence properties has turned out to be challenging due to the adopted variety of isolated metal-halide unit structures (octahedral, square-pyramidal, disphenoidal). Moreover, the majority of these Sb based 0D materials lack excitation features in the visible range and necessitates them to be paired with UV LEDs (that are currently expensive and inefficient) for their application as down-conversion phosphors.¹⁴

Tellurium(IV), featuring a $5s^2$ lone pair, also forms zero dimensional hybrids with a metal halide semiconducting unit dispersed in the organic ligand matrix.²³ The high charge density on the Te^{4+} centre supports a greater number of halide ligands and exclusively generates octahedral units irrespective of the counter organic cation.^{24–26} The most commonly adopted structure is vacancy ordered double perovskite (A_2TeX_6)^{24,27} with almost 'regular' octahedral coordination. Given this structural simplicity (compared to Sb^{3+}), high oxidative stability, and $5s^2$ configuration (similar to Sb^{3+}) for the Te(IV) halides, it is expected that low dimensional Te(IV) halides would demonstrate exceptional luminescence properties. The exclusive adoption of octahedral metal-halide geometry in $[\text{TeX}_6]^{2-}$ systems (unlike Sb^{3+} systems) would allow the formulation of a design strategy to draw any structure/distortion - PLQY correlation. Encouragingly, there have been studies on $[\text{TeX}_6]^{2-}$ hybrids that report structural^{28–32} and photo-physical properties^{25,26,33} presenting excitation features in the visible range. Unfortunately, these $[\text{TeX}_6]^{2-}$ hybrids have not been demonstrated to be strongly emissive at room temperature as the quenching temperatures are relatively low in these compounds³⁴ and those that do emit at room temperature are very weak with low PLQYs.^{25,26,33}

It is clear that enhancing the room temperature PLQY of $[\text{TeX}_6]^{2-}$ hybrids is of huge importance in deciphering the structure/distortion-property correlation that is currently absent for 0D metal halide hybrids (Pb, Sb, Sn). In this first effort, we demonstrate a tellurium(IV) chloride based zero dimensional hybrid featuring isolated, undistorted $[\text{TeCl}_6]^{2-}$ octahedral units embedded in the organic templating ligand (benzyltriethylammonium: BzTEA) matrix that show intrinsic, broad, yellow-orange, strong room temperature emission (PLQY ~ 15%) with ambient/thermal stability, and excitation

feature in the visible range (445 nm) allowing for their use as potential down-conversion phosphor materials. The synthesized $(\text{BzTEA})_2\text{TeCl}_6$ product shows long lived and broad band emission likely due to self-trapping of excitons (STEs). The emissive characteristics are observed to be independent of the particle size, surface, and other structural defects and hence the utilized synthetic route. This supports the unique and intrinsic nature of the STE based emission. This tellurium(IV) halide hybrid with room temperature emission and excitation band in the visible range could serve as a potential 'Pb-free' stable phosphor material for lighting applications as demonstrated here with a test-bed down-conversion LED architecture. Noteworthy, ambient emitting octahedral (exclusive geometry) $[\text{TeX}_6]^{2-}$ hybrids could further be leveraged to gain a rational understanding of the structure/distortion - photophysical property correlation.

Experimental section

Materials

Tellurium tetrachloride (99.99%), hydrochloric acid (37%), acetone, and dimethylformamide were purchased from Sigma Aldrich. Benzyltriethylammonium chloride (98%) was purchased from TCI Chemicals. Diethyl ether was purchased from HiMedia. All chemicals were used as purchased without further purification.

Synthesis of $(\text{BzTEA})_2\text{TeCl}_6$ crystals

For the preparation of $(\text{BzTEA})_2\text{TeCl}_6$ crystals, 0.1 mmol (26.9 mg) of tellurium tetrachloride was dissolved in 1 mL of dimethylformamide. To this, 0.1 mmol (22.7 mg) benzyltriethylammonium chloride salt was added and dissolved. The resultant solution was used for crystallization with an anti-solvent diffusion method using diethyl ether. The resulting yellow coloured crystals were filtered and washed with acetone repeatedly and dried under vacuum for further characterization. The same crystals can also be prepared using the HX method wherein hydrochloric acid is used as a solvent. For typical HX synthesis, 0.1 mmol (26.9 mg) of tellurium tetrachloride and 0.1 mmol (22.7 mg) benzyltriethylammonium chloride amine were dissolved in hydrochloric acid followed by heating to get a clear yellow solution followed by natural cooling to get the crystals. The crystals of the ground powders were used for further characterization.

Methods

UV-Vis absorbance was performed in a Shimadzu UV-VIS-NIR3600Plus spectrometer. Steady State PL and lifetime were measured using an Edinburgh FS5 spectrophotometer. TGA measurements were performed using a TAG system (Mettler-Toledo, Model TGA/SDTA851e) and samples were heated in the range of 25–800 °C at a heating rate of 5 °C min^{-1} under a nitrogen atmosphere. Absolute quantum yield measurements were carried out in a Horiba JOBIN YVON Fluoromax-4 spectrometer with a calibrated integrating sphere attachment. X-ray photoelectron spectroscopy (XPS) characterization was performed with an ESCALab spectrometer having an Al $K\alpha$ X-ray source

($h\nu = 1486.6$ eV) operating at 150 W using a Physical Electronics 04-548 dual Mg/Al anode and in a UHV system with a base pressure of $\leq 5 \times 10^{-9}$ Torr. Low temperature PL of the crystals was performed using an Edinburgh FLS1000 photoluminescence spectrometer, attached with an OptistatDN cryostat and the temperature was controlled using a Mercury iTC temperature controller (Oxford instruments). The sample was excited using a xenon lamp and emission was collected from 320 nm to 800 nm. Single crystal X-ray intensity data measurements of crystals were carried out on a Bruker D8 VENTURE Kappa Duo PHOTON II CPAD diffractometer. The intensity measurements were carried out with a Mo microfocus sealed tube diffraction source (Mo $K\alpha = 0.71073$ Å) at 100(2) K. The powder X-ray diffraction measurements were carried out on a Rigaku Micromax-007HF instrument (high intensity microfocus rotating anode X-ray generator) with R -axis detector IV++ with a scanning rate of $2^\circ 2\theta \text{ min}^{-1}$ using Cu and Mo $K\alpha$ radiation. The PXRD sample was prepared by sealing 2–3 mg of finely ground powder into a Lindeman glass capillary with an inner diameter of 1 mm. Raman spectroscopic measurements were recorded at room temperature on an HR 800 Raman spectrophotometer (Jobin Yvon, Horiba, France) using monochromatic radiation (achromatic Czerny–Turner type monochromator with silver treated mirrors) emitted by a He–Ne laser (633 nm). For down-conversion LED measurements a commercially available blue LED ($\lambda_{\text{emi}} = 447$ nm, FWHM = 20 nm) was used. The $(\text{BzTEA})_2\text{TeCl}_6$ crystal was ground and coated on the flat surface of the commercially available blue LED for spectroscopic analysis and imaging. Furthermore, the spectroscopic details were measured using an Edinburgh FS5 spectrophotometer and images were captured by using a digital camera (Canon PowerShot SX740 HS).

Results and discussion

$(\text{BzTEA})_2\text{TeCl}_6$ single crystals were synthesized by the anti-solvent diffusion method (Fig. 1a). Yellow colored single crystals of $(\text{BzTEA})_2\text{TeCl}_6$ formed within a day that emitted an intense yellow-orange light under UV illumination (Fig. 1a and b). XPS analysis confirms the presence of Te^{4+} and Cl^- ions in the product (Fig. S1, ESI†). ^1H NMR analysis confirms the presence of a cationic ligand moiety (Fig. S2, ESI†).

Optical absorption characterization of the crystals (Fig. 2a) shows a sharply rising absorption edge (absorption onset ~ 515 nm) with absorption bands at 440 nm, 380 nm, 295 nm, and 270 nm. These absorption bands originate due to the transitions between the sp excited state and the s^2 ground state of the $\text{Te}(\text{iv})$ centre: $^1\text{S}_0 \rightarrow ^3\text{P}_1$, $^3\text{P}_2$, and $^1\text{P}_1$ (free ion term symbols) and possibly due to ligand to metal charge transfer absorption at shorter wavelengths.¹³ Direct band gap Tauc plot analysis estimates an optical band gap of ~ 2.57 eV (Fig. S3, ESI†). Room temperature steady state photoluminescence (PL) characterization of the crystals (Fig. 2a) shows broad band (full width at half maximum: FWHM = 130 nm) emission with a strong PL peak ($\lambda_{\text{emi}} = 608$ nm; $\lambda_{\text{exc}} = 440$ nm).

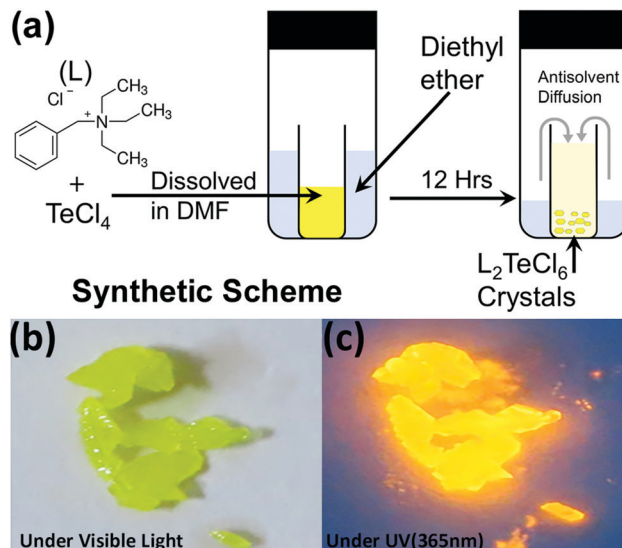


Fig. 1 (a) Reaction scheme (anti-solvent diffusion) utilized for the synthesis of single crystals of $(\text{BzTEA})_2\text{TeCl}_6$; photograph of the synthesized crystals at room temperature under (b) visible and (c) UV illumination (365 nm).

The photoluminescence excitation (PLE) spectrum of the crystals ($\lambda_{\text{emi}} = 600$ nm) shows features in the 300–500 nm range with a strong excitation band at 445 nm. The observed features and onset of PLE match well with the absorption spectra. The estimated Stokes shift is ~ 160 nm that minimizes self-reabsorption losses. The room temperature photoluminescence quantum yield (PLQY) is estimated to be 15% attesting to the observed strong visible ambient emission. Time resolved PL measurements (μs flash lamp source) across the broad band (decay profiles: Fig. 2b, extracted lifetimes, and relative weights Fig. S4, ESI†) of the crystals demonstrates long lifetime components [~ 1.1 μs (44%), ~ 9.9 μs (56%)] in line with the exciton recombination mechanism originating from the lowest triplet state ($^3\text{P}_1 \rightarrow ^1\text{S}_0$, forbidden transition). The strong spin–orbit coupling and high Te–Cl bond covalency ($\sim 80\%$) can allow for appreciable relaxation of the spin foriddances leading to strong luminescence as observed here. Furthermore, the generality of the utilized reaction procedure (solvent-antisolvent, HX) for the synthesis of $\text{Te}(\text{iv})$ based low dimensional perovskites are demonstrated here for two other ligands [tetraethylammonium chloride, tris(2-aminoethyl)amine in HCl] and their optical characterization is summarized in Fig. S5, ESI†. Noteworthy, these products have very weak ambient emission when directly compared to that of the $(\text{BzTEA})_2\text{TeCl}_6$ hybrid (Fig. S6, ESI†).

The overview of the single crystal structure of the $(\text{BzTEA})_2\text{TeCl}_6$ product (CCDC 2042525†) is shown in Fig. 3. The product crystallized in the monoclinic $P2_1/n$ space group containing one organic ligand ($[\text{C}_{13}\text{H}_{22}\text{N}]^+$) and $\frac{1}{2}$ unit of $[\text{TeCl}_6]^{2-}$ octahedron in the asymmetric unit (Fig. 3b) leading to the molecular formula of $[\text{C}_{13}\text{H}_{22}\text{N}]_2\text{TeCl}_6$. The product has an isolated metal halide octahedron periodically dispersed in the organic ligand matrix generating a zero dimensional vacancy-ordered double perovskite structure (Fig. 3a). The inorganic unit features a nearly ‘regular’ metal halide octahedron with minimal distortions

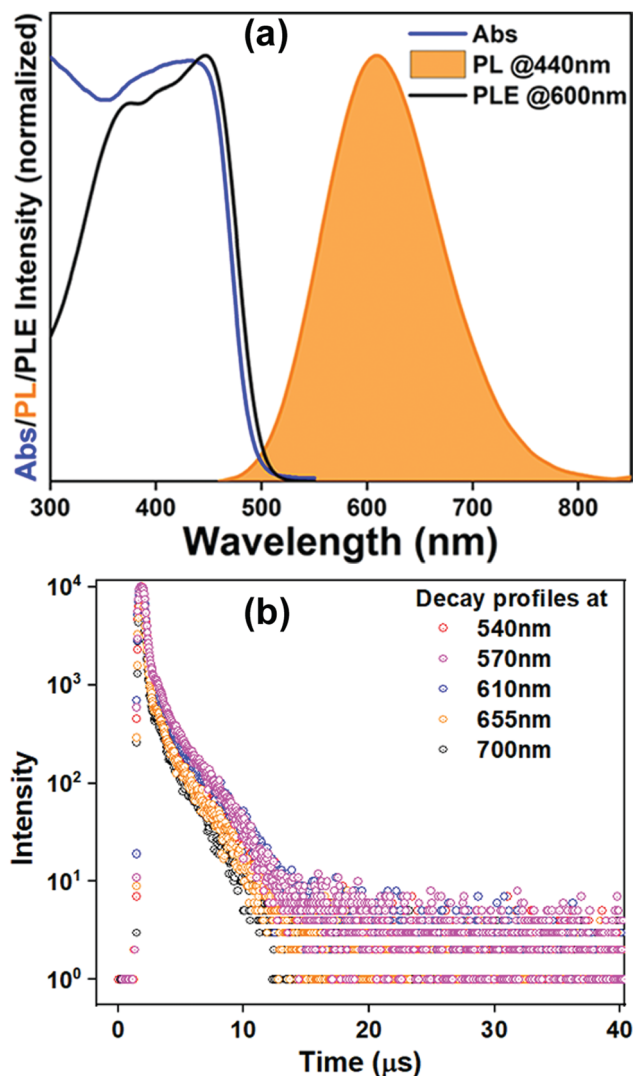


Fig. 2 Optical characterization of $(\text{BzTEA})_2\text{TeCl}_6$ showing (a) absorbance (Abs), photoluminescence (PL), and photoluminescence excitation (PLE) spectra; (b) lifetime decay profiles collected across the PL band ($\lambda_{\text{exc}} = 440$ nm).

(largest difference in Te–Cl bond length = 0.025 Å; Fig. 3c; largest deviation of the Cl–Te–Cl bond angle from ideal value = 0.9° ; Fig. S7, ESI[†]) with quadratic elongation of 1.0001 and bond angle variance of 0.33 (degree)² attesting to the low stereochemical activity of the $5s^2$ lone pair. High charge on the metal centre, supporting six coordination, reduces the static expression of the lone pair leading to a symmetric metal halide octahedral framework. This near-regularity of the metal halide unit leads to the observation of one broad, featureless, triplet dominated ($^3\text{P}_{0,1,2}$) emission peak.^{13,14} The phase purity of the product was confirmed using the powder X-ray diffraction pattern that matches well with the simulated one (Fig. 3d).

Given the broad nature of the observed PL emission peak of $(\text{BzTEA})_2\text{TeCl}_6$ crystals, it is important to decipher if the broadened emission is due to defect emission. The PL emission profile remains unchanged across a broad excitation range of 320–380 nm (Fig. S8a, ESI[†]). PLE spectra collected across the

broad emission band (Fig. S8b, ESI[†]) also remain unaltered. Furthermore, the estimated lifetime components across the broad emission band were found to remain unchanged (Fig. S4, ESI[†]). These observations suggest that unique emissive species are responsible for the broad emission and very likely do not involve extrinsic defects. Furthermore, PL/PLE studies were performed on ground powder samples. If defects led to broad band emission, sample grinding would cause a substantial change of the PL/PLE profile. However, no changes in the PL/PLE band profile were observed when the samples were ground (Fig. S9, ESI[†]). Moreover, the nature of the PL/PLE profile remains unchanged for the ground crystals when PL is collected at different excitations and PLE is collected across the broad emission band (Fig. S10, ESI[†]). In addition, the lifetimes of the ground sample across the broad emission band remain almost unchanged (Fig. S11, ESI[†]). Also, the crystal samples, when annealed at different temperatures, show no changes in the PL/PLE band profile (Fig. S12, ESI[†]). These observations clearly suggest that the broad emission is not due to the presence of the defects and is due to the presence of unique emissive species that lead to intrinsic emission.

The broad band emissions in low dimensional ns^2 metal halide hybrid materials have been attributed to self-trapping of excitons due to strong electron–phonon coupling that produces transiently localized charges (holes/electrons) that distort the metal halide unit.¹⁴ The PL emission from these STEs is phonon assisted that broadens the radiative bandwidth.¹⁰ Upon photoexcitation, the low lying transient STE states can accept carriers from the excited $^3\text{P}_1$ state and allow slow and phonon assisted radiative decay to the $^1\text{S}_0$ ground state thereby broadening the emission bandwidth. Concomitantly, the carriers can undergo thermally activated non-radiative recombination that suppresses emission with a strong temperature dependence (thermal quenching of PL due to curve crossing of the excited and ground state¹⁴). Importantly, excited state reorganization in the $^3\text{P}_1$ state and the low lying STE states together dictates the observed Stokes shift in the broad PL emission band.

Low temperature PL measurements were carried out to gain insight into the phonon assisted radiative recombination of STEs leading to the broad band emission. Photoluminescence spectra, collected over the temperature range of 300–80 K (Fig. 4a), show a gradual increase of the PL intensity and band narrowing as the temperature is lowered. Such changes have been generally observed for ns^2 metal halide based 0D materials.^{35,36} Integrated PL peak area and FWHM at different temperatures are presented in Fig. 4b. Observed strong PL intensity across the temperature range suggests a low activation energy downhill process of populating the low lying STE states from the $^3\text{P}_1$ excited state. The decrease of the PL intensity with increase in temperature further suggests that the STE states have a high self-trapping depth that allows thermally assisted de-trapping followed by fast non radiative recombination only at higher temperatures (Fig. S13, ESI[†]).^{8,15,36} The bandwidth (FWHM) of the broad emission is observed to decrease monotonically as the temperature is lowered as fewer phonon modes are thermally accessible to couple to the STEs assisting radiative recombination.

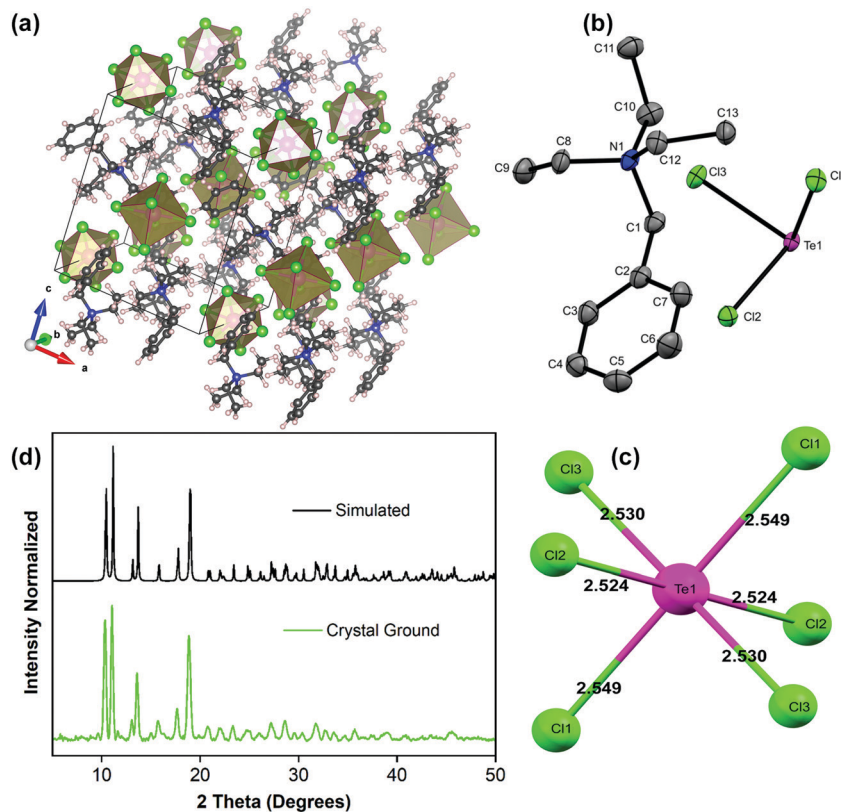


Fig. 3 XRD characterization of the $(\text{BzTEA})_2\text{TeCl}_6$ hybrid. Overview of the single crystal structure (a); asymmetric unit (b); site symmetry of Metal-Halide octahedron (c); comparison of the simulated and experimental PXRD pattern using Cu source (d). H atoms are omitted in (b) for clarity.

This temperature dependence of FWHM (Γ) can be fitted to the following equation relating coupling of electronic excitations with the longitudinal optical lattice phonons:³⁷

$$\Gamma(T) = \Gamma_0 + \Gamma_{\text{Phonon}} \left(e^{(E_{\text{LO}}/k_B T)} - 1 \right)^{-1} + \Gamma_{\text{inhomo}} e^{-E_b/k_B T}$$

where, Γ_0 = FWHM at $T = 0$ K, Γ_{phonon} represents electron-phonon coupling and E_{LO} represents the energy of longitudinal optical phonon mode, Γ_{inhomo} represents inhomogeneous broadening while E_b is the binding energy of trapped states. The fitting and its associated parameters (Fig. S13, ESI†) reflects strong electron-phonon coupling with $E_{\text{LO}} = 306 \text{ cm}^{-1}$, in agreement with the low frequency Raman stretching mode of the Te-Cl bond^{38,39} of the inorganic metal halide framework (Fig. S14, ESI†). The presence of strong Te-Cl stretching Raman peaks indicates highly polarised phonon modes arising due to strong electron-phonon coupling. The strength of electron-phonon coupling, as quantified in terms of the Huang-Rhys parameter (S), is estimated to be 12.45 (Fig. S15, ESI†). Such a high coupling constant is in close agreement with the reported electron-phonon coupling constants for 0D Sb(III) halide based hybrids.¹⁹ Time resolved PL measurements of the crystals at low temperatures (decay profiles, extracted lifetimes, and relative weights as in Fig. S16, ESI†) show progressive lengthening of the lifetime as the temperature is lowered.

With these observations in mind, the observed photo-physical properties can be rationalized in terms of a qualitative

configurational coordinate diagram (Fig. 5a) involving the ground state (1S_0), excited states (1P_1 , $^3P_{0,1,2}$) and low lying self-trapped states (STEs). Following photon absorption, an electron is promoted to an excited state and, after its thermalization, is trapped in a long-lived STE state. This trapping is then followed by a slow radiative recombination with broadband emission wherein the Stokes shift likely arises due to the excited state structural reorganization. A thermally activated (phonon assisted) de-trapping pathway, followed by a fast non-radiative recombination process (thermal quenching due to intersection of ground and STE states), is also present and competes effectively with the radiative broadband emission at high temperatures. Clearly, the observed strong intrinsic broadband emission at room temperature (and increase of PL intensity with decreasing temperature) is due to efficient STE radiative recombination that dominates over the non-radiative, high activation energy (Fig. S13, ESI†), thermal quenching pathway.

$(\text{BzTEA})_2\text{TeCl}_6$ crystals exhibit thermal/ambient stability. Thermogravimetric analysis (TGA) of the product (Fig. S17, ESI†) demonstrates thermal stability up to 160°C with ligand loss feature at $\sim 200^\circ\text{C}$ and metal halide unit loss at $\sim 500^\circ\text{C}$. The product is stable under ambient conditions over a month with strong persistent photoluminescence (Fig. S18, ESI†) and no discernible changes in the PXRD pattern (Fig. S19, ESI†). To highlight the utility of excitation features in the visible range, a proof-of-concept down-conversion LED was fabricated using a commercially available blue LED ($\lambda_{\text{emi}} = 447 \text{ nm}$,

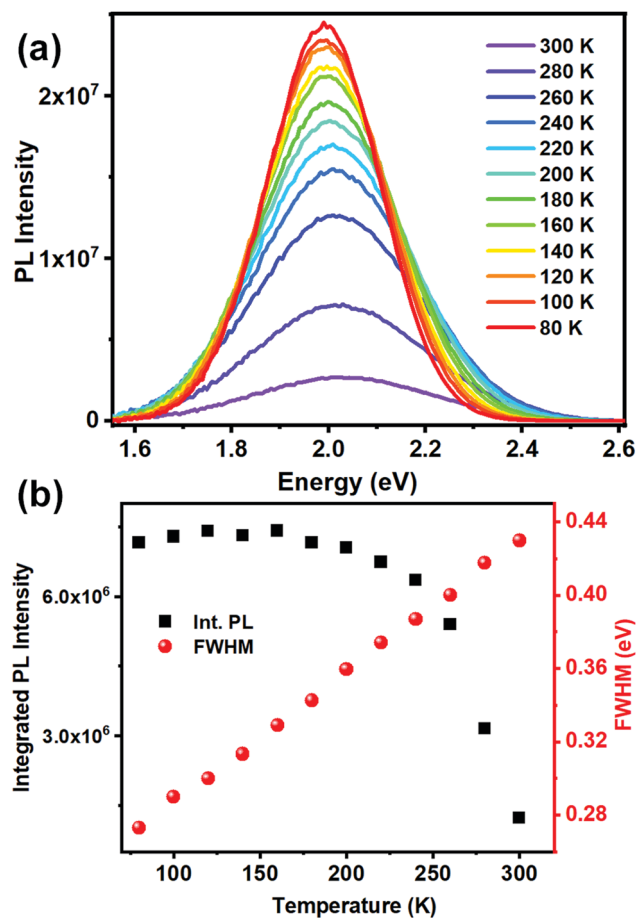


Fig. 4 (a) Low temperature PL ($\lambda_{\text{exc}} = 440 \text{ nm}$) spectra of $(\text{BzTEA})_2\text{TeCl}_6$ crystals; (b) integrated PL intensity and bandwidth (FWHM) as a function of temperature.

FWHM = 20 nm) as the optical source and $(\text{BzTEA})_2\text{TeCl}_6$ hybrid as the phosphor material coated on top of the blue LED (Fig. 5b, insets). Electrical biasing of the resultant LED architecture down-converts blue source light to yellow-orange phosphor light characteristic of the $(\text{BzTEA})_2\text{TeCl}_6$ hybrid (Fig. 5b). The perceived color of the light emanating from the $(\text{BzTEA})_2\text{TeCl}_6$ hybrid, bare LED, and down-conversion LED architecture is presented in the CIE 1931 chromaticity coordinate plot (Fig. 5c) showing successful optical down-conversion using a visible commercial LED. This, by no means, undermines the mild toxicity and rarity of elemental tellurium for their practical applications.

The relevance of the current work within the premise of the burgeoning research efforts on a variety of 0D hybrids (Pb, Sn, Sb) is noted here. Synthesis of strongly emissive (at times near unity PLQY) 0D metal halide hybrids (Sb^{3+} , Pb^{2+} , Sn^{2+}), utilizing organic counter-cationic ligands, relies on a 'hit-or-miss' approach on the choice of ligand. Furthermore, efforts on drawing any correlation between structure/distortion and PLQY for these emissive 0D hybrids (Sb, Sn) (Table S1 and S2, ESI[†]) have met with limited success due to the adoption of a variety of metal halide coordination geometries (octahedral, square pyramidal, disphenoidal, *etc.*) particularly for Sb^{3+} 0D hybrids.

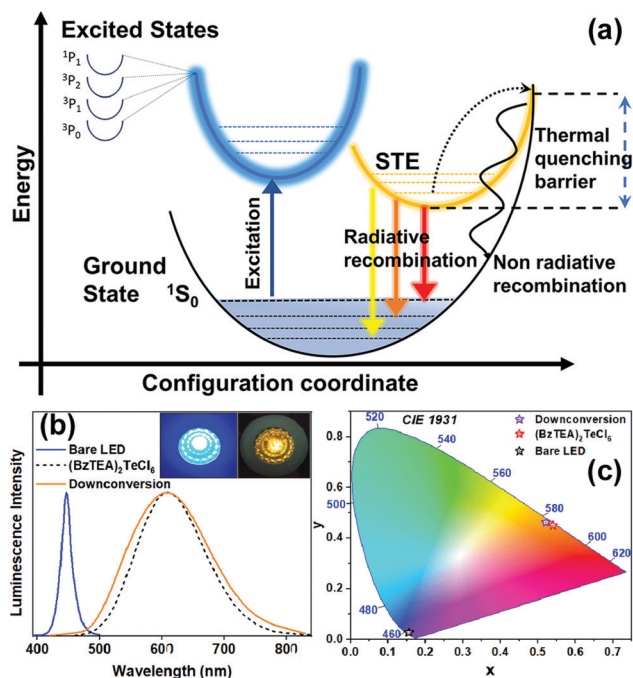


Fig. 5 (a) Schematic representation of the configurational coordinate diagram showing the STE based broad band emission and thermally activated (phonon assisted) non-radiative recombination leading to thermal PL quenching in 0D hybrids. LED characterization (b) electroluminescence of the commercial bare LED, down-converted luminescence from the sample coated LED, and neat sample photoluminescence; inset shows photographs of (i) commercial bare LED and (ii) sample coated down-conversion LED; (c) CIE 1931 Chromaticity coordinate plot for commercial blue LED, down-conversion LED, and neat sample emission.

This has deterred designing chemical control on PLQY for these 0D hybrids (Sb, Sn). Interestingly, Te(IV)halide hybrids, that exclusively adopt an octahedral geometry irrespective of the counter cationic ligand, alleviates the above cited drawback faced by Sb(III) hybrids. Hence, $[\text{TeX}_6]^{2-}$ hybrids are an apt choice for further investigation of structure/distortion-PLQY correlation studies. However, $[\text{TeX}_6]^{2-}$ hybrids typically have low PLQYs at room temperature. Encouragingly, this work demonstrates a $[\text{TeX}_6]^{2-}$ hybrid with high room temperature PLQY ($\sim 15\%$). By no means is the achieved PLQY for this $[\text{TeX}_6]^{2-}$ hybrid comparable to that of Sb/Sn based hybrids. However, the exclusivity of coordination geometry with modest ambient PLQY of the $[\text{TeX}_6]^{2-}$ hybrid opens up the possibility of deciphering structure/distortion – PLQY correlation that is currently missing for the reported main group metal halide (Pb, Sb, Sn) 0D hybrids. Further work on enhancing the ambient PLQY and drawing structure–property correlation for $[\text{TeX}_6]^{2-}$ based 0D hybrids is of enormous importance and is currently underway.

Conclusions

In conclusion, we have successfully synthesized $(\text{BzTEA})_2\text{TeCl}_6$ zero dimensional vacancy ordered double perovskite with strong room temperature luminescence featuring octahedral

Te(IV) chloride as the inorganic unit embedded in the organic ligand (benzyltriethylammonium chloride) matrix. The product shows long lived, intrinsic self-trapping induced broad band, yellow-orange photoluminescence ($\lambda_{\text{emi}} = 610 \text{ nm}$) with high PLQY (15% at room temperature), good thermal/ambient stability, and excitation feature in the visible region ($\sim 445 \text{ nm}$). A test-bed down-conversion LED, fabricated utilizing a visible commercial LED, demonstrates strong room temperature orange down-converted emission. The exclusive adoption of the 'near' regular octahedral structure of the Te(IV)-halide unit provides a unique opportunity to unravel the role played by the $5s^2$ lone pair induced distortion in shaping its luminescence properties. Further synthetic efforts on developing strongly emissive $[\text{TeX}_6]^{2-}$ hybrids utilizing a common templating ligand are underway that would allow drawing a discernible structure/distortion-photophysical property correlation for the 'Pb-free' 0D (Te, Sb, Sn) hybrid luminescent materials.

Conflicts of interest

The authors declare no competing financial interest.

Acknowledgements

The authors acknowledge Milan K Bisai (NCL Pune), Dr J. Nithyanandhan (NCL Pune), and Dr R. Vaidhyanathan (IISER Pune), for insightful discussion. This work was financially supported by DST (Grant No. CRG/2019/000252). A. B. acknowledges CSIR for the Senior Research Fellowship.

References

- C. C. Stoumpos and M. G. Kanatzidis, *Acc. Chem. Res.*, 2015, **48**, 2791–2802.
- B. Saparov and D. B. Mitzi, *Chem. Rev.*, 2016, **116**, 4558–4596.
- C. C. Stoumpos, C. D. Malliakas and M. G. Kanatzidis, *Inorg. Chem.*, 2013, **52**, 9019–9038.
- S. D. Stranks, G. E. Eperon, G. Grancini, C. Menelaou, M. J. P. Alcocer, T. Leijtens, L. M. Herz, A. Petrozza and H. J. Snaith, *Science*, 2013, **342**, 341.
- X. Hong, T. Ishihara and A. V. Nurmikko, *Phys. Rev. B: Condens. Matter Mater. Phys.*, 1992, **45**, 6961–6964.
- Z.-P. Wang, J.-Y. Wang, J.-R. Li, M.-L. Feng, G.-D. Zou and X.-Y. Huang, *Chem. Commun.*, 2015, **51**, 3094–3097.
- C. Zhou, H. Lin, Y. Tian, Z. Yuan, R. Clark, B. Chen, L. J. van de Burgt, J. C. Wang, Y. Zhou, K. Hanson, Q. J. Meisner, J. Neu, T. Besara, T. Siegrist, E. Lambers, P. Djurovich and B. Ma, *Chem. Sci.*, 2018, **9**, 586–593.
- B. M. Benin, D. N. Dirin, V. Morad, M. Wörle, S. Yakunin, G. Rainò, O. Nazarenko, M. Fischer, I. Infante and M. V. Kovalenko, *Angew. Chem., Int. Ed.*, 2018, **57**, 11329–11333.
- R. T. Williams and K. S. Song, *J. Phys. Chem. Solids*, 1990, **51**, 679–716.
- K. M. McCall, C. C. Stoumpos, S. S. Kostina, M. G. Kanatzidis and B. W. Wessels, *Chem. Mater.*, 2017, **29**, 4129–4145.
- M. D. Smith, A. Jaffe, E. R. Dohner, A. M. Lindenberg and H. I. Karunadasa, *Chem. Sci.*, 2017, **8**, 4497–4504.
- R. S. Knox, Introduction to Exciton Physics, in *Collective Excitations in Solids*, Springer, Boston, 1983.
- A. Vogler and H. Nikol, *Comments Inorg. Chem.*, 1993, **14**, 245–261.
- K. M. McCall, V. Morad, B. M. Benin and M. V. Kovalenko, *ACS Mater. Lett.*, 2020, **2**, 1218–1232.
- M. D. Smith and H. I. Karunadasa, *Acc. Chem. Res.*, 2018, **51**, 619–627.
- Z. Xiao, Z. Song and Y. Yan, *Adv. Mater.*, 2019, **31**, 1803792.
- C. Zhou, M. Worku, J. Neu, H. Lin, Y. Tian, S. Lee, Y. Zhou, D. Han, S. Chen, A. Hao, P. I. Djurovich, T. Siegrist, M.-H. Du and B. Ma, *Chem. Mater.*, 2018, **30**, 2374–2378.
- Z. Li, Y. Li, P. Liang, T. Zhou, L. Wang and R.-J. Xie, *Chem. Mater.*, 2019, **31**, 9363–9371.
- D. Chen, F. Dai, S. Hao, G. Zhou, Q. Liu, C. Wolverton, J. Zhao and Z. Xia, *J. Mater. Chem. C*, 2020, **8**, 7322–7329.
- F. Lin, H. Wang, W. Liu and J. Li, *J. Mater. Chem. C*, 2020, **8**, 7300–7303.
- V. Morad, S. Yakunin and M. V. Kovalenko, *ACS Mater. Lett.*, 2020, **2**, 845–852.
- A. Biswas, R. Bakthavatsalam, B. P. Mali, V. Bahadur, C. Biswas, S. S. K. Raavi, R. G. Gonnade and J. Kundu, *J. Mater. Chem. C*, 2021, **9**, 348–358.
- D. Liu, Q. Li, Z. Zhang and K. Wu, *New J. Chem.*, 2019, **43**, 14892–14897.
- B. Krebs and F.-P. Ahlers, *Adv. Inorg. Chem.*, 1990, **35**, 235–317.
- T. V. Sedakova, A. G. Mirochnik and V. E. Karasev, *Opt. Spectrosc.*, 2011, **110**, 755–761.
- T. V. Sedakova and A. G. Mirochnik, *Opt. Spectrosc.*, 2015, **119**, 54–58.
- A. E. Maughan, A. M. Ganose, D. O. Scanlon and R. J. Neilson, *Chem. Mater.*, 2019, **31**, 1184–1195.
- N. Kuhn, A. Abu-Rayyan, K. Eichele, C. Piludu and M. Steimann, *Z. Anorg. Allg. Chem.*, 2004, **630**, 495–497.
- M. H. Ben Ghazlen and J. W. Bats, *Acta Crystallogr., Sect. B: Struct. Crystallogr. Cryst. Chem.*, 1982, **38**, 1308–1309.
- W. Abriel, *Acta Crystallogr., Sect. B: Struct. Sci.*, 1986, **42**, 449–453.
- A. Waśkowska and J. J. Z. Czapla, *J. Alloys Compd.*, 1993, **196**, 255–257.
- I. Caracelli, *Z. Kristallogr. - New Cryst. Struct.*, 2004, **219**, 273–274.
- N.-N. Shen, M.-L. Cai, Y. Song, Z.-P. Ze-Ping Wang, F.-Q. Huang, J.-R. Li and X.-Y. Huang, *Inorg. Chem.*, 2018, **57**, 5282–5291.
- G. Blasse, G. J. Dirksen and W. Abriel, *Chem. Phys. Lett.*, 1987, **136**, 460–464.

- 35 S. S. Yakunin, B. M. Benin, Y. Shynkarenko, O. Nazarenko, M. I. Bodnarchuk, D. N. Dirin, C. Hofer, S. Cattaneo and M. V. Kovalenko, *Nat. Mater.*, 2019, **18**, 846–852.
- 36 B. M. Benin, K. M. McCall, M. Worle, V. Morad, M. Aebli, S. Yakunin, Y. Shynkarenko and M. V. Kovalenko, *Angew. Chem., Int. Ed.*, 2020, **59**, 14490–14497.
- 37 A. K. Viswanath, J. I. Lee, D. Kim, C. R. Lee and J. Y. Leem, *Phys. Rev. B: Condens. Matter Mater. Phys.*, 1998, **58**, 16333.
- 38 G. A. Ozin and A. V. Voet, *Can. J. Chem.*, 1971, **49**, 704–708.
- 39 D. J. Stufkens, *Recl. Trav. Chim. Pays-Bas*, 1970, **89**, 1185–1201.